

**Spin dynamics in a tunable Heisenberg model
realized with ultracold atoms**

by

Paul Niklas Jepsen

B.Sc., Christian-Albrechts Universität zu Kiel (2010)

Submitted to the Department of Physics
in partial fulfillment of the requirements for the degree of

Doctor of Philosophy

at the

MASSACHUSETTS INSTITUTE OF TECHNOLOGY

February 2022

© Massachusetts Institute of Technology 2022. All rights reserved.

Author
Department of Physics
December 31, 2021

Certified by
Wolfgang Ketterle
John D. MacArthur Professor of Physics
Thesis Supervisor

Accepted by
Deepto Chakrabarty
Associate Department Head of Physics

Spin dynamics in a tunable Heisenberg model realized with ultracold atoms

by

Paul Niklas Jepsen

Submitted to the Department of Physics
on December 31, 2021, in partial fulfillment of the
requirements for the degree of
Doctor of Philosophy

Abstract

Spin is the elementary unit of magnetism. The interactions between many spins give a material its magnetic properties. This thesis focusses on one of the simplest magnetic materials: A one-dimensional chain of spins with tunable nearest-neighbor interactions. This system is described by the Heisenberg model, a paradigmatic model, which has been studied for almost a century now. But so far, experiments on spin dynamics have been mostly limited to isotropic spin-spin interactions.

In this work we use ultracold atoms to implement the first quantum simulator for the anisotropic Heisenberg model, with fully adjustable anisotropy of nearest-neighbor spin-spin interactions (also called the XXZ model). We study spin dynamics in previously unexplored regimes far away from equilibrium, as well as stable spin patterns far away from the ground state, which are even exact many-body eigenstates. For this we utilize quantum quenches from initial far-from-equilibrium spin-helix patterns:

Spin transport: By using a longitudinal spin-helix pattern, which involves a modulation in the population of spin up and spin down atoms, we see a drastic impact on the transport properties, when the anisotropy is varied. When spins are coupled only along two of three possible orientations (the XX model), we find ballistic behavior of spin dynamics, whereas for isotropic interactions (the XXX model), we find diffusive behavior. More generally, for positive anisotropies, the dynamics ranges from anomalous superdiffusion to subdiffusion, whereas for negative anisotropies, we observe a crossover in the time domain from ballistic to diffusive transport.

Spin dephasing: A transverse spin-helix pattern is sensitive to additional decay mechanisms: Anisotropic spin couplings break spin-rotational symmetry. Transverse spin components are no longer conserved and can decay not only by transport, but also by fast, local dephasing. However, even for isotropic interactions, we observe dephasing due to a new effect: an effective magnetic field created by superexchange, which has its origin in the mapping from the Hubbard model and which has not been observed before.

Bethe phantom states — excited many-body eigenstates of the Heisenberg model: For a given anisotropy, there exists one special winding angle, such that the transverse

spin helix is an exact many-body eigenstate of the Hamiltonian. We find this eigenstate experimentally, by varying the winding angle and measuring the decay rate, which reveals a pronounced minimum. In a next step, we then use the sensitivity of the Bethe phantom states as a tool, to actually measure the anisotropy directly. We then find that the anisotropy can be strongly affected by nearest-neighbor off-site interactions, which have never been observed before for particles, which only interact with contact interactions.

Our new quantum simulator platform with tunable interactions opens up possibilities for many new studies which are likely to provide new insight into the rich dynamics of Heisenberg spin models and beyond.

Thesis Supervisor: Wolfgang Ketterle

Title: John D. MacArthur Professor of Physics

To my family

Acknowledgments

All the research presented in this thesis has been a huge team effort. I feel very lucky for having been part of such an amazing team. And there are countless people supporting me on the way.

Wolfgang is truly the best advisor I could have ever wished for. I feel really grateful. Wolfgang is incredibly good at physics and solving problems, but also at explaining it and communicating the science in well understandable language. It is amazing to talk about physics with Wolfgang, and I will really miss it. Thank you for teaching me your way of thinking about physics, for letting me learn in my own pace and giving us the freedom to do research the way we want. Thank you for your patience. Thank you for letting me stay in the lab to do one more experiment with Eunice and Hanzhen. Thank you for your support during times when I was struggling. No matter if you gave me amazing physics advice or amazing life advice. Grad school was the best time of my life so far. Thank you, for making me succeed in grad school. And the reason why the science worked out so well in the end, is you.

Jesse, Ivana and I have been the core team of the BEC5 lab for many years. Thank you for this amazing time together. We have built this machine from scratch and got amazing science results together in the end! But there was an intermediate time, when we did struggle, when nothing was working yet. We went through a lot together. Through exciting times and through tough times. We grew into a really good team! And I really miss working with you. You drove me to perform at my best. Thank you, that I could learn so much from both of you. And thank you for making me a better team player! I think there used to be a time, when there was nobody in the world who I spend more time with than you!

Jesse always found the perfect balance between making something perfect and also getting the job done. You always came up with new out of the box ideas. Thank you for implementing the in-situ polarization-rotation imaging. That was a game changer. Thank you for staying in lab with us as a postdoc after defending your thesis!

With Ivana's get-it-done attitude, she was always the driving force in keeping the momentum going in our team. And I would like to emphasize: You are really an amazing experimentalist: When something stopped working, Ivana was the fastest to find the correct knob to turn and fix it. So many times something was not working, and you would just throw in a random lens somewhere and the problem was fixed. Sometimes you would fix something quick and dirty in 5 minutes, for what I would spend a whole day. And I think I actually learned a lot from your way of working. Otherwise I would have never finished the last experiments. Also: Thank you for putting us on the spin $S = 1/2$ route! That was a game changer! For the longest time we were working on $S = 1$ experiments. With your experiment about the tilted Mott insulator, we really moved away from $S = 1$. And this opened up the stage for the anisotropic spin-1/2 Heisenberg model!

Thank you to Wen Wei and Eugene for this fantastic theory-experiment collaboration. Wen Wei, you really explained the Heisenberg model to us experimentalists. Thank you for also contributing so much to actively writing and editing the papers. I was unexperienced and you and Wolfgang showed me how it is done.

Thank you to Hanzhen and Eunice for being amazing new teammates. I had a blast with you this summer (2021), taking data non-stop 24 hours a day and 7 days a week. It was a huge team effort again, and it turned out so well, because both of you gave your best. You are so highly motivated, it is amazing to see how much you have learnt and driven the experiment further, since you joined the lab.

Yair, thank you for helping us in the lab and putting our experiment back together, in a time when the machine was falling apart during the pandemic.

Thank you to all past member of the BEC5 team, especially to Will Lunden, Yichao Yu, Michael Messer, David Weld, Graciana Puentes and Alex Keesling. Thank you for being an important part of our team in the past and helping us build the machine. A lot of your contributions are still crucial parts of the experiment today!

Special thanks to my thesis committee! Martin Zwierlein, when we started building our BEC5 lab, you were starting to build you Fermi2 lab, so that we had friendly competition going on. I have always admired your results, while BEC5 was stuck

with problems for a long time. But once we had results on spin physics, you have always been such a big fan of our research. And that meant a lot to me and it has been very motivating. Thank you for even inviting me to present our work at the student/postdoc triple feature. That was a big honor! And thank you for being so generous, lending us your green laser, which enabled our last experiment on the Bethe phantoms. Kyoshi Masui, thank you for serving on my thesis committee and for being so interested in our work! And special thanks for your patience. Thanks to all of you, Martin, Kyoshi, and Wolfgang, for being so understanding that instead of writing my thesis, I preferred to stay in the lab for one more experiment.

I would especially like to thank Catherine Modica. You have always been there for me for advice of any kind, especially in difficult times. You are really there for all the physics students. And you are a big part for me feeling home at MIT.

Thank you to the whole Ketterle group, present and past members. And thank you to the whole Center for Ultracold Atoms community as a whole. It is really like a cold-atoms-family. And a super special environment to be part of.

There is a special mentor I would like to thank: Dave Pritchard. He was Wolfgang's postdoc advisor, so he is my grandadvisor, so-to-speak. Dave is not just a really good physicist but also a really good sailor! Thanks to you and your wife Andy, for the countless times on the water. It is really interesting to talk with you about physics and also anything else, and you definitely explained to me the physics of sailing! You have always been there for guidance of any kind. As a junior student, when I was new to MIT, it made me settle into the MIT physics community a lot smoother, knowing that you are around.

Misha Lukin has been also a very special mentor to me. Misha is not just a really good physicist. He is also a really good hockey player! And I get to play with him most Saturdays. Thank you, Misha, for all the special mentorship on the ice. You were always there to talk about physics and hockey. Sometimes I would bring our latest results to hockey to discuss them with you afterwards. Thank you for being such a special part of my journey through grad school. It definitely kept me going and motivated. Once Misha said to Wolfgang: "I'm looking forward to seeing Niki

improve at physics as much as he has improved at hockey.”

And I would like to thank *all* of my hockey friends! Hockey has been a really important part of my grad school life: John, Yury, Alexei, Alex, Erik, Theo, Konstantin, JJ, Marco, Christoph, Blake, Eva, Melody, Mallory, Nick, Russian Nick, Timur, George, Andrew, Matt, Lee, Yiqi, Simone, Brian, Sherry, Keith, Kylie, Alan, Nolan, Henry, Aubry, Jon, Nick, Liz, Brett, ... and so many more!

And especially I would like to thank the MIT Hockey team! You made me a better team player, thank you for showing me another world at MIT, thank you for pushing me to my physical limits. I had no idea, how exhausted one could be. Special thanks to our coach and my good friend Nick! And also to coach Dave and coach Tommy for making it an amazing time!

Timur and Lawrence, you have been my best friends in grad in school and my room mates. Living with you made me really feel home in Boston. When things were not working in the lab, you were always there for me and kept me going! Sam and Russian Nick also were a big part of my time at MIT. Melody, I want to thank you for giving me self-confidence in the lab, at a time when I needed it most. Thank you that you were there for me every day when data taking was intense. You were part of the journey, through my PhD. And it was a special time! Tobi and Lilin and Matt, thank you for so many kite surf adventures. Thank you for building me back up in a time when I was struggling. This year (2021) and the last experiment would not have gone this well for me, without you. It made a huge difference. Thanks for always being there for me.

Michael and Nancy, thank you for being my American parents. You have always been welcoming into your family and it always made a huge difference for me to know that you are there. Paul and Judy, thank you for being my west coast parents. Alp and Hatice always had an eye out for me, too, and making sure I'm doing fine. Thank you all for your love and support. I would also like to thank my friends in Germany. Especially Dominik and Arne. You have been such an important part of my life and I can always rely on you.

Most importantly, I would like to thank my family, my parents Karin and Søren,

and my brother Maui. You have worked so hard to give me every opportunity to succeed. I can count on you every moment and you would do anything for me. You have never missed out on any opportunity to visit me in Boston. I could have not done a PhD like this, without your support.

Contents

1	Introduction	15
1.1	Building blocks of condensed matter systems	15
1.2	Ultracold atoms	18
1.3	Magnetism	21
2	The Heisenberg model	25
2.1	Theory	25
2.2	Previous experiments	29
3	Li⁷ in optical lattices	31
3.1	Realization of the Heisenberg model	31
3.2	Far-from-equilibrium spin-helix states	38
3.3	Polarization-rotation imaging	40
3.4	Image analysis	43
3.5	Optical resolution	44
3.6	Summary	46
4	Spin transport	49
4.1	Introduction	50
4.2	Tunable superexchange dynamics	52
4.3	XX model ($\Delta = 0$) and XXX model ($\Delta = 1$)	53
4.4	Positive anisotropies ($\Delta > 0$)	59
4.5	Negative anisotropies ($\Delta < 0$)	63

4.6	Summary	67
5	Transverse spin dynamics	71
5.1	Introduction	72
5.2	XX model	74
5.3	XXX model	78
5.4	Imaging the effective magnetic field	79
5.4.1	Observation as a beatnote	79
5.4.2	Observation through spin precession	81
5.4.3	Spectroscopic observation	84
5.5	Dephasing mechanisms for the transverse spin helix	84
6	Bethe phantom states	87
6.1	Introduction	88
6.2	Stability of transverse spin-helix states	90
6.3	Observations of phantom helix states	92
6.4	Extension to higher dimensions	96
6.5	Direct measurement of the anisotropy	99
7	Summary and Outlook	105
7.1	Summary	105
7.2	Discussion	106
7.3	Outlook	107
A	Spin transport in a tunable Heisenberg model realized with ultracold atoms	115
B	Transverse spin dynamics in the anisotropic Heisenberg model realized with ultracold atoms	137
C	Catching Bethe phantoms and quantum many-body scars: Long-lived spin-helix states in Heisenberg magnets	157

Chapter 1

Introduction

1.1 Building blocks of condensed matter systems

Atoms are the building blocks of ordinary matter. And the interactions between many atoms define its physical properties. For example, in the absence of any interactions, all the atoms would just form a non-interacting gas, the so-called ideal gas, which actually turns out to be a good approximation for many dilute gases we know. But interactions are definitely necessary to make atoms form a liquid or a solid, especially for forming a lattice structure in crystals (see Figure 1-1a). Such systems host lattice vibrations (phonons) which are governed by a dispersion relation and which enable propagation of sound waves (non-equilibrium dynamics), or contribute to heat conduction (near-equilibrium) and to a material's heat capacity (equilibrium).

Charges are the building blocks of electricity. In a solid, the interactions of the electrons with the ion cores and their lattice structure determine a material's electrical properties, such as the electrical resistivity defining whether a material is an insulator, a conductor, or a semi-conductor (see Figure 1-1b). The periodic potential for the electrons create a band structure, describing the range of energy that an electron may have (lying within a band) or may not have (band gaps). Electrons are filling up all available energy levels starting from the lowest one, forming the so-called Fermi sea and the electrical properties are typically defined by the electrons on the top of that Fermi sea: by the electrons at the Fermi surface.

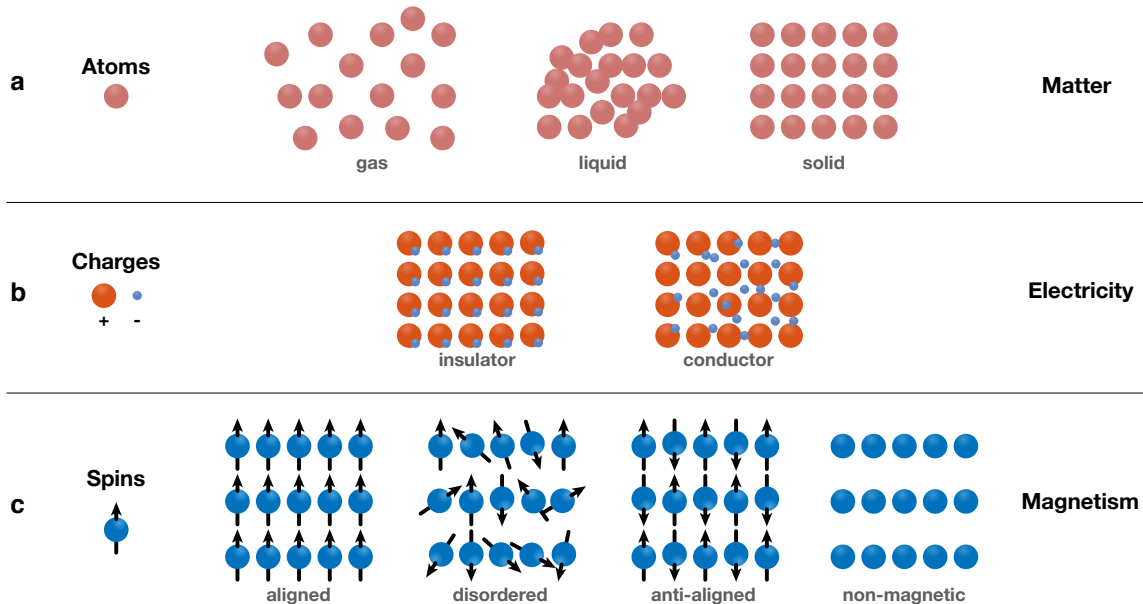


Figure 1-1: **Building blocks of condensed matter systems.** Atoms (a), charges (b), and spins (c) are the building blocks for ordinary matter, electricity, and magnetism.

Spins are the building blocks of magnetism. If all spins in a material are aligned (ferromagnet), the material is magnetized and it creates a magnetic field on its own. If the spins are disordered and point in random directions, their magnetic fields cancel out (see Figure 1-1c). But we could force the spins to align by applying an external magnetic field, which is sufficiently strong. In some materials, spin-spin interactions keep the spins aligned, even if the external magnetic field is removed (ferromagnetism). There are materials, where spins are non-interacting (paramagnetism) and independent from each other. An external field is required for spins to align, so without a field their orientation is random. And in many materials, spins even favor to anti-align with their neighbors (antiferromagnetism). Some materials also do not even have any spins at all; they are non-magnetic. Otherwise, all in all, the magnetic properties of a material are defined by the interplay of many spins and the interactions between them.

The interactions between spins can have different microscopic origins. We note that these interactions typically do *not* involve a magnetic field, as one might naively think. Of course there is a direct interaction of a pair of spins via their magnetic

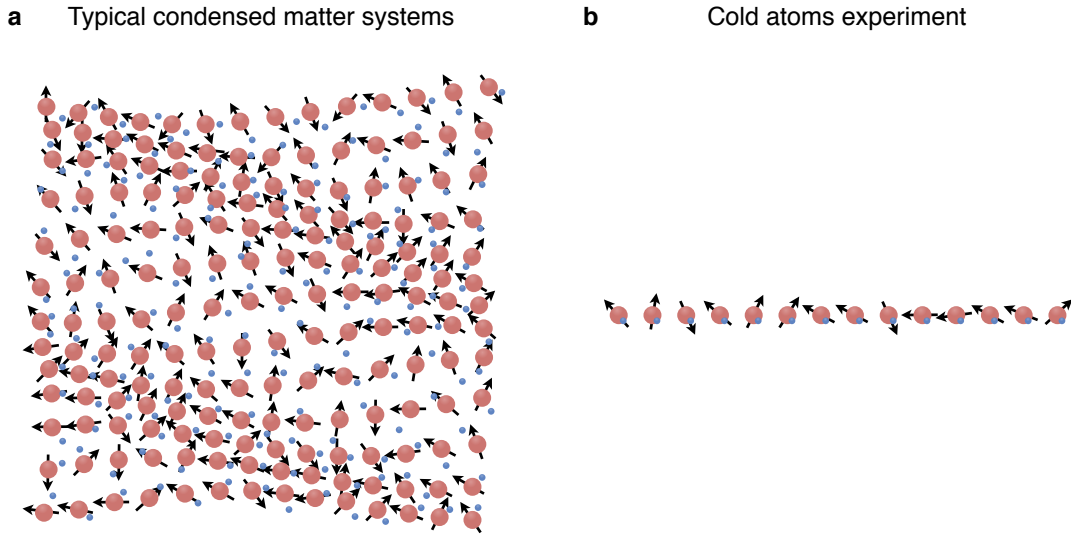


Figure 1-2: **Condensed matter systems built from ultracold atoms.** **a**, In typical condensed matter systems, lattice vibrations (phonons), electron motion, and spins exist all simultaneously and interact with each other. **b**, In order to study magnetism in its pure form, we build a one-dimensional spin-chain using ultracold atoms and engineer tunable spin-spin interactions between nearest neighbors. There are no lattice vibrations (phonons) and no electron motion.

dipole field; however, this interaction is negligible compared to much stronger interactions of different origin [1]. Ferromagnetic spin-spin interactions typically emerge due to Coulomb exchange (also called potential or direct exchange), whereas anti-ferromagnetic spin-spin interactions can be mediated through kinetic exchange from tunneling, also called superexchange.

In the end, we are always dealing with lot of particles and lot of interactions! This is the subject of *condensed matter physics* and *solid state physics* or, more generally, *many-body physics*. The typical problem is that in most materials, all of the above building blocks and interactions appear simultaneously.

Figure 1-2a shows many *atoms* arranged in a lattice structure by their interactions. But this structure is not rigid, atoms can vibrate around their equilibrium position: The lattice can host sound waves. That is illustrated by a snap shot of a large amplitude lattice vibration with a single wavelength λ along a diagonal direction.

Its amplitude is plotted in an exaggerated way. The wavelength also corresponds to a certain value of the vibration frequency. The relation between wavelength and vibration frequency is described by a dispersion relation $\omega = \omega(\mathbf{k})$ for the phonons, where \mathbf{k} is the wavevector with magnitude $|\mathbf{k}| = 2\pi/\lambda$. At any finite temperature, every lattice is filled with a lot of these lattice vibrations. Thermally excited lattice vibrations are actually one big contributor to storing heat in a solid, i.e. to a material's heat capacity.

On top, there is a Fermi sea of *electrons* which interact with the lattice and hence also with the lattice vibrations. The electrons feel the periodic potential from the ion cores, leading to a band structure (dispersion relation for the electrons), which is different from the quadratic dispersion for free electrons. And since the lattice hosts lattice vibrations, the periodic potential is not static, and that leads to electron-phonon interactions. Electrons naturally interact with each other due to Coulomb interactions; these are electron-electron interactions. Furthermore, thermally excited electrons are a second big contributor to a material's heat capacity

And finally, if the material is magnetic, there are *spins*, which also interact with the lattice vibrations, and with the motion of the electrons. Typically, it is even the electrons spin, which make a material magnetic. However, the atomic nucleus also carries a spin (but with typically 10^3 times smaller magnetic moment). And the orbitally motion of bound electrons around the nucleus can also contribute a net magnetic moment which is nonzero.

In order to study magnetism in its pure form, ideally we would like to investigate a system with only localized spins and the interactions between the spins — nothing else, no Fermi sea of electrons, no lattice vibrations (phonons), and ideally the simplest spin arrangement possible, which is still non-trivial: a single chain (as in Figure 1-2b).

1.2 Ultracold atoms

Using ultracold atoms we can build artificial materials like this, which are simplified and idealized systems. We also call this a *quantum simulation*. We simulate a real

condensed matter system, with an artificial system, which obeys the same laws of physics. By now, a number of such platforms exist [2–7], with varying capabilities. In our lab, we use the tools of atomic physics and build condensed matter systems from bottom up. Using laser light, magnetic fields and radio-frequency fields, utilizing techniques such as *laser cooling* and *evaporative cooling*, we bring atoms down to temperatures around $< 1 \mu\text{K}$, freezing out the motional degree of freedom. These ultracold atoms can then be arranged in crystal structures using optical lattices or even arbitrary controlled patterns using spatial light modulators or optical tweezer arrays [8].

Tunable interactions can be engineered between the atoms to implement a whole variety of different Hamiltonians. A strength of quantum simulators is that one can often start by studying a simplified system (e.g. a non-interacting system) and then more complexity can be added (e.g. weak or strong interactions) in a continuous and well-controlled fashion, to see how the systems properties change. In typical condensed matter experiments, interactions are fixed.

Additionally, we can study quantum dynamics far away from equilibrium. In a typical condensed matter system this would be really hard or impossible. For example, an energetically highly excited spin pattern would immediately thermalize with the bath of phonons, which absorb its energy. However, with an isolated spin system we can study the pure spin dynamics in regimes of the Hilbert space, which have never been studied before. So far, most research in condensed matter physics has been limited to *ground states* and *elementary excitations* close to the ground state, and, at higher energies, *thermal states* at finite temperature T . With our quantum simulator, we can study *highly excited pure states* and the following coherent time evolution (quantum dynamics), and even *highly excited eigenstates* of the Hamiltonian, which cannot decay, because the spin system is not coupled to a bath. This is especially true for the *most* excited state! We can study the spin dynamics under the pure Heisenberg model, a paradigmatic model for magnetism, which has been studied extensively for near-equilibrium physics.

Lastly, one-dimensional systems are not only appealing, because they have the



Figure 1-3: **Heisenberg spin chain** with nearest neighbor interactions realized with ultracold atoms. After imprinting spin patterns far away from equilibrium, we study the dynamical behavior of this interacting spin system. The background shows a real image of the spins, revealing an initially high contrast periodic modulation of the (blue) spin $|\uparrow\rangle$ atoms.

simplest geometry. Quantum fluctuations are also much more pronounced than in higher dimensional systems. 1D is the most quantum out of all possible geometries. Similarly, spin-1/2 is the “shortest” and hence the most quantum out of all spins, quantized into two states $|\uparrow\rangle$ and $|\downarrow\rangle$. This makes the spin-1/2 Heisenberg model even *integrable*, i.e. there are as many conserved quantities as degrees of freedom. That allows for especially rich dynamics compared to higher dimensions, where the vast amount of degrees of freedom leads to self-thermalization, where the system acts as its own bath, and any dynamics eventually asymptote to a “boring” thermal state.

In summary, we can say that a quantum simulator is already a simple kind of *quantum computer*. We can control and program the arrangement of the atoms. And we can control and program the interactions between them. However, it is not a *universally* programmable quantum computer. Nevertheless, it is a quantum

computer set up to solve one particular problem. And for us, this is to study the Heisenberg model, i.e. to solve Schrödinger's equation for the time evolution of certain initial states under the Heisenberg Hamiltonian. This is an analog computer.

1.3 Magnetism

Spin is the elementary unit of magnetism. The interactions between many spins give a material its magnetic properties. This thesis focusses on one of the simplest magnetic materials: A one-dimensional chain of spins with nearest-neighbor interactions (Figure 1-3). And these interactions are tunable: By varying these spin-spin interactions, we can control the magnetic material and its properties. This system is described by the Heisenberg model, a paradigmatic model, which has been studied for almost a century now. But nevertheless it is still under active experimental and theoretical investigation, especially its spin transport properties [9–13].

For spin-1/2, the one-dimensional Heisenberg model has been solved analytically almost 100 years ago with the Bethe ansatz [14]. This exact solution explains low-lying excitations very well (single magnons and few-magnon bound states). However, for dynamics far away from the ground state, the Bethe ansatz becomes very technical and it hardly provides any physical intuition, because such dynamics then has to be decomposed into magnons and magnon bound states in a complicated way. Numerical simulations for one-dimensional systems are possible, but the computation time already starts to become unfeasible for large chain lengths with more than 50 spins. Experimentally, it is very difficult to find condensed matter systems, which are described by pure one-dimensional Heisenberg chains. Typical lattice geometries are more complicated. Additionally, spin degrees of freedom couple to lattice vibrations (phonons) and electron motion, which are present in most solids. That makes it hard to study magnetism in its pure form. This is especially true for spin dynamics far away from equilibrium, where coupling to a bath (e.g. bath of phonons) leads to strong dissipation and fast thermalization. In order to study pure coherent quantum dynamics of a many-body system, it needs to be isolated from all other degrees of

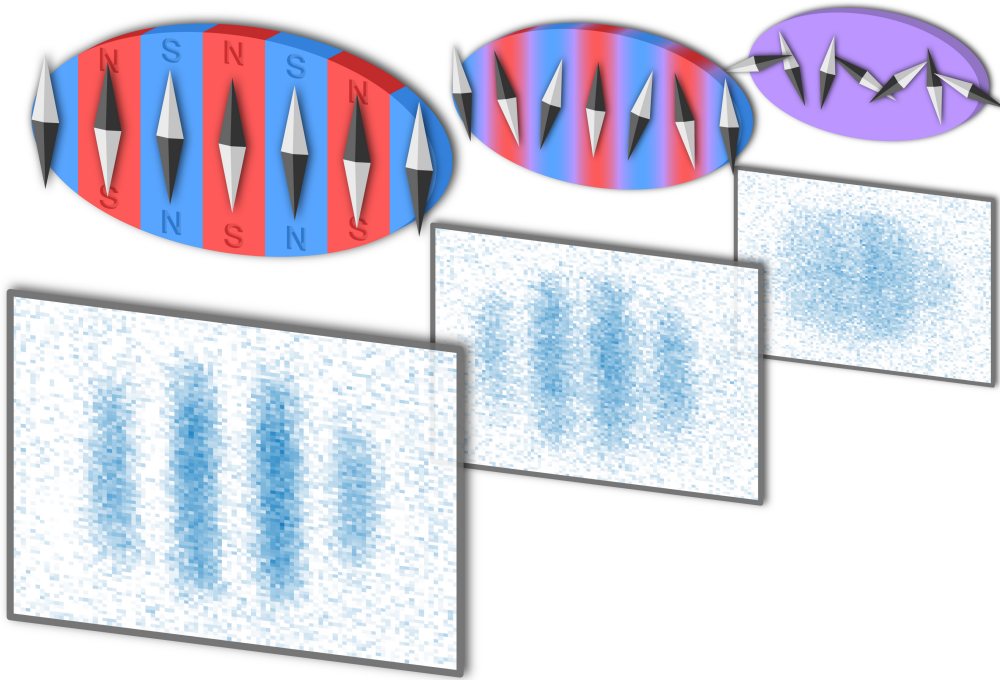


Figure 1-4: **Spin dynamics far away from equilibrium.** The red and blue magnetic domains of opposite magnetization (indicated by compass needles) fade away with time, as seen from left (an earlier image) to right. The bottom row shows real images of the blue domains, here each about 5 atoms wide. Depending on the spin-spin interactions, the domains are observed to fade away due to spin transport (domains mix) or spin dephasing (magnetization gets destroyed locally). Under certain conditions, the spin pattern is stable and does not decay.

freedom: A system which only consists of spins, and interactions between them. On top of that, in most condensed matter systems, the explicit form of the interactions between the spins are fixed and predefined by the material.

In this work we use ultracold atoms to implement the first quantum simulator for the anisotropic Heisenberg model, with fully tunable anisotropy for nearest-neighbor spin-spin interactions. Previous experiments were limited to isotropic spin-spin interactions [15–27]. And we study spin dynamics in previously unexplored regimes far away from equilibrium (Figure 1-4). Dynamical behavior gives new insights into the properties of such a Heisenberg quantum magnet. We do this, by starting with a far-from-equilibrium spin-helix pattern (Figure 1-5) and see how this spin-pattern relaxes over time. This thesis is about a series of three experiments.

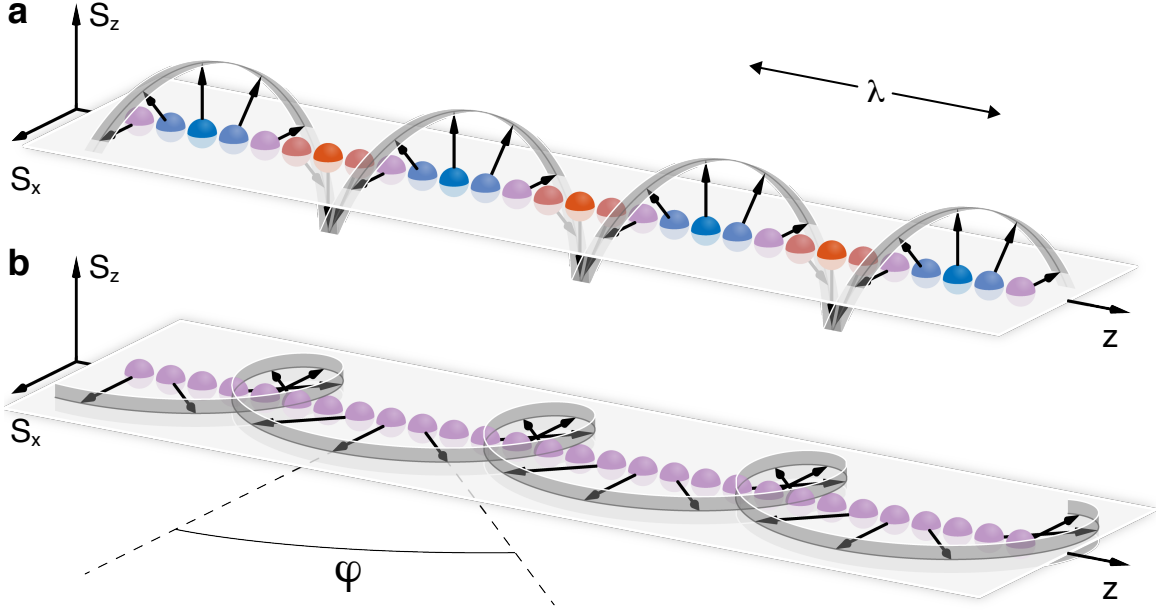


Figure 1-5: **Spin-helix patterns** with adjustable wavelength λ (and wavevector $Q = 2\pi/\lambda$ and winding angle $\varphi = Qa$) are excitations far away from equilibrium. **a**, A *longitudinal* spin helix involves a population modulation of spin $|\uparrow\rangle$ and $|\downarrow\rangle$. It can only decay by spin transport, because spin $|\uparrow\rangle$ and $|\downarrow\rangle$ atoms have to travel through the spin chain in order to mix. **b**, A *transverse* spin helix is a pure phase modulation, and it can also decay by fast, local dephasing. However, for one special winding angle φ , the transverse spin helix is an exact many-body eigenstate of the Heisenberg model, far away from the ground state, and does not decay.

1. *Spin transport* [28]: By using a longitudinal spin-helix pattern (Figure 1-5a), which involves a modulation in the population of spin $|\uparrow\rangle$ and spin $|\downarrow\rangle$ atoms, we see a drastic impact on the transport properties, when the anisotropy is varied. When spins are coupled only along two of three possible orientations (the XX model), we find ballistic behavior of spin dynamics, whereas for isotropic interactions (the XXX model), we find diffusive behavior. More generally, for positive anisotropies, the dynamics ranges from anomalous superdiffusion to subdiffusion, whereas for negative anisotropies, we observe a crossover in the time domain from ballistic to diffusive transport. Those are two strikingly different crossover phenomena: Anomalous diffusion for positive anisotropies and behavior reminiscent of a classical gas for negative anisotropies.
2. *Spin dephasing* [29]: A transverse spin-helix pattern (Figure 1-5b) is sensitive

to additional decay mechanisms: Anisotropic spin couplings in the Hamiltonian break spin-rotational symmetry. Transverse spin components are no longer conserved and can decay not only by transport, but also by fast, local dephasing. However, even for isotropic interactions, we observe dephasing due to a new effect: an effective magnetic field created by superexchange, which has its origin in the mapping from the Hubbard model and which has not been observed before. This field leads to additional dephasing mechanisms: there is dephasing due to (i) inhomogeneity of the effective field from variations of lattice depth between chains; (ii) a twofold reduction of the field at the edges of finite chains; and (iii) fluctuations of the effective field due to the presence of mobile holes in the system. The latter is a new coupling mechanism between holes and magnons.

3. *Bethe phantom states — highly excited many-body eigenstates of the Heisenberg model* [30]: For a given anisotropy, there exists one special winding angle (Figure 1-5b), such that the transverse spin-helix is an exact many-body eigenstate of the Hamiltonian. We find this eigenstate experimentally, by varying the winding angle and measuring the decay rate, which reveals a pronounced minimum. In a next step, we then use the sensitivity of the Bethe phantom states as a tool, to actually measure the anisotropy directly. We then find that the anisotropy can be strongly affected by nearest-neighbor off-site interactions, which have never been observed before for particles, which only interact with contact interactions.

Chapter 2

The Heisenberg model

2.1 Theory

The Heisenberg model describes localized spins with nearest neighbor interactions.

$$H = J \sum_{\langle ij \rangle} \mathbf{S}_i \cdot \mathbf{S}_j = J \sum_{\langle ij \rangle} (S_i^x S_j^x + S_i^y S_j^y + S_i^z S_j^z) \quad (2.1)$$

Here $\mathbf{S}_i = (S_i^x, S_i^y, S_i^z)$ are the spin vectors, and the sum is over all pairs of nearest neighbors $\langle ij \rangle$. In the classical limit, the interaction energy between the two spins \mathbf{S}_i and \mathbf{S}_j is proportional to the overlap $\mathbf{S}_i \cdot \mathbf{S}_j = S^2 \cos \theta_{ij}$, where θ_{ij} is the angle between \mathbf{S}_i and \mathbf{S}_j , and S is their length (or in other words: the projection of \mathbf{S}_i onto \mathbf{S}_j). For $J < 0$, neighboring spins favor alignment (ferromagnetic model). For $J > 0$, they favor antialignment (antiferromagnetic model). For $J = 0$, spins are non-interacting (paramagnetic model). For finite $J \neq 0$, this is the *isotropic* Heisenberg model, where spin-spin interactions are isotropic and characterized by a single parameter: the coupling constant J . The scalar product $\mathbf{S}_i \cdot \mathbf{S}_j$ is rotationally symmetric and the interaction energy between two spins only depends on the angle θ_{ij} between them. But there is no preferred overall direction in spin-space.

The Heisenberg model has been used extensively to study its ground state, equilibrium physics at a temperature T (in contact with a bath), and phase transitions. But dynamics far from equilibrium have been left relatively unexplored. If a given

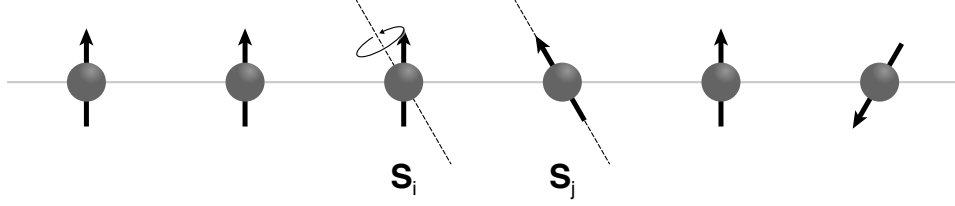


Figure 2-1: **Heisenberg model with classical spins.** A spin \mathbf{S}_i experiences a torque from its neighbor \mathbf{S}_j , given by $J \mathbf{S}_j \times \mathbf{S}_i$, forcing it to precess around the axis parallel to \mathbf{S}_j (dashed line). At the same time, it experiences a torque from its other neighbor. This leads to a set of coupled equations of motion for all spins.

spin \mathbf{S}_i is *not* aligned (or anti-aligned) with its neighbor \mathbf{S}_j , it experiences a torque $J \mathbf{S}_j \times \mathbf{S}_i$ towards the aligned ($J > 0$) or anti-aligned ($J < 0$) configuration exerted on it by its neighbor \mathbf{S}_j . Since spins carry intrinsic angular momentum, \mathbf{S}_i is then forced to precess around the axis parallel to \mathbf{S}_j , such that $d\mathbf{S}_i/dt = J \mathbf{S}_j \times \mathbf{S}_i$ is its equation of motion (see Figure 2-1). Simultaneously, also \mathbf{S}_j experiences a torque exerted by \mathbf{S}_i , so the spins are actually forced to precess around each other. For the full spins system, every given spin \mathbf{S}_i experiences a torque from each of its neighbors, leading to a set of coupled equations of motion $d\mathbf{S}_i/dt = (\partial H / \partial \mathbf{S}_i) \times \mathbf{S}_i$, which yield $d\mathbf{S}_i/dt = J (\mathbf{S}_{i-1} + \mathbf{S}_{i+1}) \times \mathbf{S}_i$ in the case of a one-dimensional spin chain, where every spin has two neighbors. These are the so-called Landau-Lifshitz equations of motion for classical spins. For a large number of spins, the collective dynamical behavior far from equilibrium can be very complicated.

In the *anisotropic* Heisenberg model, the longitudinal and transverse spin couplings J_z and J_{xy} can be different.

$$H = \sum_{\langle ij \rangle} [J_z S_i^z S_j^z + J_{xy} (S_i^x S_j^x + S_i^y S_j^y)] \quad (2.2)$$

And the anisotropy $\Delta := J_z / J_{xy}$ is defined as the ratio between the two. By changing this value, we can vary the relative importance of the two terms in the Hamiltonian. For $|J_z| > |J_{xy}|$ alignment (or antialignment) is favored in the S_z -direction, whereas for $|J_{xy}| > |J_z|$ this favored direction is within the S_x - S_y plane. $\Delta \neq 1$ implies that there is a preferred direction in spin-space, so spin-rotational symmetry of the Heisenberg

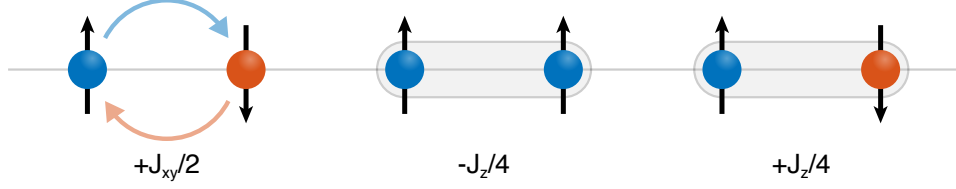


Figure 2-2: **Heisenberg model with quantum spins.** The transverse spin coupling J_{xy} leads to spin exchange (left), where two neighboring sites exchange their spins. The longitudinal spin coupling J_z is a spin-spin interaction which favors alignment for $J_z < 0$ (middle) and anti-alignment for $J_z > 0$ (right).

Hamiltonian is broken. In all previous ultracold-atoms experiments the anisotropy was fixed at $\Delta \approx 1$ [15–19, 25–27]. We, however, can adjust the anisotropy freely, going beyond previous experiments. This leads to new interesting physics which is the subject of this thesis.

For classical spins, the Landau-Lifshits equations $d\mathbf{S}_i/dt = (\partial H/\partial \mathbf{S}_i) \times \mathbf{S}_i$ still apply, but the dynamics is more complicated due to the anisotropic couplings. However, quantum mechanical spins follow the rules of quantum mechanics (Figure 2-2). They are now described by spin operators $\mathbf{S}_i = (S_i^x, S_i^y, S_i^z)$. For spin quantum number $S = 1/2$, spin $|\uparrow\rangle$ and $|\downarrow\rangle$ are the spin states pointing in the $\pm S_z$ -direction. And more generally, a spin state pointing along the direction of $\mathbf{n} = (\cos \theta, \sin \theta \cos \phi, \sin \theta \sin \phi)$ is given by $|\psi(\theta, \phi)\rangle = \cos(\theta/2) |\uparrow\rangle + \sin(\theta/2)e^{-i\phi} |\downarrow\rangle$, with polar angle θ and azimuthal angle ϕ . With spin $|\uparrow\rangle$ and $|\downarrow\rangle$ as the basis states, we can interpret the two terms in the Hamiltonian in the following way:

The first term $J_z S_i^z S_j^z$ is still a spin-spin interaction. For negative values $J_z < 0$ it favors alignment between neighboring spins. For positive values $J_z > 0$ it favors anti-alignment.

$$J_z S_i^z S_j^z |\uparrow_i \uparrow_j\rangle = +\frac{J_z}{4} |\uparrow_i \uparrow_j\rangle \quad (2.3)$$

$$J_z S_i^z S_j^z |\downarrow_i \downarrow_j\rangle = +\frac{J_z}{4} |\downarrow_i \downarrow_j\rangle \quad (2.4)$$

$$J_z S_i^z S_j^z |\uparrow_i \downarrow_j\rangle = -\frac{J_z}{4} |\uparrow_i \downarrow_j\rangle \quad (2.5)$$

$$J_z S_i^z S_j^z |\downarrow_i \uparrow_j\rangle = -\frac{J_z}{4} |\downarrow_i \uparrow_j\rangle \quad (2.6)$$

The second term $J_{xy}(S_i^x S_j^x + S_i^y S_j^y) = J_{xy}(S_i^+ S_j^- + S_i^- S_j^+)/2$ is a spin-exchange term, a coupling term, which allows two neighboring sites to exchange their spins. This term is the origin of spin transport.

$$J_{xy}(S_i^x S_j^x + S_i^y S_j^y) |\uparrow_i \uparrow_j\rangle = 0 \quad (2.7)$$

$$J_{xy}(S_i^x S_j^x + S_i^y S_j^y) |\downarrow_i \downarrow_j\rangle = 0 \quad (2.8)$$

$$J_{xy}(S_i^x S_j^x + S_i^y S_j^y) |\uparrow_i \downarrow_j\rangle = \frac{J_{xy}}{2} |\downarrow_i \uparrow_j\rangle \quad (2.9)$$

$$J_{xy}(S_i^x S_j^x + S_i^y S_j^y) |\downarrow_i \uparrow_j\rangle = \frac{J_{xy}}{2} |\uparrow_i \downarrow_j\rangle \quad (2.10)$$

That is a pure quantum effect. We note that, in contrast, in the classical limit, a state $|\uparrow_i \downarrow_j\rangle$ would not evolve. Both spins feel zero torque, because they are anti-parallel. However, in quantum mechanics, both spins have quantum fluctuations in the S^x and S^y direction, which are zero only on average. These quantum fluctuations exert a torque on each spin's neighbor and cause them to spin-flip.

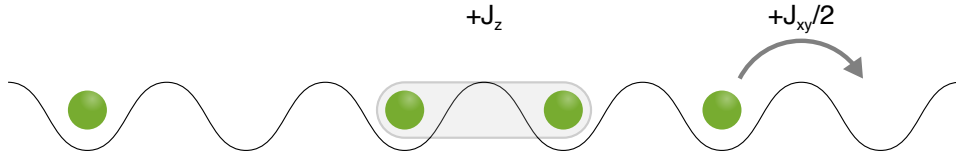


Figure 2-3: **Mapping to spin-less fermions.** By mapping spin $|\uparrow\rangle$ to a fermion $|1\rangle$ and spin $|\downarrow\rangle$ to an empty site $|0\rangle$, we can interpret J_{xy} as a hopping rate for fermions, and J_z as a nearest-neighbor interaction.

In this spin $|\uparrow\rangle$ and $|\downarrow\rangle$ basis, the Hamiltonian features a competition between two terms. The first term $J_z S_i^z S_j^z$ is an *interaction* term between $|\uparrow\rangle$ and $|\downarrow\rangle$ spins. The second term $J_{xy}(S_i^+ S_j^- + S_i^- S_j^+)/2$ is a *kinetic* term of $|\uparrow\rangle$ and $|\downarrow\rangle$ spins. In fact (at least in 1D) we can understand this system even more intuitively in terms of spin-less fermions, by mapping spin $|\uparrow\rangle$ onto one fermion and spin $|\downarrow\rangle$ onto an empty site (Figure 2-3), by the so-called Jordan-Wigner transformation [31]. Then J_{xy} can be interpreted as the hopping matrix element for the fermions, and J_z as the nearest-neighbor interaction. In our experiment we can switch-off this interaction ($J_z = 0$), or we can make it repulsive ($J_z > 0$), or we can also make it attractive ($J_z < 0$).

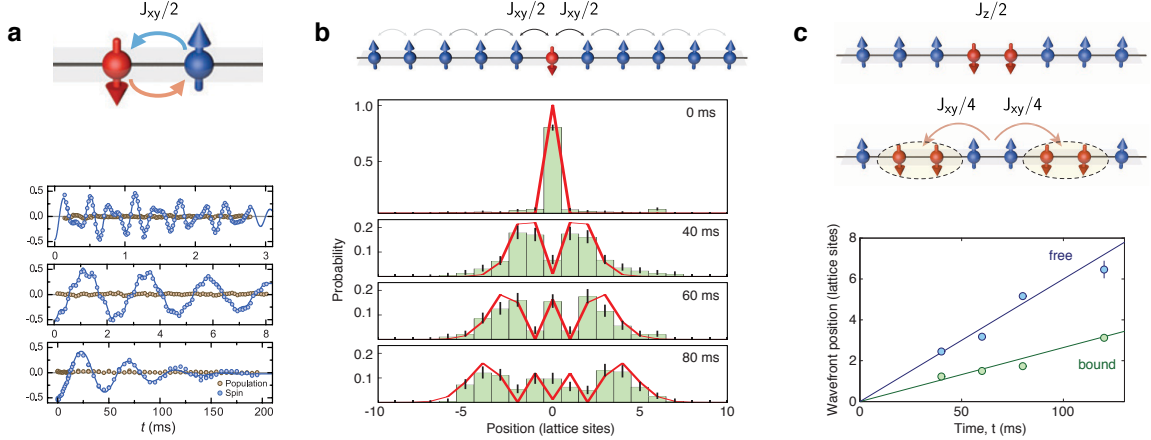


Figure 2-4: **Previous experiments** near the ground state. **a**, Superexchange with two spins [7]. Spin-imbalance (blue) and mass imbalance (gray) was measured as a function of time. **b**, One single magnon in a spin-chain [17]. The initially localized wavefunction (at time $t=0$) of the magnon spreads out as a function of time (shown for $t=40$ ms, 60 ms, 80 ms). **c**, Two interacting magnons form a bound state [18]. The wavefront positions are plotted as a function of time for both the travelling bound state (green) and for free magnons (blue), revealing a velocity ratio of 2.

2.2 Previous experiments

Spin exchange J_{xy} has first been directly observed in ultracold atoms in a double-well potential by the Bloch group [7]. Two opposite spins swap places at the spin-exchange rate J_{xy}/h (Figure 2-4a). Using a quantum gas microscope with single site resolution, the same group even directly observed spin exchange in a whole spin chain [17]. A single spin-flip travels with *ballistic* wavefronts (Figure 2-4b). Such a single free magnon, initially localized to one lattice site, then moves in both directions simultaneously through the spin chain, undergoing a quantum random walk. Interactions J_z do not play a role here, because this is a single free magnon $|\downarrow\rangle$ moving in a background of $|\uparrow\rangle$ spins. Flipping one single spin in the $|\uparrow\rangle$ -background to $|\downarrow\rangle$, has an energy cost of $2 \cdot J_z/4$, no matter where the spin $|\uparrow\rangle$ is located.

For two spin-flips this is different. Interactions J_z can now lead to a two-magnon bound state [18]. For $J_z < 0$, magnons are attractively bound. Flipping two spins in the $|\uparrow\rangle$ -background to $|\downarrow\rangle$ costs an energy of $4 \cdot J_z/4$, when they are more than one lattice site apart from each other. But if they are neighbors, the energy cost is only $2 \cdot J_z/4$. The two-magnon bound state still travels with *ballistic* wavefronts. The two

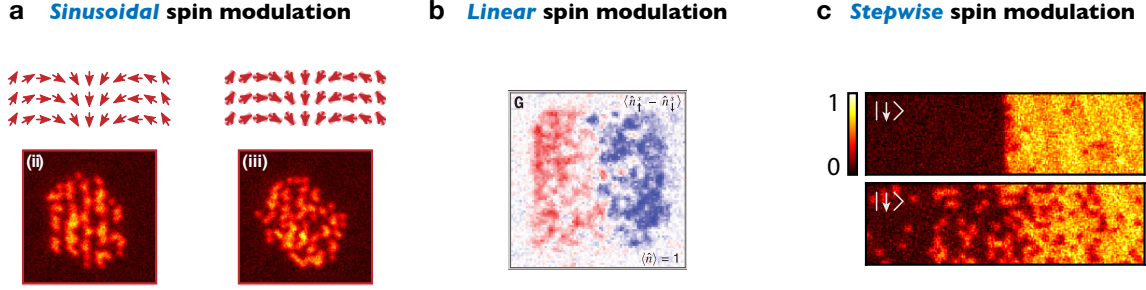


Figure 2-5: **Previous experiments** far away from equilibrium. **a**, A sinusoidal spin modulation (spin-helix) with initially 100% contrast (left) fades away (right) due to spin transport [19]. **b**, A linear spin modulation (created by a magnetic gradient) displays a spatial spin imbalance in opposite sides of the sample, which mixes due to spin transport [15]. **c**, A stepwise spin modulation (sharp domain wall) which is initially perfectly sharp (top) smoothens out (bottom) due to spin transport across the interface [33].

magnons just move together (Figure 2-4c). But the velocity is smaller, since it now requires two spin-exchange processes for the bound state to move by one lattice site. (The first magnon has to move first. Then the second magnon has to follow.) This is a higher-order process involving an intermediate with higher energy. Theory predicts that the bound magnons move a factor of 2 slower, or a factor of 2Δ for general anisotropies [32], and that is what is being observed experimentally, too. Actually, there is also a small probability that the two-magnon bound state breaks up, which has been studied experimentally by Ref. [18], as well.

For *many* spin-excitations however, interactions change the transport behavior into *diffusion*. This was observed both for a sinusoidal spatial spin modulation in Ref. [19] in 2014 (Figure 2-5a), as well as a linear spatial spin modulation in the Zwierlein group [15] in 2019 (Figure 2-5b). A recent experiment by the Bloch group [33] in 2021 (Figure 2-5c) studied the dynamics for a sharp domain wall, where the spin modulation is a step function, which shows superdiffusive behaviour.

All of these experiments realize the *isotropic* Heisenberg model, where the anisotropy is fixed at $\Delta = 1$. The following chapter explains how we implement a Heisenberg model with tunable anisotropies, using the two lowest hyperfine states of ${}^7\text{Li}$ as spin $|\uparrow\rangle$ and $|\downarrow\rangle$ states in an optical lattice, and controlling their interactions with Feshbach resonances.

Chapter 3

Li⁷ in optical lattices

3.1 Realization of the Heisenberg model

Two component bosons in an optical lattice are described by the Hubbard model

$$H = - \sum_{\langle ij \rangle \sigma} (t a_{i\sigma}^\dagger a_{j\sigma} + \text{H.c.}) + \sum_{i\sigma} \frac{U_{\sigma\sigma}}{2} n_{i\sigma} (n_{i\sigma} - 1) + \sum_i U_{\uparrow\downarrow} n_{i\uparrow} n_{i\downarrow} \quad (3.1)$$

characterized by the tunneling matrix element t and the on-site interactions $U_{\uparrow\uparrow}$, $U_{\uparrow\downarrow}$, and $U_{\downarrow\downarrow}$. In the Mott insulating regime with one atom per lattice site, the motional degree of freedom is frozen out and atoms are localized to individual lattice sites [34]. The remaining degree of freedom forms an effective spin model [35–38], where spin-spin interactions are mediated by second-order tunneling [7] (see Figure 3-1). In the limit of $t \ll U_{\uparrow\uparrow}, U_{\uparrow\downarrow}, U_{\downarrow\downarrow}$, the tunneling term $V = - \sum_{\langle ij \rangle \sigma} (t a_{i\sigma}^\dagger a_{j\sigma} + \text{H.c.})$ can be treated as a perturbation. The Hubbard model H can then be mapped to an effective spin Hamiltonian H_{eff} , by the Schrieffer–Wolff transformation [39, 40], with matrix elements

$$\langle m | H_{\text{eff}} | n \rangle = E_n \delta_{nm} + \langle m | V | n \rangle + \frac{1}{2} \sum_k \langle m | V | k \rangle \left(\frac{1}{E_m - E_k} + \frac{1}{E_n - E_k} \right) \langle k | V | n \rangle + \dots \quad (3.2)$$

where $|n\rangle$, $|m\rangle$ and $|k\rangle$ are the eigenstates of the unperturbed Hamiltonian $H_0 = \sum_{i\sigma} \frac{U_{\sigma\sigma}}{2} n_{i\sigma} (n_{i\sigma} - 1) + \sum_i U_{\uparrow\downarrow} n_{i\uparrow} n_{i\downarrow}$. The zeroth- and first-order terms are zero. The

second-order terms are called *superexchange*, or second-order tunneling, because it involves two tunneling matrix elements connecting an *initial* state $|n\rangle$ to a *final* state $|m\rangle$ via an *intermediate* state $|k\rangle$, which is detuned in energy by $E_n - E_k$ and $E_m - E_k$, respectively, appearing in the denominator. We show in the following that this effective Hamiltonian is the anisotropic Heisenberg model

$$H = \sum_{\langle ij \rangle} [J_z S_i^z S_j^z + J_{xy} (S_i^x S_j^x + S_i^y S_j^y)] - \sum_i h_z S_i^z \quad (3.3)$$

in the presence of an effective magnetic field h_z .

Figure 3-1 displays a list of all nonzero effective matrix elements for a given pair of nearest neighbors. (a), (b) and (c) are *diagonal* matrix elements, where the initial and final state are identical $|n\rangle = |m\rangle$. (d) is an *off-diagonal* matrix element, where $|n\rangle \neq |m\rangle$. In (a), both spins are aligned pointing up $|\uparrow; \uparrow\rangle$. One spin tunnels to its neighbor with matrix element $\sqrt{2}t$, this costs energy $U_{\uparrow\uparrow}$ and it tunnels back with $\sqrt{2}t$, resulting in an effective matrix element of $-2t^2/U_{\uparrow\uparrow}$. The factor of 2 is the result of Bose enhancement. (Intuitively speaking, in this process there seem to be two possible final states: The two spins $|\uparrow_1; \uparrow_2\rangle$ can either swap their places $|\uparrow_1; \uparrow_2\rangle \rightarrow |\uparrow_2; \uparrow_1\rangle$, or return to their original places $|\uparrow_1; \uparrow_2\rangle \rightarrow |\uparrow_1; \uparrow_2\rangle$. In quantum mechanics these seemingly two final states are indistinguishable, hence the factor of 2 stems from bosonic counting statistics.) There is an additional factor of 2 accounting for the two possible intermediate states: $|\uparrow\uparrow; 0\rangle$ and $|0; \uparrow\uparrow\rangle$ (both spins meeting either on the left site or on the right site). So the total effective matrix element is $-4t^2/U_{\uparrow\uparrow}$. In the case of fermions, this matrix element is zero, because two fermions cannot be in the same quantum state. Both particles are already in the same spin $|\uparrow\rangle$ state, so they cannot share the same lattice site. This effectively results in $U_{\uparrow\uparrow} \approx +\infty$ (“infinite repulsion”). A more rigorous argument is that the tunneling matrix element — instead of being *Bose enhanced*, yielding $\sqrt{2} \cdot t$ — is now *Fermi suppressed*, yielding $0 \cdot t$. (We note that the two fermions can nevertheless share the same lattice site, if they occupy different spatial wave functions, but this contribution is neglected in a lowest band description, where higher excited bands are energetically suppressed.) In (b), both

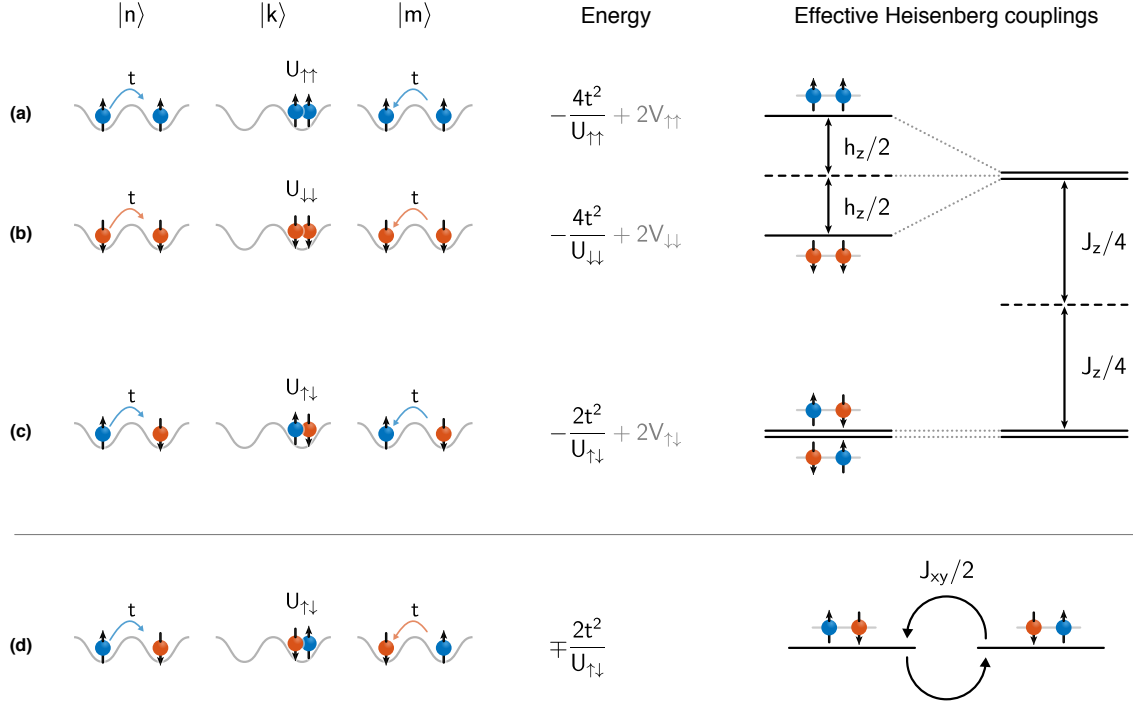


Figure 3-1: Mapping to the Heisenberg model. Spin interactions are mediated by superexchange: second-order tunneling between initial and final states $|n\rangle$ and $|m\rangle$, involving an intermediate state $|k\rangle$, which is detuned in energy. The interactions energy scales as matrix element squared over energy. The diagonal matrix elements (a)-(c) mediate the spin-spin interaction J_z . The off-diagonal matrix element (d) induces spin-exchanges J_{xy} . The energy difference between $|\uparrow\uparrow\rangle$ and $|\downarrow\downarrow\rangle$ (both aligned) can be interpreted as induced by an effective magnetic field $h_z = 4t^2/U_{\uparrow\uparrow} - 4t^2/U_{\downarrow\downarrow}$, which shifts their energies away from the averaged value $-2t^2/U_{\uparrow\uparrow} - 2t^2/U_{\downarrow\downarrow}$ (aligned configuration). Comparing this to the energy of $|\uparrow\downarrow\rangle$ and $|\downarrow\uparrow\rangle$ which is $-2t^2/U_{\uparrow\downarrow}$ (anti-aligned configuration) defines the effective spin-spin coupling $J_z/2 = 2t^2/U_{\uparrow\downarrow} - (2t^2/U_{\uparrow\uparrow} - 2t^2/U_{\downarrow\downarrow})$. There is also a contribution from direct nearest-neighbor off-site interactions $V_{\uparrow\uparrow}$, $V_{\uparrow\downarrow}$, $V_{\downarrow\downarrow}$, which adds as a correction to the effective superexchange matrix elements.

spins are aligned pointing down $|\downarrow; \downarrow\rangle$ and following the same reasoning as in (a), the effective matrix element is now $-4t^2/U_{\downarrow\downarrow}$. In (c), the spins are anti-aligned $|\uparrow; \downarrow\rangle$. We count two intermediate states again: $|\uparrow\downarrow; 0\rangle$ and $|0; \uparrow\downarrow\rangle$ resulting in a factor of 2 such that the effective matrix element is $-2t^2/U_{\uparrow\downarrow}$. But there is no Bose enhancement (or no Fermi suppression), because the particles are in different spin states. Intuitively speaking, there is only one possible final state: The two spins return to their original places $|\uparrow; \downarrow\rangle \rightarrow |\uparrow; \downarrow\rangle$. If they swap their places $|\uparrow; \downarrow\rangle \rightarrow |\downarrow; \uparrow\rangle$, this is captured by

the off-diagonal matrix element (d), also yielding $-2t^2/U_{\uparrow\downarrow}$ for bosons. In the case of fermions we get an additional factor of -1 because we interchanged the two particles, yielding $+2t^2/U_{\uparrow\downarrow}$.

These superexchange mediated interactions between spins lead to an effective spin model, which is exactly described by the anisotropic Heisenberg model, discussed in the previous chapter. So far, spin dynamics in optical lattice has been studied for repulsive on-site interactions $U_{\uparrow\uparrow}, U_{\uparrow\downarrow}, U_{\downarrow\downarrow} > 0$, because attractive interactions generally cause instabilities. Repulsive interactions ensure that a Bose-Einstein condensate is stable, and that the Mott insulator is the ground state for strong interactions in a lattice. Previous experiments were limited to isotropic interactions for the following reasons:

For fermions, the Pauli exclusion principle enforces isotropic antiferromagnetism [15, 25–27]. The two superexchange matrix elements (a) and (b) for aligned spins $|\uparrow; \uparrow\rangle$ and $|\downarrow; \downarrow\rangle$ are zero due to Fermi suppression. Superexchange interactions then affect only anti-aligned spins $|\uparrow; \downarrow\rangle$ in (c) lowering their energy to yield $-2t^2/U_{\uparrow\downarrow}$ and hence favoring this anti-aligned configuration (at least for typical systems, where interactions are repulsive $U_{\uparrow\downarrow}$). Since in a Heisenberg model, the aligned ($|\uparrow; \uparrow\rangle$ and $|\downarrow; \downarrow\rangle$) and anti-aligned ($|\uparrow; \downarrow\rangle$ and $|\downarrow; \uparrow\rangle$) configuration are split in energy by $J_z/2$, the resulting longitudinal coupling is $J_z/2 = +2t^2/U_{\uparrow\downarrow}$. Fermionic statistics also result in a positive sign for spin-exchange (d) yielding $J_{xy}/2 = +2t^2/U_{\uparrow\downarrow}$. The result is *isotropic* and *antiferromagnetic* spin couplings (for the typically repulsive interactions $U := U_{\uparrow\downarrow} > 0$):

$$J_z = J_{xy} = +\frac{4t^2}{U} > 0. \quad (3.4)$$

For bosons, the most commonly used atom, ^{87}Rb , has almost equal singlet and triplet scattering lengths (resulting in $U_{\uparrow\uparrow} \approx U_{\uparrow\downarrow} \approx U_{\downarrow\downarrow}$), implying effectively isotropic spin physics [16–19]. The two superexchange matrix elements (a) and (b) for aligned spins $|\uparrow; \uparrow\rangle$ and $|\downarrow; \downarrow\rangle$ are now Bose enhanced by a factor of 2, compared to the anti-aligned spins $|\uparrow; \downarrow\rangle$ in (c), and hence favoring the aligned configuration (at least for typical systems, where interactions are repulsive $U_{\uparrow\uparrow} \approx U_{\uparrow\downarrow} \approx U_{\downarrow\downarrow} > 0$), with longitu-

dinal coupling $J_z/2 = -2t^2/U_{\uparrow\downarrow}$. Bosonic statistics also results in a negative sign for spin-exchange (d) yielding $J_{xy}/2 = -2t^2/U_{\uparrow\downarrow}$. The result is *isotropic* and *ferromagnetic* spin couplings (for the typically repulsive interactions $U := U_{\uparrow\uparrow} = U_{\uparrow\downarrow} = U_{\downarrow\downarrow} > 0$):

$$J_z = J_{xy} = -\frac{4t^2}{U} < 0 \quad (3.5)$$

Anisotropic spin couplings $J_z \neq J_{xy}$ require bosons with on-site interactions $U_{\uparrow\uparrow}$, $U_{\uparrow\downarrow}$, $U_{\downarrow\downarrow}$, which are *not* all the same. If the intra-species interactions differ ($U_{\uparrow\uparrow} \neq U_{\downarrow\downarrow}$), this implies that both aligned configurations $|\uparrow; \uparrow\rangle$ and $|\downarrow; \downarrow\rangle$ in (a) and (b) also have different energies $-4t^2/U_{\uparrow\uparrow}$ and $-4t^2/U_{\downarrow\downarrow}$. This energy splitting can be interpreted as being caused by an effective magnetic field $h_z = 4t^2/U_{\uparrow\uparrow} - 4t^2/U_{\downarrow\downarrow}$ whose finite value shifts the two states symmetrically in opposite directions away from their average value $-2t^2/U_{\uparrow\uparrow} - 2t^2/U_{\downarrow\downarrow}$. Comparing this energy, in turn, to the value $-2t^2/U_{\uparrow\downarrow}$ of the anti-aligned configuration $|\uparrow; \downarrow\rangle$ in (c), determines which configuration is favored. And the energy difference yields the longitudinal spin coupling $J_z/2 = 2t^2/U_{\uparrow\downarrow} - 2t^2/U_{\uparrow\uparrow} - 2t^2/U_{\downarrow\downarrow}$. The spin-exchange coupling (d) $J_{xy}/2 = -2t^2/U_{\uparrow\downarrow}$ is entirely determined by $U_{\uparrow\downarrow}$. This, in general, results in *anisotropic* spin couplings

$$J_z = \frac{4t^2}{U_{\uparrow\downarrow}} - \frac{4t^2}{U_{\uparrow\uparrow}} - \frac{4t^2}{U_{\downarrow\downarrow}} \quad (3.6)$$

$$J_{xy} = -\frac{4t^2}{U_{\uparrow\downarrow}} \quad (3.7)$$

$$h_z = \frac{4t^2}{U_{\uparrow\uparrow}} - \frac{4t^2}{U_{\downarrow\downarrow}} \quad (3.8)$$

and a finite *effective magnetic field* h_z . In particular, the transverse coupling can be *ferromagnetic* ($J_{xy} < 0$) for repulsive $U_{\uparrow\downarrow} > 0$, and *antiferromagnetic* ($J_{xy} > 0$) for attractive $U_{\uparrow\downarrow} < 0$. We realize wide tunability of J_z and J_{xy} by using ${}^7\text{Li}$ atoms, whose Feshbach resonances we have characterized in previous work [41], which tune the on-site interactions $U_{\uparrow\uparrow}$, $U_{\uparrow\downarrow}$, and $U_{\downarrow\downarrow}$ as a function of an externally applied magnetic field (see Figure 3-2). Additionally, lithium with its light mass has the advantage of fast spin dynamics (set by second-order tunneling [7]), decreasing the relative importance of heating and loss processes compared to heavier atoms.

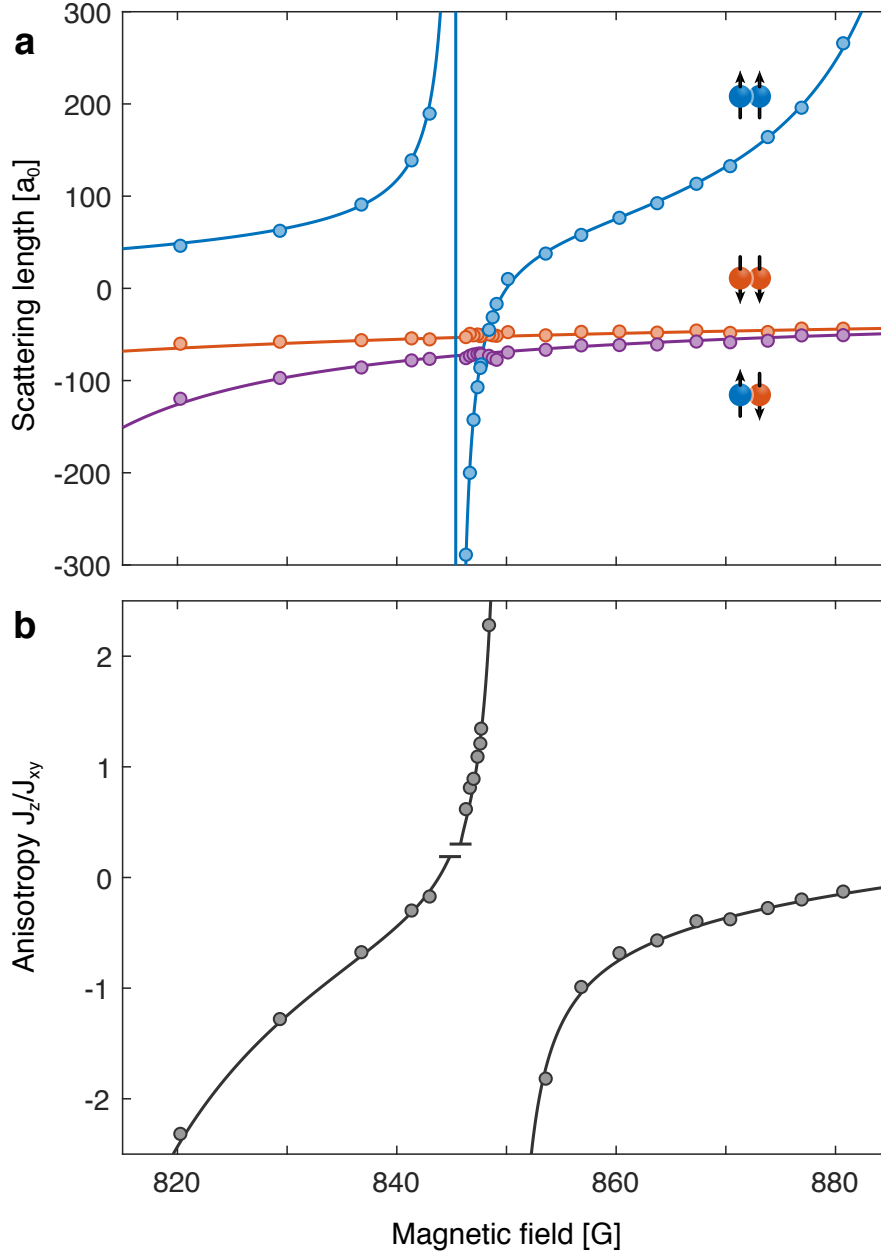


Figure 3-2: **Tunability of the anisotropy.** **a**, Scattering lengths $a_{\uparrow\uparrow}$ (blue), $a_{\uparrow\downarrow}$ (purple) and $a_{\downarrow\downarrow}$ (orange) measured in previous work using interaction spectroscopy [41]. Here a_0 is the Bohr radius. **b**, We interpolate the data points for the scattering lengths in **a** using hyperbolic fits (solid lines) and calculate values for the anisotropy $\Delta = J_z/J_{xy}$. The excluded region ($|a_{\uparrow\uparrow}| > 700 a_0$) is around a Feshbach resonance in the $|\uparrow\rangle$ state near 845.4 G.

Ultracold neutral atoms (at low densities) interact with contact interactions. Therefore, neighboring spins interact mainly through superexchange, where they experience the contact interaction as an on-site interaction through second-order tun-

neling. On-site interactions are due to the wavefunction overlap of two atoms sharing the same lattice site

$$U_{\sigma\sigma'} = \frac{4\pi\hbar^2 a_{\sigma\sigma'}}{m} \int d^3r |w(\mathbf{r})|^4 \quad (3.9)$$

where $w(\mathbf{r})$ is the (lowest-band) Wannier function of an atom localized to a lattice site. However, this wavefunction is not *perfectly* localized, but also extend slightly into the neighboring site, which is one lattice spacing $\delta\mathbf{r} = (0, 0, a)$ away. This leads to a direct nearest-neighbor off-site interaction, simply due to wavefunction overlap [42]:

$$V_{\sigma\sigma'} = \frac{4\pi\hbar^2 a_{\sigma\sigma'}}{m} \int d^3r |w(\mathbf{r})|^2 |w(\mathbf{r} + \delta\mathbf{r})|^2 \quad (3.10)$$

These direct interactions are typically really small, as on-site interactions $U_{\sigma\sigma'}$ are about 4 orders of magnitude smaller than off-site interactions $V_{\sigma\sigma'}$. They can nevertheless become the dominating form of spin-spin interactions close to a Feshbach resonance, when superexchange is suppressed by a large value of $U_{\sigma\sigma'}$ and offsite interactions $V_{\sigma\sigma'}$ are strong. Therefore we include also mention them in Figure 3-1 and include them as a correction to the anisotropy in Figure 3-2.

The magnitude of superexchange can be varied over two orders of magnitude by changing the lattice depth, which mainly affects tunneling t and scales the entire Hamiltonian. In our experiment we control the anisotropy $\Delta = J_z/J_{xy}$ by using the two lowest hyperfine states of ${}^7\text{Li}$ as spin states $|\uparrow\rangle := |F=1, m_F=+1\rangle$ and $|\downarrow\rangle := |F=1, m_F=0\rangle$ and Feshbach resonances to tune the relative interactions $U_{\uparrow\uparrow}$, $U_{\uparrow\downarrow}$, $U_{\downarrow\downarrow}$ as a functions of the applied magnetic field B (Figure 3-2), while keeping $J_{xy} > 0$ (antiferromagnetic). We measured these values [41, 43] with high precision and accuracy using interaction spectroscopy of two atoms per site in a deep Mott insulator. In principle we can also realize purely ferromagnetic couplings by changing the sign of J_{xy} using a constant force to tilt the lattice, as we demonstrated in previous work [44]. The ability to tune the anisotropy Δ over a wide range of positive and negative values allows us to explore dynamics beyond previous experiments [15–19, 25–27] in which $\Delta \approx 1$. Special cases include the XX model with $\Delta = 0$, which can be mapped onto an effective model of free spin-less fermions. Further-

more we can interpolate between $\Delta = 0$ and 1 continuously, effectively switching on interactions between these effective fermions. The isotropic point ($\Delta = 1$) is then in the strong-coupling regime. And in addition, we can also go to the regime where interactions dominate ($\Delta > 1$). More generally we can compare positive anisotropies ($\Delta > 0$) to negative anisotropies ($\Delta < 0$). Or, in the effective fermionic language, we can compare repulsive interactions to attractive interactions.

3.2 Far-from-equilibrium spin-helix states

The experiments start by adiabatically loading a Bose-Einstein condensate of about 4.5×10^4 ^7Li atoms initially in the $|\uparrow\rangle$ state into an optical lattice (spacing $a = 532$ nm), driving the system into the Mott insulating regime with one atom per site, with a strong repulsive scattering length $a_{\uparrow\uparrow} = +307 a_0$ to avoid doubly occupied sites. Two deep lattice beams ($V_x, V_y = 35 E_R$) in the x and y direction separate the lattice sites into independent one-dimensional spin chains. The third lattice beam (z direction) controls the superexchange couplings (J_z and J_{xy}) within chains. The typical chain length is 44 lattice sites. We always perform experiments simultaneously in an ensemble of ~ 1000 chains and measure an averaged result. For the preparation of the spin helix [19–21], superexchange coupling is switched off ($J_z \approx 0, J_{xy} \approx 0$) by a deep z lattice beam with a depth of $V_z = 35 E_R$.

First, we ramp the external magnetic field B to the right value required to adjust the anisotropy Δ . Then we prepare the initial state in the following way: The atoms are initially spin-polarized in the $|\uparrow\rangle$ state (Figure 3-3a):

$$|\psi_{\uparrow}\rangle = \prod_i |\uparrow\rangle_i \quad (3.11)$$

A global $\pi/2$ -pulse of $\sim 75 \mu\text{s}$ rotates all spins into the S_x - S_y plane of the Bloch-sphere (Figure 3-3b)

$$|\psi_{\rightarrow}\rangle = \prod_i (|\uparrow\rangle_i + |\downarrow\rangle_i) / \sqrt{2} \quad (3.12)$$

By applying a magnetic field gradient in z direction, the spins precess around this

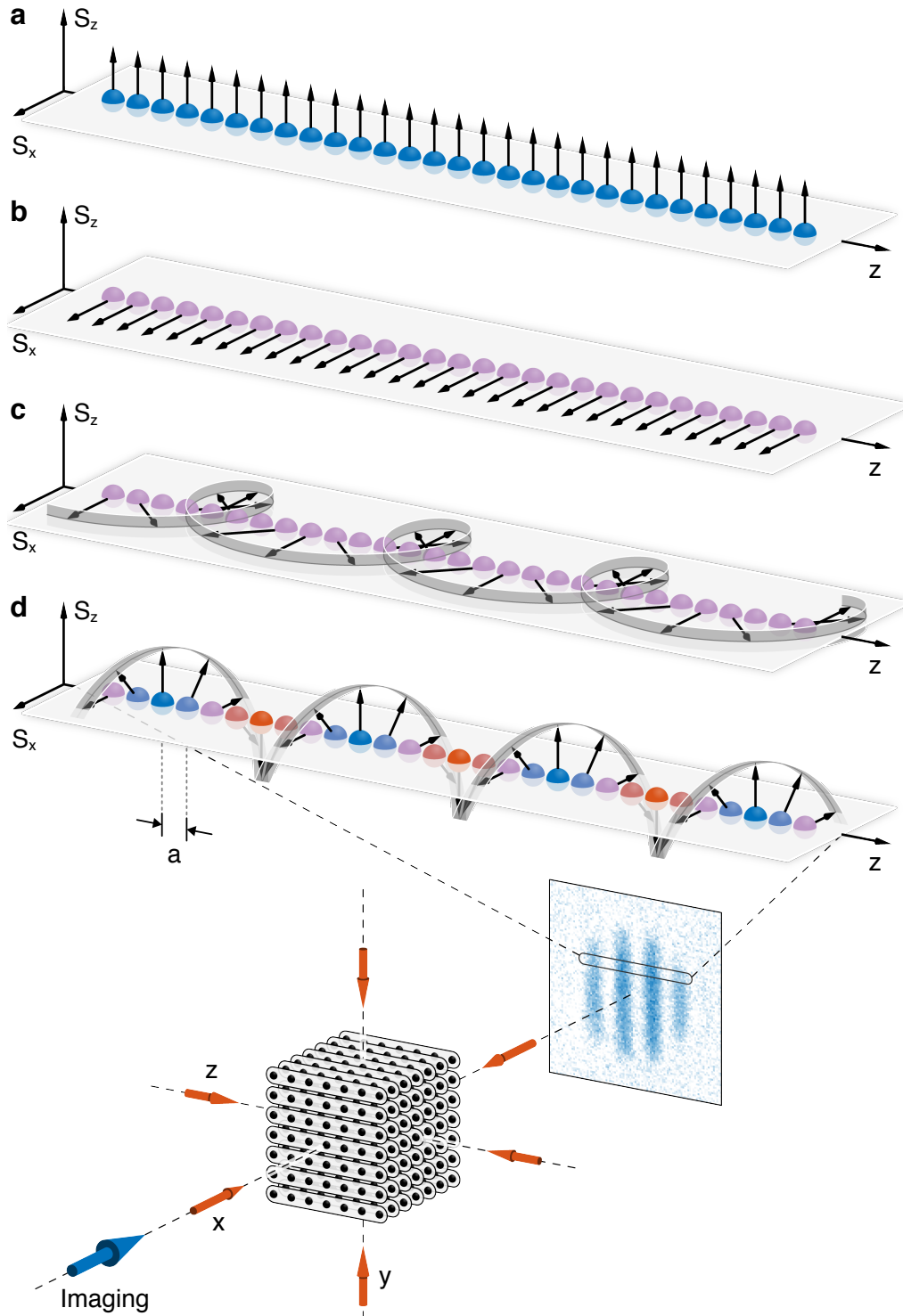


Figure 3-3: **Spin-helix preparation.** **a**, All spins are initially pointing $|\uparrow\rangle$. **b**, A global $\pi/2$ -pulse rotates them into the S_x - S_y plane of the Bloch sphere. **c**, An applied magnetic field gradient winding the spins up into a transverse spin-helix. **d**, An additional $\pi/2$ -pulse turns this into a longitudinal spin-helix.

field at slightly different rates, so that they wind up into a spin-helix (Figure 3-3c)

$$|\psi_{xy}(Q)\rangle = \prod_i \left(|\uparrow\rangle_i + e^{-iQz_i} |\downarrow\rangle_i \right) / \sqrt{2} \quad (3.13)$$

The resulting wavevector $Q = 2\pi/\lambda$ is controlled by the strength of the gradient and the winding duration. The resulting state is a *transverse* spin helix. Its winding orientation is in the S_z - S_x plane of the Bloch sphere. With an additional $\pi/2$ -pulse we can rotate this state into a *longitudinal* spin helix (Figure 3-3d)

$$|\psi_{zx}(Q)\rangle = \prod_i \left(\sin(Qz_i/2) |\uparrow\rangle_i + \cos(Qz_i/2) |\downarrow\rangle_i \right) \quad (3.14)$$

whose winding orientation is in the S_x - S_z plane of the Bloch sphere.

We then initiate the time evolution for this far-from-equilibrium state, by ramping down the z -lattice beam to a value V_z between 9 and $13 E_R$ in order to switch on superexchange couplings J_z and J_{xy} to a controlled value. We let the system evolve for a variable evolution time t up to ~ 500 spin-exchange times \hbar/J_{xy} . For detection we freeze the dynamics by rapidly increasing the lattice depth back to 35 ER.

3.3 Polarization-rotation imaging

We measure the resulting spatial spin distribution of the spin $|\uparrow\rangle$ state in-situ with state-selective polarization-rotation imaging. The imaging system is transverse to the chains and the optical resolution is about 6 lattice sites. The resulting images show a characteristic stripe pattern (Figure 3-3) which arises from the residual sinusoidal modulation of population in $|\uparrow\rangle$ in each chain.

The optical density of the atomic ensemble is too high (> 14) to allow for in-situ observation of the modulation of $\langle S^z \rangle$ via absorption imaging. Instead, we employ dispersive imaging, which uses the phase accumulated by the transmitted light in order to form an image of the atomic density distribution. When light at frequency ω_L is detuned from the atomic resonance ω_0 by many natural linewidths Γ , it picks up an approximate phase $\theta \approx -2\delta/\Gamma \times \text{OD}(y, z, \delta)$, where OD is the optical density at

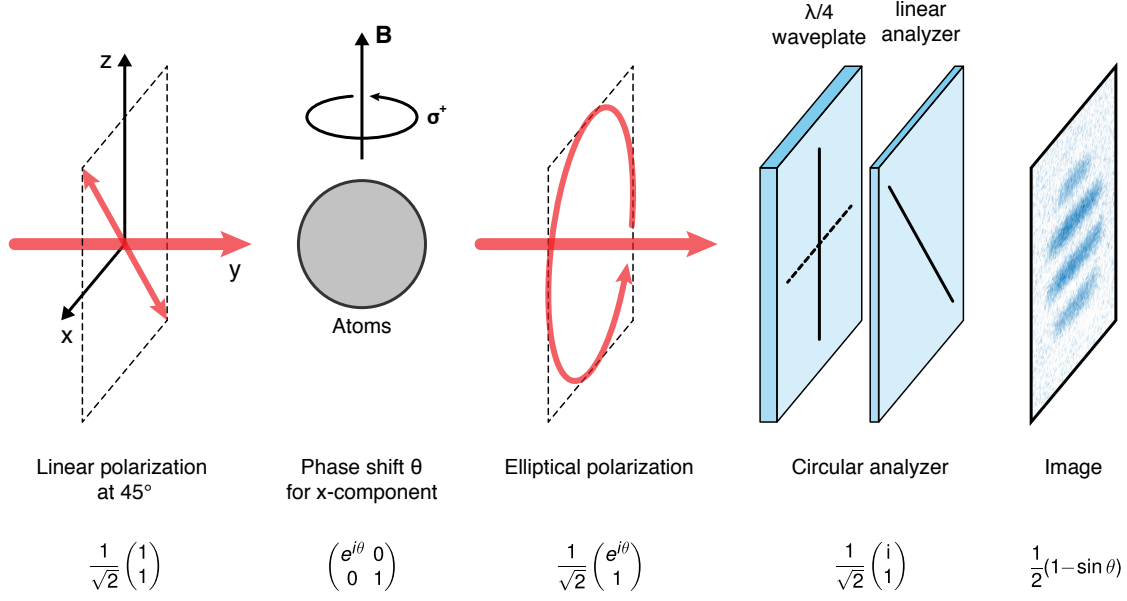


Figure 3-4: **Polarization-rotation imaging.** For imaging we address a σ^+ -transition only (and the π -transition is really far detuned). That means, when the imaging beam is coming from the side (y -direction), the atoms can only interact with a linearly x -polarized beam (because then it has overlap with σ^+ -polarization), but the atoms are transparent for linearly z -polarized beam (π -polarization). If we detune from the imaging transition by a few natural linewidths, the atoms act as a waveplate, with a fast and a slow axis. The column density is proportional to a phase shift of the slow axis. So, if the incoming beam is at an angle of 45° , its polarization is rotated. The polarization rotation can then be turned into an amplitude modulation by using a polarizer. (This setup is analogous to an electro-optical modulator configured as an amplitude modulator.)

detuning $\delta = \omega_L - \omega_0$, while absorption is suppressed by a sufficiently large detuning δ . In order to form an image, the phase-shifted light must be interfered with a reference beam. In this work, we make use of the fact that the optical transition we use for imaging is driven only by a single polarization component; after passing through the atoms, the shifted and unshifted components are combined on a polarizer. A judicious choice of input and output polarizers yields an interference signal I on the camera which is $I = I_0(1 - \sin \theta)/2$ [45, 46] (see Figure 3-4).

The imaging light is initially linearly polarized at 45° , i.e. there are two equal orthogonal polarization components in x and z direction with a (normalized) polarization vector as $\mathbf{e}_0 = \frac{1}{\sqrt{2}}(1, 1)$. The first one interacts with the atomic imaging tran-

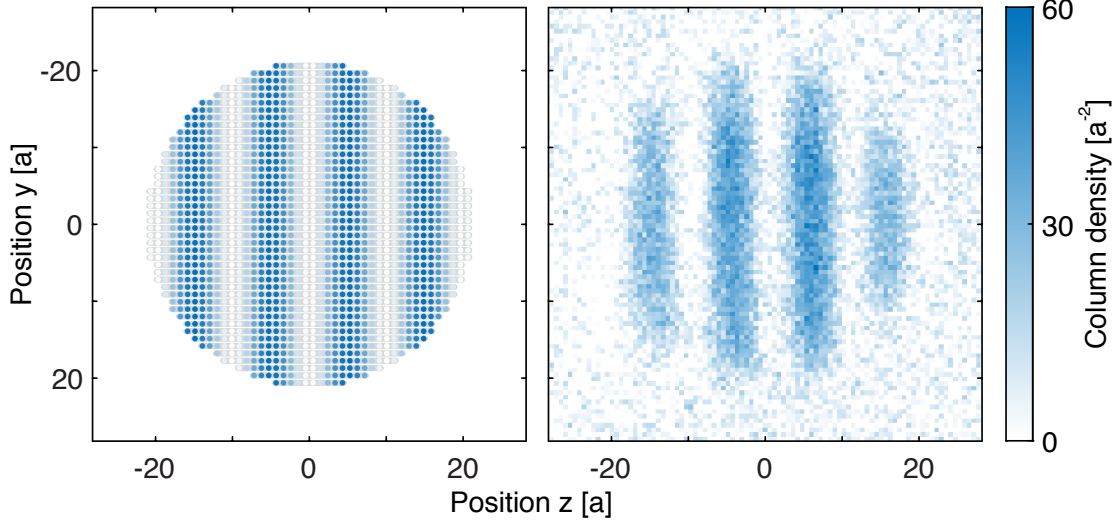


Figure 3-5: **Measured column density** of atoms in the $|\uparrow\rangle$ state after imprinting a longitudinal spin-helix along the (horizontal) z -direction with wavelength $\lambda = 10.4 a$. Right: Every pixel is a local measurement of the column density (number of atoms per unit area). The y and z axis are displayed in units of lattice spacings $a = 0.532 \mu\text{m}$. Left: Visualization of the chain length distribution within a cut through the center of the spherical Mott insulator. Its diameter determines the maximum chain length $L_{\text{max}} = 44 a$. The optical imaging resolution is about 6 lattice sites. The pixel size of the camera is $16 \mu\text{m} \times 16 \mu\text{m}$. This image was taken with a magnification of $M = 50$. So every pixel represents a region in space of size $0.32 \mu\text{m} = 0.6 a$.

sition (and experiences a phase shift θ) and the second one does not. This rotates the polarization vector to $\mathbf{e} = \frac{1}{\sqrt{2}}(e^{i\theta}, 1)$. With a circular analyzer the polarization gets projected onto $\sigma^+ = \frac{1}{\sqrt{2}}(i, 1)$ to yield the fraction of the transmitted intensity as $|\mathbf{e} \cdot \sigma^+|^2 = \frac{1}{4}|ie^{i\theta} + 1|^2 = \frac{1}{2}(1 - \sin\theta)$. The phase shift θ is related to the column density as

$$\theta(y, z) = -\frac{2\delta}{\Gamma} \text{OD}(y, z) = -\frac{2\delta}{\Gamma} \frac{\sigma_0}{1 + (2\delta/\Gamma)^2} \int dx n(x, y, z) \quad (3.15)$$

$$= -\frac{2\delta}{\Gamma} \frac{\sigma_0}{1 + (2\delta/\Gamma)^2} n_{2\text{D}}(y, z) \quad (3.16)$$

and $\sigma_0 = 6\pi(\lambda/2\pi)^2/2$ is the resonant scattering cross-section (reduced by 2, because x -polarized light only has 50% overlap with σ^+). This way we can measure the column density $n_{2\text{D}}(y, z)$ in-situ, detuned, with dispersive imaging, without scattering light (as shown in Figure 3-5).

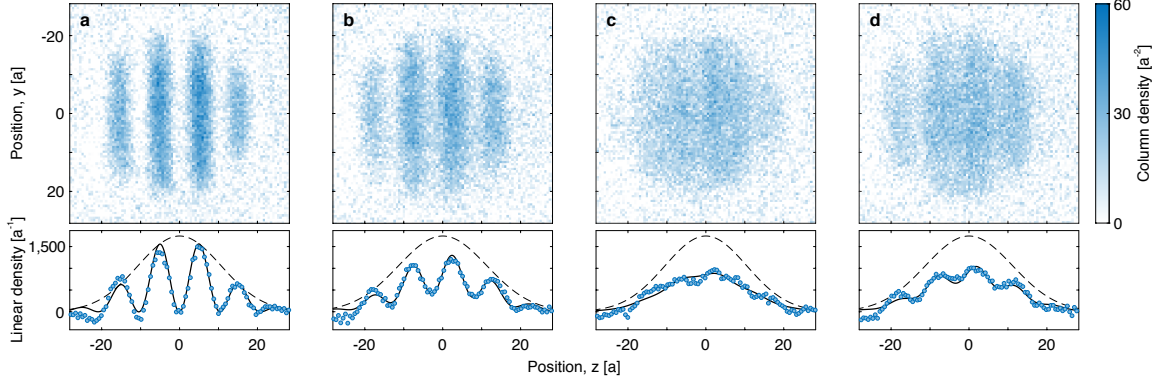


Figure 3-6: **Contrast measurement** using the linear density. The images **a-d** show the distribution of atoms in the $|\uparrow\rangle$ state. The images are projected (integrated) along the y -direction from $y = -30a$ to $+30a$ to obtain the linear density (number of atoms per unit length). The resulting 1D distributions are fitted with $f(z) = g(z) \cdot [1 + \mathcal{C} \cos(Qz + \theta)]/2$ (solid line), where $g(z)$ is a Gaussian envelope (dashed line), between $z = \pm 54a$. Examples **a-d** were measured at different evolution times (**a**) $t = 0 \hbar/J_{xy}$, (**b**) $t = 2.3 \hbar/J_{xy}$, (**c**) $t = 6.3 \hbar/J_{xy}$, (**d**) $t = 12.0 \hbar/J_{xy}$, for anisotropy $\Delta \approx 0$ and wavelength $\lambda = 10.4a$ (see chapter 4). The obtained contrast $\mathcal{C}(t)$ is shown in Figure 4-3. In general, we also normalize by the initial measured contrast $\mathcal{C}(0)$ to correct for finite optical imaging resolution. This is important for shorter wavelengths λ close to the optical resolution of $3\mu\text{m}$, where the measured contrast $\mathcal{C}(t)$ is reduced compared to the real contrast $c(t) = \mathcal{C}(t)/\mathcal{C}(0)$.

3.4 Image analysis

The imaging system already averages over chains distributed along the x direction (the imaging direction). We project the images along the y direction to average over this second transverse direction. Then we obtain the one-dimensional spin distribution averaged over all spin chains. We analyze the spin-helix pattern by obtaining the helix contrast \mathcal{C} through a fit

$$f(z) = g(z) \cdot [1 + \mathcal{C} \cos(Qz + \theta)]/2. \quad (3.17)$$

as shown in Figure 3-6. Here $g(z)$ is a Gaussian envelope function which accounts for the spatial distribution of all atoms $n = n_{\uparrow} + n_{\downarrow}$. θ is a random phase that varies from shot to shot, due to small magnetic bias field drifts.

Later on, we extended our fitting technique to the whole two-dimensional image

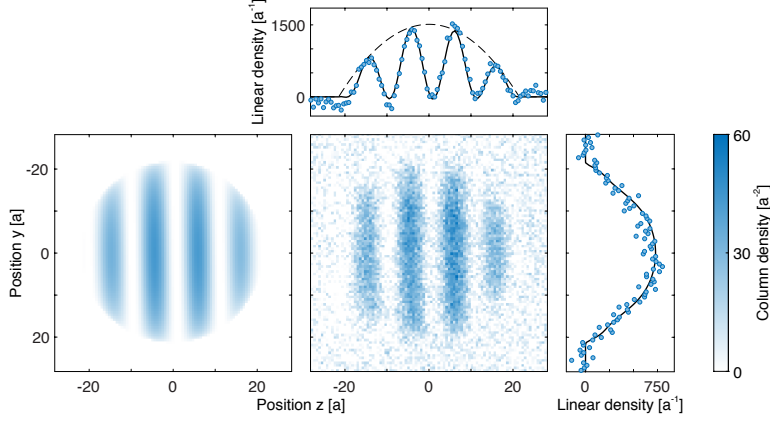


Figure 3-7: **Contrast measurement** using the column density. The central image represents raw data and shows the distribution of atoms in the $|\uparrow\rangle$ state. The left panel is the two-dimensional fit $f(y, z) = g(y, z) \cdot [1 + C \cos(Qz + \theta)] / 2$. The image is projected (integrated) both along the horizontal z direction (right panel) and vertical y direction (top panel) from $y, z = -42a$ to $+42a$ to obtain the linear densities (number of $|\uparrow\rangle$ atoms per unit length) for the measured data (points) and the fit (solid line). The dashed line in the y -projection shows the (parabolic) envelope function for the spatial density distribution in the cloud.

using the fit function

$$f(y, z) = g(y, z) \cdot [1 + C \cos(Qz + \theta)] / 2 \quad (3.18)$$

as demonstrated in Figure 3-7. Here the envelope function $g(y, z)$ also takes into account that the atoms are actually distributed in a homogeneous sphere of radius R (the Mott insulator) such that

$$g(y, z) = A \sqrt{1 - y^2/R^2 - z^2/R^2} \cdot H(1 - y^2/R^2 - z^2/R^2) \quad (3.19)$$

with $H(r)$ is the Heaviside function.

3.5 Optical resolution

The longitudinal spin helix exhibits a S_z -magnetization profile (i.e. in the spin $|\uparrow\rangle$ population), which is a sinusoidal modulation. That makes it the perfect tool to probe the modulation transfer function (MTF) directly in reciprocal space. The

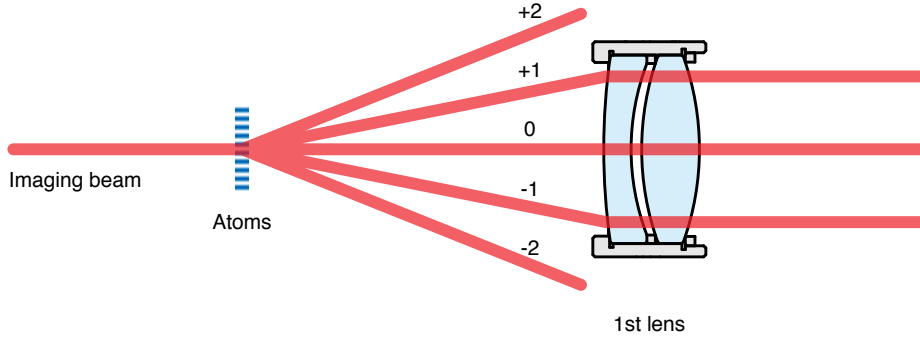


Figure 3-8: **Optical resolution limit.** The optical resolution is determined by the first lens in the imaging system. The atoms form a sinusoidal phase grating, because the longitudinal spin helix exhibits a S_z magnetization profile (i.e. in the spin $|\uparrow\rangle$ population), which is a sinusoidal modulation. That results in higher diffraction orders. (That is analogous to driving an electro-optical modulator to create a sinusoidal phase modulation in the time-domain, which adds higher-order sidebands to a laser beam.) And the angle between the orders depends on the wavevector Q of the phase modulation. We can only resolve the grating with our imaging system, if at least the first orders are captured by the first lens. We use an air-spaced doublet (Thorlabs ACA254-050-A) with a clear aperture of 20 mm and a focal length of 50 mm resulting in a numerical aperture of $NA \approx 0.2$. This yields a resolution of $\lambda/NA = 3.3 \mu\text{m}$. Note that here the prefactor is *exactly* equal to 1, because we are not imaging a point source, but a sinusoidal modulation.

optical resolution of our imaging system ($NA \approx 0.2$) was determined to have a cut-off at modulation wavelength $\lambda \approx 3.0 \mu\text{m} = 5.6 a$ (Figure 3-8). The reduction of the modulation transfer function $MTF(Q)$ near the cut-off reduces the observed contrast $\mathcal{C}(t) = MTF(Q) \cdot c(t)$ compared to the real contrast $c(t)$. Assuming that the experimental preparation sequence for the initial spin helix state achieves full contrast $c(0) = 1$ for any wavevector Q (based on careful pulse calibration and characterization), we can use $\mathcal{C}(0)$ as a direct measurement of $MTF(Q)$ and determine the real contrast as $c(t) = \mathcal{C}(t)/\mathcal{C}(0)$.

3.6 Summary

We have shown how to control the spin-exchange coupling J_{xy} using the lattice depth, and how to tune the anisotropy $\Delta := J_z/J_{xy}$ with an external magnetic field using Feshbach resonances. We can wind longitudinal and transverse spin-helix states with variable wavevectors Q . The imaging system can resolve wavevectors ranging from $Q=0$ to $Q=2\pi/6a$ and measure their contrast. By lowering the lattice depth after state preparation, and thereby switching on spin couplings, we can now study their evolution as a function of time. Figure 3-9 summarizes the experimental sequence. Chapter 4 focusses on longitudinal spin helix states and spin transport. Chapter 5 is about transverse spin helix states and spin dephasing. In Chapter 6 we find special spin-helix states which are very stable and (in an ideal system) are even exact many-

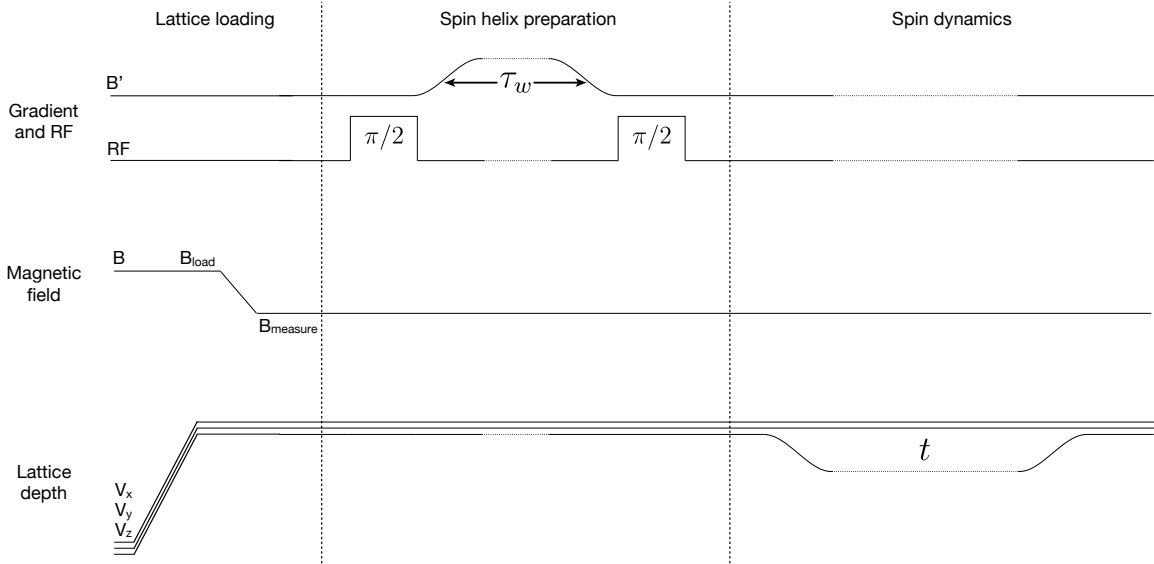


Figure 3-9: **Experimental sequence.** **a**, Ultracold ${}^7\text{Li}$ atoms in the $|\uparrow\rangle$ state are loaded into a deep optical lattice ($V_x, V_y, V_z = 35 E_R$) with a strong repulsive scattering length $a_{\uparrow\uparrow} = +307 a_0$ (selected by an appropriate magnetic field B_{load}) to avoid doubly occupied sites. The anisotropy Δ is selected by ramping to the magnetic field to and appropriate value B_{measure} , tuning the on-site interactions $U_{\uparrow\uparrow}, U_{\uparrow\downarrow}, U_{\downarrow\downarrow}$ through Feshbach resonances. **b**, A spin-helix state is prepared with RF pulses and a magnetic field gradient. **c**, Time evolution is initiated by decreasing the lattice depth V_z to a value between 9 and 13 E_R , switching on interactions between spins along the z direction. After a variable evolution time t , spin dynamics is frozen by rapidly increasing the lattice depth back to $V_z = 35 E_R$ and the spatial spin distribution is imaged.

body eigenstates of the Hamiltonian. These special transverse spin-helix states can have very short wavelengths. In order to image their contrast, we utilize a special unwinding step just before imaging, allowing us to access the whole range of possible wavevectors.

Chapter 4

Spin transport

Using a longitudinal spin-helix pattern, which is a modulation in the population of spin $|\uparrow\rangle$ and $|\downarrow\rangle$ atoms, we see a drastic impact on the transport properties, when the anisotropy is varied. When spins are coupled only along two of three possible orientations (the XX model), we find ballistic behavior of spin dynamics, whereas for isotropic interactions (the XXX model), we find diffusive behavior. More generally, for positive anisotropies, the dynamics ranges from anomalous superdiffusion to subdiffusion, whereas for negative anisotropies, we observe a crossover in the time domain from ballistic to diffusive transport. These are two strikingly different crossover phenomena: Anomalous diffusion for positive anisotropies and behavior reminiscent of a classical gas for negative anisotropies.

*This chapter supplements work reported in the following publication [28]
(included in Appendix A)*

P. N. Jepsen, J. Amato-Grill, I. Dimitrova, W. W. Ho, E. Demler, W. Ketterle
Spin transport in a tunable Heisenberg model realized with ultracold atoms
Nature **588**, 403-407 (2020)

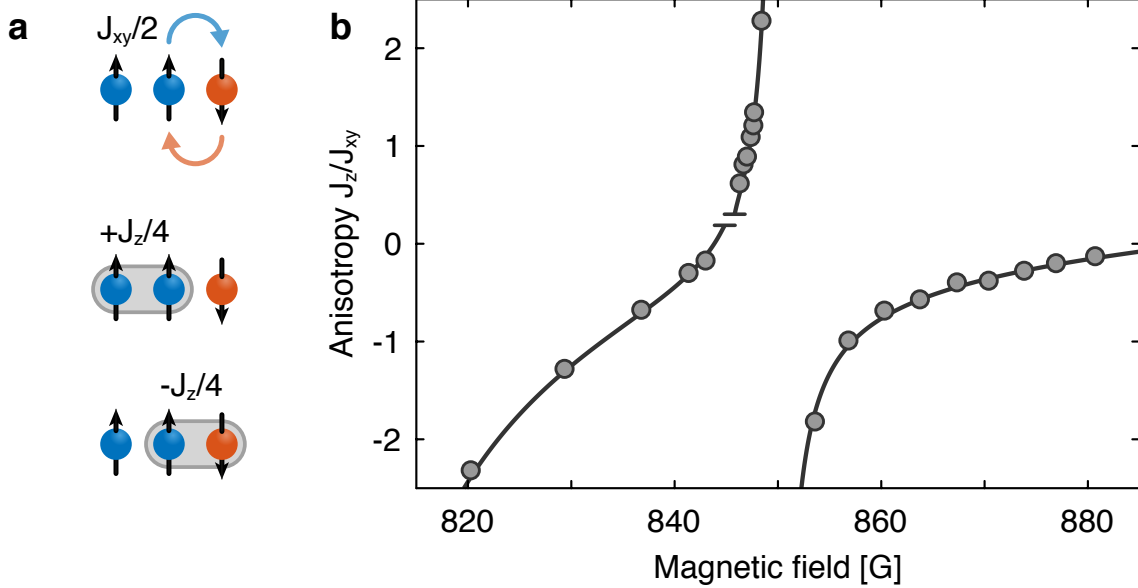


Figure 4-1: **Tunability of the XXZ model with ${}^7\text{Li}$** [28]. **a**, The Hamiltonian is characterized by two energy scales: Transverse spin coupling J_{xy} (spin exchange) and longitudinal spin coupling J_z (spin-spin interactions). **b**, Anisotropy $\Delta = J_z/J_{xy}$ as a function of applied magnetic field. The solid line is a fit to experimental data points which are calculated from measured values $U_{\uparrow\uparrow}$, $U_{\uparrow\downarrow}$, $U_{\downarrow\downarrow}$ (see chapter 3).

4.1 Introduction

Studying spin transport in one-dimensional spin chains was the first way we demonstrated fully tunable anisotropy of the spin-spin couplings (Figure 4-1). The transport properties change even drastically when the anisotropy is varied. Our initial goal has simply been to demonstrate that we implement the anisotropic Heisenberg model. This has been a long standing goal in the field of ultracold atoms and quantum simulation. Previous studies were all limited to the isotropic case. For large signal to noise ratio, we then chose to utilize full contrast spin-helix patterns (Figure 4-2), which are additionally also straight forward to prepare experimentally. This, in turn, enables us to study spin transport far from equilibrium in previously unexplored regimes. These spin-helix states exhibit maximum possible contrast, perturbing the system even as far from equilibrium as possible, and far away from the linear-response regime. A *longitudinal* spin helix (Figure 4-2) is an ideal probe to study spin transport, because it is a spatial modulation of the population in spin $|\uparrow\rangle$ and $|\downarrow\rangle$. So spin transport

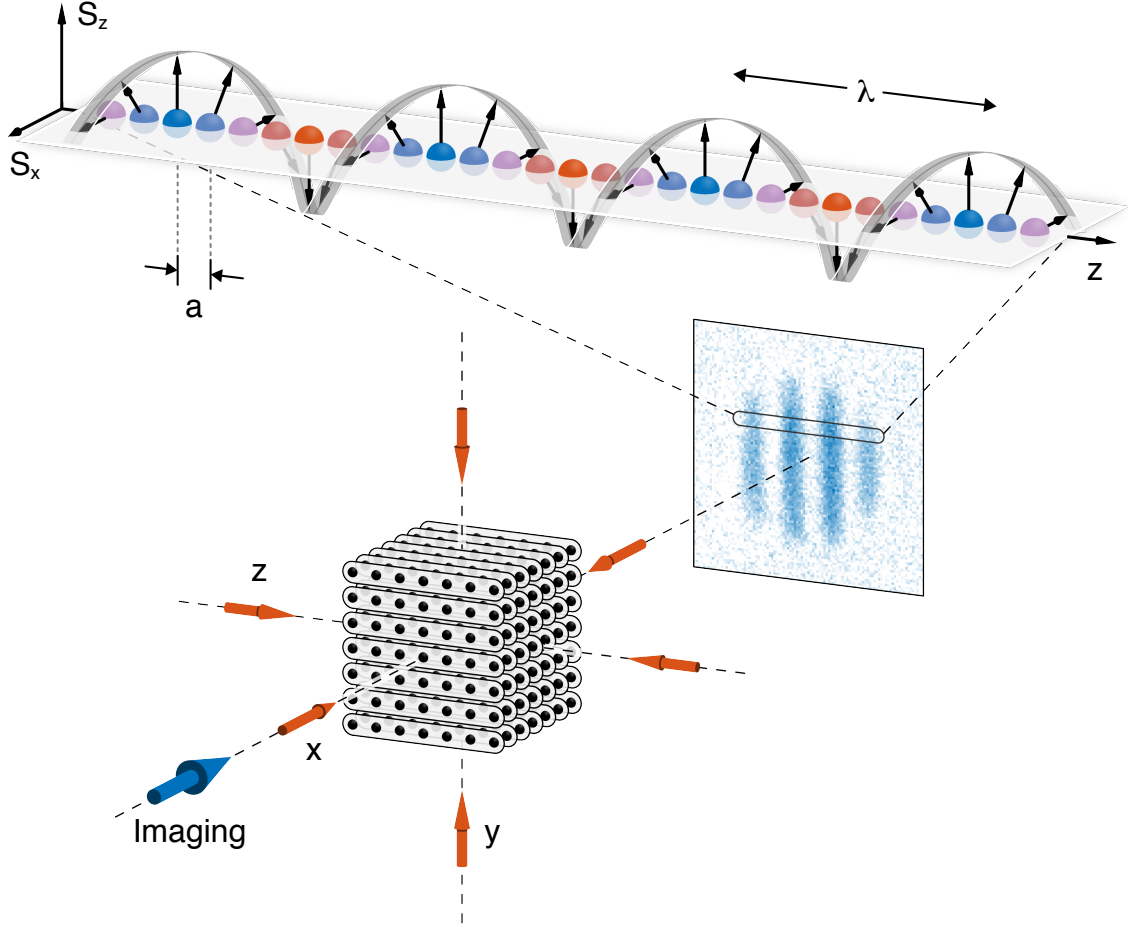


Figure 4-2: **Spin helix** realized from two hyperfine states (spin $|\uparrow\rangle$ and $|\downarrow\rangle$) [28]. The spin \mathbf{S} winds in the S_z - S_x plane as a function of position z in the spin chain. Deep optical lattices along x and y create an array of independent spin chains. The z -lattice is shallower and controls spin transport along each chain.

is the only way it can decay by. There is nothing else in the Hamiltonian, which couples spin $|\uparrow\rangle$ to $|\downarrow\rangle$, except the spin-exchange term in the Heisenberg model (Figure 4-1a), which drives motion of spins. In order to study transport behavior, we measure how the decay timescale τ depends on the modulation lengthscale λ . Note for ballistic motion time grows linearly with distance ($\tau \propto \lambda$), whereas for diffusion it grows quadratically ($\tau \propto \lambda^2$). A lot of our results were unexpected and asking for more and more data to explain them.

First of all, we confirm a similar experiment from the Bloch group [19] with spin-helix states in the isotropic system ($\Delta = 1$), which yields diffusive transport ($\tau \propto \lambda^2$). In the XX model ($\Delta = 0$), on the other hand, we measure ballistic transport ($\tau \propto \lambda$),

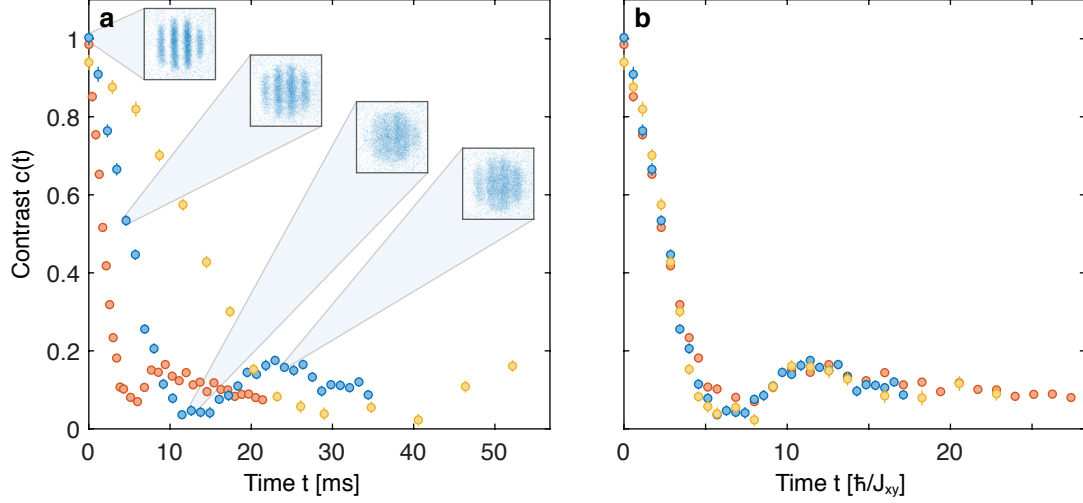


Figure 4-3: **Superexchange dynamics.** **a**, Spin helix contrast $c(t)$ for $\lambda = 10.4 a$ measured at three different lattice depths $9 E_R$ (orange), $11 E_R$ (blue), $13 E_R$ (yellow). **b**, Decay curves collapse when times are expressed in units of the corresponding spin-exchange times $\hbar/J_{xy} = 0.64$ ms, 1.71 ms, 4.30 ms, respectively.

and we find oscillations yielding a linear dispersion relation, as might be expected, since this system can be mapped to non-interacting fermions. This inspired us to revisit the isotropic case and we actually find small oscillations with a linear dispersion relation there, too, which we consider somewhat unexpected. For arbitrary positive anisotropies we find anomalous diffusion ($\tau \propto \lambda^\alpha$), with exponents ranging from superdiffusion ($1 < \alpha < 2$) to subdiffusion ($\alpha > 2$); however, we can always find (mostly small) oscillations with linear dispersion relations. For arbitrary negative anisotropies, we see a crossover from ballistic to diffusive transport in the time-domain.

4.2 Tunable superexchange dynamics

The initially full contrast spin-helix state decays due to spin transport and we measure the modulation contrast $c(t)$ as a function of time (shown in Figure 4-3 for $\lambda = 10.4 a$). We show that we can control the spin-exchange rate J_{xy} , by repeating the measurement at three different lattice depths (Figure 4-3a). If the time axis is rescaled in units of the corresponding spin-exchange times \hbar/J_{xy} , which we can calculate based on Hubbard parameters [28], we see that they collapse nicely on top of each

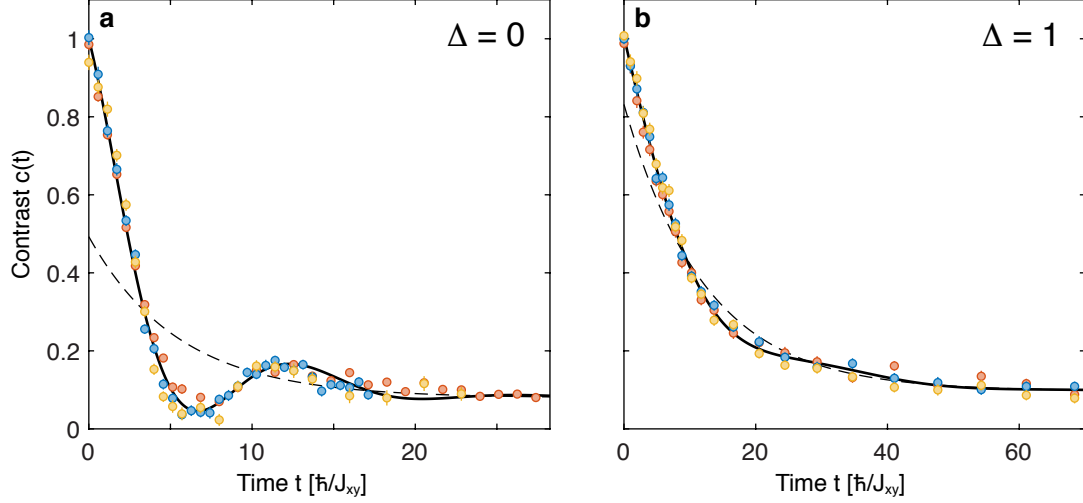


Figure 4-4: **XX model and XXX model.** Spin helix contrast $c(t)$ for $\lambda = 10.4 a$ measured at three different lattice depths $9 E_R$ (orange), $11 E_R$ (blue), $13 E_R$ (yellow) in the XX model where $\Delta = 0$ (a) and in the XXX model where $\Delta = 1$ (b).

other (Figure 4-3b). This demonstrates that we observe transport by superexchange and not some other process. Furthermore, using the external magnetic field, we can also control the anisotropy $\Delta = J_z/J_{xy}$, and we see in Figure 4-4 how the decay curve changes, comparing $\Delta = 0$ and $\Delta = 1$.

4.3 XX model ($\Delta = 0$) and XXX model ($\Delta = 1$)

We first compare two special cases: the isotropic model where $\Delta = 1$ (the so-called XXX model) which has been studied before [19] and the XX model where $\Delta = 0$, which can be mapped onto non-interacting fermions. Even for one given wavelength λ there is already a big effect. The shape of the spin-helix decay $c(t)$ is qualitatively very different for both cases, as shown in Figure 4-4 for $\lambda = 10.4 a$. Even without any fit function, we can already learn a lot from the data itself. In the following, we do a side-by-side comparison of (in the fermionic language) non-interacting fermions ($\Delta = 0$) to strongly-interacting fermions ($\Delta = 1$). For $\Delta = 0$, in addition to an overall decay, we observe a damped oscillation. The revival occurs after about ~ 10 spin-exchange times \hbar/J_{xy} for a wavelength of λ of about ~ 10 lattice sites a , intuitively suggesting a velocity of one lattice site a per spin-exchange time \hbar/J_{xy} . This can be

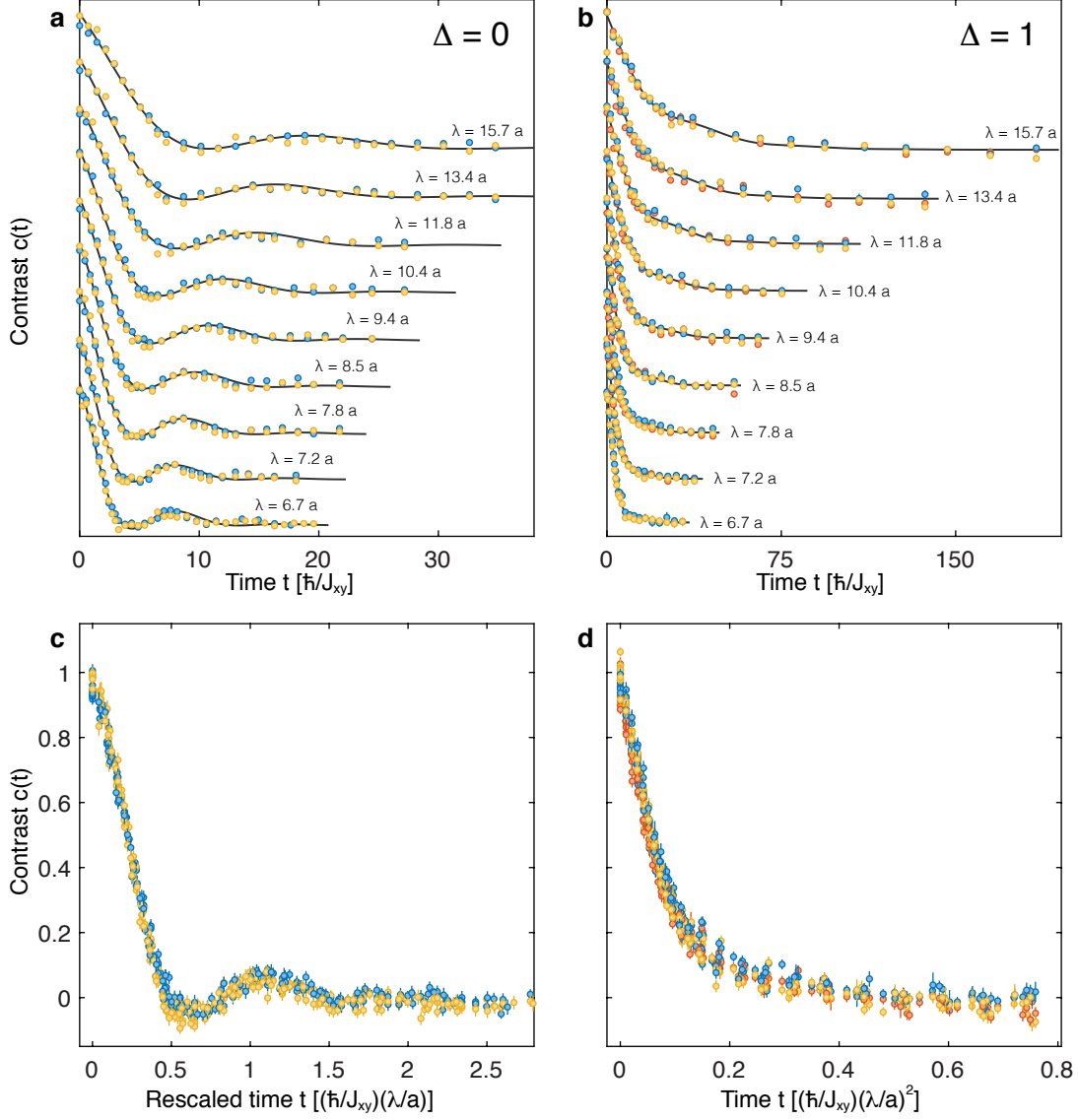


Figure 4-5: **Linear and quadratic scaling.** Spin helix contrast decay $c(t)$ for several wavelengths λ in the XX model where $\Delta = 0$ (a) and in the XXX model where $\Delta = 1$ (b). All decay curves collapse into a single curve if the time axis is rescaled by λ (c) and by λ^2 (d), respectively.

understood with a simple model, where two counter-propagating waves constructively interfere again after traveling a relative distance of one wavelength at a propagation velocity of one lattice site per super-exchange time. However, for the isotropic case of $\Delta = 1$ (strongly-interacting fermions), we observe qualitatively very different behavior: Interactions make the decay a lot slower and the oscillations are strongly suppressed.

To learn more about transport behavior, we now vary the wavelength λ , as shown

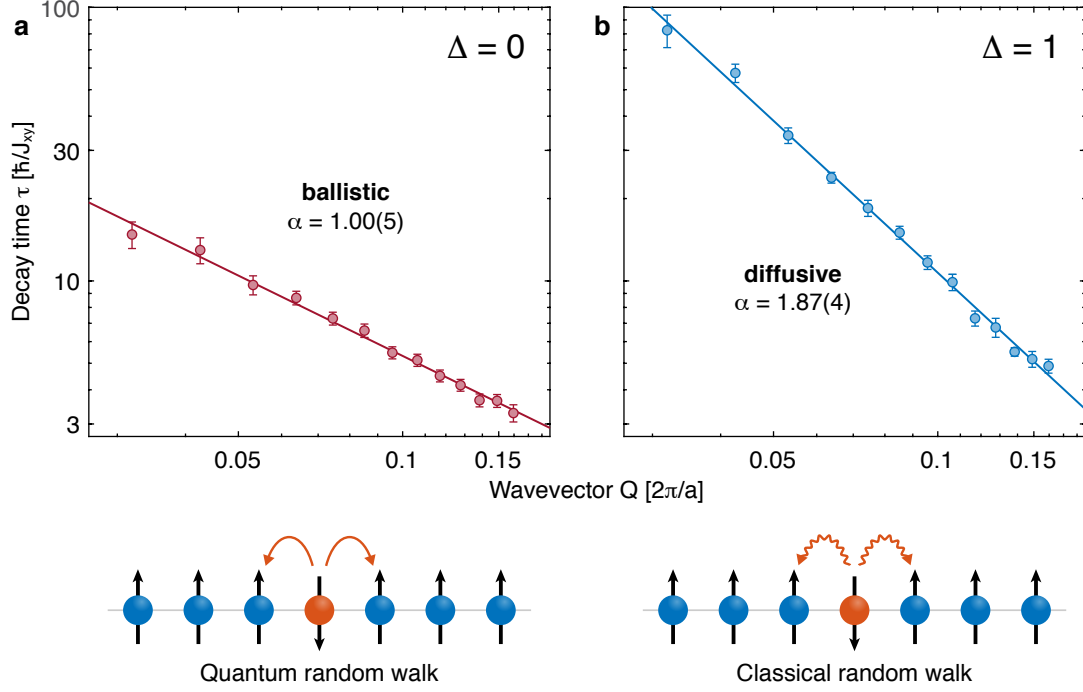


Figure 4-6: **Power-law scalings** of the decay time constants τ as a function of wavevector Q . **a**, In the XX model (non-interacting fermions) the power law scaling is linear, indicating ballistic transport, reminiscent of the quantum random walk of a single magnon [17], moving to the left and the right *coherently* with equal matrix elements. In the XXX model (strongly-interacting fermions) the power law scaling is close to quadratic, indicating diffusive transport, consistent with a classical random walk, moving to the left and the right *incoherently* with equal rates.

in the waterfall plots in Figure 4-5. For smaller wavelengths λ , the decay gets faster. But for the isotropic case ($\Delta = 1$), the decay time-scale depends much more strongly on the wavelength λ than in the free-fermion case ($\Delta = 0$). In each case, all decay curves collapse into a single curve, if the time axis is rescaled by λ (for $\Delta = 0$) or by λ^2 (for $\Delta = 1$). Linear scaling indicates ballistic transport (as one might expect for non-interacting fermions), whereas quadratic scaling indicates diffusion (as one might expect for strongly-interacting fermions).

Diffusion has already been observed in a previous experiment [19], which also revealed quadratic scaling. Diffusion also suggests a purely exponential decay, being a solution to the diffusion equation. Ballistic transport in the XX model has not been observed before, as previous work was limited to the isotropic case. Furthermore, we find that the ballistic case shows not only an overall decay, but also a

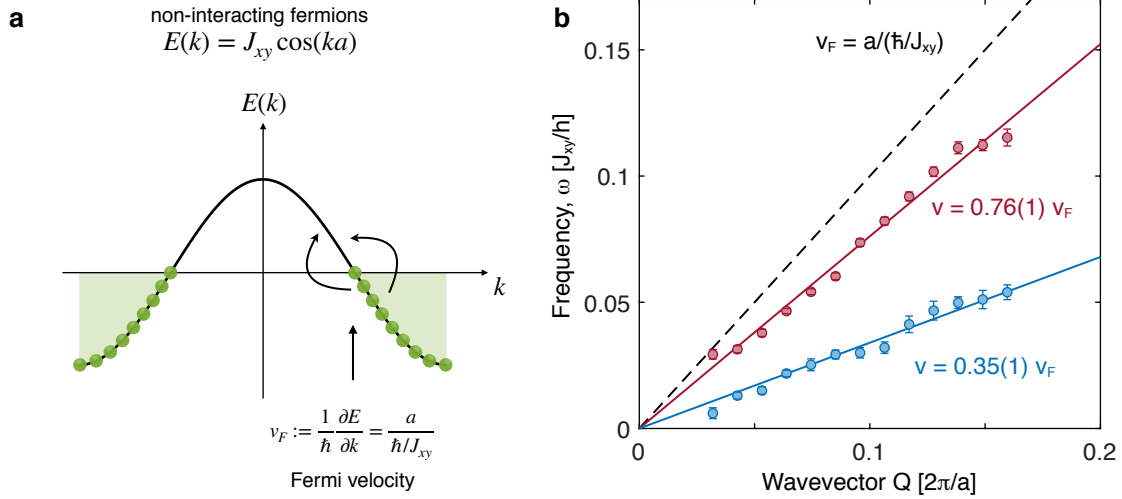


Figure 4-7: **Dispersion relations and velocities.** **a**, Fermi velocity $v_F = a/(\hbar/J_{xy})$ of a half-filled band in the non-interacting XX model. **b**, Measured oscillation frequencies follow linear dispersion relations $\omega(Q) = vQ$. For non-interacting fermions in the XX model ($\Delta = 0$) the velocity $v = 0.76(1) v_F$ (red) is close to the Fermi velocity v_F (dashed line). For strongly-interacting fermions in the XXX model ($\Delta = 1$) the velocity $v = 0.35(1) v_F$ (blue) is reduced by roughly a factor of 2.

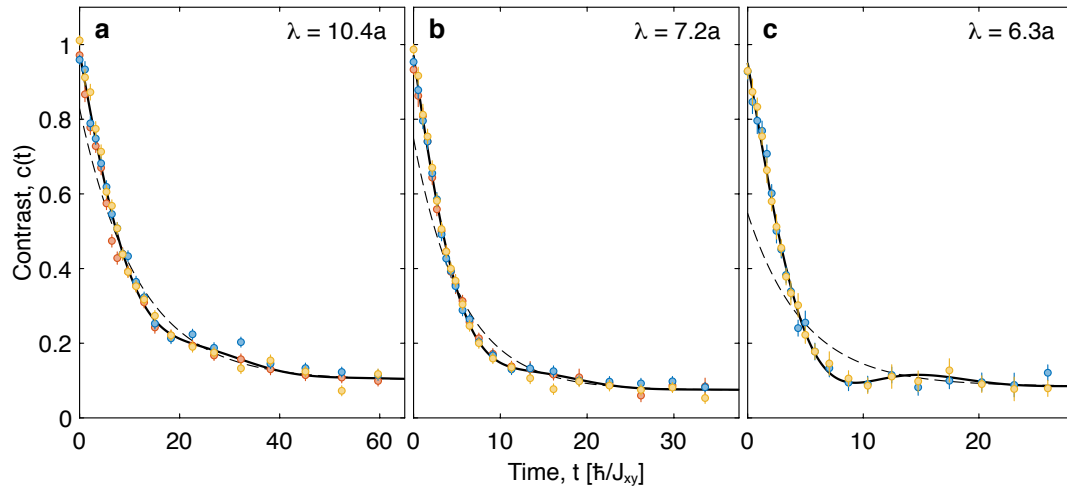


Figure 4-8: **Oscillations in the XXX model.** Decay and weak oscillation at the isotropic point $\Delta \approx 1$ measured for different wavelengths λ . Solid lines are fits $c(t) = (a_0 + b_0 \cos \omega t) e^{-t/\tau} + c_0$ and dashed lines show the overall decay $a_0 e^{-t/\tau} + c_0$, around which the oscillations take place. The oscillations become more pronounced for short wavelengths λ , because the decay time ($\tau \propto \lambda^2$) decreases with smaller wavelength more strongly than the oscillation period ($T \propto \lambda$).

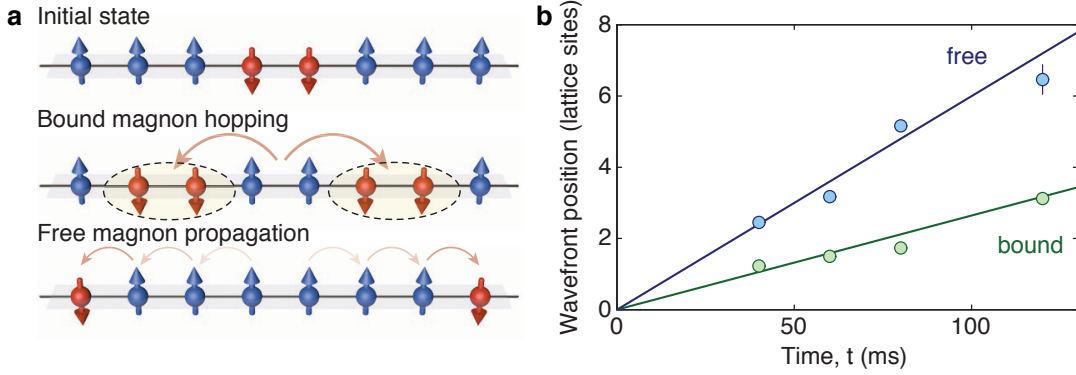


Figure 4-9: **Free and bound magnons.** **a**, Bound magnons can travel together or break up into two free magnons, as studied experimentally [18] for $\Delta = 1$. **a**, The velocity v_{bound} of the bound magnon state (green) is reduced by a factor of 2, compared to the velocity v_{free} of the free magnons (blue). This is consistent with a theoretical prediction $v_{\text{free}}/v_{\text{bound}} = 2\Delta$ for general anisotropies [32].

(damped) oscillating part. This raises the question, how finite interactions suppress these oscillations. In fact we can then notice, that small oscillations are even visible in the isotropic case! If we look very closely, the decay actually deviates from purely exponential decay ever so slightly (see Figure 4-4).

This is a great example, how studying a tunable anisotropic Heisenberg model ($\Delta \neq 0$) helps us learn something even about the isotropic system ($\Delta = 1$). We would probably have never noticed the small oscillation in the isotropic case, if we had not seen the well pronounced oscillations for $\Delta = 0$. It is easy to miss, if you are not looking for it. But it also gets more pronounced at shorter wavelengths (see Figure 4-8). The way we initially noticed this oscillation, was actually by using a fit function.

Initially, we simply used an exponential fit function $c(t) = a_0 e^{-t/\tau} + c_0$ for the decay curves at the isotropic point ($\Delta = 1$) like in Ref. [19], since an exponentially decaying amplitude is even a solution to the diffusion equation. But this definitely does not work for the decay curves in the XX model, which show oscillations as well. So we looked for a fit function which would capture the dynamics of both the XX model and the XXX model. We fit the data with the sum of a decaying part with

time constant τ and a damped oscillating part with frequency ω :

$$c(t) = (a_0 + b_0 \cos \omega t)e^{-t/\tau} + c_0 \quad (4.1)$$

with a_0 , b_0 , c_0 , ω and τ as adjustable parameters. This is plotted in Figure 4-4 as a solid line. We can see the oscillations more clearly, by plotting only the decaying part $a_0 \cos(\omega t)e^{-t/\tau} + c_0$ as a dashed line, which is so-to-speak the average trajectory, and the oscillations take place around it. In the following we study the decay time τ and the oscillation frequency ω as function of the wavevector Q . The decay time $\tau = \tau(Q)$ yields the transport behavior, whereas the oscillation frequency $\omega = \omega(Q)$ yields a dispersion relation.

For the XX model ($\Delta = 0$), the decay time τ shows a linear scaling with inverse wavevector: a power-law fit $\tau \propto Q^{-\alpha}$ yields an exponent of $\alpha = 1.00(5)$, indicating ballistic transport (Figure 4-6a). This is reminiscent of the single (free) magnon which travels with ballistic wavefronts in a spin chain according to a *quantum* random walk, where a particle moves *coherently* with equal *matrix elements* in both directions simultaneously.

For the XXX model ($\Delta = 1$), a power-law fit of the decay constant τ versus Q yields an exponent of $\alpha = 1.87(4)$, which is close to 2, indicating diffusive transport (Figure 4-6b). This is reminiscent of a single magnon which travels within a spin chain according to a *classical* random walk, where it moves *incoherently* with equal *rates* in both directions.

The oscillation frequencies ω as a function of the wavevector Q yield dispersion relations. Interestingly, we measure *linear* dispersion relations $\omega(Q) = vQ$ for both $\Delta = 0$ and 1, yielding $v = 0.76(1) v_F$ and $v = 0.35(1) v_F$, where $v_F = a/(\hbar/J_{xy})$ is the Fermi velocity (see Figure 4-7). Interaction slows this velocity down by a factor of ≈ 2 . Perhaps this is related to the observations in the bound-magnon paper [18], where interactions reduce the velocity of a bound magnon compared to a free magnon, also by a factor of 2, as shown in Figure 4-9. The theoretical prediction of the velocity ratio is 2Δ for general values of the anisotropies [32].

4.4 Positive anisotropies ($\Delta > 0$)

We gradually tune spin-spin interactions from $\Delta = 0$ (non-interacting fermions) to $\Delta = 1$ (strongly-interacting fermions) to study how the behavior of transport changes from *ballistic* to *diffusive*. Additionally, we study $\Delta > 1$, where spin-spin interactions dominate. In a classical interacting gas, for example, one would expect ballistic behavior on lengthscales smaller than the mean-free path and diffusion on larger lengthscales; and the mean-free path is determined by the interaction strength. However, we find transport which is neither ballistic nor diffusive at all measured modulation length-scales λ . For various different anisotropies Δ we measure the Q -dependence of the spin helix decay time τ (Figure 4-10a), and we find that the data is very well described by power laws $\tau = \mu Q^{-\alpha}$, at least in the measured regime $\lambda = 6$ to $30 a$. The obtained exponents α are shown in Figure 4-10b.

We observe the following general behavior: As we increase the anisotropy starting from $\Delta = 0$, initially the exponent stays close to $\alpha = 1$, but the coefficient μ increases. Above a critical anisotropy of about $\alpha = 0.5$ however, it is the exponent which increases. We identify the following regimes. Ballistic regime: As we go from $\Delta = 0$ to 0.5, transport stays ballistic but the characteristic velocity. Superdiffusive regime: Between $\Delta = 0.5$ to 1 the exponent increases smoothly from $\alpha = 1$ to $\alpha = 2$. For example we measured $\alpha = 1.48(4)$ at $\Delta = 0.78$. Subdiffusive regime: For $\Delta > 1$ the exponent continues to increase smoothly to values $\alpha > 2$. For example at $\Delta = 1.58$, we measured an exponent of $\alpha = 2.83(14)$. This observation is in contrast to a recent theoretical prediction [11], which rather suggests a sharp transition: ballistic ($\alpha = 1$) for all $\Delta < 1$, diffusive ($\alpha = 2$) for all $\Delta > 1$ and superdiffusive ($\alpha = 1.5$) only for $\Delta = 0$. But this is calculated for a partially polarized domain wall, which is a mixed (i.e. thermal) state. We, however, study a fully polarized spin-helix, which is pure state far from equilibrium. Nevertheless, we have some evidence, that for very long wavelengths $\lambda \gg a$ we would recover such a sharp transition with spin-helix states as well [28].

Remarkably, we find linear dispersion relations for all positive anisotropies $\Delta \geq 0$

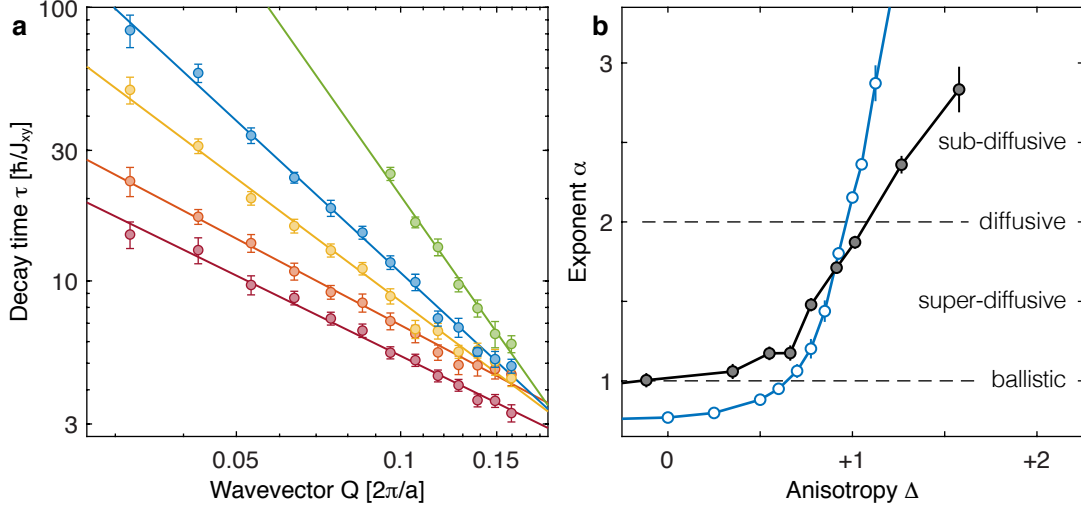


Figure 4-10: **Power law scalings** of decay time constants τ for positive anisotropies $\Delta > 0$. **a**, Experimental results for $\Delta = -0.12$ (orange), 0.35 (orange), 0.78 (yellow), 1.01 (blue), 1.58 (green). Lines are power law fits. **b**, Fitted power law exponents from experiments (filled symbols) and theory (open symbols), obtained from simulations of the defect-free XXZ model (blue). For $\Delta \geq 0$ we observe anomalous diffusion: The exponent increases smoothly from ballistic (red) to superdiffusive (yellow) to diffusive (blue) to subdiffusive (green).

(Figure 4-11). With increasing anisotropy Δ , the oscillations become smaller and the velocity decreases. We already saw that at $\Delta = 1$ the velocity is reduced by about a factor of about 2Δ . This is analogous to the velocity of bound-magnons compared to free magnons. It seems this prediction also applies qualitatively for spin-helix states for general anisotropies close to $\Delta = 1$. But we find it remarkable, that we measure linear dispersion relations at all, in the regime where the decay time τ has superdiffusive, diffusive and subdiffusive scaling.

We note that while oscillations are difficult to discern by eye (e.g. in Figure 4-8a), especially for large anisotropies Δ and small wavevectors Q , the fitted oscillations frequencies ω all fall very well on linear dispersion relations, which we regard as evidence for their significance. The linear scaling $\omega(Q) = vQ$ even persists in the superdiffusive, diffusive and subdiffusive regimes, where the power law scaling of the decay time constant $\tau \propto Q^{-\alpha}$ is strongly nonlinear.

But since the oscillations are small away from the ballistic regime, for all positive anisotropies, the decay curves can still be approximately collapsed into a single curve,

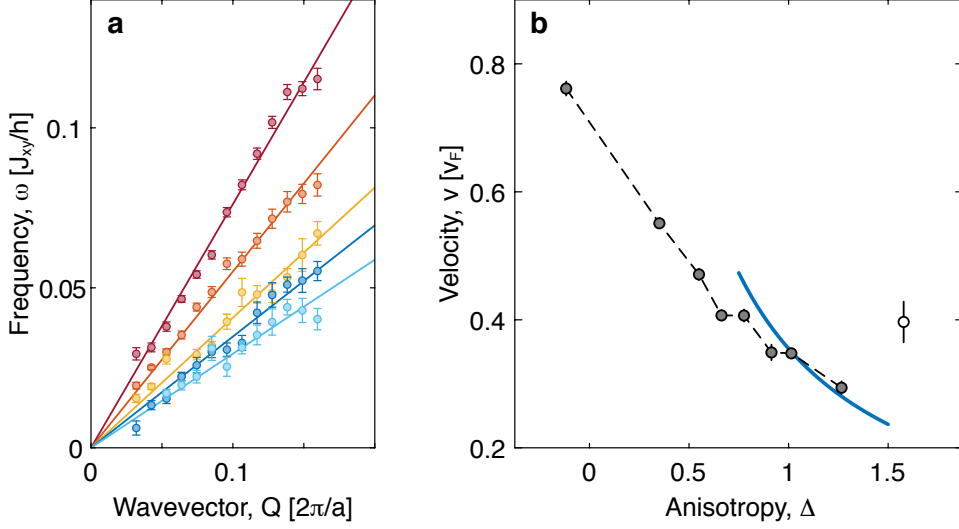


Figure 4-11: **Dispersion relations.** **a**, The oscillation frequencies follow linear dispersion relations $\omega(Q) = vQ$ shown for $\Delta = -0.12$ (red), 0.35 (orange), 0.78 (yellow), 1.01 (blue) and 1.27 (light blue). **b**, The obtained velocities v decrease with increasing anisotropy Δ . It seems that close to $\Delta = 1$ the velocity is reduced to $v_0/2\Delta$ (blue line) compared to the velocity v_0 measured for $\Delta = 0$.

if we rescale time by λ^α (Figure 4-12) This shows that this power-law scaling indeed applies for all evolution times t (which we could measure experimentally, i.e. early and intermediate times). This collapse suggests universal behavior, at least for the decaying part of the decay curve, described by the decay time τ . However, this collapse is not quite perfect, because we always find small oscillations around the overall decay, and these oscillations have a different scaling with wavelength.

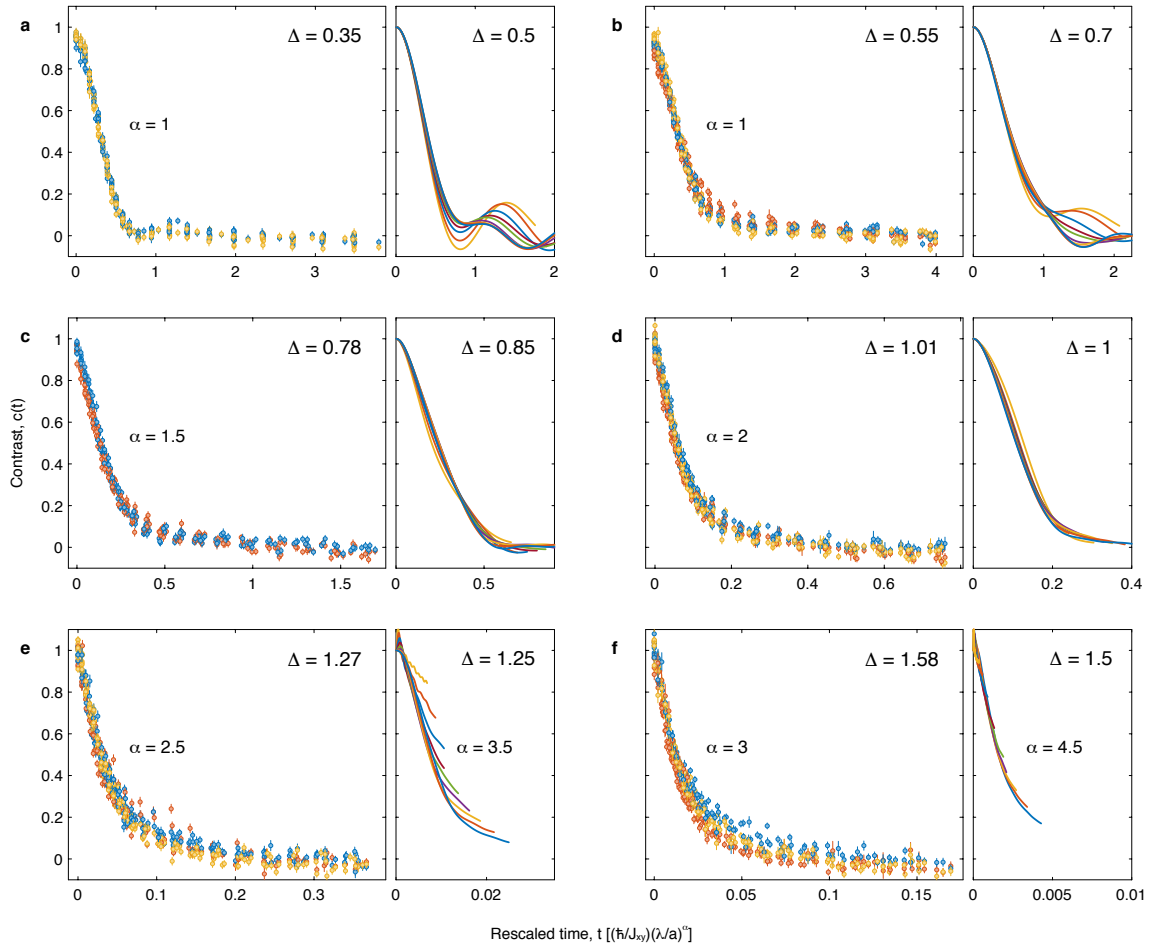


Figure 4-12: **Collapse of decay curves** for positive anisotropies $\Delta > 0$. All decay curves $c(t)$ for different wavelengths $\lambda = 15.7a, 13.4a, 11.7a, 10.4a, 9.4a, 8.5a, 7.8a, 7.2a, 6.7a$ collapse very well into a single curve for all evolution times t , when time units are rescaled by λ^α , where the exponent α is a function of anisotropy Δ , both for experiment (points) and theory (solid lines). Experimental points were measured for lattice depths $9E_R$ (red), $11E_R$ (blue), $13E_R$ (yellow). **a, b**, Ballistic regime ($\alpha = 1$), **c**, superdiffusion ($\alpha = 1.5$), **d**, diffusion ($\alpha = 2$), **e, f**, subdiffusion ($\alpha = 2.5, 3$ for experiment and $\alpha = 3.5, 4.5$ for numerical simulations). In **f**, experiments covered a reduced range $\lambda \leq 10.4a$). The experimentally measured oscillation frequencies ω follow a linear dispersion relation for all anisotropies $\Delta \geq 0$ (Figure 4-11) and have a scaling behavior different from the decay rates. However, such oscillations are small outside the ballistic regime $\alpha \approx 1$, and therefore only lead to a small deviation from the collapse behavior.

4.5 Negative anisotropies ($\Delta < 0$)

So far we looked at positive anisotropies $\Delta \geq 0$. Now we show our results for negative anisotropies $\Delta < 0$. What happens, when we switch the *sign* of the interactions? For $\Delta < 0$, the effective fermions are also interacting. But now spin-spin interactions J_z and spin exchange J_{xy} have opposite signs. This sign change introduces qualitatively very different transport behavior. We studied the spin helix decay at three different negative anisotropies $\Delta = -1.02$, -1.43 , and -1.79 . But for a long time we could not understand the data. We almost decided not to publish these datasets. The previous

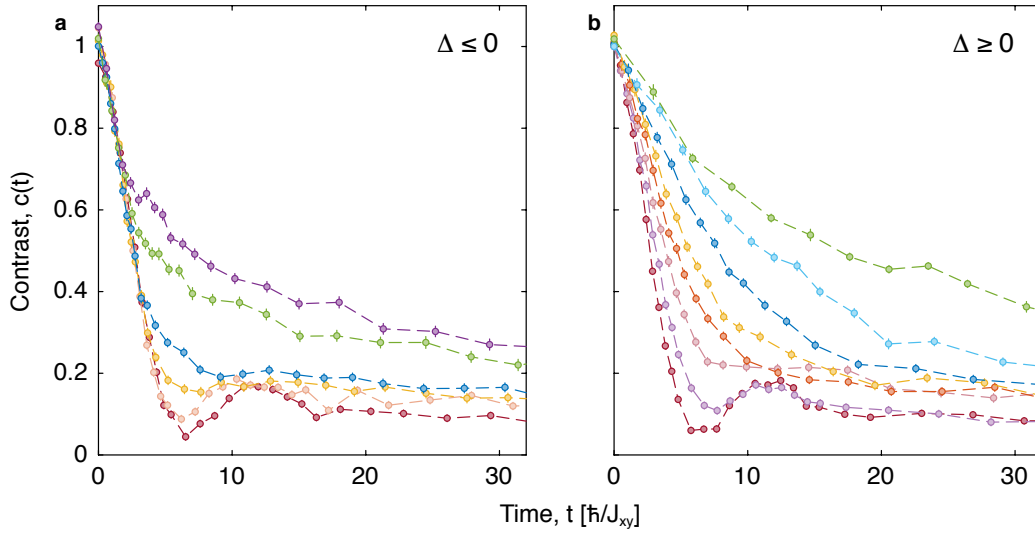


Figure 4-13: **Decay behavior as a function of anisotropy** ranging from (a) negative to (b) positive, for one fixed wavelength $\lambda = 10.4 a$. Using $\Delta \approx 0$ as a reference point, we show how the temporal profile of the decay curve $c(t)$ changes when we introduce positive or negative interactions. Every data point is an average of two measurements at lattice depths $9 E_R$ and $11 E_R$. **a**, from bottom to top: $\Delta = -0.12$ (red), -0.59 (pink), -0.81 (yellow), -1.02 (blue), -1.43 (green), -1.79 (purple). **b**, from bottom to top: $\Delta = -0.13$ (red), 0.08 (purple), 0.35 (pink), 0.55 (orange), 0.78 (yellow), 1.01 (blue), 1.27 (light blue), 1.58 (green). Regardless of the sign, for increasing $|\Delta|$ the decay always slows down and the revivals damp out more quickly. However, there is a big difference in how this slowdown happens: **b**, For increasing positive interactions $\Delta > 0$, the initial rate of decay increases continuously. **a**, In contrast, for all negative interactions $\Delta < 0$, the initial rate of decay stays constant (and is ballistic), coinciding with the $\Delta \approx 0$ case. It is only after a critical time t_0 that the decay suddenly starts slowing down (and becomes diffusive) for times $t > t_0$. This critical time t_0 decreases with increasing negative interaction strength $|\Delta|$.

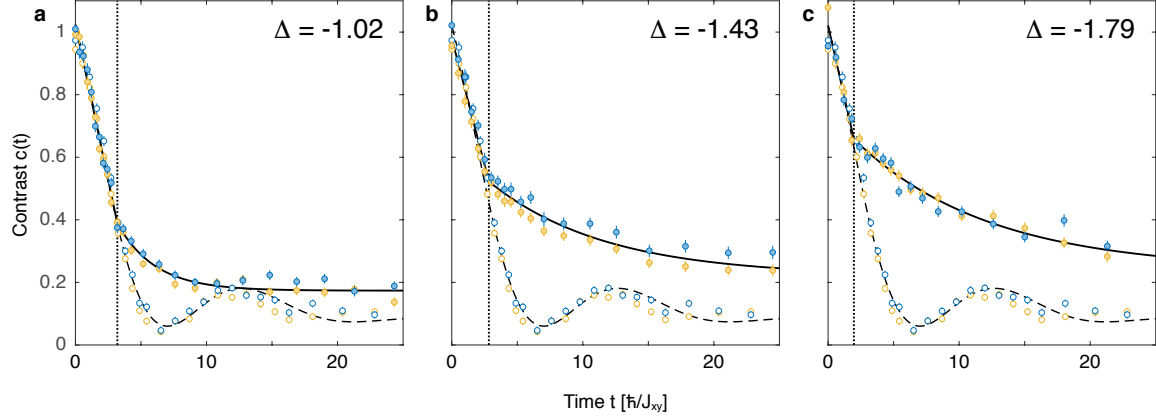


Figure 4-14: **Temporal crossover from ballistic to diffusive transport** for negative anisotropies $\Delta < 0$. Spin helix contrast $c(t)$ for $\lambda = 10.4 a$ and $\Delta = -1.02$ (a), -1.43 (b), and -1.79 (c) (filled circles) measured at lattice depths $11 E_R$ (blue) and $13 E_R$ (yellow). A piecewise fit (solid line) is linear at short times (I) and exponential at long times (II) with a crossover at $t = t_0$ (vertical dotted line). For $t < t_0$ the decay coincides well with the non-interacting case $\Delta \approx 0$ (open circles and dashed line).

fit function (which we used extensively for $\Delta \geq 0$) does not work anymore for negative anisotropies $\Delta < 0$. Only one thing was clear to us right from the start, right from taking the first such dataset: Positive and negative anisotropies are very different. But we only really understood what is going on, when we plotted the data as shown in Figure 4-13; at one fixed wavelength λ for varying anisotropies Δ .

Starting with zero interactions as a reference point, we show how the temporal profile of the decay curve changes when we introduce positive or negative interactions. On the positive side ($\Delta \geq 0$), we see how stronger interactions remove the oscillation and turn the decay more and more into an exponential. On the negative side ($\Delta \leq 0$), stronger interactions also remove the oscillation. But for short enough times, all the curves lie right on top of each other and, in particular, on top of the ballistic curve. It seems like, for short enough times, the system does not feel the interactions yet. But after enough time each curve suddenly starts to deviate from the ballistic case and decays much more slowly for later times.

Motivated by this, we tried a piecewise fit for the two regimes: (I) a linear function $1 - t/\tau_I$ at short times and (II) an exponential $e^{-t/\tau_{II}}$ at long time, with the respective time constants τ_I and τ_{II} and the crossover time t_0 as free parameters (see Figure 4-

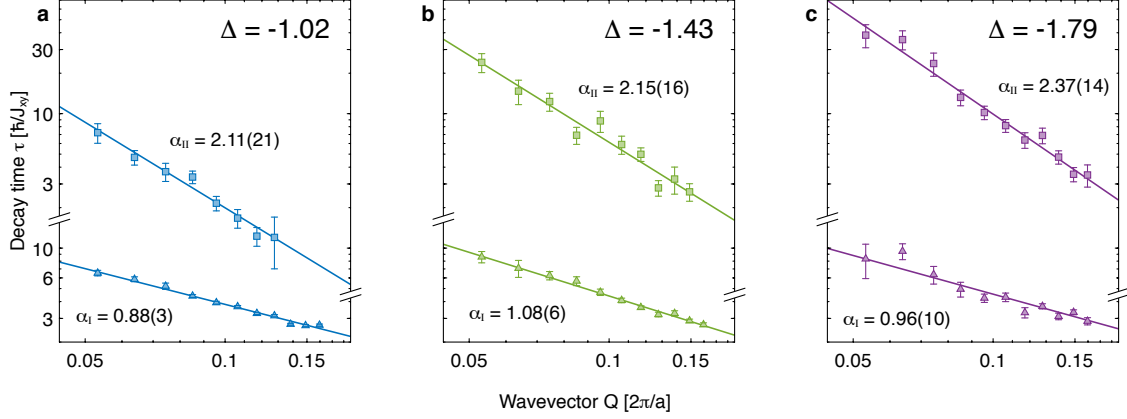


Figure 4-15: **Power law scalings** of decay time constants τ_I and τ_{II} for negative anisotropies $\Delta < 0$. Experimental results are shown for $\Delta = -1.02$ (a, blue), -1.43 (b, green), -1.79 (b, purple). Lines are power law fits. For $\Delta < 0$ we observe behavior reminiscent of a classical gas: Transport is ballistic at (I) short times (triangles) and diffusive at (II) longer times (squares).

14). This fit function reproduces the data well. And we observe that for stronger interaction $|\Delta|$ the crossover time (between the two regimes I and II) moves to earlier

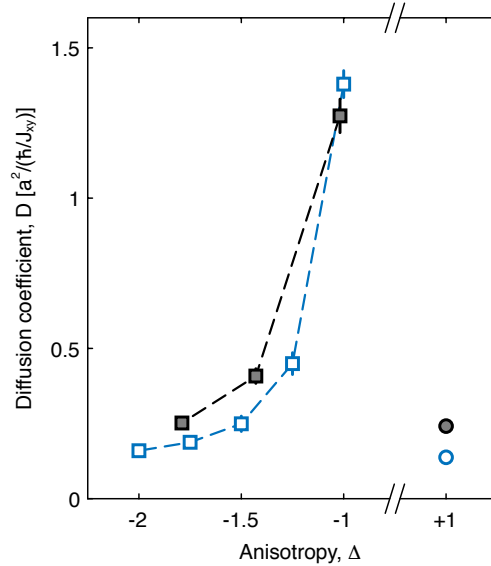


Figure 4-16: **Diffusion coefficients** for the diffusive long-time regime (II) obtained from experiment (filled symbols) and theory (open symbols). For negative anisotropies $\Delta < 0$, values were determined from quadratic power law fits $1/\tau = DQ^2$ to the data points in Figure 4-15 (experiment) and to the time constants obtained from Figure 4-17a-c (theory) for the diffusive regime (II). Note that for $\Delta \geq 0$ the system is only diffusive for $\Delta = +1$, as shown in Figure 4-6b (experiment).

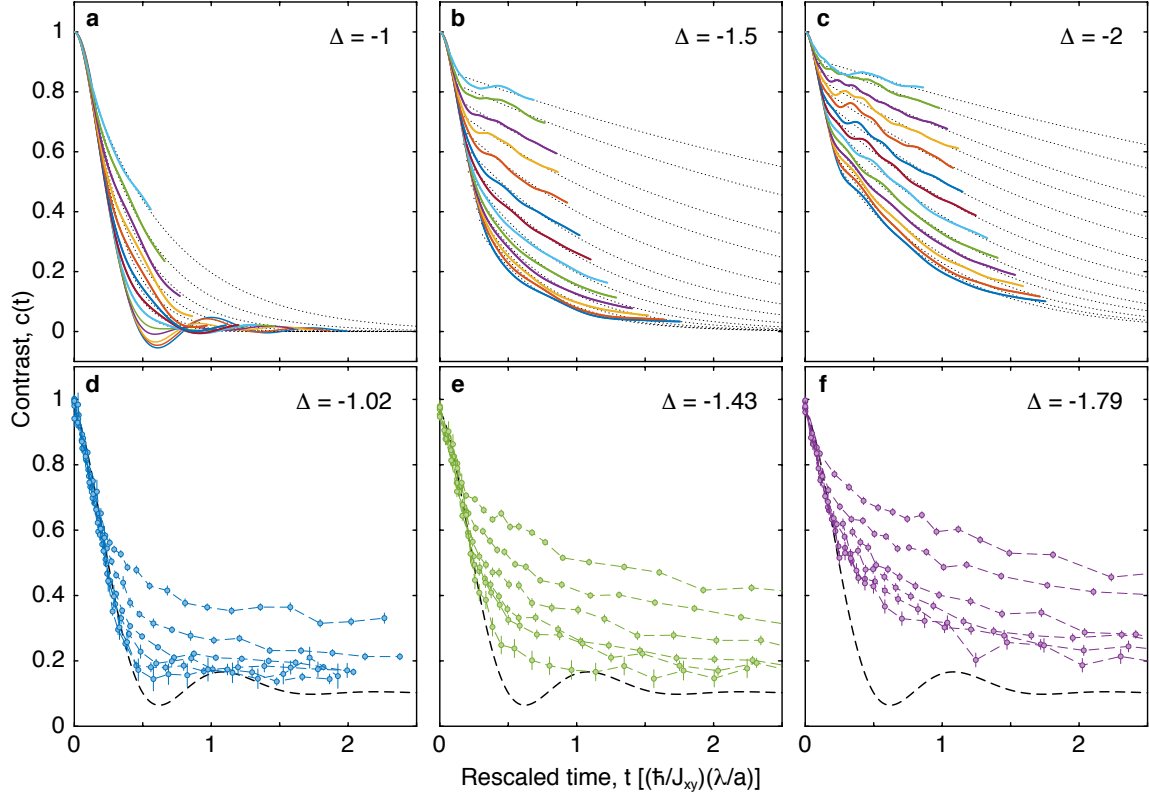


Figure 4-17: **Collapse at short times** for negative anisotropies $\Delta < 0$. All decay curves $c(t)$ for different wavelengths λ collapse into a single curve at early times, when time units are rescaled by λ (indicating ballistic behavior). For later times the decay is diffusive with different scaling. **a-c**, Theory (from top to bottom: $\lambda = 31.3 a$, $23.5 a$, $18.8 a$, $15.7 a$, $13.4 a$, $11.7 a$, $10.4 a$, $9.4 a$, $8.5 a$, $7.8 a$, $7.2 a$, $6.7 a$, $6.3 a$). The dotted lines are exponential fits $e^{-t/\tau_{\text{II}}}$ to the diffusive regime and the time constants τ_{II} are used to obtain numerical power-law exponents in Figure 4-18c and diffusion coefficients in Figure 4-16. **d-f**, Experiment (from top to bottom: $\lambda = 18.8 a$, $13.4 a$, $10.4 a$, $8.5 a$, $7.2 a$, $6.3 a$) shown for a lattice depth of $11 E_R$. The dashed line indicates the ballistic case $\Delta \approx 0$ (see Figure 4-5c).

times. We obtain the time constants τ_{I} and τ_{II} for short time and long time behavior separately and plot them as function of wavevector Q in Figure 4-15. For short times we obtain ballistic scaling. For long times, we obtain diffusive scaling. For stronger interactions, diffusion slows down. For weaker interactions, diffusion speeds up. The diffusion coefficient is changes when the anisotropy Δ is varied (Figure 4-16). This behavior is reminiscent of a classical gas: ballistic motion at short times (shorter than the mean-free time) and diffusive at longer times.

Furthermore, we can now see that all of our data for different wavelengths λ

collapses for the initial ballistic regime, if we rescale the time axis by λ , as shown in Figure 4-17d-f. The deviation from the collapsed curve indicates a crossover to diffusion where the scaling is different. This observation is reproduced by numerical simulations in Figure 4-17a-c.

4.6 Summary

For positive anisotropies $\Delta \geq 0$, we see anomalous diffusion. The exponent α varies smoothly. With increasing interaction strength $|\Delta|$ we go through a ballistic, superdiffusive, diffusive, and subdiffusive regime. This is confirmed by numerical simulations. Decay curves for different wavelengths λ (almost) collapse into a single curve, if time is rescaled by λ^α , indicating close to universal behavior. But there are small oscillations with linear dispersion relations $\omega(Q) = vQ$. For negative anisotropies $\Delta < 0$, we see behavior reminiscent of a classical gas. At short times the dynamics is ballistic. At longer times the dynamics is diffusive. This is confirmed by numerical simulations, as well. The diffusion coefficient varies smoothly as function of anisotropy Δ . These findings are summarized in Figure 4-18.

We still do not have an intuitive physical explanation, why positive and negative anisotropies cause such different behavior. Why does the sign of interactions matter so much? Is there a difference in resonant and off-resonant scattering? Is the dynamics on the positive side more coherent and on the negative side more incoherent? Here we summarize the open questions:

1. Why do we observe linear dispersion relations $\omega(Q) = vQ$ for all positive anisotropies? We already mentioned that this might be related to the propagation of bound-magnons with a reduced velocity by a factor of 2Δ , compared to the velocity of free magnons.
2. Why do we observe anomalous diffusion $\tau \propto Q^{-\alpha}$ for all positive anisotropies? We think, we have evidence, that in the continuum limit $\lambda \gg a$ there is a sharp crossover from $\alpha = 1$ to $\alpha = 2$ as a function of anisotropy. We think, that the

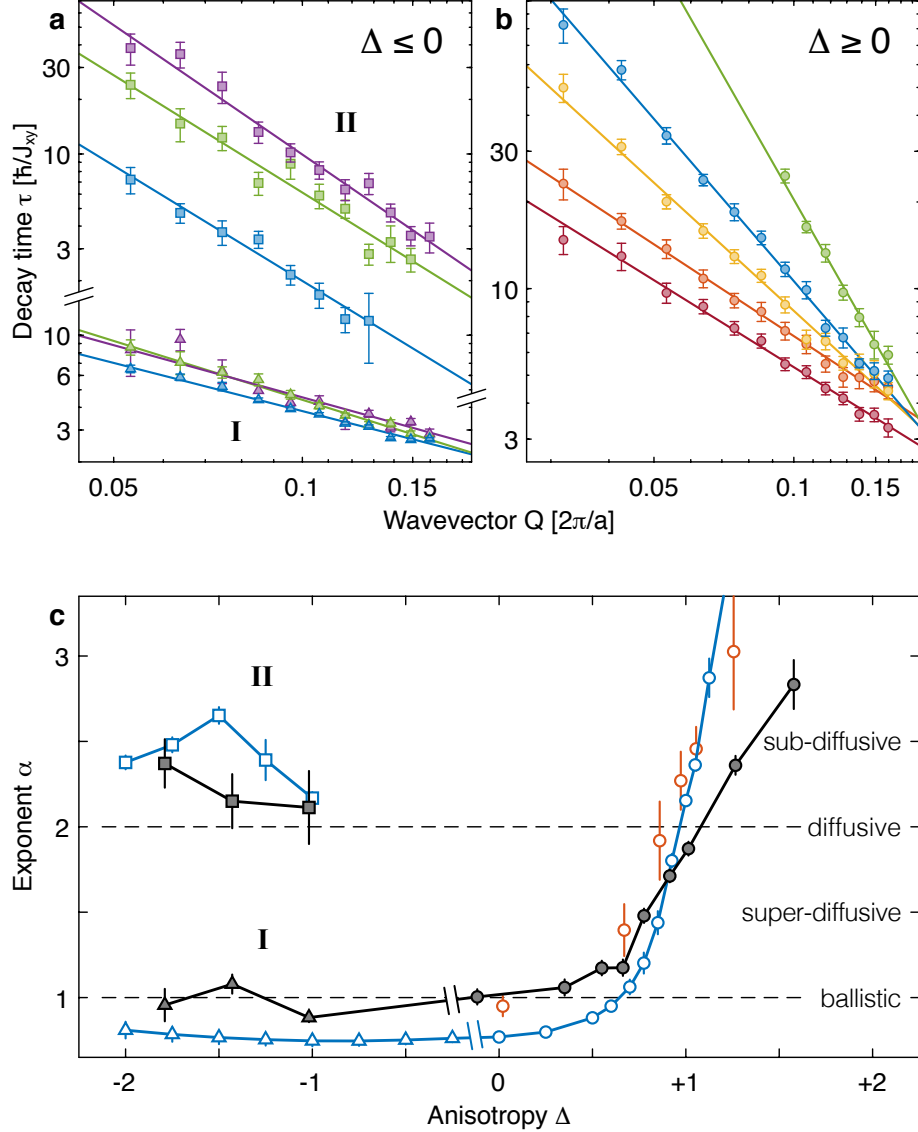


Figure 4-18: **Power law scalings** of decay time constants τ for anisotropies Δ ranging from (a) negative to (b) positive. Experimental results are shown in a for $\Delta = -1.02$ (blue), -1.43 (green), -1.79 (purple) and in b for $\Delta = -0.12$ (red), 0.35 (orange), 0.78 (yellow), 1.01 (blue), 1.58 (green). Lines are power law fits. c, Fitted power law exponents from experiments (filled symbols) and theory (open symbols), obtained from simulations of the defect-free XXZ model (blue) and t - J model with 5% hole fraction (red). a-c, For $\Delta \geq 0$ (circles) we observe anomalous diffusion: The exponent increases smoothly from ballistic (red) to superdiffusive (yellow) to diffusive (blue) to subdiffusive (green). For $\Delta < 0$ we observe behavior reminiscent of a classical gas: Transport is ballistic at (I) short times (triangles) and diffusive at (II) longer times (squares).

smooth crossover, which we observe in the experiment, is related to the relatively short wavelengths between $\lambda = 6a$ and $30a$ compared to the lattice spacing a , which we use in the experiment. In that case, the origin of anomalous diffusion is the finite lattice spacing a (see Methods section in our publication [28]).

3. Why is there a temporal crossover from ballistic to diffusive motion for negative anisotropies?
4. Why is the behavior at the isotropic point $\Delta = 1$ not superdiffusive with $\alpha = 1.5$? This was predicted by Ref. [11] for a sharp domain wall state, however which has smaller than full contrast (i.e. a mixed, thermal state). Surprisingly, the Bloch group [19] recently measured superdiffusion ($\alpha = 1.5$) even for a fully polarized sharp domain wall. I therefore expect that we can definitely observe superdiffusion with a spin-helix at the isotropic point ($\Delta = 1$), too, if we start with a partially polarized spin helix, even if it still has 50% contrast.

Chapter 5

Transverse spin dynamics

A transverse spin helix is sensitive to more decay mechanisms than a longitudinal spin helix. Anisotropic spin couplings in the Hamiltonian break spin-rotational symmetry. Transverse spin components are no longer conserved and can decay not only by transport, but also by fast, local dephasing. However, even for isotropic interactions, we observe dephasing due to a new effect: an effective magnetic field created by superexchange, which has its origin in the mapping from the Hubbard model and which has not been observed before. This field leads to additional dephasing mechanisms, because our system is not a perfect, homogeneous, and infinitely long spin-chain: there is dephasing due to (i) inhomogeneity of the effective field from variations of lattice depth between chains; (ii) a twofold reduction of the field at the edges of finite chains; and (iii) fluctuations of the effective field due to the presence of mobile holes in the system. The latter is a new coupling mechanism between holes and magnons.

*This chapter supplements work reported in the following publication [29]
(included in Appendix B)*

P. N. Jepsen, W. W. Ho, J. Amato-Grill, I. Dimitrova, E. Demler, W. Ketterle
Transverse Spin Dynamics in the Anisotropic Heisenberg Model Realized with Ultra-cold Atoms

Phys. Rev. X **11**, 041054 (2021)

5.1 Introduction

In the previous chapter, we were able to show that the anisotropy profoundly changes the nature of transport of longitudinal spin components after a quantum quench from a so-called *longitudinal* spin helix (Figure 5-1b). We observed ballistic, subdiffusive, diffusive and superdiffusive behavior controlled by the anisotropy. The decay rate is given by power laws

$$\gamma \propto (Qa)^\alpha, \quad (5.1)$$

where the exponent α depends on the anisotropy. Another way to probe the anisotropy of the Hamiltonian is to rotate the initial state and look for a change in behavior of the time evolution. Here we begin with a *transverse* spin helix (Figure 5-1a), which is related to the longitudinal spin helix (Figure 5-1b) by a $\pi/2$ -rotation. And we observe even more dramatic effects of the anisotropy. A longitudinal helix is an excellent probe of transport properties because, involving a modulation in the population of $|\uparrow\rangle$ and $|\downarrow\rangle$, it can only decay by rearrangement of physical spins over distances comparable to the modulation wavelength λ . A transverse helix, however, is a modulation entirely in the phase sector, so a loss in contrast can also be caused by spins precessing at different rates around the S_z axis. A transverse spin helix can therefore decay not only by transport, but also by local dephasing. Actually, away from the isotropic point ($\Delta = 1$), these two decay mechanisms become indistinguishable.

In the classical limit, any transverse spin helix for any anisotropy Δ is stationary, since the torques exerted by neighboring spins on a given spin cancel exactly (Figures 5-2 and 5-3). Therefore, what we study here are the effects of quantum fluctuations on their stability (Figure 5-3). And we find that the decay rate is described by

$$\gamma = \gamma_1 |\Delta - \cos(Qa)| + \gamma_0. \quad (5.2)$$

The first term $\gamma_1 |\Delta - \cos(Qa)|$ captures pure spin dynamics, which we study for the XX model ($\Delta = 0$) and XXX model ($\Delta = 1$) in the next two Sections 5.2 and 5.3. But we identify an additional isotropy breaking term in Hamiltonian, which even

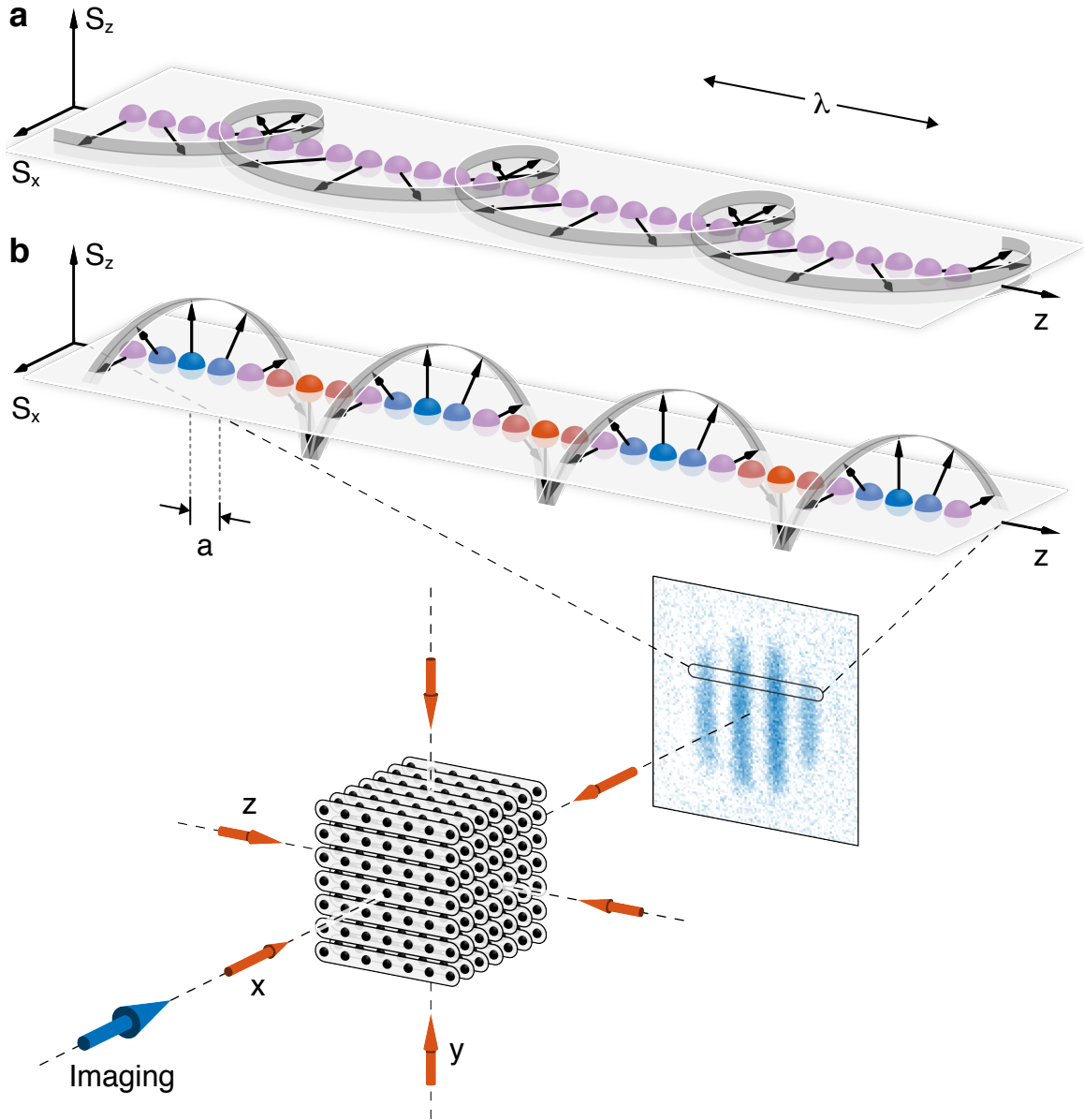


Figure 5-1: **Geometry of the experiment.** The initial state is a transverse (a) or longitudinal (b) spin helix where the spin vector winds within the S^x - S^y plane (a) or S^z - S^x plane (b). The transverse helix (a) is a pure phase modulation of spin $|\uparrow\rangle$ and $|\downarrow\rangle$ states, whereas the longitudinal helix (b) also involves population modulation. Deep optical lattices along the x and y directions create an array of independent spin chains. The z lattice is shallower and controls spin dynamics along each chain.

exists for isotropic interactions: an effective magnetic field created by superexchange, which arises from the mapping from the underlying Hubbard model. This field induces additional dephasing mechanisms which are captured by a nonzero background decay rate $\gamma_0 > 0$. We find three different ways to observe this field directly (Section 5.4).

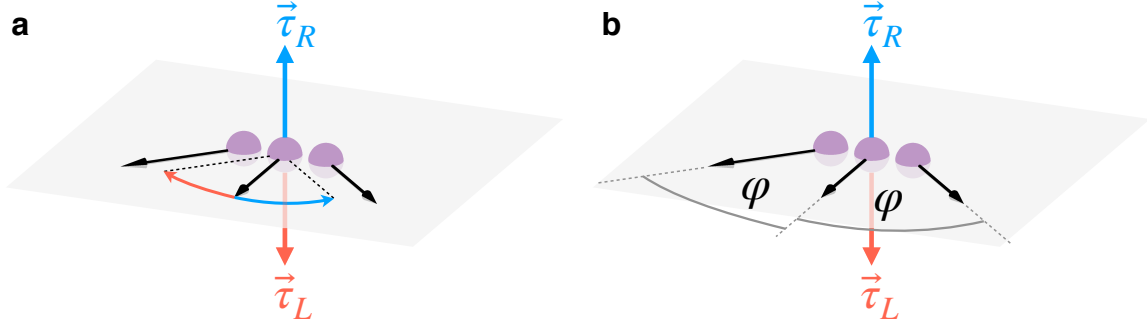


Figure 5-2: **Classical spins.** **a**, The spin in the middle experiences a torque τ_R (blue) from the spin to its right, towards the aligned ($J_{xy} < 0$) or anti-aligned ($J_{xy} > 0$) configuration. At the same time, it experiences an opposite torque τ_L (red) from the spin to its left. **b**, In a transverse spin helix, the torques from both neighbors cancel exactly $\tau_L + \tau_R = 0$, because the angles $\varphi = Qa$ between neighboring spins are equal. A *classical* transverse spin helix is stationary.

Lastly, we discuss how this effective magnetic field induces dephasing (Section 5.5). If this effective magnetic field was *uniform*, it should not influence the dynamics but only lead to uniform spin precession on top of the overall spin dynamics. Such a uniform magnetic field term could formally be removed from the Hamiltonian, by transforming into a corotating frame. However, finite chain length, holes in the system, and inhomogenous lattice beams lead to overall dephasing, because these effects make this effective field *non-uniform*. In an ideal homogeneous system (one infinitely long spin chain without holes) these dephasing mechanisms would be absent and $\gamma_0 = 0$. On one hand, a finite $\gamma_0 > 0$ is due to imperfections of the system. On the other hand, such an imperfect system allows to detect the effective magnetic field directly. Furthermore, mobile holes could even be used to study hole-magnon coupling.

5.2 XX model

We realize a very anisotropic system by tuning to the non-interacting point ($\Delta = 0$). As before, we confirm that the dynamics is driven by superexchange in the Heisenberg model, by repeating the experiment at two different lattice depths $9 E_R$ and $11 E_R$. Figure 5-4a shows that the decay of a transverse spin helix is generally fast for the whole range of wavelengths $\lambda = 6a$ to $30a$ which we studied. Varying the wavelength

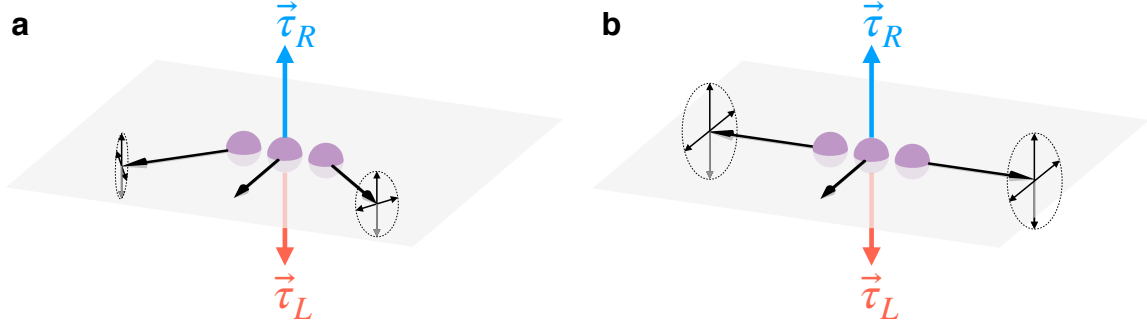


Figure 5-3: **Quantum spins.** **a**, Quantum fluctuations of the spins lead to a fluctuating torque which is only zero on average $\langle \tau_L + \tau_R \rangle = 0$. A *quantum* transverse spin helix decays as a result of quantum fluctuations. **b**, For $\Delta = 0$, i.e. for vanishing longitudinal coupling $J_z = 0$, the quantum fluctuations of the neighboring spins do not couple to the spin in the middle, if spins are at an angle of $\varphi = 90^\circ$.

shows that for very short wavelengths the decay gets even slower! This is in stark contrast to the linear Q -dependence of a longitudinal spin helix at $\Delta = 0$, where spin-helix states with shorter wavelengths decay faster. This shows, in particular, that the decay is not caused by transport, but by local dephasing.

We were very surprised, that the decay slowed down for shorter wavelengths. In particular, since only the three largest values of Q in our dataset showed this effect, where we were already pushing our imaging system to its resolution limit. At that time, we did not even know if this effect is real, especially since this was only a $\sim 20\%$ reduction in the decay rate. Only much later we found out that we were already seeing the signature of an exact many-body eigenstate [47, 48], which is realized at $Qa = \pi/4$, when neighboring spins are at an angle of 90° . This is the topic of chapter 6, where we extended our observable range of wavevectors Q all the way to $Qa = \pi$.

Nevertheless, shortly after this first measurement, our theory collaborator Wen Wei Ho already found out that the decay rates should scale as $\gamma \propto |\cos(Qa)|$. Our data did not show such *strong* dependence on Q . Nevertheless, the data can still be explained, if we assume that there exists one more large background dephasing rate γ_0 , which is Q -independent. It took us a long time to justify to ourselves, that this is appropriate. But we also observe such a Q -independent background decay rate γ_0 much more directly in the isotropic model ($\Delta = 1$), because there the longitudinal and transverse spin helix should behave exactly the same.

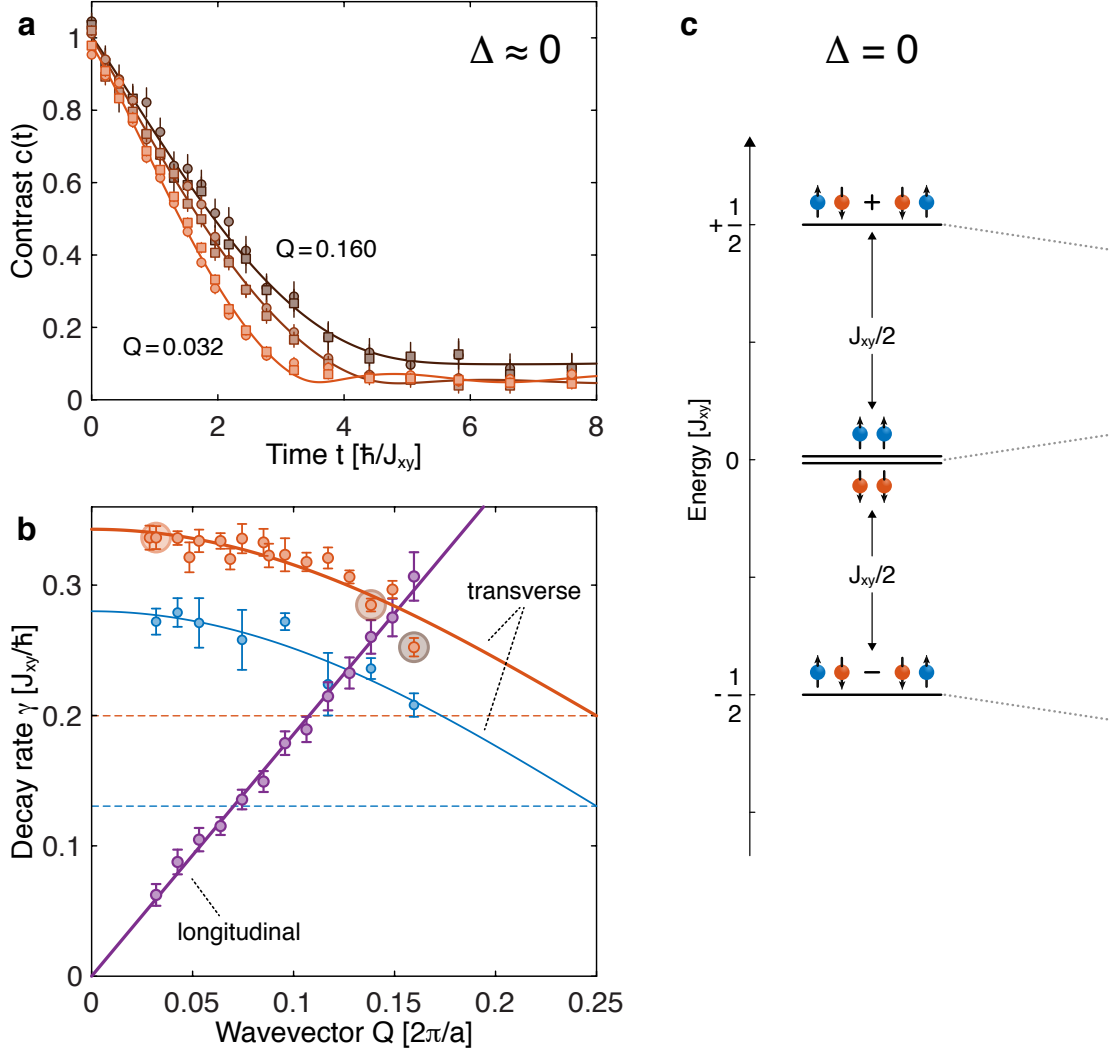


Figure 5-4: **Spin dephasing and spin transport** for the XX model ($\Delta \approx 0$). **a, Spin relaxation.** Transverse spin-helix contrast $c(t)$ for $Qa = 2\pi \times 0.032, 0.138$ and 0.160 (bright to dark orange). The curves for different lattice depths $11 E_R$ (\circ) and $13 E_R$ (\square) collapse when times are rescaled in units of the corresponding spin-exchange times $\hbar/J_{xy} = 1.71$ ms (\circ) and 4.30 ms (\square). The transverse spin decays on a time scale of a few spin-exchange times which increases for smaller wavelengths $\lambda = 2\pi/Q$. **b, Wavevector dependence.** The initial decay rates (orange points; with values from **a** highlighted) follow a cosine dependence $\gamma(Q) = \gamma_1 \cos(Qa) + \gamma_0$ (solid orange line) with a constant background rate $\gamma_0 = 0.20(2) J_{xy}/\hbar$ (dashed orange line). This is in strong contrast to the longitudinal spin helix (purple) which shows linear scaling with Q (indicating ballistic transport). A spin echo (π -pulse at time $t/2$) reduces the background rate to $\gamma_0 = 0.13(3) J_{xy}/\hbar$ (dashed blue line). **c, Energy levels** of the Heisenberg Hamiltonian for two spins in a double-well potential. For $\Delta \neq 1$, the triplet states are split, causing dephasing for an x polarized state $|\rightarrow\rightarrow\rangle = (|\uparrow\rangle + |\downarrow\rangle)(|\uparrow\rangle + |\downarrow\rangle) = |\uparrow\uparrow\rangle + (|\uparrow\downarrow\rangle + |\downarrow\uparrow\rangle) + |\downarrow\downarrow\rangle$.

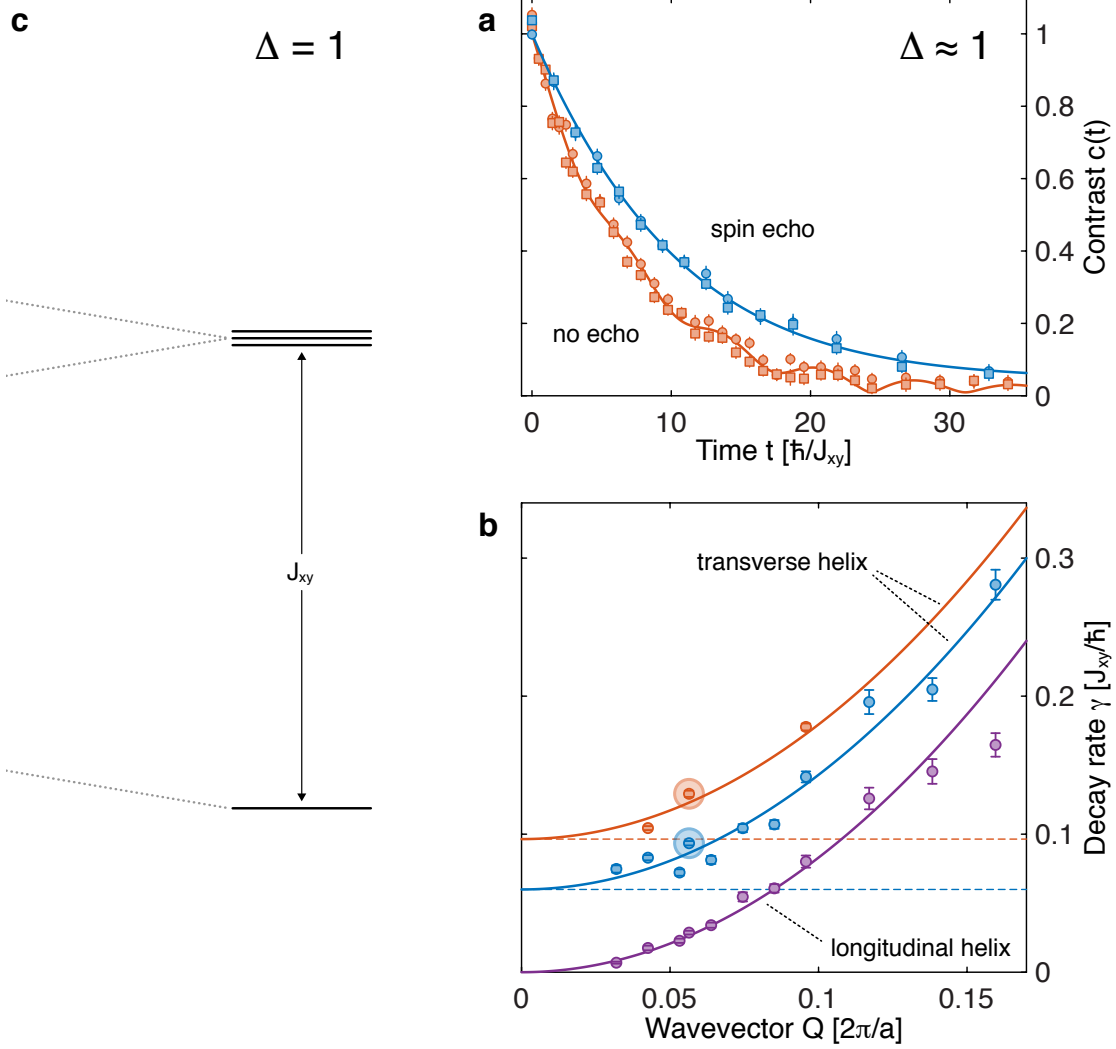


Figure 5-5: **Spin dephasing and spin transport** for the XXX model ($\Delta \approx 1$). **a, Spin relaxation.** Transverse spin-helix contrast $c(t)$ for $Qa = 2\pi \times 0.056$ without spin echo (orange) and with spin echo (blue). The difference shows the presence of inhomogeneous dephasing. The curves taken for different lattice depths $11 E_R$ (\circ) and $13 E_R$ (\square) collapse when times are rescaled in units of the corresponding spin-exchange times $\hbar/J_{xy} = 2.55$ ms (\circ) and 6.42 ms (\square). **b, Wavector dependence.** Decay rates for the transverse helix (orange and blue points; with values from **d** highlighted) and longitudinal helix (purple points), for $\Delta \approx 1$. The orange (no echo) and blue (with echo) solid lines are fits $\gamma(Q) = DQ^2 + \gamma_0$ assuming two contributions to the decay rate: one quadratic term (indicating diffusive transport) with diffusion constant D (taken from the longitudinal spin dynamics shown in purple), the other Q -independent γ_0 (shown by the dashed lines). **c, Energy levels** of the Heisenberg Hamiltonian for two spins in a double-well potential. For $\Delta = 1$, the triplet states are degenerate. Therefore, the x polarized state $|\rightarrow\rightarrow\rangle = (|\uparrow\rangle + |\downarrow\rangle)(|\uparrow\rangle + |\downarrow\rangle) = |\uparrow\uparrow\rangle + (|\uparrow\downarrow\rangle + |\downarrow\uparrow\rangle) + |\downarrow\downarrow\rangle$ is an eigenstate.

5.3 XXX model

When $\Delta = 1$, we realize the isotropic Heisenberg model. Here, the time evolution of the transverse and longitudinal spin-helix should be exactly the same, just as the transverse and longitudinal spin coupling are the same $J_{xy} = J_z$.

However, they are not the same, but at least they are similar. In particular, the longitudinal helix exhibits a purely diffusive scaling with wavevector Q . Its decay rate obeys $\gamma(Q) = DQ^2$, where D is the diffusion constant (as shown in the previous chapter and our publication [32]), whereas the transverse helix has an additional Q -independent decay rate of $\gamma_0 = 0.096(10) J_{xy}/\hbar$, with the net decay rate fitted well by $\gamma(Q) = DQ^2 + \gamma_0$ (Figure 5-5). So the decay separates into two parts: One transport channel, which scales as Q^2 , and one dephasing channel, which is Q -independent. So for the XXX model, the transverse and longitudinal spin helix behave in a very similar way and only differ by a background decay γ_0 . In contrast, for the XX model, their behavior is very different, as expected for a very anisotropic system ($\Delta = 0$).

The dynamics of the longitudinal spin helix can be described by *power laws* for both the XX model ($\gamma \propto Q$) and the XXX model ($\gamma \propto Q^2$). Both cases have a common description. On the other hand, the transverse spin helix shows a cosine dependence for the XX model ($\gamma = \gamma_1 |\cos(Qa)| + \gamma_0$) and diffusive transport for the XXX model ($\gamma(Q) = DQ^2 + \gamma_0$). That is a much more striking difference than in the longitudinal case. Nevertheless, we can still find a common description. Wen Wei showed that the expression $\gamma(Q) = \gamma_1 |\cos(Qa)| + \gamma_0$ for $\Delta = 0$ can be generalized to arbitrary anisotropies Δ in the following way

$$\gamma(Q) = \gamma_1 |\Delta - \cos(Qa)| + \gamma_0 \quad (5.3)$$

which, for $\Delta = 1$, even reduces to the (diffusive) quadratic case

$$\gamma(Q) = \gamma_1 [1 - \cos(Qa)] + \gamma_0 \approx \frac{\gamma_1}{2} (Qa)^2 + \gamma_0 \quad (5.4)$$

if the wavelength is long $\lambda \gg a$ compared to the lattice spacing. We will study the

first part of the expression, $\gamma_1|\Delta - \cos(Qa)|$, extensively in Chapter 6.

The remaining part of this chapter focusses on the background decay rate γ_0 , which is present for any value of Δ . It is induced by the effective magnetic field h_z which is created by superexchange.

5.4 Imaging the effective magnetic field

When we measured our first decay curve for a transverse spin-helix for the isotropic model $\Delta = 1$ (similar to Figure 5-5a), we really expected to get the same result as for the longitudinal spin helix. And we were very confused, when we saw fast decay, with these pronounced oscillations instead. What was going on? At that point, we had no idea that this oscillation at frequency Ω was exactly the signature of the effective magnetic field $h_z = \hbar\Omega$. And it was right in front of us! But one thing we figured out pretty quickly: Wolfgang immediately realized that the only symmetry breaking term in the Hamiltonian can be the effective magnetic field h_z . And we showed that a spin echo removes the oscillations and decreases the decay rate. By repeating the experiment at two different lattice depths (9 and 11 E_R) and thereby varying the spin-exchange time \hbar/J_{xy} , Figure 5-5a clearly shows that the time dependence of this effect scales with superexchange. This indicates that we are indeed seeing a magnetic field which is created by superexchange, and *not* a real magnetic field. This is already an *indirect* observation of the effective magnetic field. Over time we found different ways to measure it *directly* and confirm that it is indeed the effective magnetic field given by $h_z = 4t^2/U_{\uparrow\uparrow} - 4t^2/U_{\downarrow\downarrow}$.

5.4.1 Observation as a beatnote

If we assume that the ensemble experiences two pronounced values of the effective magnetic field, then the time evolution of the cloud-averaged contrast $c(t)$ will show a beat note at a frequency which corresponds to the difference of the two values of the effective magnetic field. This is the case for our atom clouds, which feature a Mott insulator plateau surrounded by a dilute shell of individual atoms [28] which are

pinned to their lattice sites by the gradient of the harmonic trapping potential [44]. Many of these individual atoms do not have neighbors for spin exchange and, therefore, do not feel an effective magnetic field, while those in the Mott insulator plateau do. The observed beat frequencies $\Omega = 0.90(1) J_{xy}/\hbar$ (Figure 5-6) agree well with the predicted value of the superexchange-generated effective magnetic field $h_z = 0.89 J_{xy}$. As expected, the beat note is more pronounced by spatially selecting the outer parts of the cloud (Figure 5-6a, blue) and disappears with a spin echo (Figure 5-6b).

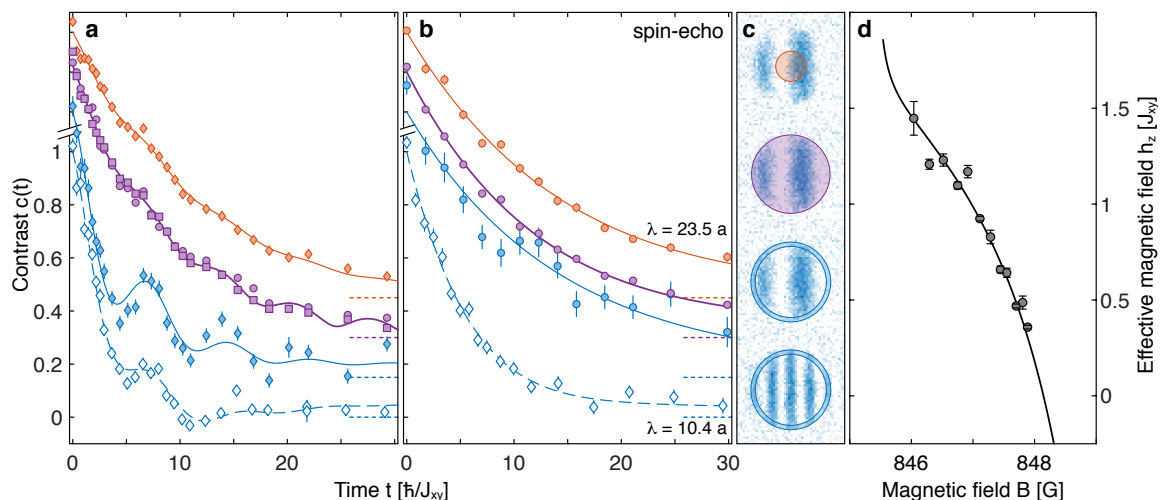


Figure 5-6: **Absolute measurement of the effective magnetic field value h_z** as a beat note between the spin precession frequencies in the inner and outer parts of the cloud. **a**, Transverse spin-helix contrast $c(t)$ for $\lambda = 23.5 a$ (all filled symbols) and $\Delta \approx 1$. For measurements averaged over the whole atom cloud (purple), they were performed at $11 E_R$ (\circ) and $13 E_R$ (\square). The contrast at the center of the atom cloud for radii $r \leq 8.5 a$ (orange filled symbols) decays slower with less pronounced oscillations, whereas the contrast in the spatial wings for radii $r \geq 20 a$ (blue filled symbols, including $\approx 7\%$ of the atoms in the cloud) decays faster with more pronounced oscillations. Data points for diamonds are an average of measurements at $11 E_R$ and $13 E_R$. Open diamond symbols represent data for $\lambda = 10.4 a$ and show the same oscillation frequency but decay faster due to spin transport. Lines are fits described in the Appendix of the paper [29]. Curves are offset from each other for clarity. The dotted lines indicate their respective zeros. **b**, The oscillations disappear with a spin-echo. **c**, Different regions used to obtain a contrast measurement. **d**, The beat frequency Ω varies as a function of the externally applied magnetic field B . The measured values for $\hbar\Omega$ (points) follow the theoretical prediction (without any adjustable parameter) for the effective magnetic field h_z (solid line) which is tuned by varying the scattering lengths via Feshbach resonances.

5.4.2 Observation through spin precession

The fact that our lattice depth is slightly inhomogeneous between the chains (due to its Gaussian cross section) causes inhomogeneity in the effective magnetic field, too. The ensemble of spin helices then precess at slightly different rates. We can therefore observe the effective field directly by purposefully displacing the z lattice beam vertically. In this way we create a controlled gradient in the effective field across the ensemble of chains. This leads to a gradient in precession speed which causes the stripes in the recorded images to rotate. In Figure 5-7 we plot the rotation angle as a function of time. The data points for two lattice depths collapse, if time is plotted in

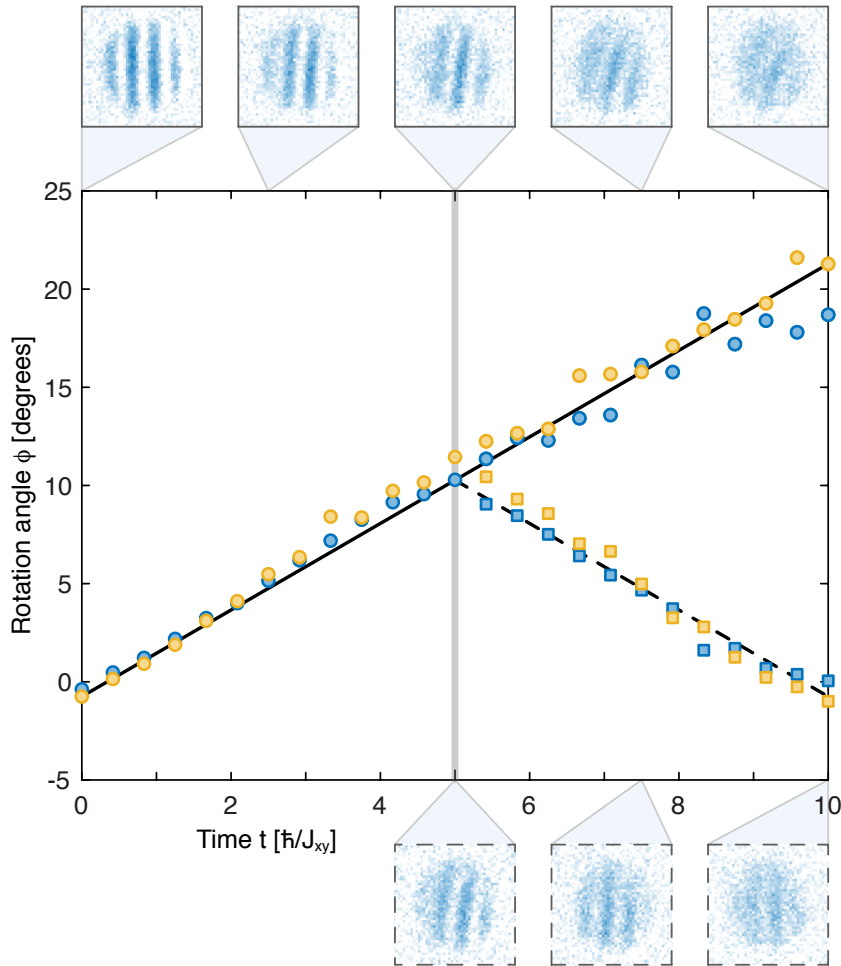


Figure 5-7: **Direct observation of the effective magnetic field through spin precession.** Rotation angle of the stripe pattern as function of evolution time t (filled symbols) for two lattice depths $11 E_R$ (blue) and $13 E_R$ (yellow) without (solid line) and with (dashed line) spin echo pulse at $t = 5 \hbar/J_{xy}$.

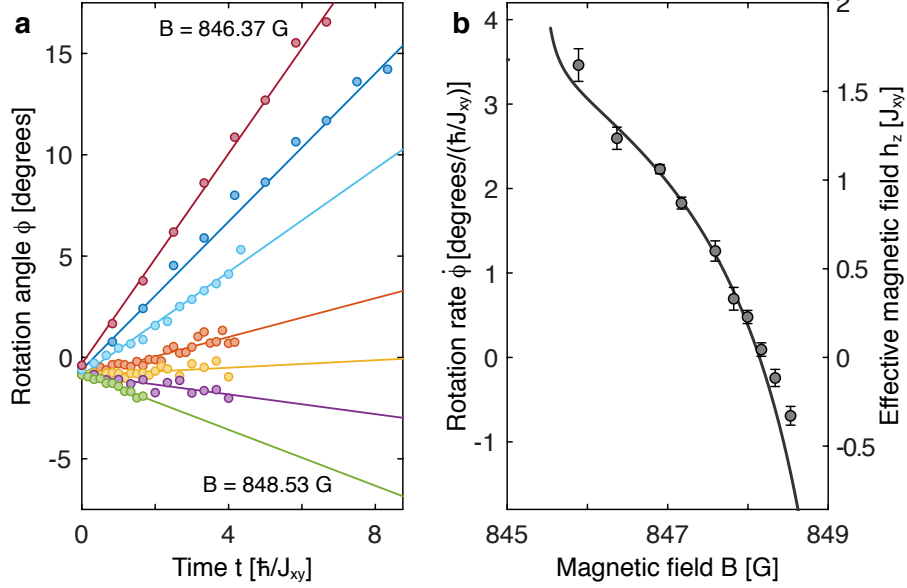


Figure 5-8: **Tunability of the effective magnetic field.** **a**, Rotation angle as a function of evolution time t for different magnetic fields $B = 846.37$ G (red), 847.17 G (blue), 847.59 G (light blue), 848.00 G (orange), 848.17 G (yellow), 848.34 G (purple), 848.53 G (green). **b**, Angular velocities obtained from linear fits in **a** compared to predicted effective magnetic fields h_z (solid line) with the scale factor between the two y axes as a fitting parameter yielding $\dot{\phi} \hbar/J_{xy} = 0.037 h_z/J_{xy} = 2.1^\circ h_z/J_{xy}$, representing the (uncalibrated) gradient of the lattice depth. Times are normalized by the spin-exchange time \hbar/J_{xy} for the central part of the atom cloud. The scaling factor is consistent with a displacement of the z -lattice beam ($1/e^2$ radius of $125 \mu\text{m}$) by an amount of $29 \mu\text{m} = 55 a$.

units of spin-exchange time, which confirms that the rotation is superexchange driven dynamics. And a π -pulse reverses the direction of the rotation, so that the spin helices can rephase, if applied after half of the evolution time. That confirms nicely, that the spin echo works.

The slope in Figure 5-7 (rotation speed) is a direct measurement of the effective field strength. We now use our Feshbach resonances to tune the value of the effective magnetic field h_z . And then we measure it using the rotation speed and see if it matches our prediction. Figure 5-8a shows how the rotation speed varies with increasing Feshbach field. In particular, we see how the rotation speed gets smaller and even changes sign. The position of the zero-crossing in the effective field is in good agreement with our prediction. The predicted curve in Figure 5-8b has

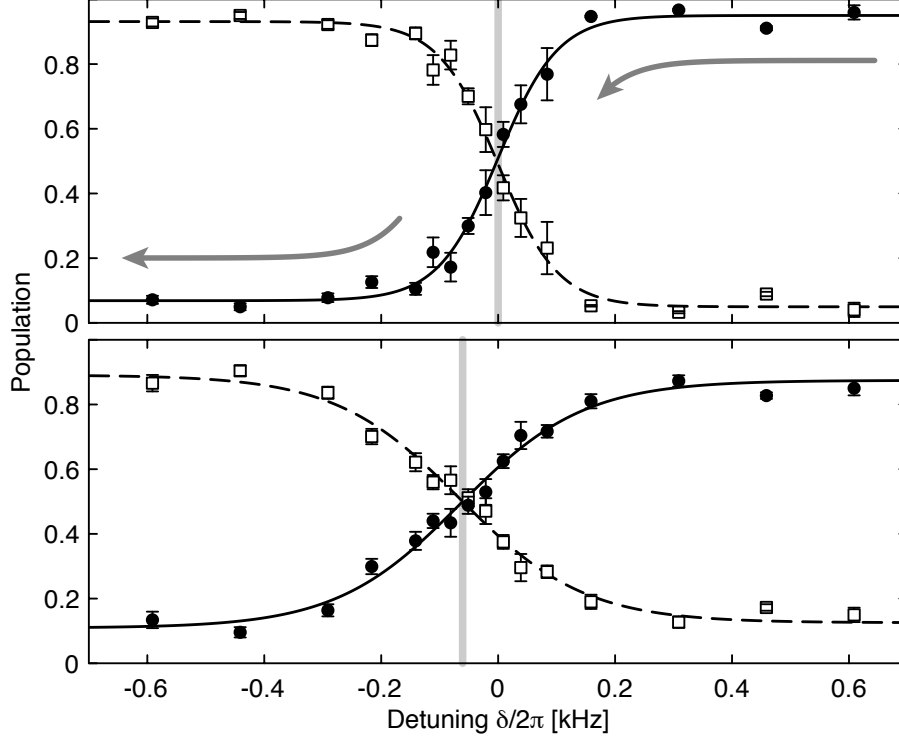


Figure 5-9: **Spectroscopic observation of the effective magnetic field h_z** as a shift in the spin-flip frequency for $h_z < 0$ (bottom panel) compared to $h_z \approx 0$ (top panel). Shown is the fraction of atoms in each state as a function of the final detuning δ of a 22ms sweep of the RF frequency, starting at $\delta = +30$ kHz with all atoms in the $|\uparrow\rangle$ state (closed circles) and no atoms in the $|\downarrow\rangle$ state (open squares). The detuning is relative to the single-particle transition frequency. The power of the RF drive is also ramped to zero after the frequency sweep to make the transition sharper. A nonzero detuning δ for equal spin populations compensates for the effective magnetic field h_z which shifts the curves for $11 E_R$ (bottom panel) lattice depth compared to $35 E_R$ (top panel) where $h_z \approx 0$. For the sweep experiment, we chose the second-lowest (closed circles) and third-lowest (open squares) hyperfines states of ${}^7\text{Li}$ due to the smaller sensitivity to external magnetic fields (due to a smaller differential magnetic moment). At 1025 G, the scattering lengths are approximately $a_{\uparrow\uparrow} \approx a_{\uparrow\downarrow} \approx -50 a_0$ and $a_{\downarrow\downarrow} \approx +350 a_0$, leading to an estimate for effective magnetic field of $h_z \approx -1.14 J_{xy} \sim h \times (-100 \text{ Hz})$ which is consistent with our observation.

only been multiplied by one free parameter, which accounts for the amount of beam displacement.

5.4.3 Spectroscopic observation

A spatially uniform effective magnetic field can always be transformed away in a suitable rotating frame. However, even then, it can still be observed as a shift of the spin-flip resonance. We compare decoupled atoms in a deep lattice ($V_z = 35 E_R$), where the effective magnetic field is $h_z = 0$, and interacting atoms in a shallow lattice ($V_z = 11 E_R$), where the effective field h_z has a finite value. We determine the resonance position with adiabatic frequency (Landau-Zener) sweeps, to find the ending frequency where half of the atoms are transferred from spin $|\uparrow\rangle$ to $|\downarrow\rangle$.

The sweep detuning corresponds to an external B_z field (in the rotating frame) and the Rabi frequency to a transverse B_x field, realizing a Heisenberg model with magnetic fields. Starting from a fully polarized state with all atoms in the $|\uparrow\rangle$ state and large detuning of the radio frequency, we reduce the B_z field adiabatically and observe the spin imbalance. The spins are balanced when the detuning compensates for the effective magnetic field created by superexchange. With this method, we can observe the effective field for different lattice depths (Figure 5-9).

5.5 Dephasing mechanisms for the transverse spin helix

We identified three different mechanisms how the effective magnetic field leads to dephasing and summarize them here:

1. Effect of inhomogeneity in the effective magnetic field between chains: This arises from slight variations in the lattice depth from the Gaussian nature of the laser beams, and can be eliminated by applying a spin-echo pulse at half of the evolution time t , as we can see in Figures 5-5 and 5-6.
2. Effect of finite chain lengths: For a 1D chain, the effective magnetic field is reduced to $h_z/2$ at the ends, half the value in the bulk (Figure 5-10). For $h_z \neq 0$, this nonuniformity hence cannot simply be transformed away by going

into an appropriate corotating frame. Although this reduced field is localized at the ends of the chain, it cannot be eliminated with an echo protocol, since its effect propagates along the chain via spin dynamics as illustrated in Figure 5-11

3. Effect of mobile holes: Every hole acts as if it carries a magnetic field $-h_z/2$ experienced by spins next to it. A mobile hole then leads to a fluctuating magnetic field in space and in time.

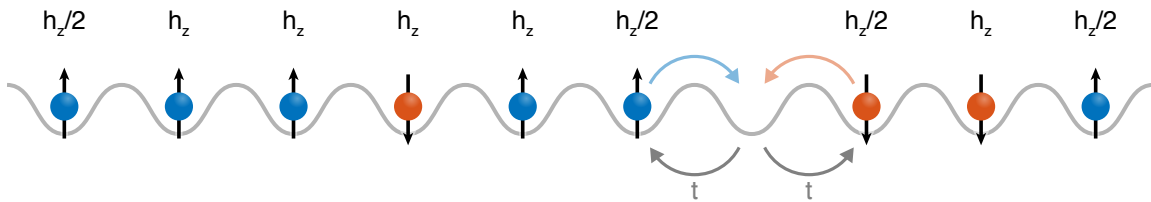


Figure 5-10: **Dephasing from the edges of the chains and mobile holes.** The effective magnetic field h_z is created by superexchange. If a spin has only one neighbor (instead of two), the value of the effective field is reduced by a factor of two. This is the case for the atoms at the ends of a finite spin chain. Also a mobile hole reduces the effective magnetic field of its two neighboring by a factor of two. Then the hole acts as if it carries a magnetic field $-h_z/2$. This leads to a coupling between spin and motional degrees of freedom (hole-magnon coupling).

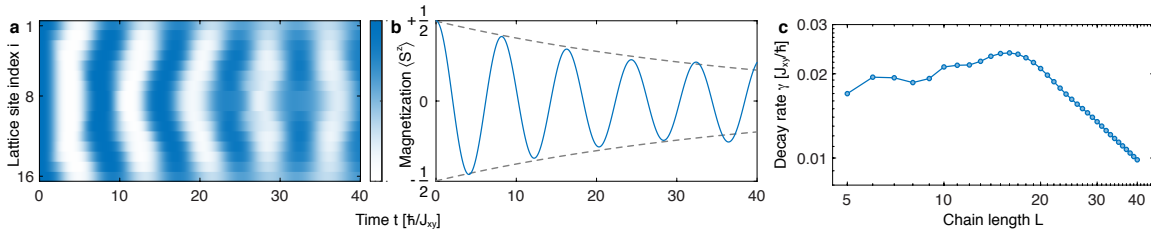


Figure 5-11: **Dephasing from the edges of the chains.** **a,b**, Dynamics of an S_x -polarized ($Q = 0$) state for a $L = 16$ finite chain, with anisotropy $\Delta = 1$ and $h_z = 0.8 J_{xy}$ reflecting the parameters of the experiment. Fig. **(a)** shows how the initially homogeneous phase of the locally-measured transverse spin $\langle S_i^x(t) \rangle$ gets distorted at the edges, and how this perturbation propagates through the chain, leading to a loss of overall contrast of the total transverse magnetization $\sum_i \langle S_i^x(t) \rangle$ **(b)**. A fit (dashed lines) to $\cos(\omega t + \phi)e^{-\gamma t}/2$ determines the decay rate γ which is shown as a function of system size L in panel **c**. A log-log plot shows the scaling $\gamma \propto L^{-1}$ for large L .

Chapter 6

Bethe phantom states

Exact solutions for quantum many-body systems are rare. Yet, for or a given interaction anisotropy, there exists one special winding angle, such that the transverse spin-helix is an exact many-body eigenstate of the Heisenberg Hamiltonian. We find this eigenstate experimentally, by varying the winding angle and measuring the decay rate, which reveals a pronounced minimum. This finding confirms the recent prediction of phantom Bethe states, exact many-body eigenstates carrying finite momenta yet no energy. We then use the sensitivity of these phantom helix states as a tool, to measure the interaction anisotropy directly. This reveals that the anisotropy can be strongly affected by nearest-neighbor off-site interactions, which have never been observed before for particles, which only interact with contact interactions.

*This chapter supplements work reported in the following publication [30]
(included in Appendix C)*

P. N. Jepsen, Y. K. Lee, H. Lin, I. Dimitrova, Y. Margalit, W. W. Ho, W. Ketterle
Catching Bethe phantoms and quantum many-body scars: Long-lived spin-helix
states in Heisenberg magnets
arXiv:2110.12043 (2021)

6.1 Introduction

The previous chapter showed that a *transverse* spin helix is really sensitive to the anisotropy Δ and that its decay rate can be described by

$$\gamma = \gamma_1 |\Delta - \cos(Qa)| + \gamma_0 \quad (6.1)$$

The background decay rate γ_0 accounts for effects such as finite chain length and holes in the spin chain, which we studied extensively in the previous chapter. These effects would be absent ($\gamma_0 = 0$) in an ideal spin chain, infinitely long and without holes, such that every spin has two neighbors. This chapter focusses on studying the decay due to pure spin dynamics $\gamma_1 |\Delta - \cos(Qa)|$ in detail. Especially, we experimentally find the spin helix states fulfilling the so-called *phantom condition*

$$\Delta = \cos(Qa) \quad (6.2)$$

where the decay rate vanishes. This *phantom helix state* is even a perfect many-body eigenstate of the anisotropic Heisenberg model with anisotropy Δ [47, 48]. In this eigenstate, neighboring spins are just at the right angle $\varphi = Qa = \arccos \Delta$, such that for each spin, the interactions with its two neighbors cancel exactly (Figure 6-1). This angle depends on the value of the anisotropy Δ .

In the isotropic system ($\Delta = 1$), this special angle is $\varphi = 0^\circ$ and the spin helix trivially reduced to the ferromagnetic state, where all spins are aligned (within the S_x - S_y plane). Indeed, we have already seen in the previous chapter, that the decay rate is minimum at $Q = 0$ (Figure 5-5b). In the XX model ($\Delta = 0$), this special angle increases to a value of $\varphi = 90^\circ$, forming a spin helix with a wavelength of 4 lattice sites ($\lambda = 4a$). This is too short for observing this state directly, because our imaging resolution is limited to wavelengths $\lambda > 6a$. Nevertheless, we have already seen the signature of this many-body eigenstate, as the decay rates started to decrease with increasing angle $\varphi = Qa$ in Figure 5-4b.

In this chapter we extend our range of observations to arbitrary wavevectors Q ,

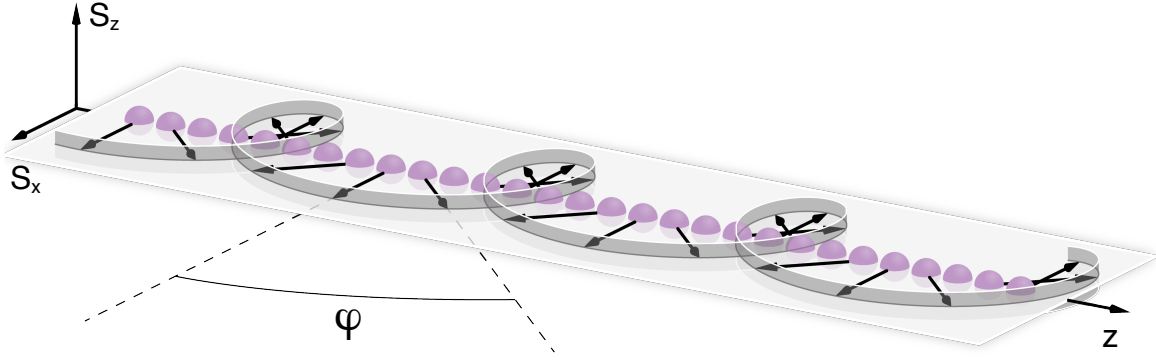


Figure 6-1: **Spin-helix state** in the S_x - S_y plane with winding angle φ . It is an exact eigenstate of the anisotropic Heisenberg model, if its winding angle fulfills the phantom condition $\Delta = \cos \varphi$.

all the way up to $Q = \pi/a$, where neighboring spins are anti-aligned. Such wavelength ($\lambda = 2a$) is way too small for our imaging system to resolve and would require single-site resolution. In order to measure the modulation contrast nevertheless, we utilize a novel unwinding step (applying an inverse magnetic gradient), just before imaging (see Figure 6-2).

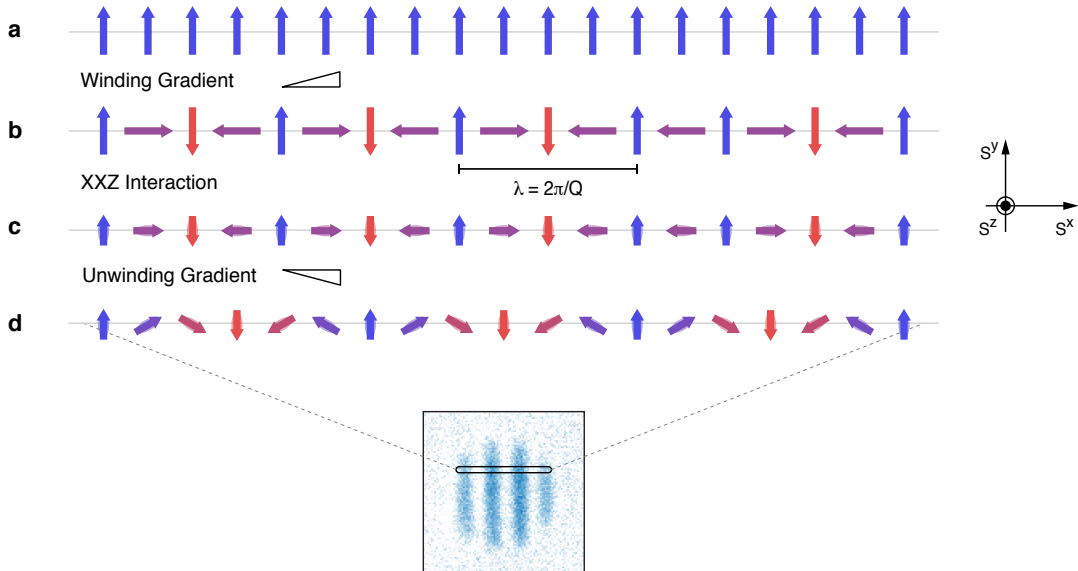


Figure 6-2: **Preparation and observation of spin-helix states.** An initially spin-polarized state in the S^y direction (a) is wound into a spin helix with variable wavevector Q using a magnetic field gradient, here illustrated for $Qa = \pi/2$ (b). This state evolves under the XXZ Heisenberg Hamiltonian (c). After unwinding the remaining spin modulation to a resolvable wavevector (d), the local S^y -magnetization is imaged in-situ. Only the S^x and S^y components of the spin are shown.

6.2 Stability of transverse spin-helix states

In classical physics, in chains with purely classical spins, *every* transverse spin helix is stable, for any wavevector Q , and even for any anisotropy Δ . The reason is simple. We have already mentioned this before in Chapter 5, but it is so important for this Chapter 6, that we will explain the argument again here. Every spin experiences a torque from each of its two neighbors (Figure 6-3). But since the two angles between this spin and its two neighbors are exactly equal ($\varphi = Qa$) in a spin helix, the two

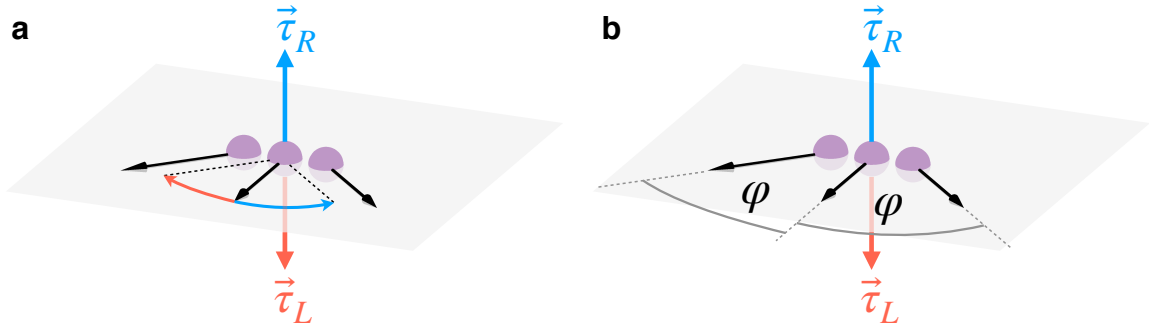


Figure 6-3: **Classical spins.** **a**, The spin in the middle experiences a torque τ_R (blue) from the spin to its right, towards the aligned ($J_{xy} < 0$) or anti-aligned ($J_{xy} > 0$) configuration. At the same time, it experiences an opposite torque τ_L (red) from the spin to its left. **b**, In a transverse spin helix, the torques from both neighbors cancel exactly $\tau_L + \tau_R = 0$, because the angles $\varphi = Qa$ between neighboring spins are equal. A classical transverse spin helix is stationary.

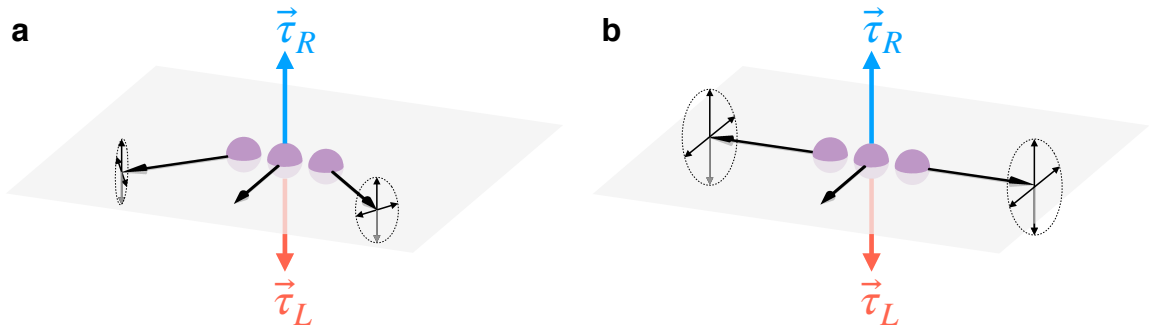


Figure 6-4: **Quantum spins.** **a**, Quantum fluctuations of the spins lead to a fluctuating torque which is only zero on average $\langle \tau_L + \tau_R \rangle = 0$. A quantum transverse spin helix decays as a result of quantum fluctuations. **b**, For $\Delta = 0$, i.e. for vanishing longitudinal coupling $J_z = 0$, the quantum fluctuations of the neighboring spins do not couple to the spin in the middle, if spins are at an angle of $\varphi = 90^\circ$, so that such a quantum transverse spin helix is stationary.

torques cancel exactly $\tau_L + \tau_R = 0$. The classical spin helix is stationary! Also, the longitudinal spin coupling J_z in the S_z direction does not matter for classical spins in

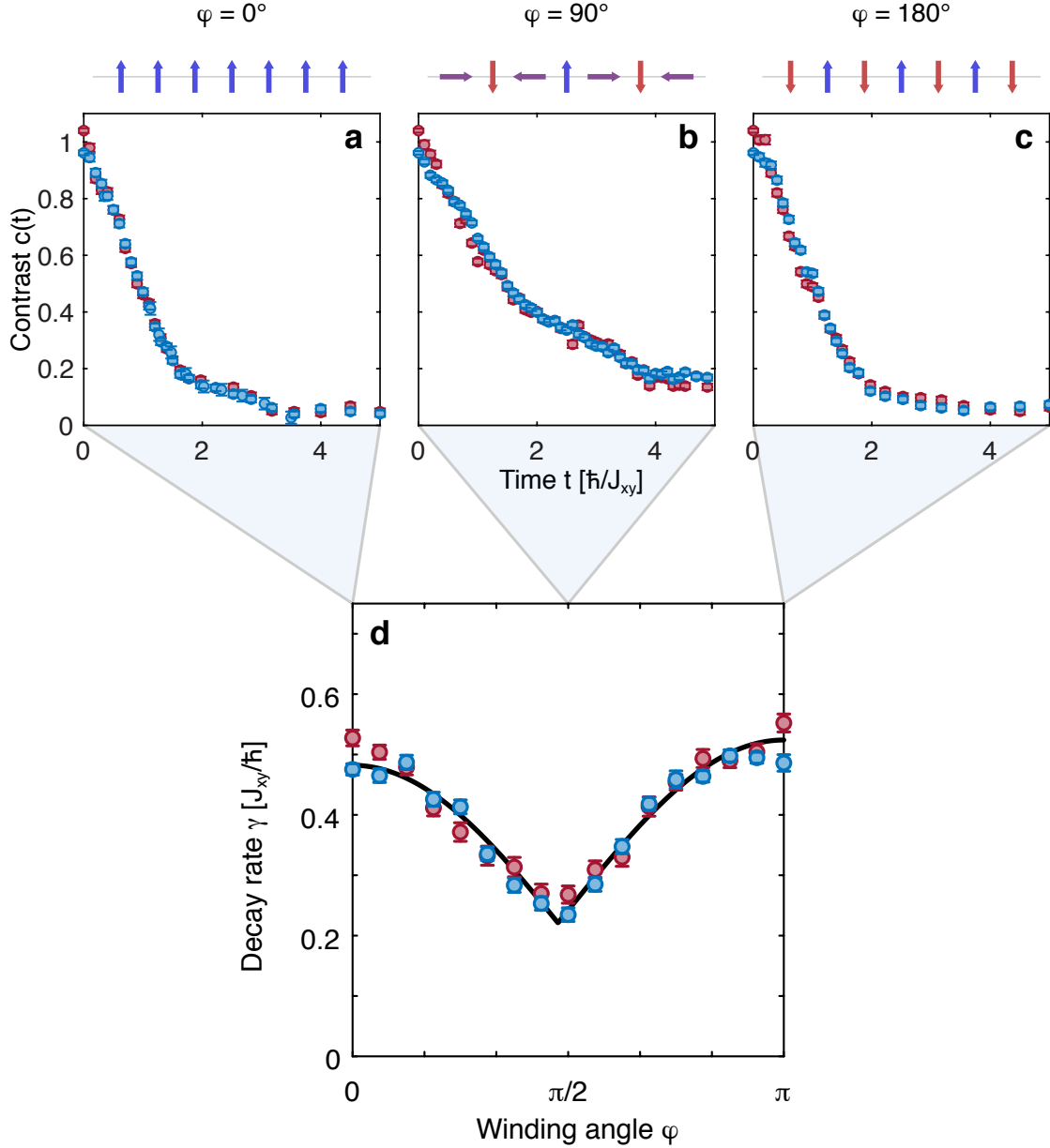


Figure 6-5: **Decay of transverse spin-helix states.** **a-c**, Contrast decay $c(t)$ measured for $\Delta \approx 0$ at two different lattice depths $9 E_R$ (red) and $11 E_R$ (blue), for three winding angles $\varphi = Qa$. All spins aligned $\varphi = 0^\circ$ (**a**), neighboring spins perpendicular $\varphi = 90^\circ$ (**b**), all spins anti-aligned $\varphi = 180^\circ$ (**c**). Decay curves collapse in each case when times are normalized in units of \hbar/J_{xy} . **d**, The spin-helix lifetime is significantly larger for $\varphi = 90^\circ$ compared to $\varphi = 0^\circ$ and $\varphi = 180^\circ$. The decay rate γ shows a pronounced minimum for $\varphi = 90^\circ$.

a transverse spin helix, because the spins have a vanishing z -component $S_z = 0$. Only the transverse coupling J_{xy} matters. The anisotropy $\Delta = J_z/J_{xy}$, therefore, does not play a role then.

But in quantum mechanics, the spins have quantum fluctuations, random quantum noise, which is uncorrelated (Figure 6-4a). The two torques τ_L and τ_R only cancel on average $\langle \tau_L + \tau_R \rangle = 0$. Only the expectation value for the total torque is zero, but with a finite variance $\langle (\tau_L + \tau_R)^2 \rangle = 0$. Therefore, the spin in the middle experiences a fluctuating torque, and thus the decay of this spin-helix state is due to quantum fluctuations. A classical spin helix would be stable. That is the difference between *classical magnetism* and *quantum magnetism*. In particular, there are also quantum fluctuations in the S_z direction, which is the reason why the anisotropy $\Delta = J_z/J_{xy}$ starts to play a role.

For example, if we choose the value $\Delta = 0$ (XX model) we can avoid the effect of the quantum fluctuations, by making the angle $\varphi = Qa$ between neighboring spins $\varphi = 90^\circ$ (Figure 6-4b). The quantum fluctuations are then either in S_z direction, but with $\Delta = 0$ the J_z coupling is switched off. Or the quantum fluctuations are aligned with the neighboring spin and, therefore, do not cause a torque. This state should be stable, even in the presence of quantum fluctuations. Therefore, we looked for this stable state experimentally.

6.3 Observations of phantom helix states

We tune the anisotropy to $\Delta = 0$, and we systematically vary the winding angle φ between neighboring spins, while measuring the decay rate γ . And indeed, Figure 6-5 shows a pronounced minimum in the decay rate when neighboring spins are at an angle of 90° . This is the signature of the helix phantom state! The fastest decay occurs for the ferromagnetic state, when all spins are aligned within the S_x - S_y plane, and for the Néel state, when all spins are anti-aligned.

When we increase the anisotropy Δ , we observe how the minimum shifts to a smaller angle φ . For an anisotropy of $\Delta = +1/2$ the special is at $\varphi = 60^\circ$ (Figure 6-

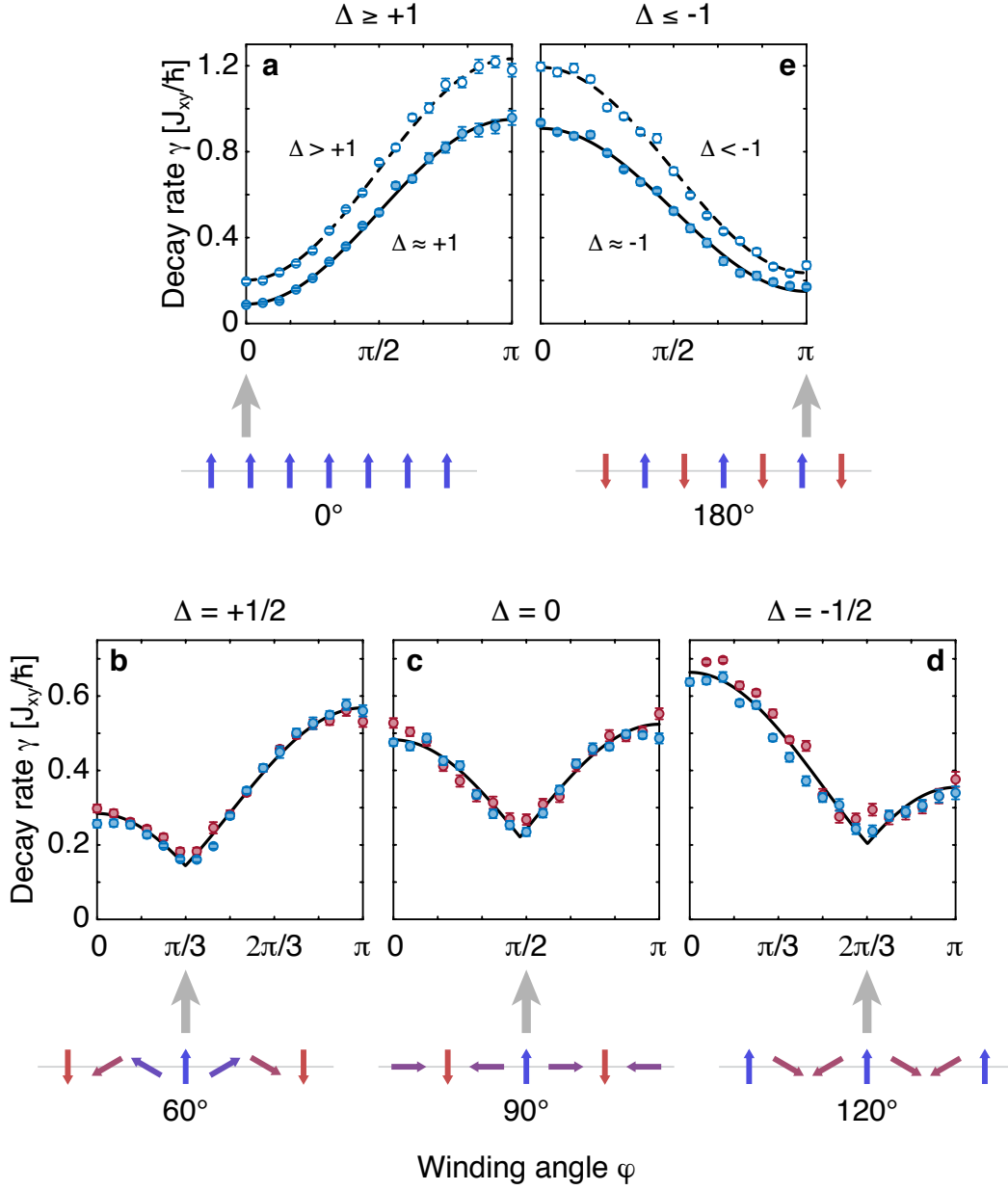


Figure 6-6: **Observation of phantom helix states.** Decay rate γ as a function of wavevector Q , shown for fitted anisotropies Δ ranging from positive (a-b) through zero (c) to negative values (d-e) measured at lattice depths of $9 E_R$ (red) and $11 E_R$ (blue). The decay rate minimum occurs at a winding angle φ which increases smoothly from $\varphi = 0$ for $\Delta \approx +1$ (a) to $\varphi = 180^\circ$ for $\Delta \approx -1$ (e). The long-lived spin pattern in the S_x - S_y plane is illustrated below each panel. Fits $\gamma(\varphi) = \gamma_1 |\Delta - \cos \varphi| + \gamma_0$ (lines) are used to find φ which minimizes the decay rate γ and to find the anisotropies Δ shown in Figures 6-10 and 6-11. The curves above were measured at applied magnetic fields of $B = 847.887$ G ($\Delta > 1$) and 847.286 G ($\Delta \approx 1$) (a), 845.760 G (b), 842.905 G (c), 839.376 G (d), 833.004 G ($\Delta \approx -1$) and 827.287 G ($\Delta < -1$) (e).

6b). When we decrease the anisotropy Δ , the minimum shifts to a larger angle φ . For $\Delta = -1/2$ we find the special angle at $\varphi = 120^\circ$ (Figure 6-6d). The solid lines are a fit function which our theory collaborator Wen Wei Ho derived [29], originally in a short-time expansion:

$$\gamma(\varphi) = \gamma_1|\Delta - \cos \varphi| + \gamma_0 \quad (6.3)$$

We treat the scaling constant γ_1 , the background decay rate γ_0 , and the anisotropy Δ as free fit parameters. This fit function is rigorously valid only in the short-time limit $c(t) = 1 - \gamma^2 t^2 + \dots$. So we have always taken it with a grain of salt. Nevertheless, it is amazing how well it describes the data, for arbitrary anisotropies ranging all the way from large negative values $\Delta < -1$ to positive values $\Delta > +1$. For example, the fit function even works for $\Delta = 1$, the isotropic point, where

$$\gamma(\varphi) = \gamma_1(1 - \cos \varphi) + \gamma_0 \quad (6.4)$$

and the ferromagnetic state ($\varphi = 0^\circ$) is the most long-lived state (Figure 6-6a). For $\lambda \gg a$, we recover the quadratic scaling for diffusive transport, if the wavelengths are long, as we already showed in the previous chapter: $1 - \cos Qa \approx (Qa)^2/2$. However, when the wavelengths λ become so short that they are comparable with the lattice spacing a , diffusive transport breaks down, and we see that the curve is actually a cosine $\gamma = \gamma_1(1 - \cos Qa) + \gamma_0$ and not a parabola $\gamma = \frac{\gamma_1}{2}(Qa)^2 + \gamma_0$. The most unstable spin helix is the Néel state ($\varphi = 180^\circ$), where spins are anti-aligned. This is a direct experimental demonstration that this *classical* antiferromagnetic state is not the ground state of the *quantum* antiferromagnetic Heisenberg Hamiltonian, which we actually implement here. For $\Delta = -1$ it is exactly the other way round:

$$\gamma(\varphi) = \gamma_1(1 + \cos \varphi) + \gamma_0 \quad (6.5)$$

Here, the Néel state *is* an eigenstate state (Figure 6-6e). And the ferromagnet is the most unstable spin helix. Interestingly, for $\Delta > +1$, the fit function still gives the correct prediction which fits the data (Figure 6-6a). The curve just shifts up by a

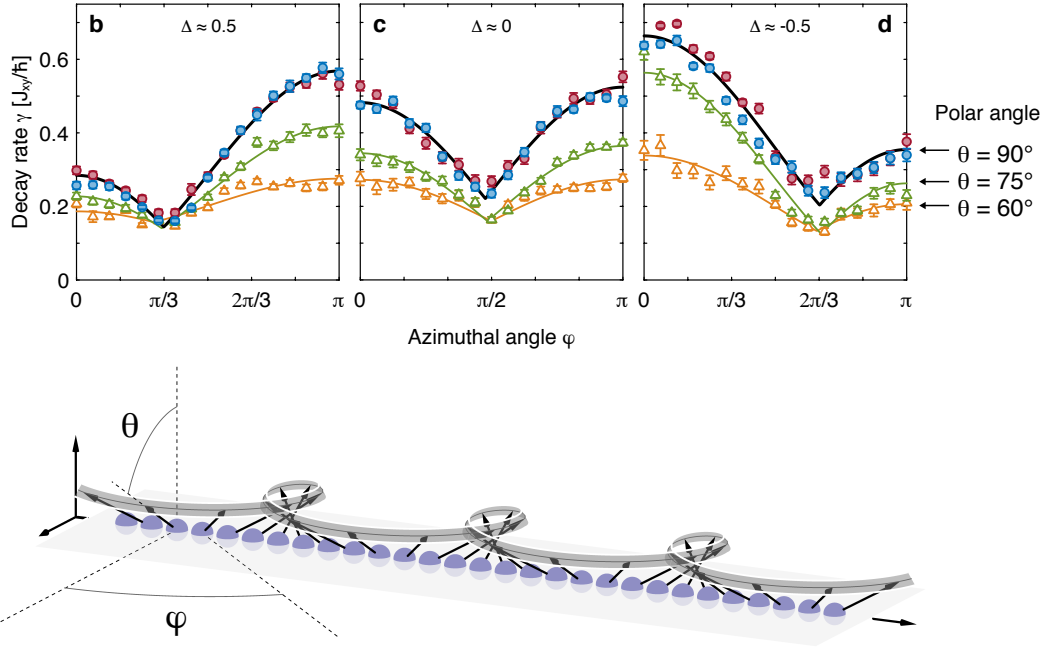


Figure 6-7: **Phantom helix states for several polar angles.** In addition to the purely transverse helices (polar angle $\theta = \pi/2$, circles), we also show the decay of spin helices with polar angles $\theta = 5\pi/12$ (green triangles) and $\theta = 2\pi/3$ (orange triangles).

constant amount (compared to the $\Delta = 1$ case):

$$\gamma(\varphi) = \gamma_1(1 - \cos \varphi) + \gamma_1(\Delta - 1) + \gamma_0 \quad (6.6)$$

But now the ferromagnetic state ($\varphi = 0^\circ$) is not a many-body eigenstate anymore. Even in an ideal system (infinite spin chain without holes), where the background decay is $\gamma_0 = 0$, the ferromagnetic state still decays with a finite decay rate of $\gamma_1(\Delta - 1)$. And the same is true for $\Delta < -1$ (see Figure 6-6e), where the curve also shifts up by a constant amount (compared to the $\Delta = -1$ case):

$$\gamma(Q) = \gamma_1(1 + \cos Qa) - \gamma_1(\Delta + 1) + \gamma_0 \quad (6.7)$$

Here the Néel state ($\varphi = 180^\circ$) still decays with a finite decay rate of $-\gamma_1(\Delta - 1)$, in addition to the background decay γ_0 , so it is not an eigenstate anymore, either.

For anisotropies $|\Delta| > +1$, there exist no solutions to the phantom condition

$\Delta = \cos \varphi$, at least not for any *real* winding angle φ . There are solutions only for *imaginary* winding angles φ . Hence, there are corresponding many-body eigenstates which are no spin-helix states but they rather look like smooth domain walls [47], where the domain-wall width is related to Δ . These smooth domain-wall states might be an interesting direction for future experiments.

So far, we only looked at transverse spin-helix states which are fully lying within the S_x - S_y plane. We have been varying only the *azimuthal* angle $\varphi = Qa$, but so far the *polar* angle has always been $\theta = 90^\circ$, such that the z -magnetization was $\langle S_z \rangle = 0$. We can easily tilt the spin helix out of plane, decreasing the polar angle, and measure its effect on the decay rate γ . In Figure 6-7 we repeat the same experiment for several polar angles θ , tilting the spin helix out of plane by just 15° (green) and 30° (orange). We observe that the decay slows down quite a lot. But the minimum in the decay rate is always at the same azimuthal angle φ . This shows that there is a whole *family* of phantom helix states for a given value of the anisotropy Δ . It is straightforward to show, that these states are exact eigenstates of the anisotropic Heisenberg Hamiltonian [30]. These phantom helix states were originally discovered theoretically in 1D as a coherent superposition of phantom Bethe states, special degenerate solutions to the Bethe ansatz equations [47,48].

6.4 Extension to higher dimensions

The Bethe ansatz works only in 1D. This raises the question if they are a phenomenon tied exclusively to 1D and integrable systems. We find that they are not: We can easily see that they are a more general phenomenon. Spin helix eigenstates also exist in higher dimensions and in other non-integrable systems, as Wen Wei Ho realized [30], and we will now show a few examples.

Spin helix eigenstates can be found on a square lattice as shown in Figure 6-8. This example is a perfect many-body eigenstate for anisotropy $\Delta \approx 0.771$, because the spins are oriented in such a way, that any line through this lattice forms a one-dimensional phantom helix state with winding angle of $\varphi \approx 39.6^\circ$. Or in other words,

any spin in this lattice experiences an interaction from each of its four neighbors. But the two interactions from each pair of opposite neighbors cancel exactly.

Phantom helix states can be found even for other lattice geometries. For example, a triangular lattice supports such a solution, too, but only for anisotropy $\Delta = -1/2$ and hence a winding angle of $\varphi = 120^\circ$, as shown in Figure 6-9 (left). Again, any line through this lattice forms a one-dimensional phantom helix state with winding angle

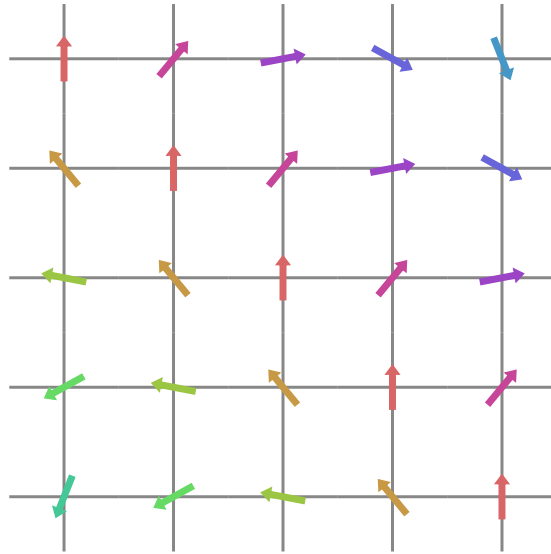


Figure 6-8: **Phantom spin helix for the square lattice.**

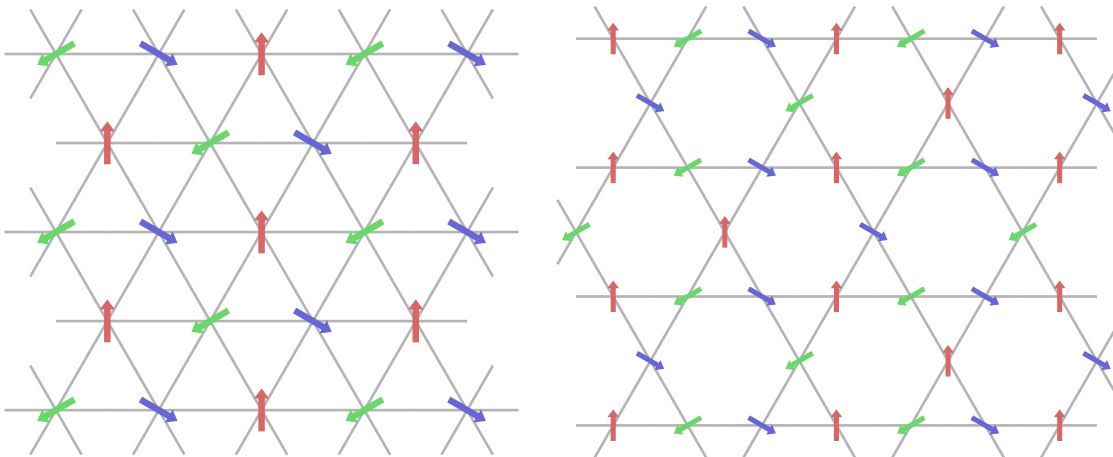


Figure 6-9: **Phantom spin helices for triangular and kagome lattices.**

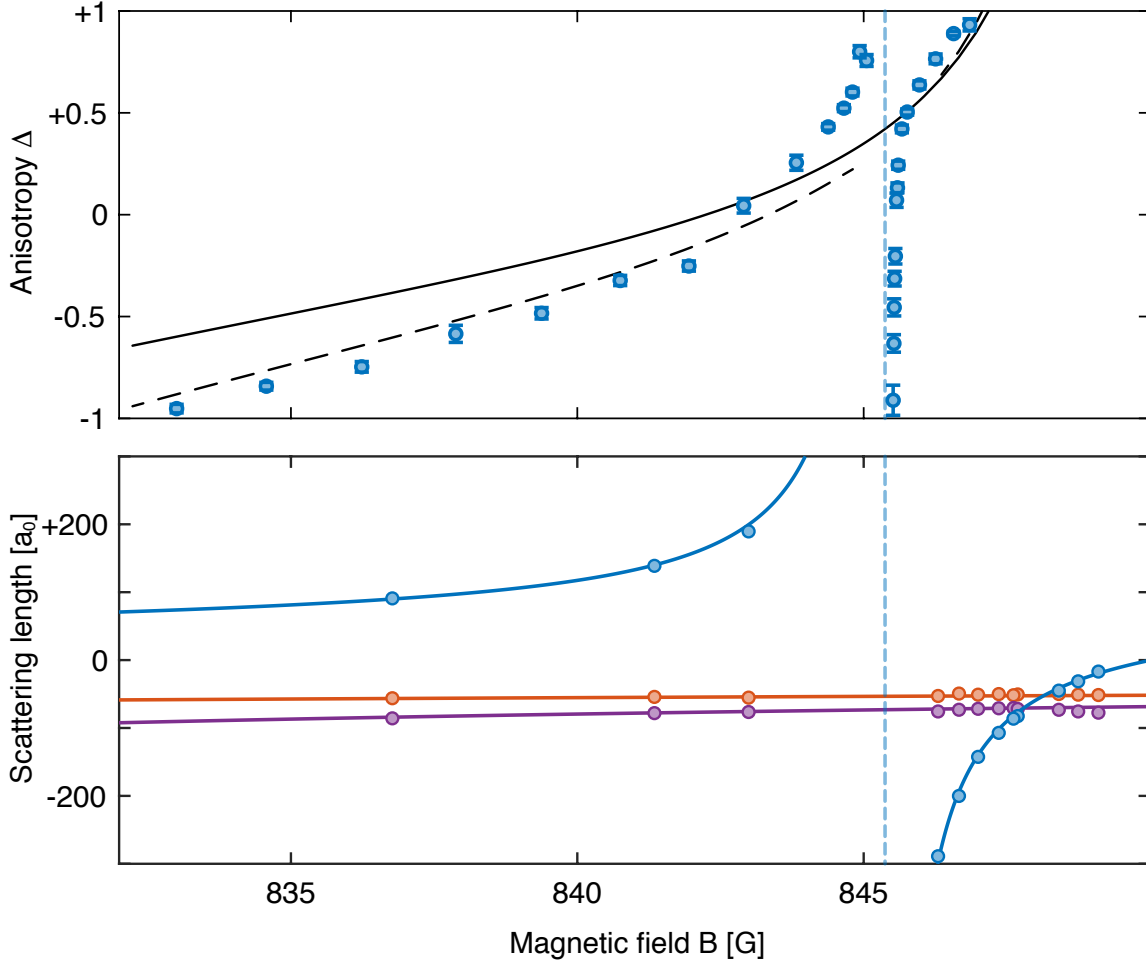


Figure 6-10: **Tuning the anisotropy with magnetic fields** around the narrow Feshbach resonance in the $|\uparrow\rangle$ state. The bottom panel shows the scattering lengths $a_{\uparrow\uparrow}$ (blue), $a_{\uparrow\downarrow}$ (purple) and $a_{\downarrow\downarrow}$ (orange) measured in previous work using interaction spectroscopy. Near the resonance, the anisotropy (top panel) follows the $a_{\uparrow\uparrow}$ scattering length.

of $\varphi \approx 120^\circ$. The phantom helix state in the triangular lattice is also known as the *120 degrees Néel ordered state*. It is the ground state of the *classical* antiferromagnetic Heisenberg model with $\Delta = +1$. We have just seen that it is also an eigenstate of the *quantum* Heisenberg model with $\Delta = -1/2$. The kagome lattice for $\Delta = -1/2$ and $\varphi \approx 120^\circ$ is another such example, as shown in Figure 6-9 (right).

So the spin-helix eigenstates, which we found experimentally in one dimension, are a more general phenomenon not tied to 1D or integrability, but instead this phenomenon relies on a delicate cancellation of interactions.

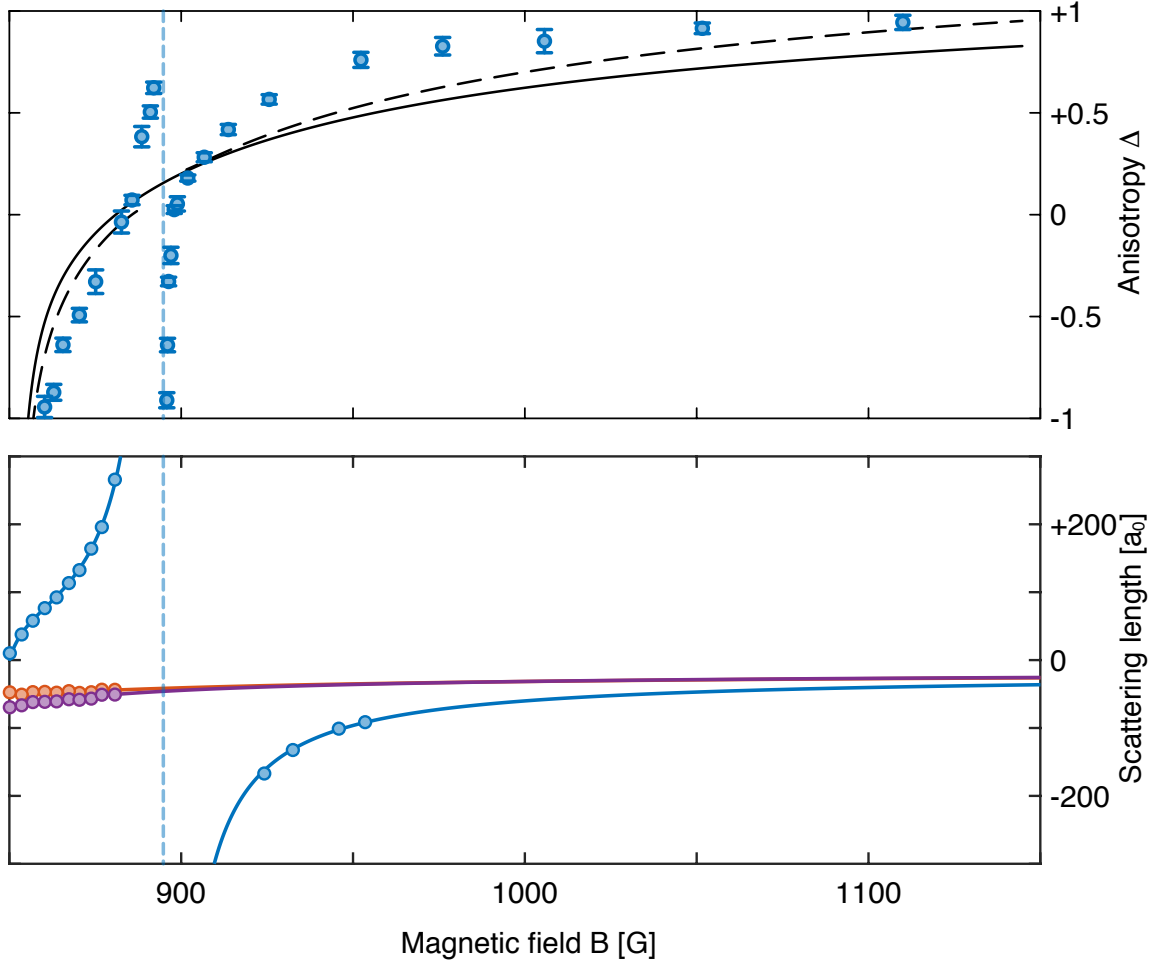


Figure 6-11: **Tuning the anisotropy with magnetic fields** around the broad Feshbach resonance in the $|\uparrow\rangle$ state. The bottom panel shows the scattering lengths $a_{\uparrow\uparrow}$ (blue), $a_{\uparrow\downarrow}$ (purple) and $a_{\downarrow\downarrow}$ (orange) measured in previous work using interaction spectroscopy. Near the resonance, the anisotropy (top panel) follows the $a_{\uparrow\uparrow}$ scattering length.

6.5 Direct measurement of the anisotropy

Now that we understand the phantom helix states, we can turn the whole thing around! We can use these states as a tool to actually measure the anisotropy Δ , based on the decay rate minimum we find. Until now we had no way to measure it directly, and had to calculate it, based on our measurements of the on-site interactions $U_{\uparrow\uparrow}$, $U_{\uparrow\downarrow}$, and $U_{\downarrow\downarrow}$. However, we had no tool to confirm, that this prediction is correct — until now! So we have gone full circle. Measuring the anisotropy Δ with the phantom helix states is a way to check, if our superexchange- and Hubbard-model description is

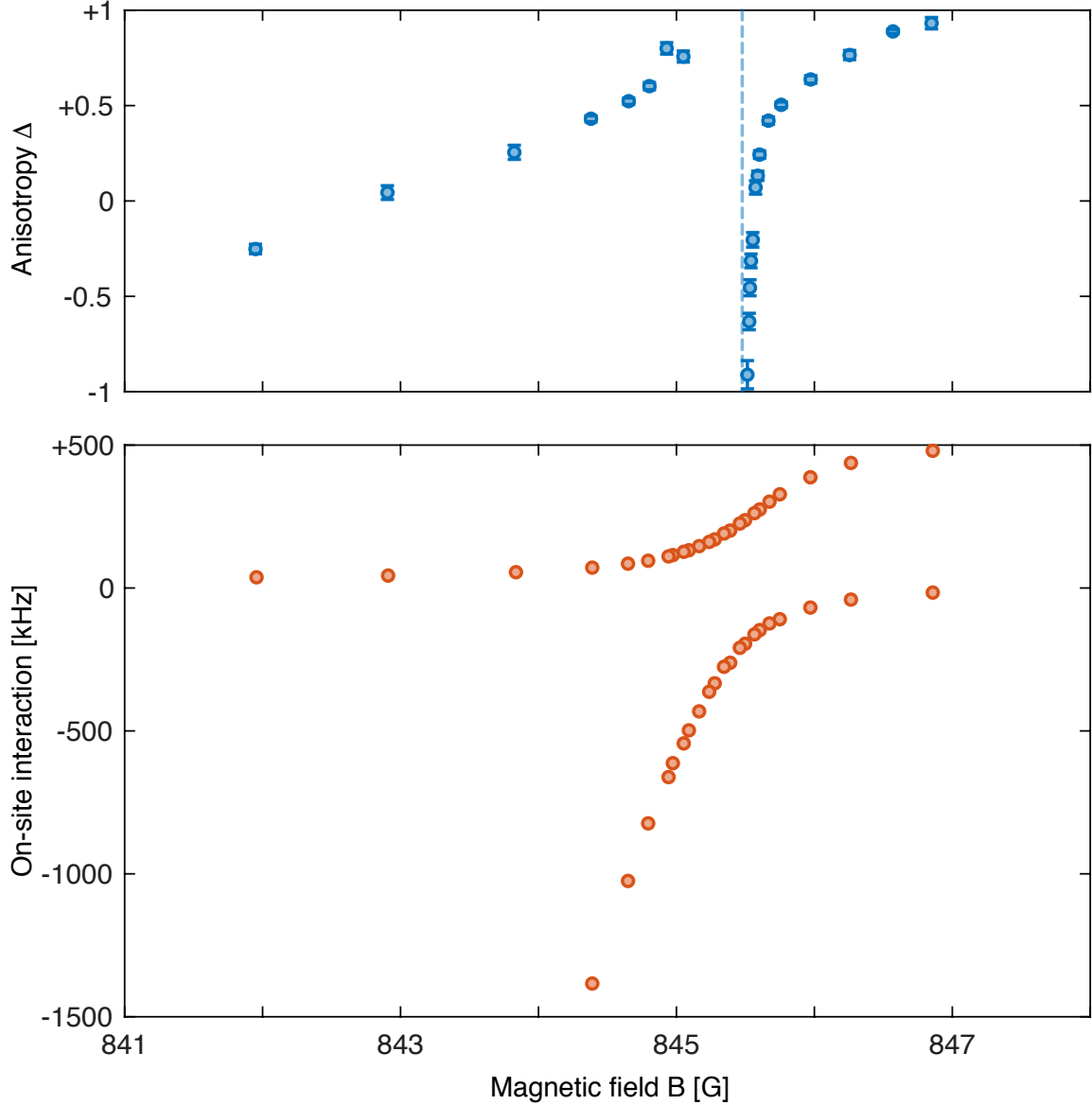


Figure 6-12: **Tuning the anisotropy with magnetic fields** around the narrow Feshbach resonance in the $|\uparrow\rangle$ state. The bottom panel shows interaction spectroscopy and almost perfectly follows the theory in the Thomas Busch paper [49].

even correct or complete. This is especially true close to the two Feshbach resonances in the $|\uparrow\rangle$ state, where the on-site interactions $U_{\uparrow\uparrow}$ between two $|\uparrow\rangle$ atoms diverge.

Figure 6-10 and 6-11 compare the measured anisotropies Δ to the standard model for superexchange (solid line) using previously measured scattering lengths [43]. The black dashed line includes the bond-charge correction to tunneling [50] and a small adjustment of the background scattering length of $a_{\uparrow\downarrow}$, which was not tightly constrained

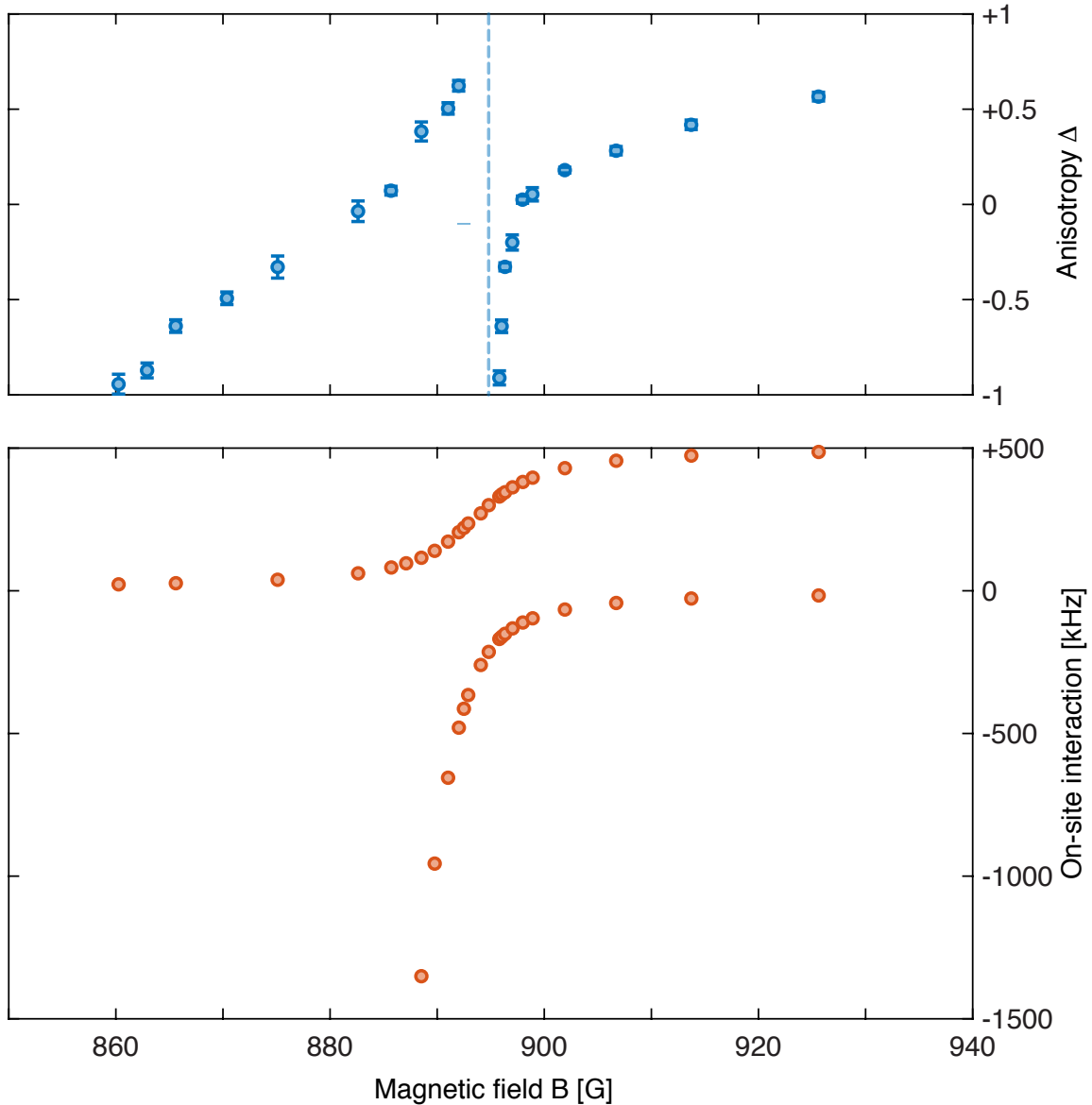


Figure 6-13: **Tuning the anisotropy with magnetic fields** around the broad Feshbach resonance in the $|\uparrow\rangle$ state. The bottom panel shows interactions spectroscopy and almost perfectly follows the theory in the Thomas Busch paper [49].

by previous measurements. Major deviations near the two Feshbach resonances at 845.506 and 893.984 G (vertical dotted lines) are evidence for off-site interactions.

Away from the Feshbach resonances, the measurement roughly agrees with the general trend of the prediction. We think that the discrepancy is due to some slight uncertainties in the measured on-site interactions. But near the Feshbach resonances, we measure something qualitatively new! This effect can only be explained by nearest

neighbor off-site interactions V . Since, superexchange scales as t^2/U , it is supposed to be suppressed and should not explode, when the on-site interactions get really large, because U appears in the denominator. However, two neighboring atoms, even if they only have contact interactions, also have a direct off-site interaction V , because the wave function leaks into the neighboring lattice site. But the overlap integral

$$V = \frac{4\pi\hbar^2 a}{m} \int d^3r |w(\mathbf{r})|^2 |w(\mathbf{r} + \delta\mathbf{r})|^2 \quad (6.8)$$

is really small for two Wannier functions $w(\mathbf{r})$ localized on two neighboring lattice sites, one lattice spacing $\delta\mathbf{r} = (0, 0, a)$ apart. Typically, off-site interactions are 4 orders of magnitude smaller than on-site interactions

$$U = \frac{4\pi\hbar^2 a}{m} \int d^3r |w(\mathbf{r})|^4 \quad (6.9)$$

where the wave function overlap is a lot larger. For this reason, the common believe has been that off-site interactions are completely negligible and unobservable. However, in spin physics with one atom per site, both effect appear with opposite scaling! Away from the Feshbach resonance superexchange $J = 4t^2/U$ dominates. And close to the Feshbach resonance off-site interactions V dominate. This is the first observation of nearest-neighbor off-site interactions for particles, which only have contact interactions.

However, it turns out that the current model of off-site interactions in equation 6.8 is insufficient near a Feshbach resonance. In order to explain the large effects on the anisotropy, we would require a scattering length $a_{\uparrow\uparrow} \sim 6000 a_0$. That is much larger than the theoretical limit: the harmonic oscillator length $\sim 500 a_0$ (for on-site trapping on a lattice site). Therefore, near the Feshbach resonances we are observing much stronger off-site interactions than theory allows. In order to characterize the Feshbach resonances better really close to unitarity, we perform interaction spectroscopy in a deep Mott insulator (lattice depth $35 E_R$ corresponding to ≈ 500 kHz band gap between 0th and 2nd band) with two atoms per site, from the weakly interacting state $|\uparrow\downarrow\rangle$ to the strongly interacting state $|\uparrow\uparrow\rangle$, in Figures 6-12 and 6-13. This is

a direct measurement of $U_{\uparrow\uparrow} - U_{\uparrow\downarrow}$. With the combined knowledge of the on-site interaction $U_{\uparrow\uparrow}$, and the anisotropy Δ (which is an indirect measurement of the off-site interaction $V_{\uparrow\uparrow}$) we hope to develop a correct model for off-site interactions near a Feshbach resonance. This will be the topic of a forthcoming publication.

Chapter 7

Summary and Outlook

We have used ultracold atoms to implement the Heisenberg model with tunable anisotropy. This is the first quantum simulation of the anisotropic Heisenberg model. We studied spin dynamics in previously unexplored regimes far-away from equilibrium. Some of our results are unexpected. There are many open questions which our new quantum simulator platform allows to be addressed in the future.

7.1 Summary

We studied both quantum many-body dynamics far-away-from equilibrium as well as stable spin patterns far away from the ground state, which are exact many-body eigenstates of the anisotropic Heisenberg model. Longitudinal spin-helix patterns decay by spin transport, where the decay rate is well described by power laws

$$\gamma \propto (Qa)^\alpha \tag{7.1}$$

where the transport exponent α is a function of the anisotropy Δ . Transverse spin-helix patterns decay also by local spin dephasing, such that the decay rate has a different form:

$$\gamma = \gamma_1 |\Delta - \cos(Qa)| + \gamma_0 \tag{7.2}$$

For the special case of isotropic interactions ($\Delta = 1$), both descriptions agree for long wavelengths $\lambda \gg a$, since $\gamma_1 |1 - \cos(Qa)| \approx \frac{\gamma_1}{2} (Qa)^2$. The background rate γ_0 accounts for dephasing induced by the effective magnetic field enabled by finite chain length, mobile holes in the chain, and inhomogeneity between chains due to the finite size of the optical lattice beams, which would be zero for an ideal system. For a given anisotropy Δ , there exists one special spin helix with a winding angle $\varphi = Qa$ fulfilling the phantom condition

$$\Delta = \cos(Qa) \tag{7.3}$$

where the decay rate vanishes (at least in an ideal system where the background decay is $\gamma_0 = 0$). This phantom helix state is a perfect many-body eigenstate of the anisotropic Heisenberg model with anisotropy Δ .

We have confirmed the connection of the Heisenberg model to the underlying Hubbard model. We showed that we can control J_z and J_{xy} with the lattice depth and Feshbach resonances. This has a dramatic impact on spin transport. We also found a way to directly measure the anisotropy $\Delta = J_z/J_{xy}$ using the phantom helix states. We identified an effective magnetic field which is created by superexchange and showed that this is a real part of this mapping, and we demonstrated that one can measure this field directly in three different ways: with a beatnote, through spin-precession, and spectroscopically. The effective magnetic field varies with the Feshbach resonances in the expected way. On top of superexchange, we found a direct interaction between spins (zeroth-order in tunneling), a nearest-neighbor off-site interaction, and studied how it modifies the interaction anisotropy.

7.2 Discussion

Recently, there has been strong interest and a big debate about transport in the Heisenberg model at the isotropic point ($\Delta = 1$). The question is, if transport behavior is described by diffusion ($\alpha = 2$) or by superdiffusion ($\alpha = 1.5$). There was a

very recent result by the Bloch group [33], which might be considered unexpected. For $\Delta = 1$ they studied a quench from a sharp domain wall with variable contrast, and they find superdiffusion ($\alpha = 1.5$) for *all* values of the contrast, both for a partially polarized domain wall (as predicted by Refs. [11, 12]) and also for a fully polarized domain wall (in contradiction to Ref. [51] which predicts diffusion). Interestingly, for a (fully polarized) spin-helix state we find diffusion ($\alpha = 2$) both experimentally and with numerical simulations. This also confirms a previous experiment [19] (also both experimentally and with numerical simulations). However we note, that our obtained scaling exponent α depends slightly on how we treat the observed (ballistic) oscillations. If we ignore the oscillations and fit pure exponentials $a_0 e^{-t/\tau}$ to the decay curves $c(t)$, then the exponent is very close to ($\alpha = 2$). If we account for the oscillations in the fit function $(a_0 + b_0 \cos \omega t) e^{-t/\tau}$, this reduced the observed exponent to $\alpha = 1.87(4)$. Furthermore, our experiment might have been performed at an anisotropy which was slightly higher than $\Delta = 1$, since Δ is only calibrated up to ± 0.1 . So the true value of the exponent α at the isotropic point might even be lower than $\alpha = 1.87(4)$. To address these questions, the following two experiments would be especially interesting:

1. Spin-helix states with 50% contrast. I expect this to be superdiffusive with $\alpha = 1.5$.
2. A sharp domain wall (both 100% and 50% contrast).

With our quantum simulator platform, both experiment can be done as a function of Δ , tuning the anisotropy, as well as a function of interchain coupling, to study the crossover from 1D to 2D, which is a continuous knob on an *integrability breaking* term.

7.3 Outlook

Generally, there are of course many more possible experiments. They mainly fall into the following categories:

- Different initial states: sharp domain walls, smooth domain walls, partially-polarized (i.e. mixed) states
- Different Hamiltonians: higher spatial dimensions (2D or 3D), higher spin quantum numbers (e.g. $S=1$)
- Different observables: Single site resolution with a quantum gas microscope

Spin dynamics in higher spatial dimensions

Our experimental protocol is not restricted to studying one-dimensional chains; it can easily be extended to two or three spatial dimensions, by using not only *one* shallow lattice to control superexchange coupling in a single direction, but by using *two* or *three* shallow lattices. Studying coupled one-dimensional chains is interesting as a continuous crossover from 1D to 2D. Inter-chain coupling can be understood as an integrability breaking term. An experimental complication in higher spatial dimensions is that deeper lattices are required to keep atoms localized on individual lattice sites, than compared to one dimension, which slows down superexchange dynamics. Quantum many-body dynamics in two or three dimensions is completely out of range for numerical simulations, at least for reasonable system sizes. Preparing phantom helix states in higher dimensions would realize an exception to the usual expected thermalizing dynamics in non-integrable systems.

A sharp domain wall

We studied spin transport with quantum quenches from a far-from-equilibrium spin helix

$$\prod_i (\sin Qz_i/2 |\uparrow\rangle_i + \cos Qz_i/2 |\downarrow\rangle_i) \quad (7.4)$$

which involves a sinusoidal modulation of the S_z -magnetization (population of spin $|\uparrow\rangle$ and $|\downarrow\rangle$ atoms) with wavevector Q . That is a measurement in momentum space, at a single value of Q . In contrast, a quench from a sharp domain wall

$$|\cdots \uparrow\uparrow\uparrow\uparrow\uparrow\uparrow\uparrow\uparrow\downarrow\downarrow\downarrow\downarrow\downarrow\downarrow\downarrow\downarrow \cdots\rangle \quad (7.5)$$

between two magnetized domains, is a measurement in real space. This scenario has been extensively studied theoretically [51–54]. The modulation of the S_z magnetization is a step function. This situation is reminiscent of mixing two different classical gases, which are initially separated in two opposite sides of the system. This scenario has been studied theoretically for the fully polarized domain wall [51] and the isotropic case ($\Delta = 1$), revealing diffusive behavior (however with a ballistic light-cone). However, for a sharp domain wall with *partially* polarized domains (infinite temperature) transport behavior changes into superdiffusion ($\alpha = 1.5$) for $\Delta = 1$ [11, 12], which can be understood from generalized hydrodynamics involving local equilibration of conserved quantities [55, 56]. This was experimentally confirmed by Ref. [33], although they even find superdiffusion for the *fully* polarized domain wall. Our platform can extend these experimental studies to arbitrary anisotropies. We cannot optically resolve domain walls, which are sharper than 6 lattice sites. Upgrading our setup to a quantum gas microscope with single site resolution, would address this issue. Nevertheless, our current resolution might be good enough to interesting dynamics.

Bethe phantom states for anisotropies $|\Delta| > 1$

For anisotropies $|\Delta| \leq 1$, the transverse spin-helix state with wavevector Q satisfying the phantom condition

$$\cos(Qa) = \Delta \tag{7.6}$$

is an exact many-body eigenstate of the Hamiltonian — the Bethe phantom state. However, for anisotropies $|\Delta| > 1$ there exists no such spin helix, since the phantom condition does not have a solution for any *real* wavevector Q . Nevertheless, there are solutions for *imaginary* wavevectors Q , which means that, instead, the Bethe phantom state takes a different form, which is a *smooth* domain wall with a finite width [47], which depends on the anisotropy Δ . It would be interesting to study the stability of domain wall states as a function of their width, where we expect to find a pronounce minimum in the decay rate for one specific width.

Partially polarized spin-helix

So far, we studied the relaxation of spin-helix states starting with a 100% modulation, i.e. a pure state. Theoretical studies have shown in the case of sharp domain walls [11, 12, 51], that the dynamical behavior can change significantly, if the two domains are not fully polarized. We can also create spin-helix states with <100% modulation depth, by winding a spin-helix not starting from a fully polarized state, but from a partially polarized state. A partially polarized state can be created with the following protocol.

1. We start with spin $|\uparrow\rangle$ on every site.

$$\rho = |\uparrow\rangle \langle\uparrow| \quad (7.7)$$

2. We tilt the spins to a polar angle θ with an RF pulse so that the state is $\cos(\theta/2) |\uparrow\rangle + \sin(\theta/2) |\downarrow\rangle$ on every site. This is a pure state with density matrix

$$\rho = \cos^2(\theta/2) |\uparrow\rangle \langle\uparrow| + \frac{1}{2} \sin(\theta) |\uparrow\rangle \langle\downarrow| + \frac{1}{2} \sin(\theta) |\downarrow\rangle \langle\uparrow| + \sin^2(\theta/2) |\downarrow\rangle \langle\downarrow| \quad (7.8)$$

3. We dephase the S_x and S_y components and turn this into a mixed state, by lowering the lattice and switching on superexchange, while the anisotropy is tuned to $\Delta = 0$, for example. The transverse components of that state should decay after a few spin-exchange times \hbar/J_{xy} . Afterwards we ramp the lattice back up to $V_z = 35 E_R$ and end up with a mixed state on every lattice site, with density matrix

$$\rho = \cos^2(\theta/2) |\uparrow\rangle \langle\uparrow| + \sin^2(\theta/2) |\downarrow\rangle \langle\downarrow| \quad (7.9)$$

4. Starting from this partially polarized state, we can now wind a spin helix, exactly with the same procedure as we did earlier, where we started with a fully polarized state.

We can conveniently use anisotropic spin couplings ($\Delta \neq 1$) to dephase transverse spin components. The experiment in Ref. [33] is limited to $\Delta = 1$, which makes this much

harder. They actually used single site resolution to apply randomized light shifts to individual spins, which varied from run to run, to dephase the transverse components manually.

Single site resolution with a quantum gas microscope

With a quantum gas microscope it would be possible to directly image holes in the system. And this would open the door to studying the boson t-J model with single site resolution. The lattice depth allows us to control the dynamics of holes (tunneling) and spins (superexchange; second-order tunneling) separately. The study of hole-magnon coupling may be interesting for other system where such couplings are present such as high temperature superconductors [57–59].

Mapping out hole dynamics in the frequency domain

Even without single site resolution it should be possible to study hole dynamics and hole-magnon coupling. We have shown that a spin-echo can rectify the fluctuations of hole dynamics [29]. Since holes carry a localized magnetic field which couples to spin dynamics, this leads to enhanced dephasing. By using a series of echo pulses at frequency ω , one could map out the frequency spectrum of the effective magnetic field and hence follow the hole dynamics in the frequency domain, using concepts from dynamic decoupling [60].

Higher spin quantum numbers

A spin-1 Heisenberg model can be realized with two atoms per site and realizing three spin states $|\uparrow\rangle := |\uparrow\uparrow\rangle$, $|\circ\rangle := |\uparrow\downarrow\rangle$, and $|\downarrow\rangle := |\downarrow\downarrow\rangle$. This system is restricted to realizing isotropic spin couplings ($\Delta=1$). But it includes an additional term, the so-called single-ion anisotropy u , as it is commonly called in condensed matter systems:

$$H = J \sum_{\langle ij \rangle} \mathbf{S}_i \cdot \mathbf{S}_j + u \sum_i (\mathbf{S}_i)^2 \quad (7.10)$$

The single-ion anisotropy $u = (U_{\uparrow\uparrow} + U_{\downarrow\downarrow})/2 - U_{\uparrow\downarrow}$ can be tuned through Feshbach res-

onances in our system. It would be interesting to create a spin-Mott state $|\circ\circ\circ\cdots\circ\rangle$ which we can do easily using a π -pulse $|\uparrow\uparrow\rangle \rightarrow |\uparrow\downarrow\rangle$, while $|\uparrow\downarrow\rangle \rightarrow |\downarrow\downarrow\rangle$ can be far detuned from resonance ($U_{\uparrow\uparrow} - U_{\uparrow\downarrow} \neq U_{\uparrow\downarrow} - U_{\downarrow\downarrow}$) causing an interaction blockade [41]. This spin-Mott is the ground state for $u \ll J$. Starting from this state, we can study a quantum quench by suddenly switching on spin interactions J to a finite values (by ramping down the lattice depth), while the single-ion anisotropy is set to $u=0$ or $u>0$. An experimental complication might be, that there is 3-body loss, which limits the coherence. This time constraint might inhibit adiabatic state preparation. But it might be enough time to observe interesting spin dynamics far away from the ground state.

A transverse spin-helix has a macroscopic spin current

For transverse spin-helix states, so far, we have only studied the transverse magnetization S_x . However, a transverse spin helix intrinsically has a macroscopic spin current along the spin chain, which over time should lead to an increasing spatial imbalance of spin $|\uparrow\rangle$ and spin $|\downarrow\rangle$ population. This effect should be observable by measuring the S_z magnetization profile after a quench from an initial transverse spin-helix state, as a function of time.

Extended Hubbard model

The discovered nearest-neighbor off-site interactions V close to a Feshbach resonance can be used to implement extended Hubbard models:

$$H = -t \sum_{\langle ij \rangle} (a_{i\sigma}^\dagger a_{j\sigma} + \text{H.c.}) + \sum_i \frac{U}{2} n_i (n_i - 1) + 2V \sum_{\langle ij \rangle} n_i n_j \quad (7.11)$$

For example, analogous to a Mott-insulator, where strong on-site repulsion U can suppress double occupancies and can localize atoms on individual lattice sites if $t \ll U$, strong nearest-neighbor off-site interactions V prevent atoms to be nearest neighbors, i.e. this can lead to a density modulation.

In summary, our new quantum simulator platform with tunable interactions opens up the possibilities for many new studies which are likely to provide new insight into the rich dynamics of Heisenberg spin models, t-J models with hole-magnon couplings and Hubbard models with offsite interactions.

Appendix A

Spin transport in a tunable Heisenberg model realized with ultracold atoms

P. N. Jepsen, J. Amato-Grill, I. Dimitrova, W. W. Ho, E. Demler, W. Ketterle
Spin transport in a tunable Heisenberg model realized with ultracold atoms
Nature **588**, 403-407 (2020)

Spin transport in a tunable Heisenberg model realized with ultracold atoms

<https://doi.org/10.1038/s41586-020-3033-y>

Received: 18 May 2020

Accepted: 25 September 2020

Published online: 16 December 2020

 Check for updates

Paul Niklas Jepsen^{1,2,3}✉, Jesse Amato-Grill^{1,2,3}, Ivana Dimitrova^{1,2,3}, Wen Wei Ho^{3,4}, Eugene Demler^{3,4} & Wolfgang Ketterle^{1,2,3}

Simple models of interacting spins have an important role in physics. They capture the properties of many magnetic materials, but also extend to other systems, such as bosons and fermions in a lattice, gauge theories, high-temperature superconductors, quantum spin liquids, and systems with exotic particles such as anyons and Majorana fermions^{1,2}. To study and compare these models, a versatile platform is needed. Realizing such systems has been a long-standing goal in the field of ultracold atoms. So far, spin transport has only been studied in systems with isotropic spin–spin interactions^{3–12}. Here we realize the Heisenberg model describing spins on a lattice, with fully adjustable anisotropy of the nearest-neighbour spin–spin couplings (called the XXZ model). In this model we study spin transport far from equilibrium after quantum quenches from imprinted spin-helix patterns. When spins are coupled only along two of three possible orientations (the XX model), we find ballistic behaviour of spin dynamics, whereas for isotropic interactions (the XXX model), we find diffusive behaviour. More generally, for positive anisotropies, the dynamics ranges from anomalous superdiffusion to subdiffusion, whereas for negative anisotropies, we observe a crossover in the time domain from ballistic to diffusive transport. This behaviour is in contrast with expectations from the linear-response regime and raises new questions in understanding quantum many-body dynamics far away from equilibrium.

Quantum dynamics is an active research area in many-body physics. Even the linear-response (near-equilibrium) behaviour of many-body systems can be very complex. For example, spin transport in one-dimensional Heisenberg XXZ quantum spin chains, despite being a topic that is decades old, is still under active investigation because of the rich dynamics connected to integrability^{13–17}. Dynamics in highly out-of-equilibrium scenarios, such as from continual drives or quantum quenches^{18–22}, is even less well understood. It is hence highly desirable to have a quantum simulator that can realize well isolated, programmable and controllable spin systems. By now, a number of such platforms exist^{21–27}, with varying capabilities.

Ultracold atoms in optical lattices offer an especially promising platform with which to realize tunable Heisenberg spin models²⁷: in deep lattices where atoms become localized on individual sites, forming a Mott insulator²⁸, the dynamics of the remaining degrees of freedom is governed by effective spin–spin interactions realizing nearest-neighbour Heisenberg XXZ spin models. For bosons, the most commonly used atom, ⁸⁷Rb, has almost equal singlet and triplet scattering lengths, implying effectively isotropic spin physics^{4–7}. For fermions, the Pauli exclusion principle enforces isotropic antiferromagnetism³. Many theoretical proposals have suggested ways to obtain richer spin models in optical lattices^{29–32} over the past 20 years, and we now report here the realization of the spin-1/2 Heisenberg model with fully adjustable anisotropy in the spin–spin interactions. This enables simulations of anisotropic magnetic materials with easy-axis or easy-plane alignment.

The wide tunability is realized using ⁷Li atoms, the Feshbach resonances of which we have characterized in previous work³³. Additionally, lithium, with its light mass, has the advantage of fast spin dynamics (set by second-order tunnelling)²⁶, decreasing the relative importance of heating and loss processes compared to heavier atoms. We use this fast and tunable platform to study far-from-equilibrium spin transport in previously unexplored regimes.

For many-body quantum simulation experiments, an ideal starting point is a simple benchmark system to which more complexity can be added. In this work, we first implement the XX model in one dimension, which is exactly solvable by mapping to a system of non-interacting fermions. We then tune the anisotropy to arbitrary values, which in the fermionic language corresponds to adding nearest-neighbour interactions. To implement the spin model, we use a system of two-component bosons in an optical lattice, which is well described by the Bose–Hubbard model. The two states, labelled $|\uparrow\rangle$ and $|\downarrow\rangle$, form a spin-1/2 system. In the Mott insulating regime at unity filling the effective Hamiltonian is given by the spin-1/2 Heisenberg XXZ model^{29–32}

$$H = \sum_{\langle ij \rangle} [J_{xy} (S_i^x S_j^x + S_i^y S_j^y) + J_z S_i^z S_j^z], \quad (1)$$

where nearest-neighbour ($\langle ij \rangle$) couplings are mediated by superexchange. To leading order, $J_{xy} = -4\tilde{t}^2/U_n$ and $J_z = 4\tilde{t}^2/U_n - (4\tilde{t}^2/U_n + 4\tilde{t}^2/U_n)$, where \tilde{t} is the tunnelling matrix element between neighbouring sites,

¹Department of Physics, Massachusetts Institute of Technology, Cambridge, MA, USA. ²Research Laboratory of Electronics, Massachusetts Institute of Technology, Cambridge, MA, USA.

³MIT-Harvard Center for Ultracold Atoms, Cambridge, MA, USA. ⁴Department of Physics, Harvard University, Cambridge, MA, USA. ✉e-mail: jepsen@mit.edu

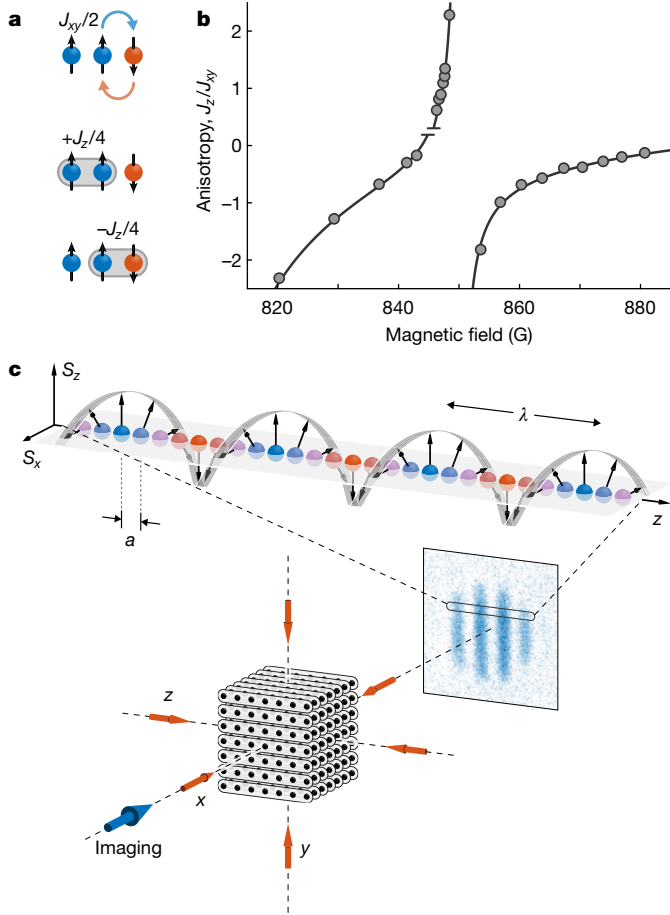


Fig. 1 | Tunability of the XXZ model with ^7Li and implementation of a spin helix. **a.** The Hamiltonian (equation (1)) is characterized by two energy scales: the transverse spin coupling J_{xy} (spin exchange) and the longitudinal spin coupling J_z (spin–spin interaction). **b.** Anisotropy $\Delta = J_z/J_{xy}$ as a function of applied magnetic field. The solid line is a fit to experimental data points, which are calculated from measured values $U_{\uparrow\uparrow}, U_{\uparrow\downarrow}, U_{\downarrow\downarrow}$ (see Methods and Extended Data Fig. 1). **c.** Spin helix realized from two hyperfine states (spin $|\uparrow\rangle$ and $|\downarrow\rangle$). The spin vector winds in the S_z – S_x plane as a function of position z in the spin chain. Deep optical lattices along x and y create an array of independent spin chains. The z lattice is shallower and controls spin transport along each chain.

and $U_{\uparrow\uparrow}, U_{\uparrow\downarrow}, U_{\downarrow\downarrow}$ are the on-site interaction energies. The transverse coupling J_{xy} induces spin exchange between neighbouring sites and is the origin of spin transport. The longitudinal coupling J_z corresponds to a nearest-neighbour spin–spin interaction (Fig. 1a).

The magnitude of superexchange can be varied over two orders of magnitude by changing the lattice depth, which scales the entire Hamiltonian. We control the anisotropy $\Delta = J_z/J_{xy}$ via an applied magnetic field that tunes the interactions through Feshbach resonances in two hyperfine states (Fig. 1b) while keeping $J_{xy} > 0$ (antiferromagnetic). The ability to tune the anisotropy over a wide range of positive and negative values allows us to explore dynamics beyond previous experiments^{3–7} in which $\Delta \approx 1$.

An array of one-dimensional (1D) chains is implemented by a deep optical lattice (of depth $V_x, V_y = 35E_R$) in the x and y directions. The lattice depth V_z along the z direction controls the superexchange rate within the chains (Fig. 1c). Here $E_R = \pi^2\hbar^2/(2ma^2)$ denotes the recoil energy, where a is the lattice spacing, m the atomic mass and \hbar the reduced Planck constant. After preparing an identical spin helix^{7–9} with wavelength λ in each chain (see Methods), time evolution is initiated by rapidly lowering V_z . The dynamics following this quench is governed by the 1D XXZ model (equation (1)) with an anisotropy Δ selected by an appropriate applied magnetic field. After an evolution time t of up to

$500\hbar/J_{xy}$ (well below the heating lifetime, approximately 1 s, of the Mott insulator), the dynamics is frozen by rapidly increasing V_z and the atoms are imaged in the $|\uparrow\rangle$ state via state-selective polarization-rotation imaging with an optical resolution of about 6 lattice sites (see Methods).

Integrating the images along the direction perpendicular to the chains yields a 1D spatial profile of the population in the $|\uparrow\rangle$ state, averaged over all spin chains (see Extended Data Fig. 2). This is equivalent to a measurement of the local magnetization $\langle S_i^z \rangle = (n_{i\uparrow} - n_{i\downarrow})/2 = n_{i\uparrow} - 1/2$ which, as in Fig. 1c, shows a sinusoidal stripe pattern. We determine the contrast \mathcal{C} by a fit $f(z) = g(z)[1 + C\cos(Qz + \theta)]/2$, where $Q = 2\pi/\lambda$ is the wavevector, $g(z)$ is a Gaussian envelope function that accounts for the spatial distribution of all atoms $n = n_{\uparrow} + n_{\downarrow}$, and θ is a random phase that varies from shot to shot, owing to small magnetic bias field drifts. During the evolution time t the contrast $\mathcal{C}(t)$ decays, and we study the dependence of $c(t) = \mathcal{C}(t)/\mathcal{C}(0)$ on lattice depth V_z , wavelength λ , and anisotropy Δ .

For all data, we measure spin dynamics at two or three different lattice depths V_z and verify that the decay curves $c(t)$ collapse when time is rescaled by the spin-exchange time \hbar/J_{xy} (see for example, Fig. 2a). This demonstrates that we observe transport by superexchange and not some other process. To study transport behaviour, we measure how the decay timescale τ depends on the modulation lengthscale λ . We note that for ballistic motion, this decay constant grows linearly with distance ($\tau \propto \lambda$), whereas for diffusion it grows quadratically ($\tau \propto \lambda^2$). Throughout this Article, we normalize time by the spin-exchange time \hbar/J_{xy} , length by the lattice spacing a , and velocities by the Fermi velocity $v_F = a/(\hbar/J_{xy})$. These units are obtained from the experimentally determined lattice depth using an extended Hubbard model and have an estimated systematic calibration error of about $\pm 10\%$, in addition to quoted statistical errors. The accuracy of Δ is estimated to be ± 0.1 (see Methods). Unless noted otherwise, all error bars and uncertainties herein are purely statistical and represent 1σ uncertainty of the fits. Each data point for the contrast $c(t)$ is obtained by simultaneously fitting several images (usually six, but up to 15).

XX model

We first study the case $\Delta = 0$, which can be mapped by the Jordan–Wigner transformation³⁴ to non-interacting spinless fermions undergoing nearest-neighbour hopping on a lattice. In this mapping, $|\uparrow\rangle$ corresponds to a site occupied by a fermion, and $|\downarrow\rangle$ to an empty site. Small excitations around the Fermi sea at half-filling are spin waves with wavevector q and a linear dispersion relation $\omega(q) = v_F q$.

Figure 2a shows the decay of the contrast $c(t)$ for $\Delta \approx 0$ (see Methods for calibration of Δ). In addition to an overall decay, a local maximum corresponding to a partial revival of the initial spin modulation appears after about 12 spin-exchange times. We find the decay curves can be well described by the sum of a decaying part with time constant τ and a (damped) oscillating part with frequency ω , resulting in a fitting function $c(t) = [a_0 + b_0 \cos(\omega t)]e^{-t/\tau} + c_0$, with a_0, b_0, c_0, ω and τ as adjustable parameters (Methods and Extended Data Fig. 4 discuss the offset c_0). Numerical simulations, also shown in Fig. 2a, reproduce the major features of the experimental dynamics very well (decay time τ and first oscillation), but differ in details, probably owing to a difference in hole fraction, uncertainties in Δ , or non-idealized initial-state preparation. By varying the wavelength $\lambda = 2\pi/Q$ of the helix (Fig. 2b) we obtain a dispersion relation $\omega(Q)$ for the oscillations (Fig. 2d). A linear fit $\omega(Q) = vQ$ yields a characteristic velocity $v = 0.76(1)v_F$, similar to the near equilibrium dynamics, as expected for a non-interacting system.

The decay time constant τ also shows a linear scaling with inverse wavevector: a power-law fit $\tau \propto Q^{-\alpha}$ yields an exponent of $\alpha = 1.00(5)$, indicating ballistic transport (Fig. 3b, red). Indeed, if we plot $c(t)$ in time units rescaled by λ , all curves for different helix wavelengths collapse into a single curve (Fig. 2c), showing that all aspects of the observed spin dynamics in the XX model are ballistic and governed by one characteristic velocity.

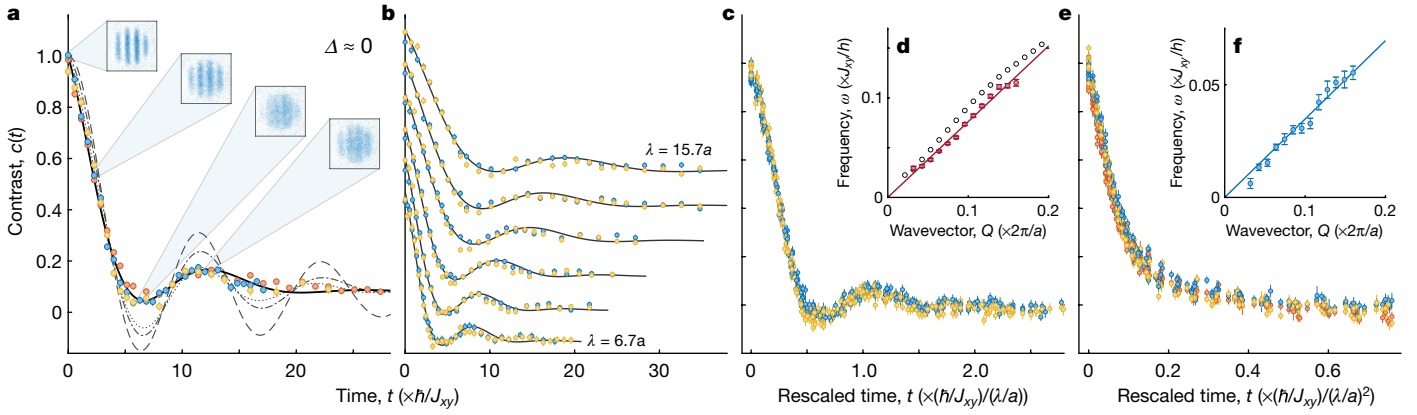


Fig. 2 | Ballistic and diffusive spin transport. **a–d**, XX model, ballistic behaviour ($\Delta \approx 0$, non-interacting fermions). **a**, Spin-helix contrast $c(t)$ for $\lambda = 10.4a$ measured at three different lattice depths $9E_R$ (orange), $11E_R$ (blue) and $13E_R$ (yellow). Decay curves collapse when times are expressed in units of $\hbar/J_{xy} = 0.64$ ms, 1.71 ms and 4.30 ms, respectively. The fit (black line) shows a decay with time constant $\tau = 5.5(2)\hbar/J_{xy}$ and a damped oscillation with period $T = 2\pi/\omega = 13.7(2)\hbar/J_{xy}$. The fit is typically applied to data points from all lattice depths simultaneously, but analysing each lattice depth separately yields identical results. Numerical simulations are also shown for the XX model (dashed line) and bosonic \tilde{t} - J model with 5% holes (dash-dotted line) and 10% holes (dotted line). **b**, Decay curves for different wavelengths $\lambda = 15.7a, 13.4a, 11.7a, 9.4a, 7.8a$ and $6.7a$ (offset for clarity). **c**, The decay curves in **b** collapse

XXX model

For finite Δ , the Jordan–Wigner transformation results in fermions with nearest-neighbour interactions. The isotropic case $\Delta = 1$ corresponds to strong interactions, which should generically turn fast ballistic transport into slow diffusive transport. Indeed, the decay slows down for increasing wavelength λ much more dramatically than in the $\Delta \approx 0$ case (also illustrated in Extended Data Fig. 3a–c). A power-law fit of the decay constant τ versus Q yields an exponent of $\alpha = 1.87(4)$, which is close to 2, indicative of a diffusive process (Fig. 3b, blue). If time units are rescaled by λ^2 , then all contrast curves $c(t)$ collapse very well into a single curve (Fig. 2e). However this collapse is not perfect, because of a (small) oscillating part that still obeys a linear dispersion relation $\omega(Q) = \nu Q$ (Fig. 2f).

Using $1/\tau = DQ^2$, a diffusion constant can be determined as $D = 0.242(7)a^2/(\hbar/J_{xy})$. Interpreting $D = \frac{1}{2}\delta x^2/\delta t$ as arising from a random walk of step size δx (the mean free path) and time δt between steps, and using $\nu = \delta x/\delta t = 0.35(1)\nu_F$ (obtained from the dispersion relation in Fig. 2f), we find $\delta x = 1.39(5)a$. A mean free path on the order of the lattice constant is analogous to the Mott–Ioffe–Regel limit for resistivity where simple quasi-particle pictures break down^{35,36}, implying that the isotropic Heisenberg model is strongly interacting.

Our observation of diffusive behaviour and the value for the diffusion coefficient are consistent with previous results⁷ (for zero hole fraction) on the 1D isotropic Heisenberg model with $J_{xy} < 0$. Our system is antiferromagnetic ($J_{xy} > 0$), and so this indicates that the overall sign of the Hamiltonian is irrelevant, as expected from theoretical arguments involving time-reversal symmetry (see Methods). However the small (ballistic) oscillatory component has not been previously reported. We note that a two-dimensional Fermi–Hubbard system can also show diffusive decay and ballistic oscillations³⁷.

By tuning the interactions over a large range of Δ , we can study how the transport behaviour changes. For an interacting gas of classical particles or quasiparticles, one would expect ballistic behaviour on timescales shorter than the collision time and diffusion for longer times. We indeed find this for $\Delta < 0$, whereas for $\Delta \geq 0$ we observe qualitatively very different behaviour (also illustrated in Extended Data Fig. 5).

into a single curve, if time is rescaled by λ (indicating ballistic transport) and offsets c_0 are subtracted. **d**, Oscillation frequencies (filled symbols) follow a linear dispersion relation $\omega(Q) = \nu Q$ with velocity $\nu = 0.76(1)\nu_F$ and agree at the 10% level with numerical simulations (open symbols) yielding $\nu = 0.85(1)\nu_F$. Theoretical frequencies are obtained as the inverse of the first revival time. Owing to damping, this may be an overestimate of 10%. **e**, **f**, XXX model, diffusive behaviour ($\Delta \approx 1$, strongly interacting fermions). Oscillations are strongly suppressed and time has to be rescaled by λ^2 (indicating diffusive transport) for collapse. However this collapse is not perfect, because of the presence of small oscillations (see Extended Data Fig. 3) that follow a linear dispersion relation (**f**) with a velocity $\nu = 0.35(1)\nu_F$.

Positive anisotropies ($\Delta \geq 0$)

All measured decay curves $c(t)$ are well described by the fitting function previously used. The observed oscillation frequencies ω follow linear dispersion relations $\omega(Q) = \nu Q$ (Extended Data Fig. 3), whereas the decay time constants τ show power-law scaling $\tau \propto Q^{-\alpha}$ (Fig. 3) in the following way: as the anisotropy is increased from $\Delta = -0.12$ to $\Delta = 0.55$, the exponent stays close to $\alpha = 1$ (‘ballistic regime’) and the characteristic velocity of oscillations decreases by a factor of about 1.6, to $\nu = 0.47(1)\nu_F$. Between $\Delta \approx 0.5$ and 1 the exponent increases smoothly from $\alpha = 1$ to $\alpha \approx 2$ (‘superdiffusive regime’), for example, $\alpha = 1.48(4)$ at $\Delta = 0.78$ (Fig. 3b, yellow). For $\Delta > 1$ transport slows down even more, and the exponent also continues to increase smoothly to values $\alpha > 2$ (‘subdiffusive regime’), for example, $\alpha = 2.83(14)$ at $\Delta = 1.58$ (Fig. 3b, green). For each $\Delta \geq 0$, the measured decay curves collapse into a single curve, if time units are rescaled by λ^α (Extended Data Fig. 6).

Power-law exponents between 1 and 2 (superdiffusion) are often associated with Lévy flights or fractional Brownian motion where step sizes are correlated^{38,39}. Power-law exponents larger than 2 (subdiffusion) typically arise for transport through a disordered medium^{40,41} and have also been recently observed in a tilted Fermi–Hubbard system⁴². However, the XXZ Heisenberg Hamiltonian we study has no disorder.

Negative anisotropies ($\Delta < 0$)

Here the behaviour is qualitatively very different compared to positive Δ of similar magnitude. We find a crossover in the time domain from ballistic to diffusive behaviour. For example, at $\Delta = -1.43$ the initial decay of $c(t)$ is fast and, in fact, coincides well with the non-interacting (ballistic) case $\Delta \approx 0$ (Fig. 4a), in stark contrast to the positive case $\Delta = +1.58$ (Extended Data Fig. 5). At $t = t_0 \approx 2.8\hbar/J_{xy}$ (dotted line) the decay suddenly slows down. We therefore parameterize the decay curve $c(t)$ by a piecewise fit with two timescales: (I) a linear function $(1 - t/\tau_I)$ at short times and (II) an exponential $e^{-t/\tau_{II}}$ at longer times, with respective time constants τ_I, τ_{II} . When the wavevector Q is varied, both τ_I and τ_{II} follow a power law (Fig. 3a), but with different exponents: $\alpha_I = 1.08(6)$ (ballistic) and $\alpha_{II} = 2.15(16)$ (diffusive), respectively (Fig. 3c). In both experimental

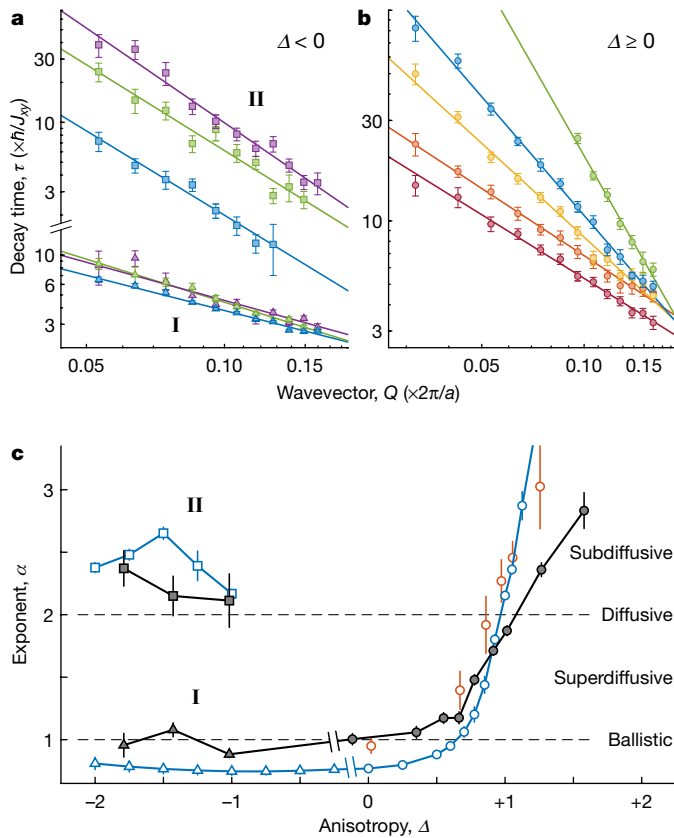


Fig. 3 | Power-law scalings. **a, b**, The power-law scalings of the decay time constants τ for anisotropies Δ ranging from negative (**a**) to positive (**b**). Experimental results are shown in **a** for $\Delta = -1.02$ (blue), -1.43 (green) and -1.79 (purple) for the two timescales τ_i and τ_{ii} ; and in **b** for $\Delta = -0.12$ (red), 0.35 (orange), 0.78 (yellow), 1.01 (blue) and 1.58 (green). Lines are power-law fits. **c**, Fitted power-law exponents from experiments (filled symbols) and theory (open symbols), obtained from simulations of the defect-free XXZ model (blue) and \tilde{t} - J model with 5% hole fraction (orange). **a-c** can be summarized as follows. For $\Delta \geq 0$ (circles), we observe anomalous diffusion: the exponent increases smoothly from ballistic (red and orange) to superdiffusive (yellow) to diffusive (blue) to subdiffusive (green). For $\Delta < 0$, we observe behaviour reminiscent of a classical gas: transport is ballistic at short times (I; triangles) and diffusive at longer times (II; squares). (For diffusion coefficients and theory see Extended Data Fig. 8.).

(Fig. 4b) and numerical results (Fig. 4c), all decay curves collapse for short times before ‘peeling off’ at later times, if time is rescaled by λ .

Similar behaviour is observed for other negative anisotropies (Fig. 3a; also Extended Data Fig. 7), with the initial ballistic temporal decay (regime I) almost independent of Δ . However, for larger $|\Delta|$, we find that t_0 (the range of regime I) is smaller, and the diffusion timescales τ_{ii} in regime II are longer. The diffusion coefficient decreases from $D = 1.27(6)a^2/(\hbar/J_{xy})$ to $0.25(2)a^2/(\hbar/J_{xy})$ between $\Delta = -1.02$ and -1.79 (Extended Data Fig. 8c). Figure 3c summarizes the different transport behaviours uncovered for the anisotropic Heisenberg model and represents the main result of this paper.

Theoretical simulations

To validate our platform as a quantum simulator, we have carried out numerical simulations of quench dynamics starting from a spin helix, using a combination of exact diagonalization and tensor network methods (see Methods). We simulate the dynamics of the system without holes (XXZ Hamiltonian), as well as with a small probability of holes (bosonic \tilde{t} - J model), and compare the simulated contrast to experimental results. The timescales of decay generally agree fairly well. A qualitative difference in the decay curves is illustrated in Fig. 2a: the simulations always show an

initial quadratic decay (as expected from time-reversal symmetry, see Methods), and revivals are generally more pronounced. The initial quadratic decay happens in the pure-spin simulations on the timescale of \hbar/J_{xy} , whereas an addition of 5% to 10% holes reduces this to the timescale \hbar/\tilde{t} (where \tilde{t} is the tunnelling amplitude in the \tilde{t} - J model)⁷ and reduces the amplitude of revivals. However, the presence of holes does not affect the overall behaviour of the decay times of the spin contrast: the simulations of both the XXZ and the \tilde{t} - J model yield power-law scalings of time constants, with exponents that agree reasonably well with experimental ones (see Fig. 3c and Methods section ‘Power-law scalings in the continuum limit’).

Discussion

Our work on spin transport illustrates the strength of a combined experimental and theoretical quantum simulation. Our quantum simulator platform enables us to probe dynamical regimes that are difficult to achieve in numerical simulations, such as large system sizes or long times (Extended Data Figs. 6, 7), which require prohibitively large computational resources. On the other hand, numerical simulations provided valuable insight into effects that could not be studied experimentally, such as that of holes (Figs. 2a, 3c), different phases of the helix, and the role of boundary conditions (Extended Data Figs. 9, 10).

Our observations are consistent with some theoretical predictions for spin transport in the anisotropic Heisenberg model, but differ sharply from others. For example, studies of quantum quenches from pure states involving a single domain wall^{43–46} have suggested ballistic dynamics at $\Delta = 0$ and diffusive dynamics at $\Delta = 1$ (albeit with logarithmic corrections), similar to our findings. In addition to diffusive transport, a ballistic light-cone has been observed⁴⁶ in numerics at $\Delta = 1$, which may be related to the small ballistic oscillatory component we have observed experimentally. In contrast to our findings, theoretical studies of long-time linear response of spin transport at high temperatures (that is, mixed states) have indicated a sharp transition from ballistic ($\Delta < 1$) to diffusive ($\Delta > 1$), with superdiffusive behaviour ($\alpha = 3/2$) exactly at the transition point $\Delta = 1$ ^{15,16}, which can be understood from generalized hydrodynamics involving local equilibration of conserved quantities^{47,48}. The situation we have studied is different, because the initial spin-helix state is a pure state far from equilibrium. An accurate description of coherent dynamics using the exact eigenstates from the Bethe ansatz⁴⁹ is a very challenging problem. Ultimately, the spin-helix state will relax into a thermal state (or quasi-thermal generalized Gibbs state), but probably outside the time window studied here. The rich phenomenology observed in our experiments and dramatic differences with the cases studied in the literature calls for a deeper understanding of this dynamical regime, both theoretically and experimentally.

Our studies can be extended in many different directions: the role of integrability, which the XXZ Hamiltonian possesses, should be explored, for example by adding next-nearest-neighbour integrability-breaking terms realized through appropriate Rydberg dressing of atoms. We can explore different initial conditions, including single domain walls^{43–46} and finite temperatures (by using partially polarized (mixed) states) and study the decay of transverse spin via transport and dephasing. An interesting question is whether the power-law scalings change for very large wavelengths that approach the continuum limit (see preliminary theoretical analysis in Methods and Extended Data Fig. 8). We can furthermore realize Heisenberg models in two or three spatial dimensions, or with purely ferromagnetic couplings by changing the sign of J_{xy} using a constant force to tilt the lattice⁵⁰.

Online content

Any methods, additional references, Nature Research reporting summaries, source data, extended data, supplementary information, acknowledgements, peer review information; details of author contributions and competing interests; and statements of data and code availability are available at <https://doi.org/10.1038/s41586-020-3033-y>.

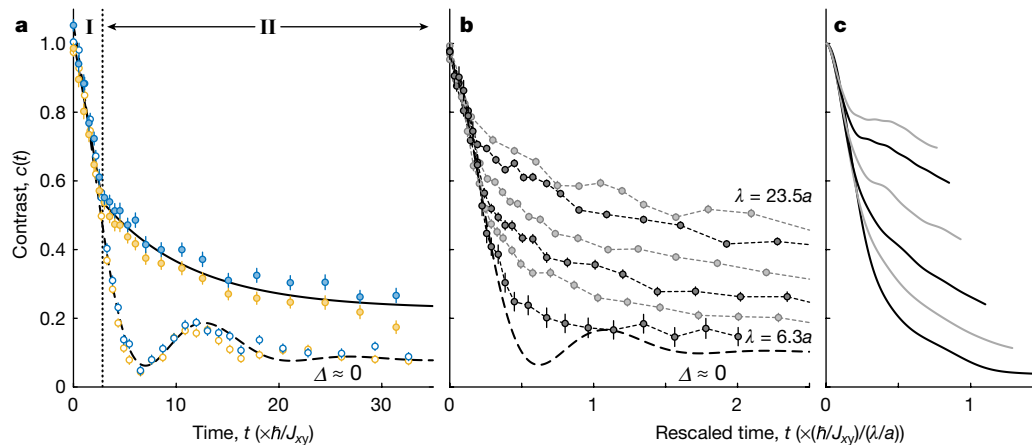


Fig. 4 | Temporal crossover from ballistic to diffusive transport for negative anisotropies $\Delta < 0$. **a**, Spin-helix contrast $c(t)$ for $\lambda = 10.4a$ and $\Delta = -1.43$ (filled circles) measured at lattice depths $11E_R$ (blue) and $13E_R$ (yellow). A piecewise fit (solid line) is linear at short times (I) and exponential at longer times (II) with a crossover at $t = t_0$ (vertical dotted line). For $t < t_0$ the decay coincides well with the non-interacting case $\Delta \approx 0$ (open circles and dashed line). **b**, Decay curves for different wavelengths $\lambda = 23.5a, 18.8a, 13.4a, 10.4a, 8.5a$ and $6.3a$ (average of

measurements at lattice depths $11E_R$ and $13E_R$) collapse into a single curve at early times if time is rescaled by λ (as for ballistic behaviour) and follow the non-interacting case (thick dashed line). At later times, the decay is diffusive with different scaling (see Fig. 3a). **c**, Numerical simulations for $\Delta = -1.5$ and the same wavelengths λ as in **b** show similar behaviour, although the range of time probed is more limited. Simulations could not be extended to longer times, owing to the exponential increase in computation time.

- Lee, P. A. From high temperature superconductivity to quantum spin liquid: progress in strong correlation physics. *Rep. Prog. Phys.* **71**, 012501 (2007).
- Broholm, C. et al. Quantum spin liquids. *Science* **367**, eaay0668 (2020).
- Nichols, M. A. et al. Spin transport in a Mott insulator of ultracold fermions. *Science* **363**, 383–387 (2019).
- Brown, R. C. et al. Two-dimensional superexchange-mediated magnetization dynamics in an optical lattice. *Science* **348**, 540–544 (2015).
- Fukuhara, T. et al. Quantum dynamics of a mobile spin impurity. *Nat. Phys.* **9**, 235–241 (2013).
- Fukuhara, T. et al. Microscopic observation of magnon bound states and their dynamics. *Nature* **502**, 76–79 (2013).
- Hild, S. et al. Far-from-equilibrium spin transport in Heisenberg quantum magnets. *Phys. Rev. Lett.* **113**, 147205 (2014).
- Koschorreck, M., Pertot, D., Vogt, E. & Köhl, M. Universal spin dynamics in two-dimensional Fermi gases. *Nat. Phys.* **9**, 405–409 (2013); corrigendum **10**, 170 (2014).
- Trotzky, S. et al. Observation of the Leggett–Rice effect in a unitary Fermi gas. *Phys. Rev. Lett.* **114**, 015301 (2015).
- Palzer, S., Zipkes, C., Sias, C. & Köhl, M. Quantum transport through a Tonks–Girardeau gas. *Phys. Rev. Lett.* **103**, 150601 (2009).
- Sommer, A., Ku, M., Roati, G. & Zwerlein, M. W. Universal spin transport in a strongly interacting Fermi gas. *Nature* **472**, 201–204 (2011).
- Krinner, S. et al. Mapping out spin and particle conductances in a quantum point contact. *Proc. Natl. Acad. Sci. USA* **113**, 8144–8149 (2016).
- Vasseur, R. & Moore, J. E. Nonequilibrium quantum dynamics and transport: from integrability to many-body localization. *J. Stat. Mech.* **2016**, 064010 (2016).
- Bertini, B. et al. Finite-temperature transport in one-dimensional quantum lattice models. Preprint at <https://arxiv.org/abs/2003.03334> (2020).
- Ljubotina, M., Žnidarič, M. & Prosen, T. Spin diffusion from an inhomogeneous quench in an integrable system. *Nat. Commun.* **8**, 16117 (2017).
- Gopalakrishnan, S. & Vasseur, R. Kinetic theory of spin diffusion and superdiffusion in XXZ spin chains. *Phys. Rev. Lett.* **122**, 127202 (2019).
- Ilievski, E., De Nardis, J., Medenjak, M. & Prosen, T. Superdiffusion in one-dimensional quantum lattice models. *Phys. Rev. Lett.* **121**, 230602 (2018).
- Else, D. V., Monroe, C., Nayak, C. & Yao, N. Y. Discrete time crystals. *Annu. Rev. Condens. Matter Phys.* **11**, 467–499 (2020).
- Basov, D. N., Averitt, R. D. & Hsieh, D. Towards properties on demand in quantum materials. *Nat. Mater.* **16**, 1077–1088 (2017).
- Langen, T., Gasenzer, T. & Schmiedmayer, J. Prethermalization and universal dynamics in near-integrable quantum systems. *J. Stat. Mech.* **2016**, 064009 (2016).
- Zhang, J. et al. Observation of a many-body dynamical phase transition with a 53-qubit quantum simulator. *Nature* **551**, 601–604 (2017).
- Bernien, H. et al. Probing many-body dynamics on a 51-atom quantum simulator. *Nature* **551**, 579–584 (2017).
- Barends, R. et al. Digital quantum simulation of fermionic models with a superconducting circuit. *Nat. Commun.* **6**, 7654 (2015).
- Davis, E. J. et al. Protecting spin coherence in a tunable Heisenberg model. *Phys. Rev. Lett.* **125**, 060402 (2020).
- Signoles, A. et al. Glassy dynamics in a disordered Heisenberg quantum spin system. Preprint at <https://arxiv.org/abs/1909.11959> (2019).
- Trotzky, S. et al. Time-resolved observation and control of superexchange interactions with ultracold atoms in optical lattices. *Science* **319**, 295–299 (2008).
- Gross, C. & Bloch, I. Quantum simulations with ultracold atoms in optical lattices. *Science* **357**, 995–1001 (2017).
- Jaksch, D., Bruder, C., Cirac, J. I., Gardiner, C. W. & Zoller, P. Cold bosonic atoms in optical lattices. *Phys. Rev. Lett.* **81**, 3108–3111 (1998).
- Kuklov, A. B. & Svistunov, B. V. Counterflow superfluidity of two-species ultracold atoms in a commensurate optical lattice. *Phys. Rev. Lett.* **90**, 100401 (2003).
- Duan, L.-M., Demler, E. & Lukin, M. D. Controlling spin exchange interactions of ultracold atoms in optical lattices. *Phys. Rev. Lett.* **91**, 090402 (2003).
- Garcia-Ripoll, J. J. & Cirac, J. I. Spin dynamics for bosons in an optical lattice. *New J. Phys.* **5**, 76 (2003).
- Altman, E., Hofstetter, W., Demler, E. & Lukin, M. D. Phase diagram of two-component bosons on an optical lattice. *New J. Phys.* **5**, 113 (2003).
- Amato-Grill, J., Jepsen, N., Dimitrova, I., Lunden, W. & Ketterle, W. Interaction spectroscopy of a two-component Mott insulator. *Phys. Rev. A* **99**, 033612 (2019).
- Jordan, P. & Wigner, E. Über das Paulische Äquivalenzverbot. *Z. Phys.* **47**, 631–651 (1928).
- Ioffe, A. F. & Regel, A. R. Non-crystalline, amorphous and liquid electronic semiconductors. *Prog. Semiconduct.* **4**, 237–291 (1960).
- Mott, N. F. Conduction in non-crystalline systems IX. the minimum metallic conductivity. *Philos. Mag.* **A26**, 1015–1026 (1972).
- Brown, P. T. et al. Bad metallic transport in a cold atom Fermi–Hubbard system. *Science* **363**, 379–382 (2019).
- Dubkov, A. A., Spagnolo, B. & Uchaikin, V. V. Lévy flight superdiffusion: an introduction. *Int. J. Bifurc. Chaos* **18**, 2649–2672 (2008).
- Andreev, A. È. et al. Correlation theory of processes with stationary random increments of order n . *Am. Math. Soc. Transl.* **8**, 87 (1958).
- Agarwal, K., Gopalakrishnan, S., Knap, M., Müller, M. & Demler, E. Anomalous diffusion and Griffiths effects near the many-body localization transition. *Phys. Rev. Lett.* **114**, 160401 (2015).
- Vosk, R., Huse, D. A. & Altman, E. Theory of the many-body localization transition in one-dimensional systems. *Phys. Rev. X* **5**, 031032 (2015).
- Guardado-Sanchez, E. et al. Subdiffusion and heat transport in a tilted two-dimensional Fermi–Hubbard system. *Phys. Rev. X* **10**, 011042 (2020).
- Antal, T., Rácz, Z., Rákos, A. & Schütz, G. M. Transport in the XX chain at zero temperature: emergence of flat magnetization profiles. *Phys. Rev. E* **59**, 4912–4918 (1999).
- Gobert, D., Kollath, C., Schollwöck, U. & Schütz, G. Real-time dynamics in spin- $\frac{1}{2}$ chains with adaptive time-dependent density matrix renormalization group. *Phys. Rev. E* **71**, 036102 (2005).
- Misguich, G., Pavloff, N. & Pasquier, V. Domain wall problem in the quantum XXZ chain and semiclassical behavior close to the isotropic point. *SciPost Phys.* **7**, 025 (2019).
- Ljubotina, M., Žnidarič, M. & Prosen, T. A class of states supporting diffusive spin dynamics in the isotropic Heisenberg model. *J. Phys. A Math. Theor.* **50**, 475002 (2017).
- Castro-Alvaredo, O. A., Doyon, B. & Yoshimura, T. Emergent hydrodynamics in integrable quantum systems out of equilibrium. *Phys. Rev. X* **6**, 041065 (2016).
- Bertini, B., Collura, M., De Nardis, J. & Fagotti, M. Transport in out-of-equilibrium XXZ chains: exact profiles of charges and currents. *Phys. Rev. Lett.* **117**, 207201 (2016).
- Caux, J.-S. & Mossel, J. Remarks on the notion of quantum integrability. *J. Stat. Mech.* **2011**, P02023 (2011).
- Dimitrova, I. et al. Enhanced superexchange in a tilted Mott insulator. *Phys. Rev. Lett.* **124**, 043204 (2020).

Publisher's note Springer Nature remains neutral with regard to jurisdictional claims in published maps and institutional affiliations.

© The Author(s), under exclusive licence to Springer Nature Limited 2020

Extended Hubbard model

To determine the parameters J_{xy} and J_z in equation (1)

$$J_{xy} = -\frac{4\tilde{t}^2}{U_{\uparrow}}, J_z = \frac{4\tilde{t}^2}{U_{\uparrow}} - \left(\frac{4\tilde{t}^2}{U_{\downarrow}} + \frac{4\tilde{t}^2}{U_{\downarrow}} \right)$$

we use measurements of the lattice depths V_x, V_y, V_z and of the three scattering lengths $a_{\uparrow}, a_{\downarrow}, a_{\downarrow}$. From the calibrated lattice depths, the Hubbard parameters $\tilde{t}^{(0)}$ (in the non-interacting limit) and $U^{(0)}$ (in the single-band approximation) are calculated as²⁸

$$\tilde{t}^{(0)} = -\int dz w_z^*(z-a) \left[-\frac{\hbar^2}{2m} \frac{d^2}{dz^2} + V_z \sin^2(kz) \right] w_z(z),$$

and

$$U_{\sigma\sigma'}^{(0)} = g_{\sigma\sigma'} \int d^3r |w(\mathbf{r})|^4,$$

where $g_{\sigma\sigma'} = 4\pi\hbar^2 a_{\sigma\sigma'}/m$ and $\sigma, \sigma' = \uparrow, \downarrow$ and $w(\mathbf{r}) = w_x(x)w_y(y)w_z(z)$ using the calculated lowest-band Wannier functions $w_x(x), w_y(y)$ and $w_z(z)$ for each lattice depth⁵¹.

For the precision needed to compare experiment to theory, three corrections are applied^{7,52-54}.

Correction 1. Tunnelling is modified by the so-called single-band bond charge⁵⁴, which for single-occupancy is

$$\tilde{t}_{\sigma\sigma'} = \tilde{t}^{(0)} - g_{\sigma\sigma'} \int d^3r w^*(\mathbf{r}-\delta\mathbf{r})w^*(\mathbf{r})w(\mathbf{r})w(\mathbf{r}),$$

where $\delta\mathbf{r} = (0, 0, a)$ is a displacement by one lattice constant a in the tunnelling direction. Through this correction, the tunnelling matrix elements $\tilde{t}_{\uparrow\uparrow}, \tilde{t}_{\downarrow\downarrow}$ and $\tilde{t}_{\downarrow\uparrow}$ are now slightly spin-dependent.

Correction 2. For the on-site interaction, we include admixtures of higher bands^{53,54}. The dominant part is captured by a perturbative correction due to the first and second excited bands

$$U_{\sigma\sigma'} = U_{\sigma\sigma'}^{(0)} - g_{\sigma\sigma'}^2 \sum_{\mathbf{n}_1, \mathbf{n}_2} \frac{1}{E_{\text{bg}}} \int d^3r w_{\mathbf{n}_1}^*(\mathbf{r})w_{\mathbf{n}_2}^*(\mathbf{r})w(\mathbf{r})w(\mathbf{r}),$$

where \mathbf{n}_1 and \mathbf{n}_2 are the three-dimensional band indices of the two atoms and E_{bg} is the sum of the bandgap energies. Corrections to the tunnelling rate \tilde{t} owing to population of higher bands is negligible for a Mott insulator with occupation $n = 1$, because higher bands are admixed only through virtual doubly occupied sites. These modifications of \tilde{t} and U both contribute to a modification of superexchange J_{xy} and J_z (Extended Data Fig. 1). The relative correction to $J_{xy}^{(0)} = -4(\tilde{t}^{(0)})^2/U_{\uparrow}^{(0)}$, given by $(J_{xy} - J_{xy}^{(0)})/J_{xy}^{(0)}$, is almost independent of lattice depth (for the range of lattice depths studied here), and in the experiment J_{xy} is typically reduced by 10% to 15%. Note that the correction has the opposite sign as in ref. ⁷, because $J_{xy} > 0$ is antiferromagnetic in the present work.

Correction 3. To accurately determine J_z , one must also consider off-site interactions of the form⁵⁴

$$V_{\sigma\sigma'} = g_{\sigma\sigma'} \int d^3r w^*(\mathbf{r}-\delta\mathbf{r})w^*(\mathbf{r})w(\mathbf{r}-\delta\mathbf{r})w(\mathbf{r}),$$

where $\delta\mathbf{r}$ is defined as before. One finds that J_z is modified by the addition of $2(V_{\uparrow\uparrow} + V_{\downarrow\downarrow} - 2V_{\downarrow\uparrow})$. Depending on the signs and magnitudes of the three interactions, the off-site terms can add to or subtract from the two previously discussed corrections to J_z (Extended Data Fig. 1).

Determination of the Heisenberg parameters

We calibrate the lattice depth using amplitude modulation spectroscopy⁵⁵. We record the excitation spectrum of a Bose–Einstein condensate in a 1D lattice when the depth of the lattice is modulated by 3% providing the cloud-averaged lattice depth with a statistical uncertainty of 0.2%. Owing to an asymmetric excitation profile, we estimate a systematic error of 1%.

The lowest and second-lowest hyperfine states of ⁷Li realize the $|\downarrow\rangle$ and $|\uparrow\rangle$ states. We use our previous measurements of U_{\uparrow} and U_{\downarrow} (lattice-depth modulation) as well as measurements of $U_{\uparrow} - U_{\downarrow}$ and $U_{\uparrow} - U_{\downarrow}$ (interaction spectroscopy)³³ to determine the three scattering lengths $a_{\uparrow}, a_{\downarrow}$ and a_{\downarrow} (under inclusion of higher-band corrections) for several magnetic fields B . The determined anisotropies Δ are shown in Fig. 1b (points). Hyperbolic fits to $a_{\uparrow}(B), a_{\downarrow}(B)$ and $a_{\downarrow}(B)$ are used to interpolate the values for the anisotropy (solid line). Extended Data Fig. 1 shows $a_{\uparrow}, a_{\downarrow}$ and a_{\downarrow} , as well as J_{xy}, J_z and Δ with (and without) corrections. A recent detailed theoretical analysis⁵⁶ of the interaction spectroscopy data also provided precise scattering lengths across several Feshbach resonances. However, this analysis slightly disagreed with our lattice-depth modulation data in the range of magnetic fields studied here, and therefore we relied on the experimental data.

The Gaussian intensity profile of the lattice beams ($1/e^2$ radius of 125 μm) causes inhomogeneity of the lattice depth by up to 1.7% across a Mott insulator of 44 lattice sites in diameter. The 1.0% variation of U across the atom cloud can be neglected. The tunnelling coefficient \tilde{t} within the spin chains is defined by the lattice depth V_z along the chains. Although it is constant within each spin chain, it varies among the chains by up to 4.4%, which increases superexchange J_{xy} by up to 9.0%. The curvature of the transverse lattice beams (with $V_x, V_y = 35E_R$) causes harmonic confinement $\frac{1}{2}m\omega_{\text{trap}}^2 z^2 = \frac{1}{2}\kappa z^2$ along the chains with $\omega_{\text{trap}} = 2\pi \times 770$ Hz or curvature $\kappa = \hbar \times 116.6$ Hz a^{-2} , where \hbar is the Planck constant. The curvature leads to a varying energy offset δ between neighbouring lattice sites, which is largest at the ends $z = \pm 22a$ of the longest spin chains. It modifies the energy of the intermediate state in the superexchange process $U \rightarrow U \pm \delta$ (refs. ^{26,50}) and therefore increases the superexchange rate at the ends of the longest chains by 24% ($\Delta \approx 0$) and 11% ($\Delta \approx 1$), with an average value over all atoms of 4.2% ($\Delta \approx 0$) and 2.0% ($\Delta \approx 1$), respectively.

The lattice depth calibration and the experimental determination of the scattering length a_{\downarrow} lead to an uncertainty for the spin-exchange times \hbar/J_{xy} of about $\pm 10\%$. The accuracy of the determined anisotropies Δ is limited by the experimental determination of all scattering lengths $a_{\uparrow}, a_{\downarrow}, a_{\downarrow}$. The uncertainty of Δ is estimated to be about ± 0.1 .

In the experiment (see Fig. 1b), $\Delta \approx 0$ was realized by tuning the magnetic field to $B_0 = 882.63$ G. Here the measured Hubbard parameters result in $\Delta = -0.12$ including higher-order corrections (and $\Delta = -0.02$ without corrections). We find that the spin dynamics in this regime is only weakly dependent on Δ , so we refer to measurements here as $\Delta \approx 0$. $B'_0 = 842.95$ G is a second magnetic field value, which also realizes $\Delta \approx 0$ ($\Delta = -0.13$ including corrections and $\Delta = 0.01$ without corrections). We directly compare these two points B_0 and B'_0 in Extended Data Fig. 5, and observe quantitative agreement. Arbitrary anisotropies were realized by using the magnetic field region in between: $B'_0 < B < B_0$. In particular, for values $\Delta > 0$ ($\Delta < 0$) we used magnetic fields $B < 850$ G ($B > 850$ G). The isotropic point $\Delta \approx 1$ was realized at $B_1 = 847.30$ G (actually $\Delta = 1.01$ and corrections here are negligible).

In the following we give typical absolute values for Hubbard parameters at a lattice depth of $V_z = 11E_R$ and $V_x, V_y = 35E_R$. The recoil energy is $E_R/\hbar = 25.12$ kHz.

XX model. $\Delta \approx 0$ is realized by the scattering lengths $a_{\uparrow} = +307a_0, a_{\downarrow} = -50a_0$ and $a_{\downarrow} = -44a_0$, resulting in the following values for the on-site interactions $U_{\uparrow}/\hbar = +30.6$ kHz, $U_{\downarrow}/\hbar = -5.8$ kHz and $U_{\downarrow}/\hbar = -5.1$ kHz. The bare single-particle tunnelling coefficient is

given by $\tilde{t}^{(0)}/h = 380$ Hz, but interactions make tunnelling spin-dependent: $\tilde{t}_\uparrow/h = 480$ Hz, $\tilde{t}_\downarrow/h = 370$ Hz, and $\tilde{t}_{\downarrow\uparrow}/h = 370$ Hz. That results in the following Heisenberg parameters: $J_{xy}/h = 93.3$ Hz and $J_z/h = -10.9$ Hz.

XXX model. $\Delta \approx 1$ is realized by the scattering lengths $a_\uparrow = -107a_0$, $a_\downarrow = -71a_0$ and $a_{\downarrow\uparrow} = -53a_0$, resulting in $U_\uparrow/h = -12.7$ kHz, $U_\downarrow/h = -8.4$ kHz and $U_{\downarrow\uparrow}/h = -6.1$ kHz; and $\tilde{t}^{(0)}/h = 380$ Hz, $\tilde{t}_\uparrow/h = 350$ Hz, $\tilde{t}_\downarrow/h = 360$ Hz and $\tilde{t}_{\downarrow\uparrow}/h = 370$ Hz; and $J_{xy}/h = 62.6$ Hz and $J_z/h = 63.5$ Hz.

Superexchange coupling ($J_{xy}^\perp/h \approx 20$ mHz) between chains is negligible, owing to the deep transverse optical lattices ($V_x, V_y = 35E_R$) and is 3 to 4 orders of magnitude smaller than J_{xy}/h within the chains.

Experimental setup

In the experiment, we prepare 4.5×10^4 Li atoms in an optical lattice with spacing $a = 532$ nm in the Mott insulating regime with one atom per site⁵⁰. A Bose–Einstein condensate (with barely detectable thermal fraction $N_{\text{th}}/N \leq 0.05$) with all atoms in the $|\uparrow\rangle$ state is loaded into the optical lattice, with the scattering length set to strong repulsive interactions $a_\uparrow = +307a_0$. This suppresses doubly occupied sites⁵⁰, which we counted directly by interaction spectroscopy³³ to be $\leq 0.5\%$ of the total atom number. (Even a long spin chain of length $L = 44a$ has then only a probability $\leq 20\%$ to contain a doubly occupied site.) The hole fraction is estimated to be between 5% and 10% through comparison of spin dynamics with theory (Fig. 2a). The density degree of freedom is frozen out after loading into the deep optical lattice, and the on-site interactions U_\uparrow, U_\downarrow and $U_{\downarrow\uparrow}$ can then be varied freely without affecting the global atom distribution, as long as the atoms stay in the Mott insulating regime⁵⁰.

We then prepare a far-from-equilibrium initial spin state and probe the spin dynamics in one dimension. The lattice beams in the x and y directions are kept at a large constant depth of $V_x, V_y = 35E_R$ separating the atoms into an array of independent 1D chains, with a typical maximum length of $L_{\text{max}} = 44a$ (given by the diameter of the Mott insulator), and with an average length of $\langle L \rangle = 33a$ (Extended Data Fig. 10). The depth of $35E_R$ is sufficient to prevent superexchange coupling in the x and y directions ($\hbar/J_{xy}^\perp \approx 10$ s) on experimental timescales. Initially, the z -lattice depth is also $35E_R$. The magnetic field is then ramped to the value required for a desired anisotropy Δ . Using radio frequency pulses and a magnetic field gradient, a helical spin pattern is created where the spin component along the chain winds in the xz plane of the Bloch sphere with a wavevector $Q = 2\pi/\lambda$, where λ is the wavelength of the spin helix (see Fig. 1c and Methods section ‘Preparation of the spin helix’). For λ smaller than the system size, the total magnetization of this state is close to zero.

The power of the lattice beam in the z direction controls the superexchange rate within the chains. Time evolution is initiated by ramping down the z -lattice depth V_z to a value between $9E_R$ and $13E_R$. The ramp time is 0.5 ms, fast compared to superexchange \hbar/J_{xy} , but slow compared to tunnelling \hbar/\tilde{t} . The ensuing coherent dynamics along each chain is governed by a 1D Heisenberg XXZ model with anisotropy Δ , equation (1). This is a quantum quench to a far-from-equilibrium initial state. After a variable evolution time t the dynamics is frozen by rapidly increasing the lattice depth back to $35E_R$. The atoms are then imaged in the $|\uparrow\rangle$ state via state-selective polarization-rotation imaging (see below).

Preparation of the spin helix

A global $\pi/2$ pulse of 75 μs rotates the spin $|\uparrow\rangle_i$ on each site i into the xy plane of the Bloch sphere $|\varphi\rangle_i = [|\uparrow\rangle_i + |\downarrow\rangle_i]/\sqrt{2}$. An applied magnetic field gradient in the z direction causes spin precession at rates that depend linearly on position z_i of the spin thus creating a spin helix $|\varphi\rangle_i = [|\uparrow\rangle_i + e^{-iQz_i}|\downarrow\rangle_i]/\sqrt{2}$ where the spin winds in the xy plane⁷⁻⁹. The strength and duration of the gradient determine the wavevector $Q = 2\pi/\lambda$ where λ is the wavelength of the spin helix. After turning off the gradient, an additional $\pi/2$ pulse rotates the spin helix into a state where the spin winding occurs in the xz plane

$|\varphi\rangle_i = \cos(Qz_i/2)|\downarrow\rangle_i - \sin(Qz_i/2)|\uparrow\rangle_i$, so that the full many-body xz spin-helix state is $|\psi(Q)\rangle = \prod_i |\varphi\rangle_i$. In practice, the phase of the winding, θ , varies from realization to realization, which amounts to replacing $Qz_i \mapsto Qz_i + \theta$. This is caused by small magnetic bias field drifts on the 10^{-5} level. The range of λ used in the experiment was limited on the short side by optical resolution to $\lambda \geq 5.6a$ and on the long side by the length of the chains $L_{\text{max}} = 44a$.

When turning off the magnetic field gradient, special care was taken to cancel any residual gradients to better than $|B'| \leq 0.4$ mG cm^{-1} . The differential magnetic moment is typically $\Delta\mu/h = (\mu_\uparrow - \mu_\downarrow)/h \approx 30$ kHz G^{-1} (it varies by approximately 10% depending on the bias field B). This translates to a maximum energy difference of $\Delta\mu B L_{\text{max}}/h = 0.3$ Hz across the chain length, completely negligible compared to the spin-exchange coupling J_{xy}/h , which is 2 to 3 orders of magnitude larger.

Imaging

The optical density of the atomic ensemble is too high (>14) to allow for in situ observation of the modulation of $\langle S^z \rangle$ via absorption imaging. Instead, we use dispersive imaging, which uses the phase accumulated by the transmitted light to form an image of the atomic density distribution. When light at frequency ω_L is detuned from the atomic resonance ω_0 by many natural linewidths Γ , it picks up an approximate phase $\theta \approx -2\Delta\omega/\Gamma \times \text{OD}(y, x, \Delta\omega)$, where OD is the optical density at detuning $\Delta\omega = \omega_L - \omega_0$, while absorption is suppressed by a sufficiently large detuning $\Delta\omega$. To form an image, the phase-shifted light must be interfered with a reference beam. In this work, we make use of the fact that the optical transition we use for imaging is driven only by a single polarization component; after passing through the atoms, the shifted and unshifted components are combined on a polarizer. A judicious choice of input and output polarizers yields an interference signal I on the camera^{57,58} that is $I = I_0(1 - \sin\theta)/2$.

The optical resolution of our imaging system (with a numerical aperture of $\text{NA} \approx 0.2$) was determined to have a cut-off at modulation wavelength $\lambda \approx 3.0 \mu\text{m} = 5.6a$ (330 line pairs per mm). The reduction of the modulation transfer function $\text{MTF}(Q)$ near the cut-off reduces the observed contrast $C(t) = \text{MTF}(Q)c(t)$ compared to the real contrast $c(t)$. This does not affect the decay times τ . Assuming that the experimental preparation sequence for the initial spin-helix state achieves full contrast $c(0) = 1$ for any wavevector Q (based on careful pulse calibration and characterization), we can use $C(0)$ as a direct measurement of $\text{MTF}(Q)$ and determine the real contrast as $c(t) = C(t)/C(0)$.

Constant background contrast

For long evolution times t , the contrast $c(t)$ does not fully decay, but reaches a background value c_0 , for example $c_0 = 0.08(1)$ in Fig. 2a. The numerical simulations, however, show a decay to zero. Therefore we add here the fit value for c_0 to the simulations for better comparison with experimental results. The experimental offset is caused by the inhomogeneous density of the atom cloud: only 90% of the atoms are in the Mott insulator state, which realizes an array of 1D spin chains. A small fraction of atoms are in dilute spatial wings, separated by holes that are immobile, owing to the gradient of the trapping potential (which suppresses first-order tunnelling, as shown in our previous work)⁵⁰. These atoms preserve an imprinted spin-modulation pattern for long times. We have checked this mechanism by increasing the amount of thermal atoms and clearly observe an increase of the background c_0 (Extended Data Fig. 4). Furthermore, a position-sensitive measurement of the contrast confirms that the main contribution is indeed from atoms in the spatial wings (Extended Data Fig. 4f–g). In agreement with this model, numerical simulations always show a decay to zero for long spin chains (see Extended Data Figs. 6, 7, 9, 10). Experiments throughout this Article were performed with the lowest thermal fraction $N_{\text{th}}/N \leq 0.05$, where the contrast decays (almost) uniformly across the whole atom cloud, and offsets are small, so that it was not necessary to restrict the fits to the central part of the cloud (see Extended Data Fig. 2).

Article

Time-reversal invariance of spin dynamics

For an xz spin-helix initial state and time evolution via the XXZ Hamiltonian, the contrast is time-reversal symmetric: $c(t) = c(-t)$, which follows because the state, Hamiltonian and observable (the local magnetization S_i^z) can be all expressed as real. This also implies invariance against the overall sign of the Hamiltonian $H \mapsto -H$. The same argument holds for the system with holes evolving under the bosonic \tilde{t} - J model. The initial dynamics of the contrast (in the ideal scenario) in both cases is therefore quadratic, $c(t) = 1 + \Gamma^2 t^2 + \dots$, with

$$\Gamma^2 = -\frac{1}{\hbar^2} \frac{2a}{L} \sum_i \cos(Qz_i + \theta) \langle \psi(Q) | [H, [H, S_i^z]] | \psi(Q) \rangle.$$

Therefore the timescale of the initial quadratic decay $|\Gamma|^{-1}$ is the superexchange timescale \hbar/J_{xy} (XXZ model) or the tunnelling timescale \hbar/\tilde{t} (\tilde{t} - J model). The fact that, experimentally, we do not observe an initial quadratic behaviour indicates either (i) the presence of holes, but that we are not resolving the fast timescale \hbar/\tilde{t} ; or (ii) that the initial state is not time-reversal invariant (that is, cannot be expressed as real, in the same basis that the Hamiltonian is written in). The latter could arise from pulse imperfections, or the fact that the ramp-down of the optical lattice takes place over a finite duration of time, leading to deviations from the ideal initial state. Nevertheless, we expect that the overall behaviour of the decay of the contrast—for example, the scaling behaviour of dynamics with wavevector Q —is not strongly affected by (i) or (ii).

Power-law scalings in the continuum limit

In the experiments we measured the exponents α of the power laws $\tau \propto Q^{-\alpha}$ in the short-wavelength regime $Q = 2\pi/(30a)$ to $2\pi/(6a)$ (Fig. 3). Now we investigate how the exponents depend on the range of wavevectors Q , in particular in the continuum limit $Q \rightarrow 0$ (where the wavelength λ of the modulation becomes large compared to the lattice spacing a and the discreteness of the underlying lattice is no longer relevant).

The short-time ($t \ll \hbar/J_{xy}$) Taylor expansion of the contrast $c(t) = 1 + \Gamma^2 t^2 + \dots$ enables us to define a ‘time constant’ $\tau = |\Gamma|^{-1}$, which we can compute analytically even in the thermodynamic limit $L/a \rightarrow \infty$. This is because the object $\langle \psi(Q) | [H, [H, S_i^z]] | \psi(Q) \rangle$ is a strictly local quantity as the spin-helix state $|\psi(Q)\rangle$ is a product state and the commutator of the Hamiltonian with the local term S_i^z only produces terms near site i . Evaluating (with $\theta = 0$ for simplicity), we obtain

$$\Gamma^2 = \frac{J_{xy}}{\hbar^2} \frac{1}{16} [7 - \Delta - 8 \cos(Qa) + 2 \cos(2Qa) + (\Delta - 1) \cos(3Qa)].$$

The limiting behaviour of τ as $Q \rightarrow 0$ is therefore $\tau \approx (Q^2 a^2/4)^{-1} \hbar/J_{xy}$ for $\Delta = 1$ and $\tau \approx [(3\sqrt{2}/8)Qa\sqrt{1-\Delta}]^{-1} \hbar/J_{xy}$ for $\Delta < 1$.

This implies a sharp crossover from ballistic scaling to diffusive scaling as Δ approaches 1 from below in the regime of small enough wavevectors, as shown in Extended Data Fig. 8d, e. In the same figure, we show the exponents determined for a range of finite wavevectors ($Q = 2\pi/(20a)$ to $2\pi/(6a)$) as used in experiments and numerics, and find a smooth crossover from a superdiffusive regime to diffusive regime, in agreement with numerical simulations in Fig. 3.

Although this short-time analysis for $t \ll \hbar/J_{xy}$ predicts the scalings seen in the numerical simulations, it is not clear how much of this analysis is applicable to the intermediate to long times t at which the experiments were performed. It also remains an open question as to why numerics predict a superballistic exponent $\alpha < 1$ for the XX model ($\Delta = 0$), but the experiment measures a ballistic exponent $\alpha \approx 1$. The discrepancy is possibly caused by the presence of holes, as suggested by the \tilde{t} - J model simulation (Fig. 3c).

Numerical simulations

In the numerical simulations we consider: (i) a spin-helix quench under XXZ Hamiltonian (equation (1)) dynamics, and (ii) a spin helix with

5% to 10% hole probability evolving under the bosonic \tilde{t} - J model (that is, assuming no doubly occupied sites), given by

$$H = \sum_{\langle ij \rangle} [J_{xy} (S_i^x S_j^x + S_i^y S_j^y) + J_z S_i^z S_j^z] + H_d,$$

$$H_d = - \sum_{\sigma, \langle ij \rangle} \tilde{t} a_{\sigma i}^\dagger a_{\sigma j} - \sum_{\sigma, \langle ijk \rangle} \left[\frac{\tilde{t}^2}{U_{\tilde{n}}} a_{\sigma i}^\dagger n_{\sigma j} a_{\sigma k} + \frac{\tilde{t}^2}{U_{\tilde{n}}} a_{\sigma i}^\dagger S_j^\sigma a_{\sigma k} + \frac{2\tilde{t}^2}{U_{\sigma\sigma}} a_{\sigma i}^\dagger n_{\sigma j} a_{\sigma k} \right] + \text{h.c.},$$

where spin $\sigma = \uparrow, \downarrow$. Here $a_{\sigma i}$ and $a_{\sigma i}^\dagger$ are bosonic lowering and raising operators at site i , respectively, $S_i^z \equiv S_i^z$ is defined as $a_{\uparrow i}^\dagger a_{\downarrow i}$ and $S_i^y \equiv S_i^y$ is defined as $a_{\downarrow i} a_{\uparrow i}$. We use parameters from experiments and focus on a lattice depth of $11E_R$, in which case we have $U_{\uparrow}/U_{\downarrow} = 1.206, 1.406, 1.401, 1.398, 1.397$ and 1.392 , $U_{\tilde{n}}/U_{\tilde{t}} = -0.188, 0.264, 0.459, 0.575, 0.659$ and 0.862 , and $U_{\tilde{n}}/\tilde{t} = -17.94, -24.32, -24.17, -24.08, -24.05$ and -23.94 for anisotropies $\Delta = 0.020, 0.670, 0.860, 0.973, 1.055$ and 1.256 , respectively. In the absence of holes, the action of the term H_d vanishes, and the Hamiltonian reduces to the XXZ Hamiltonian.

In both cases we use the real-time time-evolving block decimation (TEBD) method with matrix product states (MPS) on a spin chain with open boundary conditions. In case (i): local Hilbert space dimension = 2, length $L = 40a$ and bond dimensions up to 800; case (ii): local Hilbert space dimension = 3, $L = 40a$ for $\Delta = 0$, or $L = 20a$ for all other Δ . Simulations are cut-off in simulated time, owing to the rapid increase in entanglement of the state, requiring ever-increasing computational times. For the special case $\Delta = 0$, without holes, we alternatively use free fermionic methods, considerably speeding up the calculations. For technical reasons, instead of simulating the full distribution of holes we simply average over the situations in which there are either exactly one or two (or four) holes in the chain. For $L = 20a$ ($40a$), a single hole corresponds to an average of 5% (2.5%) holes.

To obtain the contrast, we determine the local magnetization $\langle S_i^z(t) \rangle = [\langle n_{i\uparrow}(t) \rangle - \langle n_{i\downarrow}(t) \rangle]/2$ and determine the Fourier component at wavevector Q via $c(t) = \frac{4a}{L} \sum_i \langle S_i^z(t) \rangle \cos(Qz_i + \theta)$, assuming that the initial spin helix has wavevector Q with a given phase θ (see Methods section ‘Creation of the spin helix’); we then compare this to the experimental contrast. However, as noted in Methods section ‘Time-reversal invariance of spin dynamics’, the numerically simulated contrast always has an initial quadratic decay, unlike that seen in the experiments. We therefore determine the decay timescales and its power-law scaling with Q using one of the following methods. For positive anisotropies $\Delta \geq 0$, we define the decay time constant as the time it takes for the contrast $c(t)$ to decay from 1 to 0.6, divided by $-\ln(0.6)$ to convert to a ‘1/e’ time (see Extended Data Fig. 6). For negative anisotropies $\Delta < 0$, for regime I we take the time to decay from 1 to 0.9, multiplied by 10 to extrapolate to zero, whereas for regime II we fitted a simple exponential-decay profile to obtain the decay timescales once the curves start ‘peeling off’ when plotted with time units rescaled by λ (see Fig. 4c and Extended Data Fig. 7). The resulting power-law scalings (Extended Data Fig. 8) and resulting exponents (Fig. 3c) are in reasonable agreement with the experimental results.

Finite-size effects

Numerical simulations can study the effect of different chain lengths L and initial phases θ of the spin helix on the dynamics. This is relevant because in the experiment, the atoms are distributed uniformly over a sphere with a typical diameter of $L_{\max} = 44a$ in three dimensions, leading to an ensemble of 1D chains of varying lengths. The experimentally measured contrast $c(t)$ is an average over all chain lengths with a probability distribution shown in Extended Data Fig. 10. Furthermore, owing to drifts of the applied magnetic field, the initial phase θ of the spin-helix state varies from shot to shot. Here we study numerically both effects.

We concentrate on the XX model ($\Delta = 0$) without holes. Extended Data Fig. 9 shows that the strong dependence of the contrast $c(t)$ on the initial phase θ is due to reflection of magnetization off the boundaries of the chain. This suggests that averaging over various chain lengths or averaging over initial phases should give similar results, which is confirmed in Extended Data Fig. 10. It is even sufficient to average over only two phases, $\theta = 0$ and $\pi/2$, to achieve insensitivity to initial and boundary conditions. The distribution of chains, and the simulation of a magnetization profile averaged over this distribution of chains, are illustrated in Extended Data Fig. 10b–d.

The conclusion is that the experiment is naturally performing an average over different phases and different chain lengths, washing out the sensitive dependence of the spin dynamics on initial conditions. For comparison with simulations, it is sufficient to use a system with a fixed chain length $L = 40a$, and average over only the two phases $\theta = 0$ and $\pi/2$.

Data availability

The data that support the findings of this study are available from the corresponding author upon reasonable request.

51. Greiner, M. *Ultracold Quantum Gases in Three-dimensional Optical Lattice Potentials*. PhD thesis, Ludwig-Maximilians-Universität München (2003).
52. Łącki, M., Delande, D. & Zakrzewski, J. Dynamics of cold bosons in optical lattices: effects of higher Bloch bands. *New J. Phys.* **15**, 013062 (2013).
53. Will, S. et al. Time-resolved observation of coherent multi-body interactions in quantum phase revivals. *Nature* **465**, 197–201 (2010).
54. Lühmann, D.-S., Jürgensen, O. & Sengstock, K. Multi-orbital and density-induced tunneling of bosons in optical lattices. *New J. Phys.* **14**, 033021 (2012).
55. Stöferle, T., Moritz, H., Schori, C., Köhl, M. & Esslinger, T. Transition from a strongly interacting 1D superfluid to a Mott insulator. *Phys. Rev. Lett.* **92**, 130403 (2004).
56. Secker, T., Amato-Grill, J., Ketterle, W. & Kokkelmans, S. High-precision analysis of Feshbach resonances in a Mott insulator. *Phys. Rev. A* **101**, 042703 (2020).
57. Bradley, C. C., Sackett, C. A. & Hulet, R. G. Bose–Einstein condensation of lithium: observation of limited condensate number. *Phys. Rev. Lett.* **78**, 985–989 (1997).
58. Ketterle, W., Durfee, D. S. & Stamper-Kurn, D. M. Making, probing and understanding Bose–Einstein condensates. In *Bose–Einstein Condensation in Atomic Gases* (eds Inguscio, M. et al.) 67–176 (IOS Press, 1999).

Acknowledgements We thank M. D. Lukin, N. Y. Yao and M. Knap for discussions, Y. K. Lee for experimental assistance, as well as C. M. E. Paus for sharing computing resources, and J. de Hond for comments on the manuscript. We acknowledge support from the NSF through the Center for Ultracold Atoms and grant number 1506369, NSF (grant number OAC-193471), ARO-MURI Non-Equilibrium Many-Body Dynamics (grant number W911NF-14-1-0003), AFOSR-MURI Photonic Quantum Matter (grant number FA9550-16-1-0323), AFOSR-MURI Quantum Phases of Matter (grant number FA9550-14-1-0035), ONR (grant number N00014-17-1-2253), ARO (grant number W911NF-20-1-0163), the Vannevar Bush Faculty Fellowship, and the Gordon and Betty Moore Foundation EPIQS Initiative (grant number GBMF4306).

Author contributions P.N.J., J.A.-G., I.D. and W.K. conceived the experiment. P.N.J., J.A.-G. and I.D. developed the experimental setup and took the data. P.N.J. led the data analysis. W.W.H. and E.D. developed the theoretical analysis. W.W.H. performed the numerical simulations. All authors discussed the results and contributed to the writing of the manuscript.

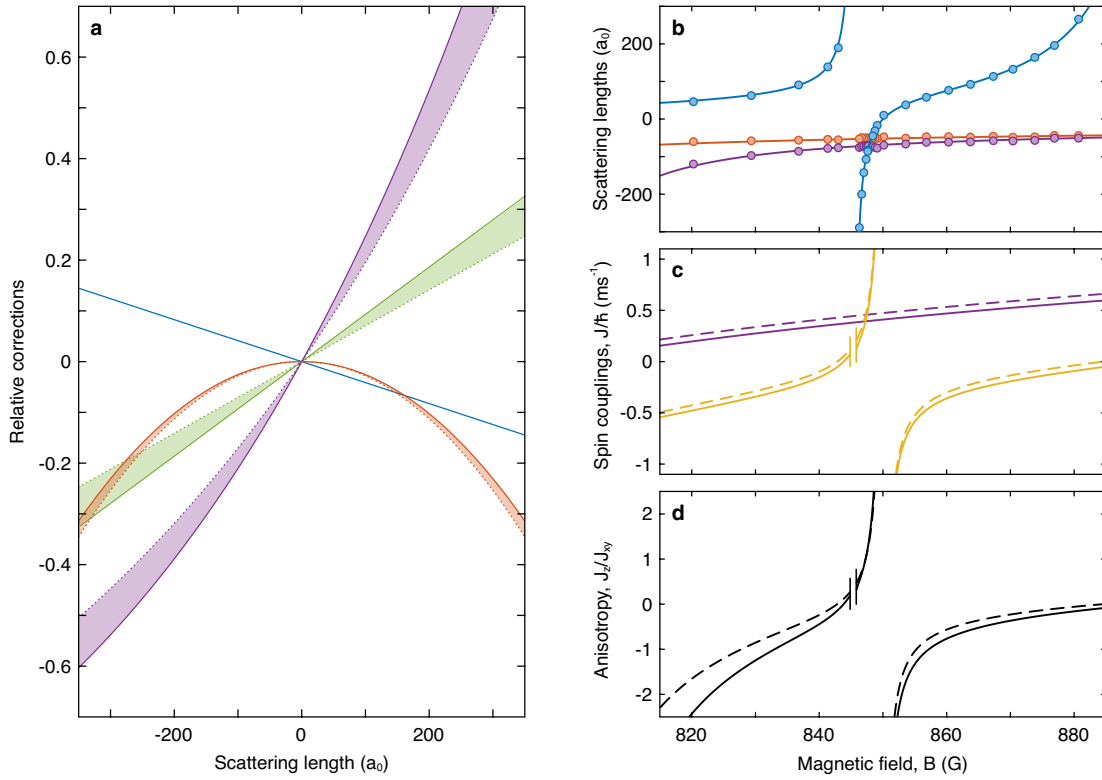
Competing interests The authors declare no competing interests.

Additional information

Correspondence and requests for materials should be addressed to P.N.J.

Peer review information *Nature* thanks Jean-Philippe Brantut, Tomaž Prosen and the other, anonymous, reviewer(s) for their contribution to the peer review of this work.

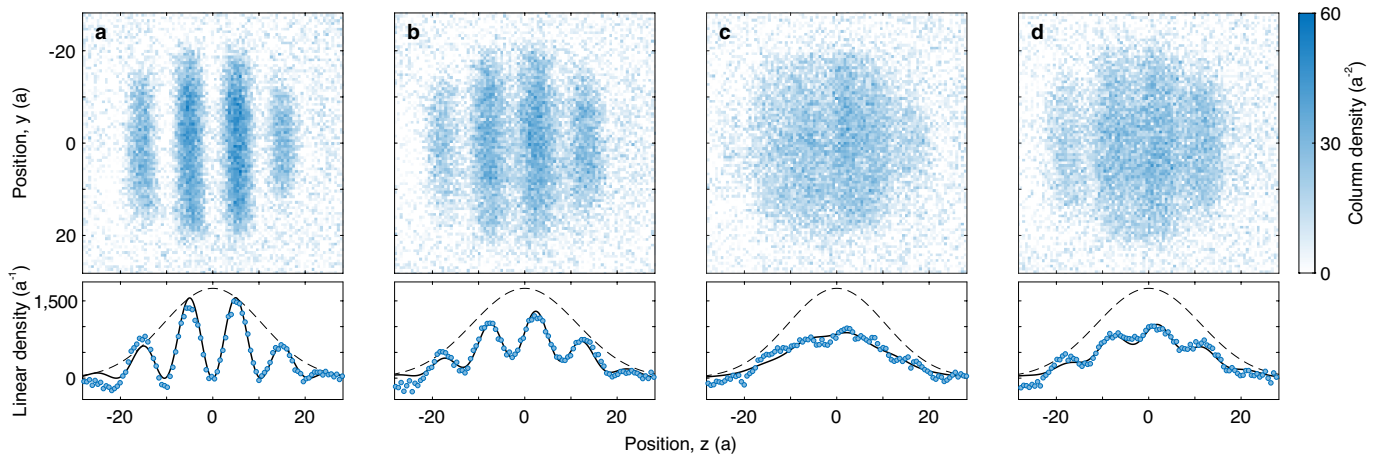
Reprints and permissions information is available at <http://www.nature.com/reprints>.



Extended Data Fig. 1 | Determination of the Heisenberg parameters.

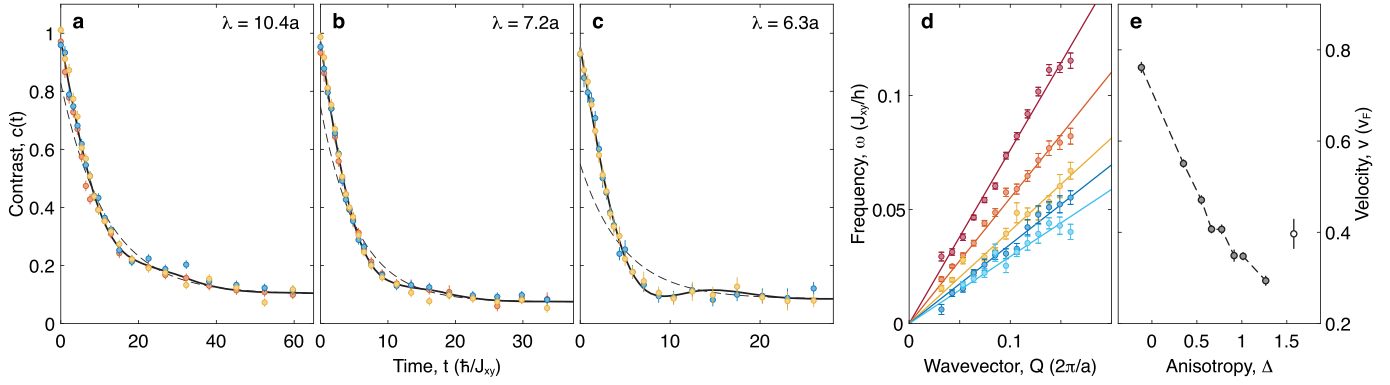
a, Corrections for tunnelling $(\tilde{t} - \tilde{t}^{(0)})/\tilde{t}^{(0)}$ (green), on-site interactions $(U - U^{(0)})/U^{(0)}$ (blue), superexchange $(J - J^{(0)})/J^{(0)}$ (purple) and off-site interactions $-2V/J^{(0)}$ (orange), where $\tilde{t}^{(0)}$, $U^{(0)}$ and $J^{(0)} = 4(\tilde{t}^{(0)})^2/U^{(0)}$ are the uncorrected values and \tilde{t} , U and $J = 4\tilde{t}^2/U$ include corrections, at a lattice depth of $13E_R$ (solid line) and $9E_R$ (dotted line). **b**, As a function of magnetic field B we show the scattering lengths a_{\parallel} (blue), a_{\perp} (purple) and $a_{\parallel\perp}$ (orange) measured in our

previous work (points)³³. Here a_0 is the Bohr radius. **c, d**, We interpolate the data in **b** using hyperbolic fits (solid lines) and calculate values for the transverse coupling constant J_{xy} (purple), the longitudinal coupling constant J_z (yellow) and the anisotropy $\Delta = J_z/J_{xy}$ (black), without corrections (dashed line) and including corrections (solid line) for a lattice depth of $11E_R$. The excluded region ($|a_{\parallel}| > 700a_0$) is around a Feshbach resonance in the $|\uparrow\rangle$ state near 845.4 G.



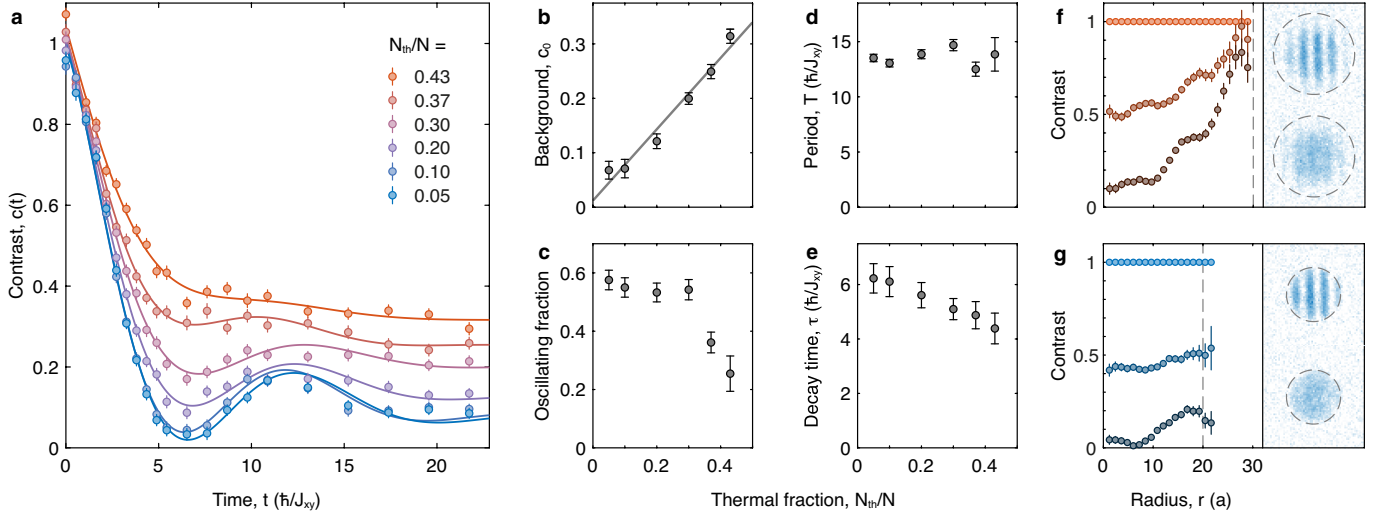
Extended Data Fig. 2 | Contrast measurement. a–d, The distribution of atoms in the $|\uparrow\rangle$ state. Every pixel is a local measurement of the column density (number of atoms per unit area). The y and z axes are displayed in units of the lattice spacing $a = 0.532 \mu\text{m}$. The images are projected (integrated) along the y direction from $y = -30a$ to $+30a$ to obtain the linear density (number of atoms per unit length). The resulting 1D distributions are fitted with $f(z) = g(z)[1 + C \cos(Qz + \theta)]/2$ (solid line), where $g(z)$ is a Gaussian envelope

(dashed line), between $z = \pm 54a$. The data in **a–d** were measured at different evolution times $t = 0$ (**a**), $2.3\hbar/J_{xy}$ (**b**), $6.3\hbar/J_{xy}$ (**c**) and $12.0\hbar/J_{xy}$ (**d**), for anisotropy $\Delta \approx 0$ and wavelength $\lambda = 10.4a$. The obtained contrast $C(t)$ is shown in Fig. 2a. In general, we also normalize by the initial contrast $C(0)$ to correct for finite optical imaging resolution. This is important for shorter wavelengths λ close to the optical resolution of $3 \mu\text{m}$, where the measured contrast $C(t)$ is reduced compared to the real contrast $c(t) = C(t)/C(0)$.



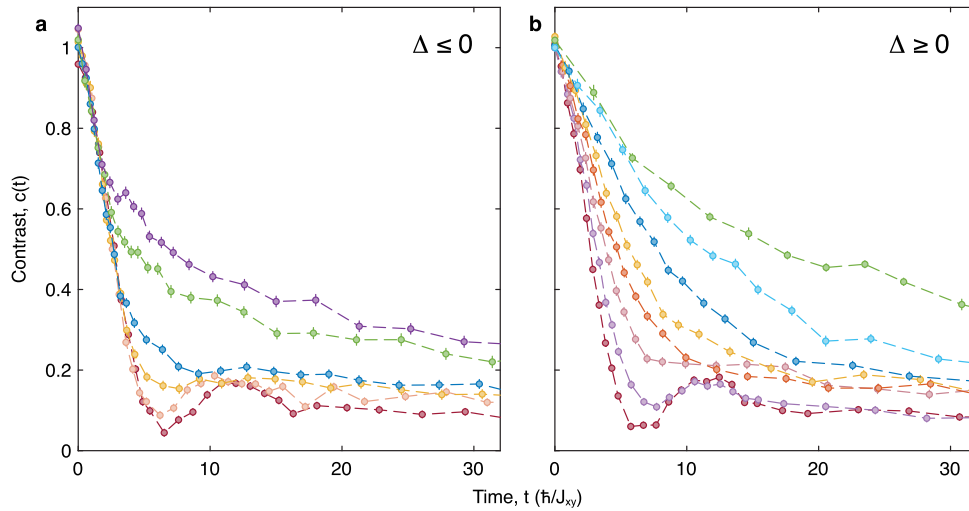
Extended Data Fig. 3 | Dispersion relations. For all positive anisotropies $\Delta \geq 0$, the time evolution of the contrast $c(t)$ shows a damped oscillatory component, in addition to the overall exponential decay. For larger Δ , the oscillations become smaller. **a–c**, Decay and weak oscillation at the isotropic point $\Delta \approx 1$ measured for different wavelengths λ , at three different lattice depths $9E_R$ (orange), $11E_R$ (blue) and $13E_R$ (yellow). Solid lines are fits $c(t) = [a_0 + b_0 \cos(\omega t)]e^{-t/\tau} + c_0$ and dashed lines show the overall decay $a_0 e^{-t/\tau} + c_0$, around which the oscillations take place. The oscillations become more pronounced for short wavelengths λ , because the decay time ($\tau \propto \lambda^2$) decreases with smaller wavelength more strongly than the oscillation period ($T \propto \lambda$). **d**, The oscillation frequencies follow linear dispersion relations $\omega(Q) = vQ$ shown for $\Delta = -0.12$ (red), 0.35 (orange), 0.78 (yellow), 1.01 (blue) and 1.27 (light blue). **e**, The obtained velocities v decrease with increasing

anisotropy Δ . For $\Delta = 1.58$ (open symbol), oscillations are small and the measurement was limited to large values of Q , which precluded recording a full dispersion relation. We note that although the oscillations are difficult to discern by eye (for example, in **a**), especially for large anisotropies Δ and small wavevectors Q , the fitted oscillation frequencies ω all fall very well on linear dispersion relations, which demonstrates that those barely visible oscillations are real. The linear scaling $\omega(Q) = vQ$ persists even in the superdiffusive, diffusive and subdiffusive regimes, where the power-law scaling of the decay time constant $\tau \propto Q^{-\alpha}$ is strongly nonlinear. This small ballistic (oscillatory) component may be related to our initial condition of a spin helix, which in the mapping to lattice fermions is a 100% density modulation, which reduces scattering at early times.



Extended Data Fig. 4 | Effect of finite hole concentration. By varying the thermal fraction N_{th}/N of the Bose–Einstein condensate before it is loaded into the optical lattice, we vary the energy and entropy of the atoms in the spin chain, and therefore the concentration of holes. (For our conditions, doubly occupied sites have higher energies than holes). Measurements are shown here for $\Delta \approx 0$ and $\lambda = 10.4a$, at a lattice depth of $11E_R$. **a**, Decay curves $c(t)$ for varying hole concentrations ranging from low (blue) to high (orange) thermal fraction. Solid lines are fits $c(t) = [a_0 + b_0 \cos(\omega t)]e^{-t/\tau} + c_0$. **b**, The background contrast c_0 increases monotonously with thermal fraction N_{th}/N . A linear fit (solid line) extrapolates to $c_0 = 0.01(2)$, consistent with zero, for $N_{th}/N = 0$. This suggests that all of the background contrast is due to hole excitations. **c**, Higher hole concentrations suppress the oscillating fraction $b_0/(a_0 + b_0)$. **d**, Holes do not affect the oscillation period $T = 2\pi/\omega$. **e**, Holes decrease the decay time τ , albeit slightly. **b–e** show that almost all of our measurements are not sensitive to a small thermal fraction, which is usually $N_{th}/N \leq 0.05$ throughout this work. The behaviour shown in **c** and **e** is most probably caused by mobile holes in the central part of the Mott insulator. Indeed, numerical simulations of the \tilde{t} - j model reproduce such effects (Fig. 2a). Note though that for the isotropic

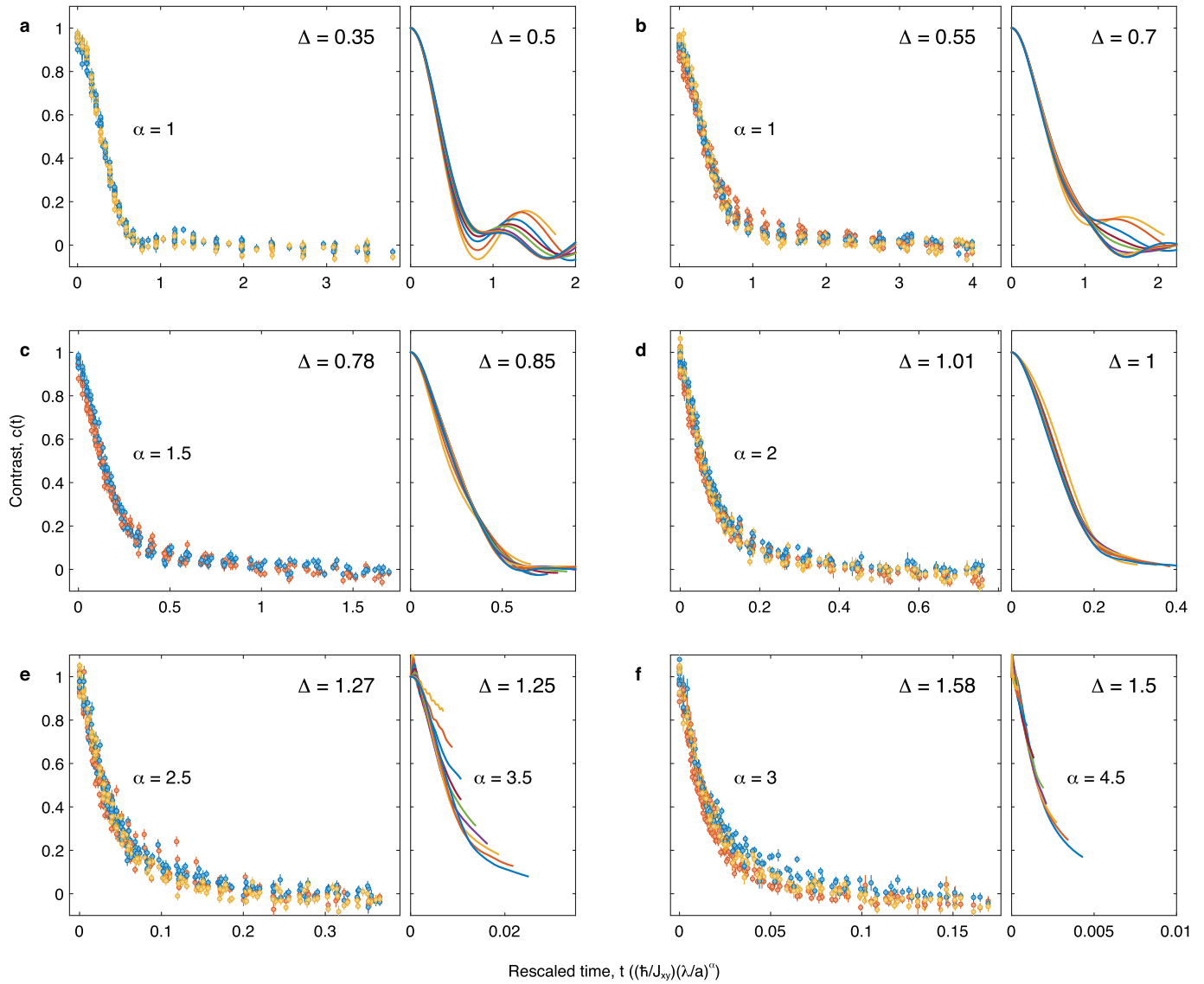
case $\Delta \approx 1$, a previous work⁷ found a -50% change in decay time when the hole concentration changed from 0 to 5%. Our numerical simulations (Extended Data Fig. 8b) do not show such strong sensitivity (for any anisotropy, even at $\Delta = 1$), possibly owing to asymmetry in the on-site interactions ($U_{ii} \neq U_{ij} \neq U_{ji}$) in our system. On the other hand, a finite background contrast (**b**) is probably caused by immobile holes located in the outer parts of the atom distribution where first-order tunnelling is suppressed by the gradient of the (harmonic) trapping potential⁵⁰. Immobile holes disrupt spin transport, and so we expect that the imprinted spin modulation in these regions will not (or only very slowly) decay. **f, g**, The region with immobile holes is visible as a shell of low atomic density surrounding the Mott insulator in the in situ images for large hole concentration (**f**) and is absent for low hole concentration (**g**). The three curves in both **f** and **g** show the local contrast as a function of distance r from the centre of the atom cloud for the evolution times $t = 0$ (top), $2.7\hbar/J_{xy}$ (middle) and $21.7\hbar/J_{xy}$ (bottom). The two in situ images in both **f** and **g** are for $t = 0$ (top) and $21.7\hbar/J_{xy}$ (bottom). The dashed lines indicate contours of constant radius, $r = 30a$ (**f**) and $r = 20a$ (**g**).



Extended Data Fig. 5 | Decay behaviour as a function of anisotropy.

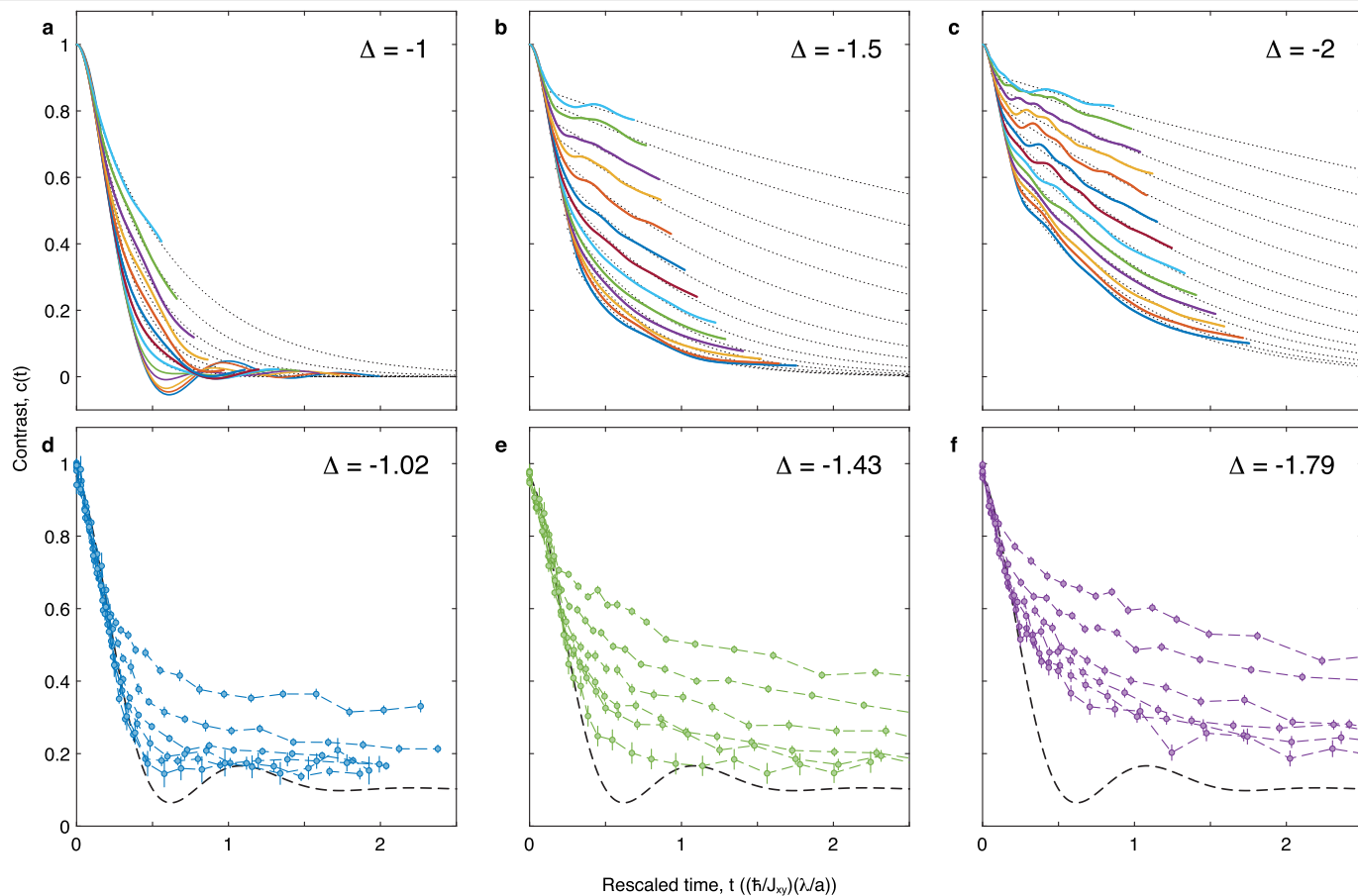
a, b, Decay behaviour ranging from negative (**a**) to positive (**b**) anisotropy, for a fixed wavelength $\lambda = 10.4a$. Using $\Delta \approx 0$ as a reference point, we show how the temporal profile of the decay curve $c(t)$ changes when we introduce positive or negative interactions. Every data point is an average of two measurements at lattice depths $11E_R$ and $13E_R$. In **a**, from bottom to top: $\Delta = -0.12$ (red), -0.59 (pink), -0.81 (yellow), -1.02 (blue), -1.43 (green) and -1.79 (purple). In **b**, from bottom to top: $\Delta = -0.13$ (red), 0.08 (purple), 0.35 (pink), 0.55 (orange), 0.78 (yellow), 1.01 (blue), 1.27 (light blue) and 1.58 (green). Regardless of sign,

for increasing $|\Delta|$ the decay always slows down and the revivals damp more quickly. However, there is a big difference in how this slowdown happens: for increasing positive interactions $\Delta > 0$, the initial rate of decay decreases continuously (**b**); by contrast, for all negative interactions $\Delta < 0$, the initial rate of decay stays constant (and is ballistic), coinciding with the $\Delta \approx 0$ case (**a**). It is only after a critical time t_0 that the decay suddenly starts slowing down (and becomes diffusive) for times $t > t_0$. This critical time t_0 decreases with increasing negative interaction strength $|\Delta|$.



Extended Data Fig. 6 | Collapse of decay curves for positive anisotropies. All decay curves $c(t)$ for wavelengths $\lambda = 15.7a, 13.4a, 11.7a, 10.4a, 9.4a, 8.5a, 7.8a, 7.2a$ and $6.7a$ collapse very well into a single curve for all evolution times t , when time units are rescaled by λ^α , where the exponent α is a function of anisotropy Δ , both for experiment (points) and theory (solid lines). Experimental points were measured for lattice depths $9E_R$ (red), $11E_R$ (blue) and $13E_R$ (yellow). **a, b**, Ballistic regime ($\alpha=1$). **c**, Superdiffusion ($\alpha=1.5$). **d**, Diffusion ($\alpha=2$). **e, f**, Subdiffusion ($\alpha=2.5, 3$ for experiment and $\alpha=3.5, 4.5$ for numerical simulations; in

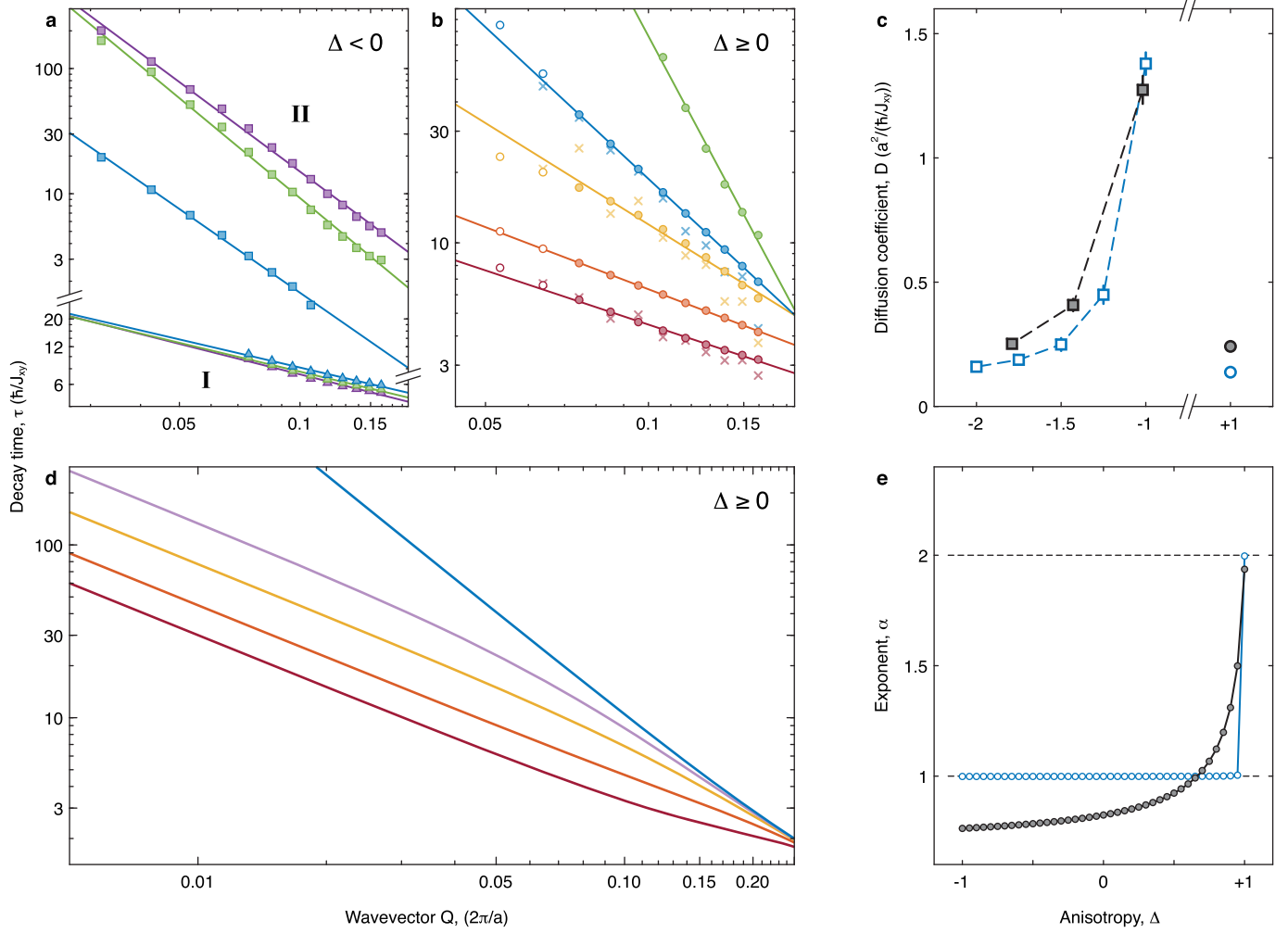
f, experiments covered a reduced range $\lambda \leq 10.4a$). For all anisotropies $\Delta \geq 0$ (**a-f**) the experimentally measured oscillation frequencies ω follow linear dispersion relations (Extended Data Fig. 3) and have a scaling behaviour different from the decay rates. However, such oscillations are small outside the ballistic regime $\alpha \approx 1$, and therefore only lead to a small deviation from the collapse behaviour. Note also the different timescales in experiments and simulations for $\Delta > 1$.



Extended Data Fig. 7 | Collapse at short times for negative anisotropies. All decay curves $c(t)$ for different wavelengths λ collapse into a single curve at early times, when time units are rescaled by λ (indicating ballistic behaviour). For later times the decay is diffusive with different scaling. **a–c**, Theory (from top to bottom: $\lambda = 31.3a, 23.5a, 18.8a, 15.7a, 13.4a, 11.7a, 10.4a, 9.4a, 8.5a, 7.8a, 7.2a,$

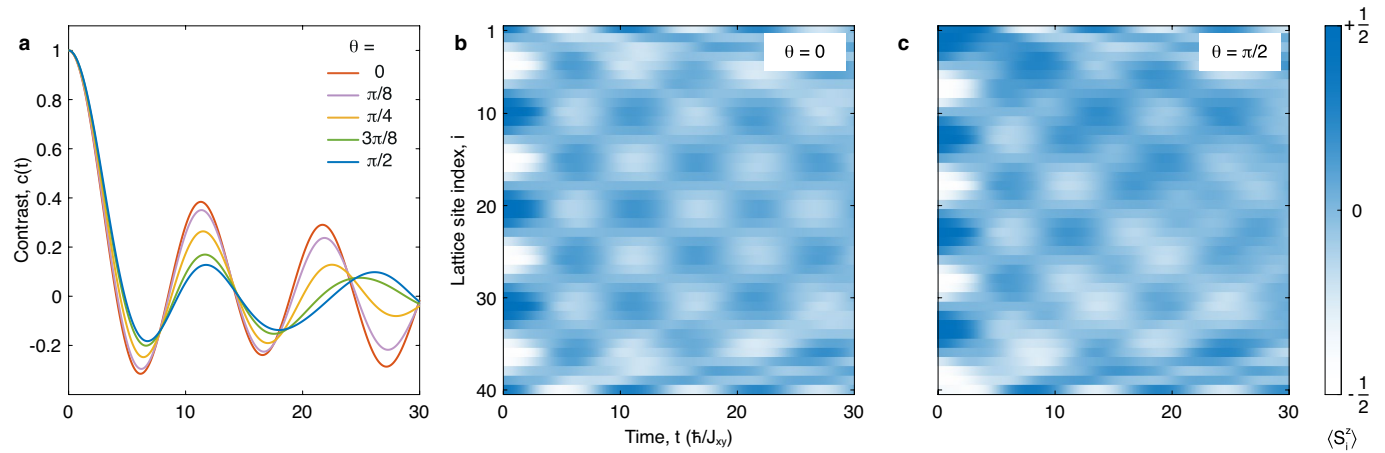
$6.7a$ and $6.3a$). The dotted lines are exponential fits $e^{-t/\tau_{II}}$ to the diffusive regime and the time constants τ_{II} are shown in Extended Data Fig. 8a.

d–f, Experiment (from top to bottom: $\lambda = 18.8a, 13.4a, 10.4a, 8.5a, 7.2a$ and $6.3a$). Every data point is an average of two measurements at lattice depths $11E_R$ and $13E_R$. The black dashed line indicates the ballistic case $\Delta \approx 0$ (see Fig. 2c).



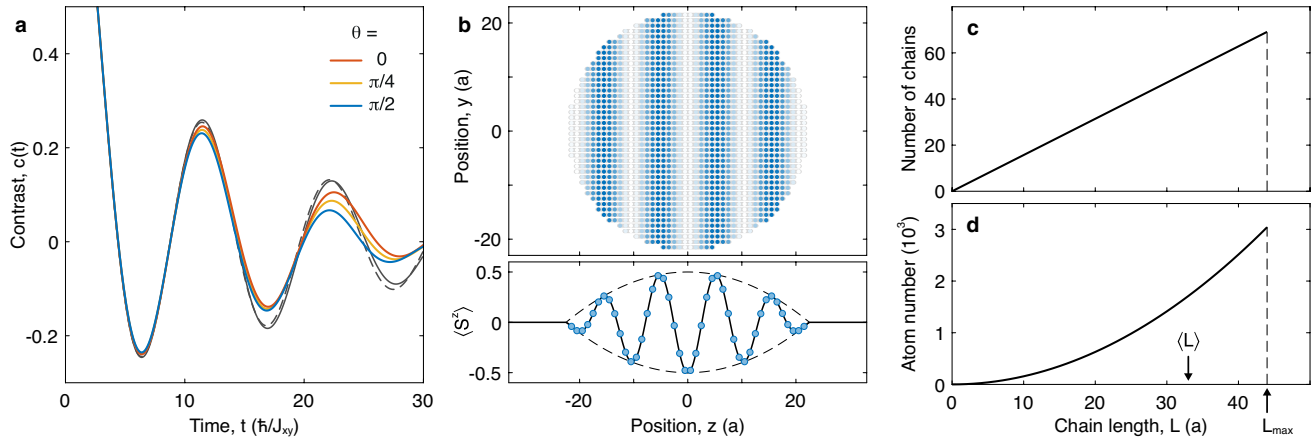
Extended Data Fig. 8 | Power-law scalings (theory) and diffusion coefficients. **a, b,** Decay time constants τ for different anisotropies Δ ranging from negative (**a**) to positive (**b**). Numerical results are shown in **a** for $\Delta = -1$ (blue), -1.5 (green) and -2 (purple) and in **b** for $\Delta = 0$ (red), 0.5 (orange), 0.85 (yellow), 1 (blue) and 1.5 (green). Solid lines are power-law fits (to the filled symbols). Open symbols are excluded from the fit owing to finite-size effects. Crossed symbols are results from $\tilde{t}-J$ model simulations including 5% hole fraction. Fitted power-law exponents are shown in Fig. 3c. For positive anisotropies $\Delta \geq 0$ the decay time τ is defined as $\tau = \tau' / \ln(1/0.60)$ with $c(\tau') = 0.60$. For negative anisotropies $\Delta < 0$, the decay time τ_I for short times (I) is defined as $\tau_I = 10\tau'$ with $c(\tau'_I) = 0.90$. For longer times (II), the decay time τ_{II} is obtained from exponential fits $e^{-t/\tau_{II}}$ to the diffusive long-time tail (see dotted curves in Extended Data Fig. 7a-c). **c,** Diffusion coefficients for the diffusive long-time regime (II) obtained from theory (open symbols) and experiment (filled symbols). For negative anisotropies $\Delta < 0$, values were determined from quadratic power-law fits $1/\tau = DQ^2$ to the data points in **a** (theory) and Fig. 3a (experiment) for the diffusive regime (II). Note that for $\Delta \geq 0$ the system is only diffusive for $\Delta = +1$, as shown in **b** (theory) and Fig. 3b (experiment). From

the experimental diffusion coefficients, we estimate mean free paths δx using the velocity $v = 0.76(1)v_f$ from the ballistic short-time regime (I), and obtain $\delta x = 3.35(15)a$, $1.07(7)a$ and $0.66(4)a$ for $\Delta = -1.02$, -1.43 and -1.79 , respectively. **d,** Short-time ($t \ll h/J_{xy}$) decay constant $\tau = |f|^{-1}$ obtained from Taylor expansion of the contrast $c(t) = 1 + f^2 t^2 + \dots$ as a function of Q , for $\Delta = 0$ (red), 0.55 (orange), 0.85 (yellow), 0.95 (purple) and 1 (blue). For $\Delta < 1$ all curves in the log-log plot asymptote to the same slope as $Q \rightarrow 0$ (continuum limit), whereas there are deviations for larger wavevectors Q . For $\Delta = 1$ the slope is instead different. This indicates that the power-law exponent α in $\tau \propto Q^{-\alpha}$ depends on the range of wavevectors Q used to determine it. **e,** Power-law exponents α determined for the short-wavelength regime between $\lambda = 6a$ and $20a$ (filled symbols) as in experiments and numerics, and for the long-wavelength regime between $\lambda = 150a$ and $200a$ (open symbols) approaching the continuum limit. In the former case, the exponents show a smooth crossover from superballistic to diffusive as $\Delta \rightarrow 1$ similar to that in the experiments and numerics, whereas in the latter case the exponents show a sharp jump from ballistic to diffusive occurring exactly at $\Delta = 1$.



Extended Data Fig. 9 | Finite-size effects from the initial phase of the spin helix. **a**, The time evolution of the contrast $c(t)$ depends strongly on the initial phase θ , illustrated here by simulations for $\Delta = 0$ and $\lambda = 10.4$. **b, c**, The dynamics of the local magnetization $\langle S_i^z(t) \rangle$ for phases $\theta = 0$ (**b**) and $\pi/2$ (**c**)

reveals that this arises owing to the reflection of ballistically propagating magnetization off the ends of the chain. Depending on the initial phase of the spin helix, the reflected magnetization interferes constructively or destructively with the pattern of the bulk magnetization.



Extended Data Fig. 10 | Finite-size effects from the chain length. **a**, Contrast $c(t)$ obtained after a weighted average over all different chain lengths between $L = 0$ and $44a$ (shown in **b**), for $\Delta = 0$ and $\lambda = 10.4a$. The averaged dynamics (orange, yellow, blue) shows almost no dependence on the phase θ , in contrast to the dynamics determined from a single chain length $L = 40a$ (Extended Data Fig. 9a). Also overlaid are the contrasts for a fixed chain length ($L = 40a$) averaged over all initial phases $0 \leq \theta < 2\pi$ (black solid line), and averaged over only the two phases $\theta = 0$ and $\pi/2$ (black dashed line). The close agreement implies that averaging over either chain lengths or phases suppresses the dependence on initial or boundary conditions. **b**, A cut through

the spherical Mott insulator with diameter $L_{\max} = 44a$ (as in the experiment) illustrates the distribution of different chain lengths (oriented along the z direction). Averaging the local magnetization S^z over the x and y directions provides a 1D magnetization profile (bottom panel), which is an average over all chains. **c**, The number of chains with length L is given by $(\pi/2)(L/a)$. The total number of chains is $\pi L_{\max}^2/(2a^2) \approx 1,500$. **d**, The number of atoms in chains with length L is given by $(\pi/2)(L/a)^2$. The contribution of each chain to the imaging signal is proportional to the atom number in the chain, and so the relevant average over chain lengths is weighted by the atom number and is $\langle L \rangle = (3/4)L_{\max} = 33a$.

Appendix B

Transverse spin dynamics in the anisotropic Heisenberg model realized with ultracold atoms

P. N. Jepsen, W. W. Ho, J. Amato-Grill, I. Dimitrova, E. Demler, W. Ketterle
Transverse Spin Dynamics in the Anisotropic Heisenberg Model Realized with Ultra-
cold Atoms

Phys. Rev. X **11**, 041054 (2021)

Transverse Spin Dynamics in the Anisotropic Heisenberg Model Realized with Ultracold Atoms

Paul Niklas Jepsen^{1,2,3,*} Wen Wei Ho^{3,4,5} Jesse Amato-Grill^{1,2,3,6} Ivana Dimitrova^{1,2,3,4}
Eugene Demler^{3,4,7} and Wolfgang Ketterle^{1,2,3}

¹*Department of Physics, Massachusetts Institute of Technology, Cambridge, Massachusetts 02139, USA*

²*Research Laboratory of Electronics, Massachusetts Institute of Technology, Cambridge, Massachusetts 02139, USA*

³*MIT-Harvard Center for Ultracold Atoms, Cambridge, Massachusetts 02139, USA*

⁴*Department of Physics, Harvard University, Cambridge, Massachusetts 02138, USA*

⁵*Department of Physics, Stanford University, Stanford, California 94305, USA*

⁶*QuEra Computing Inc., Boston, Massachusetts 02135, USA*

⁷*Institute for Theoretical Physics, Wolfgang-Pauli-Strasse 27, ETH Zurich, 8093 Zurich, Switzerland*



(Received 14 March 2021; accepted 23 August 2021; published 17 December 2021)

In Heisenberg models with exchange anisotropy, transverse spin components are not conserved and can decay not only by transport, but also by dephasing. Here, we utilize ultracold atoms to simulate the dynamics of 1D Heisenberg spin chains and observe fast, local spin decay controlled by the anisotropy. However, even for isotropic interactions, we observe dephasing due to a new effect: an effective magnetic field created by superexchange. If spatially uniform, it leads only to uniform spin precession and is, therefore, typically ignored. However, we show through experimental studies and extensive numerical simulations how this superexchange-generated field is relevant and leads to additional dephasing mechanisms over the exchange anisotropy: There is dephasing due to (i) inhomogeneity of the effective field from variations of lattice depth between chains; (ii) a twofold reduction of the field at the edges of finite chains; and (iii) fluctuations of the effective field due to the presence of mobile holes in the system. The latter is a new coupling mechanism between holes and magnons. All these dephasing mechanisms have not been observed before with ultracold atoms and illustrate basic properties of the underlying Hubbard model.

DOI: [10.1103/PhysRevX.11.041054](https://doi.org/10.1103/PhysRevX.11.041054)

Subject Areas: Atomic and Molecular Physics
Condensed Matter Physics, Magnetism

I. INTRODUCTION

The famous Heisenberg Hamiltonian, also called the Heisenberg–Dirac–van Vleck Hamiltonian [1–3], describes localized particles on a lattice interacting via spin-exchange couplings. Despite its apparent simplicity, it serves as a paradigmatic model for a host of emergent phenomena, such as ferromagnetism (due to Coulomb exchange, also called potential or direct exchange), antiferromagnetism (due to kinetic exchange from tunneling, also called superexchange) [4], and spin-glass physics [5], as well as exotic states of matter like topologically ordered quantum spin liquids [6]. The dynamics of such models is also very rich and multifaceted and is under active, intense investigation. For example, in one dimension, Heisenberg spin models (with spin quantum number $S = 1/2$) have the special property of being integrable, whereby stable quasiparticles exist at all

temperatures. This gives rise to a breakdown of simple hydrodynamics with accompanying varied spin transport behaviors [7–11]. Understanding this has led to the recent development of a theory of generalized hydrodynamics [12,13]. In higher dimensions, the interplay of spontaneous symmetry breaking can lead to long-lived, metastable, prethermal states in addition to the onset of regular spin diffusion [14–16] or even turbulent relaxation with universal scaling of spin-spin correlations [17].

Ultracold atoms in optical lattices form an ideal platform to realize Heisenberg spin models and probe their dynamics in a controlled fashion [18]. In deep lattices where atoms are localized and Mott insulators form [19], superexchange processes via second-order tunneling yield effective Heisenberg spin models, with potential tunability of the strength, sign, and anisotropy of the spin-exchange interactions [20–23]. Until very recently, all experimental studies addressed the special case of an isotropic Heisenberg model [24–31]. However, in Ref. [32], we show how to overcome this limitation and implement Heisenberg models with *tunable* anisotropy of the nearest-neighbor spin-spin couplings, by using ^7Li and varying the interactions through Feshbach resonances. We are able to show that the anisotropy profoundly changes the nature of transport of longitudinal

*jepsen@mit.edu

Published by the American Physical Society under the terms of the [Creative Commons Attribution 4.0 International license](https://creativecommons.org/licenses/by/4.0/). Further distribution of this work must maintain attribution to the author(s) and the published article's title, journal citation, and DOI.

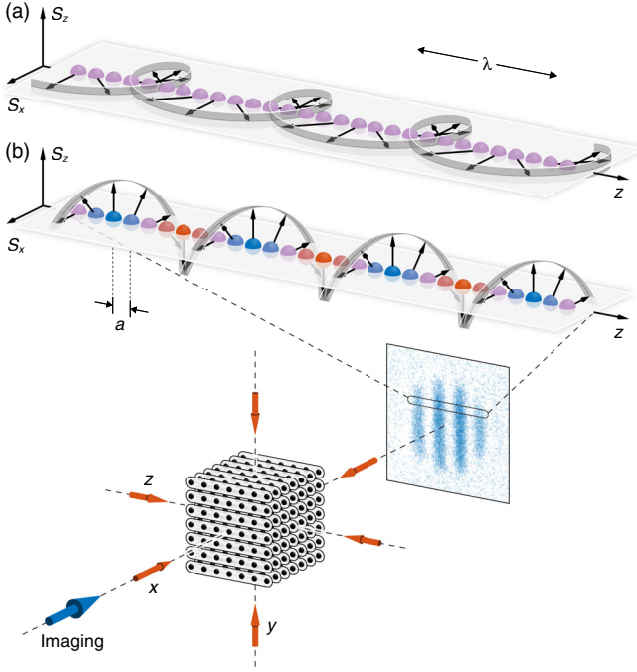


FIG. 1. Geometry of the experiment. The initial state is a transverse (a) or longitudinal (b) spin helix where the spin vector winds within the S_x - S_y plane (a) or S_z - S_x plane (b). The transverse helix (a) is a pure phase modulation of spin $|\uparrow\rangle$ and $|\downarrow\rangle$ states, whereas the longitudinal helix (b) also involves population modulation. Deep optical lattices along the x and y directions create an array of independent spin chains. The z lattice is shallower and controls spin dynamics along each chain.

spin components after a quantum quench from a so-called longitudinal spin helix [Fig. 1(b)] and observe ballistic, subdiffusive, diffusive, and superdiffusive behavior in different parameter regimes. These results bear some similarities with those of spin transport close to equilibrium but strikingly differ in other aspects, prompting the need for further theoretical investigation.

In this paper, we study the relaxation of transverse spin components after quantum quenches from a transverse spin helix [Fig. 1(a)] and observe even more dramatic effects of the anisotropy. In the classical limit, *any* transverse spin helix for *any* anisotropy is stationary, since the torques exerted on a given spin by its neighboring spins cancel exactly (see the Appendix C 1). Therefore, what we study here are the effects of quantum fluctuations on their stability. In contrast to longitudinal spin patterns, which can decay only by transport, transverse spin components can decay also by dephasing. We focus here on two paradigmatic models, which represent complementary spin physics: the XX model, which has only transverse spin-spin couplings and can be mapped to a noninteracting system of fermions, and the XXX model, which has isotropic spin couplings. For the XX model, we observe and explain that the decay is faster for spin-helix patterns with longer

wavelengths, in strong contrast to spin transport, where slower dynamics occurs for longer modulations. We also identify several dephasing mechanisms not discussed before. For the XXX model, we identify a symmetry-breaking term in the Bose-Hubbard model: an effective magnetic field caused by different scattering lengths for the spin $|\uparrow\rangle$ and spin $|\downarrow\rangle$ states. This superexchange-induced effective magnetic field is often ignored, since a spatially uniform field can be eliminated in the bulk by going into an appropriate corotating frame. Here, we show that the presence of the effective field is actually significant and gives rise to three additional dephasing mechanisms, all of which more or less contribute equally, resulting in drastically different decay behavior of spin-helix patterns with different orientations, i.e., transverse or longitudinal. (Both would have naïvely been expected to decay with identical timescales for isotropic spin interactions.) One is an inhomogeneous effect where the effective magnetic field is nonuniform between different chains in our sample. This can be eliminated with a spin-echo technique. The second is due to dephasing occurring at the ends of finite chains. The third is due to the presence of mobile holes resulting in a fluctuating effective magnetic field in the bulk, i.e., a hole-magnon coupling.

Our work shows the limitations of a pure spin model in capturing spin dynamics realized with ultracold atoms and demonstrates the need for a theoretical model explicitly featuring hole-magnon couplings (the so-called bosonic \tilde{t} - J model) in order to reach a more complete description of experiments. The new insight into hole-magnon coupling should be important for other systems and materials where such couplings are present, such as high-temperature superconductors [33–35].

II. EXPERIMENTAL METHODS

The spin models are implemented with a system of two-component bosons in an optical lattice, which is well described by the Bose-Hubbard model. These two states (lowest and second-lowest hyperfine states of ^7Li), labeled $|\downarrow\rangle$ and $|\uparrow\rangle$, form a spin-1/2 system. In the idealized scenario of a Mott insulating regime at unity filling, bosons cannot tunnel, and the effective Hamiltonian for the remaining spin degree of freedom is given by the spin-1/2 Heisenberg XXZ model [20–23]:

$$H = \sum_{\langle ij \rangle} \left[J_{xy} (S_i^x S_j^x + S_i^y S_j^y) + J_z S_i^z S_j^z - \frac{h_z}{2} (S_i^z + S_j^z) \right], \quad (1)$$

where S^x , S^y , and S^z are the spin-1/2 Pauli operators and the sum is over nearest-neighbor pairs of sites $\langle ij \rangle$. In leading order, one obtains for the transverse coupling $J_{xy} = -4\tilde{t}^2/U_{\uparrow\downarrow}$ and for the longitudinal coupling $J_z = 4\tilde{t}^2/U_{\uparrow\downarrow} - (4\tilde{t}^2/U_{\uparrow\uparrow} + 4\tilde{t}^2/U_{\downarrow\downarrow})$, both mediated by superexchange. Here, \tilde{t} is the tunneling matrix element between neighboring sites, while $U_{\uparrow\uparrow}$, $U_{\uparrow\downarrow}$, and $U_{\downarrow\downarrow}$ are

the on-site interaction energies. The effective magnetic field strength is $h_z = 4\tilde{t}^2/U_{\uparrow\uparrow} - 4\tilde{t}^2/U_{\downarrow\downarrow}$. Note that the total magnetization $\sum_i S_i^z$ in the S_z direction is conserved by the Hamiltonian.

The magnitude of superexchange can be varied over 2 orders of magnitude by changing the lattice depth, which scales the entire Hamiltonian. The anisotropy $\Delta := J_z/J_{xy}$ is controlled via an applied magnetic field which tunes the interactions through Feshbach resonances in the lowest two hyperfine states. In the regime studied here, the transverse coupling is positive ($J_{xy} > 0$). The ability to tune the anisotropy over a wide range of values, both positive and negative, allows us to explore dynamics beyond previous experiments [24–28] in which $\Delta \approx 1$.

One-dimensional (1D) chains are created by two perpendicular optical lattices whose depths $V_x, V_y = 35E_R$ are sufficient to prevent superexchange coupling on experimental timescales. A third orthogonal lattice along the z direction with adjustable depth V_z controls the superexchange rate in the chains (Fig. 1). Here, $E_R = \hbar^2/(8ma^2)$ denotes the recoil energy, where $a = 0.532 \mu\text{m}$ is the lattice spacing, m the atomic mass, and \hbar Planck's constant. After preparing a transverse spin helix [Fig. 1(a); this work] or a longitudinal spin helix [Fig. 1(b); as in our previous work [32]] with wavelength λ (and wave vector $Q = 2\pi/\lambda$) in each chain [27,36,37], time evolution is initiated by rapidly lowering V_z . The dynamics following this quench is then (approximately) governed by the 1D XXZ model Eq. (1). After an evolution time t , the dynamics is frozen by rapidly increasing V_z , and the atoms are imaged in the $|\uparrow\rangle$ state via state-selective polarization-rotation imaging with an optical resolution of about six lattice sites. For imaging the transverse spin, we apply a $\pi/2$ pulse first, so that we observe the magnetization in the S_x direction. To distinguish homogeneous from inhomogeneous dephasing, we can use a spin echo by applying a π pulse (with a typical duration of $t_\pi = 150 \mu\text{s} \ll \hbar/J_{xy}$) after half of the evolution time t .

Integrating the images along the direction perpendicular to the chains yields a 1D spatial profile of the population in the $|\uparrow\rangle$ state, averaged over all spin chains. As in Fig. 1, the spin helix exhibits a sinusoidal spatial modulation of the density of $|\uparrow\rangle$ atoms, observed as a characteristic stripe pattern with a normalized contrast $c(t)$. During the evolution time t , the 100% contrast of the initial spin helix decays, and we determine the dependence of $c(t)$ on lattice depth V_z , wave vector Q , and anisotropy Δ . Analyzing each decay curve $c(t)$ yields a decay rate γ , among other fit parameters (see Fig. 6 in Appendix A for data fitting methods).

In general, we measure the spin dynamics at two or more different lattice depths V_z and verify that the decay curves $c(t)$ collapse when time is rescaled by the corresponding spin-exchange time \hbar/J_{xy} , confirming that the dynamics is driven by superexchange. These time units are obtained from the experimentally determined lattice depth using an extended Hubbard model (detailed in Ref. [32]).

III. RESULTS

A. XX model

We first consider a very anisotropic system by realizing the Heisenberg model tuned to the noninteracting point ($\Delta = 0$) and study the decay of the transverse spin helix for different wave vectors Q [Figs. 2(a) and 2(b)]. We find the decays are quick, all having timescales on the order of a few spin-exchange times \hbar/J_{xy} , much faster than the decay of the longitudinal spin helix which is driven by ballistic transport. Importantly, the transverse decay rate even *increases for longer wavelengths* of the helix, showing that the decay is not caused by transport where magnetization redistributes in space and equilibrates, for which we would expect slower rates for longer modulations, but by dephasing where magnetization is locally created or removed.

Some insight into the fast timescales of transverse decay is obtained by taking the $Q \rightarrow 0$ limit, where the initial state becomes a uniformly polarized state. This state is obviously not an eigenstate of the quantum XX model and is, therefore, unstable. Further simplification to a two-site (double-well) system allows us to analytically diagonalize the Heisenberg Hamiltonian, which gives a level structure as shown in Fig. 2(c) (for $h_z = 0$). When $\Delta = 1$, the transverse spin state $|\rightarrow\rangle := (|\uparrow\rangle + |\downarrow\rangle)(|\uparrow\rangle + |\downarrow\rangle)/2$ is an eigenstate of the Hamiltonian as all triplet states are degenerate and, hence, does not evolve. However, for $\Delta \neq 1$, the degeneracy is lifted, and the state $|\rightarrow\rangle$ shows a beat note at the frequency of the energy splitting $J_{xy}(1 - \Delta)/2$. For $\Delta = 0$, this indicates a dephasing time for transverse spins on the order of a few spin-exchange times \hbar/J_{xy} , in qualitative agreement with our observations. For many sites, there will be a spectrum of beat frequencies leading to irreversible dephasing locally.

We can explain the unusual Q dependence of the experimentally observed transverse decay with a semiclassical analysis of spin dynamics (see Appendices C 1 and C 2). In the classical limit, spin-helix states satisfy the Landau-Lifshitz equations of motion $\partial_t \vec{S}_i(t) = (\partial H / \partial \vec{S}_i) \times \vec{S}_i(t) = 0$ for any wave vector Q and, therefore, do not decay (this is, in fact, true for any anisotropy Δ), because the torques exerted on \vec{S}_i by its neighbors cancel exactly. Here, \vec{S}_i is a classical spin vector, which corresponds to the $S \rightarrow \infty$ limit of a quantum mechanical spin. For finite S , we can study the effects of quantum fluctuations with a large spin ($1/S$) expansion. We find that the Fourier modes of the fluctuations carrying momentum k have a dispersion relation $\omega_k \propto J_{xy} |\cos(Qa) \sin(ka/2)|$. As the characteristic energy scales of all modes are proportional to $|\cos(Qa)|$, this indicates, in a somewhat surprising fashion, that the dynamics of the spin helix is faster for longer wavelengths than for smaller wavelengths. The slowest dynamics occurs at $Qa = \pi/2$ (or $\lambda = 4a$), where neighboring spins are at an angle of 90° . This state is robust (at least to leading order)

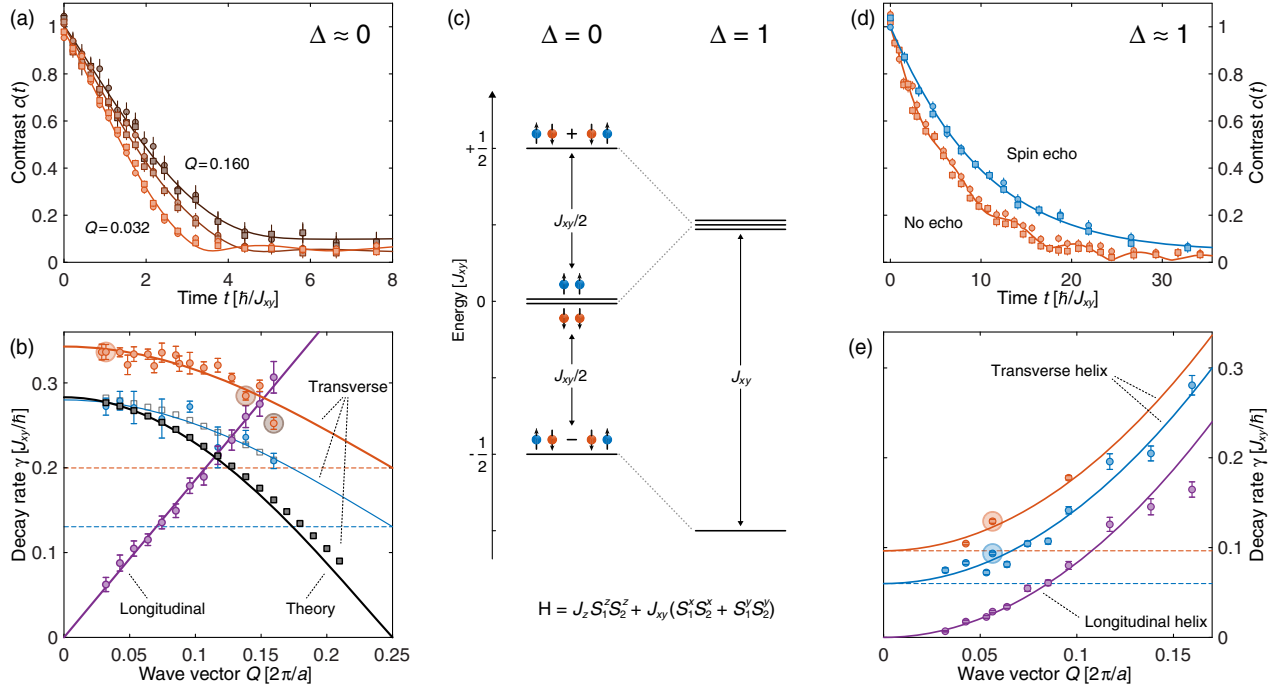


FIG. 2. Spin dephasing and spin transport for the XX model [$\Delta \approx 0$, (a),(b)] and the isotropic XXX model [$\Delta \approx 1$, (d),(e)]. (a) Spin relaxation at $\Delta \approx 0$. Transverse spin-helix contrast $c(t)$ for $Qa = 2\pi \times 0.032, 0.138$, and 0.160 (bright to dark orange). The curves for different lattice depths $11E_R$ (\circ) and $13E_R$ (\square) collapse when times are rescaled in units of the corresponding spin-exchange times $\hbar/J_{xy} = 1.71$ (\circ) and 4.30 ms (\square). The transverse spin decays on a timescale of a few spin-exchange times which increases for smaller wavelengths $\lambda = 2\pi/Q$. (b) Wave-vector dependence. The initial decay rates [orange points; with values from (a) highlighted] follow a cosine dependence $\gamma(Q) = \gamma_1 \cos(Qa) + \gamma_0$ (solid orange line) with a constant background rate $\gamma_0 = 0.20(2)J_{xy}/\hbar$ (dashed orange line). This is in strong contrast to the longitudinal spin helix (purple) which shows linear scaling with Q (indicating ballistic transport). A spin echo (π pulse at time $t/2$) reduces the background rate to $\gamma_0 = 0.13(3)J_{xy}/\hbar$ (dashed blue line). The black solid squares are numerical results for a single chain and the defect-free XX model (with $h_z = 0$) with a fit $\gamma(Q) = \gamma_1 \cos(Qa)$ (solid line) to the points with $Qa \leq 2\pi \times 0.075$. The gray open squares are numerical results for the \tilde{t} - J model with 5% hole fraction (see Appendix E 1). (c) Energy levels of the Heisenberg Hamiltonian for two spins in a double-well potential. For $\Delta \neq 1$, the triplet states are split. (d) Spin relaxation at $\Delta \approx 1$. Transverse spin-helix contrast $c(t)$ for $Qa = 2\pi \times 0.056$ without spin echo (orange) and with spin echo (blue). The difference shows the presence of inhomogeneous dephasing. The curves taken for different lattice depths $11E_R$ (\circ) and $13E_R$ (\square) collapse when times are rescaled in units of the corresponding spin-exchange times $\hbar/J_{xy} = 2.55$ (\circ) and 6.42 ms (\square). (e) Wave-vector dependence. Decay rates for the transverse helix [orange and blue points; with values from (d) highlighted] and longitudinal helix (purple points), for $\Delta \approx 1$. The orange (no echo) and blue (with echo) solid lines are fits $\gamma(Q) = DQ^2 + \gamma_0$ assuming two contributions to the decay rate: one quadratic term (indicating diffusive transport) with diffusion constant D (taken from the longitudinal spin dynamics shown in purple), the other Q -independent γ_0 (shown by the dashed lines). The spin echo reduces the background decay rate γ_0 by an amount of $0.036J_{xy}/\hbar$ (e) and $0.069J_{xy}/\hbar$ (b). These values are consistent with an inhomogeneous dephasing rate proportional to the effective magnetic field h_z , with (predicted) values $h_z = 0.89J_{xy}$ (e) and $1.43J_{xy}$ (b).

against decay induced by quantum fluctuations, because the fluctuations of a spin which points, e.g., in the S_x direction are in the S_y - S_z plane and, for $\Delta = 0$, do not cause any precession of their immediate neighboring spins (which point along the $\pm S_y$ direction).

This prediction is furthermore corroborated by a fully quantum ($S = 1/2$) but short-time expansion of the order parameter of the spin helix (see Appendix C 3). Numerical simulations, as seen in Figs. 2(b) and 8(a), also verify this by showing a very good collapse of the decay curves of all experimentally considered wave vectors Q upon rescaling time by a factor of $\cos(Qa)$. This holds even up to

evolution times t longer than would be expected to be valid for the semiclassical analysis or short-time expansion. Unsurprisingly, deviations from this relation are seen as the wave vector approaches $Q = \pi/(2a)$, for which the simple approaches would predict a vanishing decay rate. However, note that the transverse spin helix with $Q = \pi/(2a)$ can be shown to be an exact eigenstate of the XX model with appropriate boundary conditions [38,39].

Experimentally, we find that the decay rate of the transverse helix as a function of wave vector Q can be fitted very well as the sum of the predicted $\cos(Qa)$ dependence together with a constant term, as shown in

Fig. 2(b). The constant term represents additional dephasing mechanisms that go beyond the idealizations of the spin model (1), which we discuss below.

B. XXX model

When $\Delta = 1$, we realize the isotropic Heisenberg spin model which, aside from the effective magnetic field h_z , satisfies $[H, \sum_i S_i^\alpha] = 0$ ($\alpha = x, y, z$). The presence of the effective magnetic field term $\sum_{\langle ij \rangle} (h_z/2)(S_i^z + S_j^z)$ in Eq. (1), which we can rewrite as $\sum_i h_{z,i} S_i^z$, explicitly breaks this spin-rotational symmetry. Now, a uniform (i.e., site- i -independent) field $h_{z,i}$ can be transformed away by going into an appropriate rotating frame. In such a case, the transverse and the longitudinal spin helix should show exactly the same dynamical behavior.

However, as the results in Figs. 2(d) and 2(e) show, there is a dramatic difference: The transverse helix decays much faster than the longitudinal helix with the same wave vector Q . In particular, the longitudinal helix exhibits a purely diffusive scaling with wave vector Q ; i.e., its decay rate obeys $\gamma(Q) = DQ^2$, where D is a diffusion constant (as shown in Ref. [32]), whereas the transverse helix has an additional Q -independent decay rate of $\gamma_0 = 0.096(10)J_{xy}/\hbar$, with the net decay rate fitted well by $\gamma(Q) = DQ^2 + \gamma_0$. This lends naturally to the interpretation that the system at this point realizes dynamics close, but not equal, to a model where global transverse magnetization is exactly conserved. In other words, there is not only a transport channel under which the transverse helix decays by, such that local magnetization profiles redistribute in space and eventually equilibrate, but also a nontransport (dephasing) channel, whereby transverse magnetization can be created or removed locally, arising from explicit symmetry-breaking terms. (Note that for the highly anisotropic case $\Delta = 0$ we cannot separate out such a transport part.)

In the following, we discuss and quantify three plausible mechanisms leading to such dephasing. First, a careful read of the Hamiltonian Eq. (1) indicates that the effective magnetic field $h_{z,i}$ is *explicitly* nonuniform for systems of finite sizes, as encountered in experiments. This stems from the fact that all terms in the Hamiltonian arise from superexchange, which requires *pairs* of sites, and that sites at the edges of the system have fewer neighbors than sites in the bulk (discussed further below). Hence, relevant symmetry-breaking terms (i.e., which cannot be transformed away) are already present in the idealized spin model. Second, our experiment consists of an *ensemble* of 1D systems, and there is a small inhomogeneity in the effective magnetic field strengths between chains due to slight variations in the lattice depth caused by the Gaussian shape of the laser beam. This can lead to a loss of measured (ensemble-averaged) contrast due to destructive interference from spins precessing at different rates, leading to a Q -independent decay rate. Third, a natural deviation of our

experiment from the idealized spin physics governed by the pure Heisenberg Hamiltonian Eq. (1) is the presence of a small fraction of mobile holes in the spin chains caused by nonadiabatic preparation of the Mott insulator and nonzero temperature. Typical hole fractions lie between 5% and 10% in the central part of the Mott insulator [27,32]. In a simplified picture, holes cause dephasing, because spins next to holes experience only half the effective magnetic field. A mobile hole, therefore, creates a fluctuating effective magnetic field, causing dephasing of the transverse spin component. Below, we present experimental studies and extensive numerical simulations which find that all of these effects contribute roughly equally a Q -independent decay rate.

We note also that, in the final data analysis, a reevaluation of the scattering lengths shows that our data is actually not taken exactly at the isotropic point but at $\Delta = 0.93 \pm 0.05$. This deviation from isotropy is responsible for a Q -independent decay rate of $0.015J_{xy}/\hbar$, or 15% of the observed difference between longitudinal and transverse spin decay (Appendix E 3). When all these effects are taken together, this accounts approximately for the experimentally measured Q -independent decay rate γ_0 for the transverse helix.

C. Imaging the effective magnetic field

All the symmetry-breaking mechanisms we discuss above involve the effective magnetic field. Therefore, we first present how this field can be directly observed and quantified.

If we assume that the ensemble experiences two pronounced values of the effective magnetic field, then the time evolution of the cloud-averaged contrast $c(t)$ will show a beat note at a frequency which corresponds to the difference of the two values of the effective magnetic field. This is the case for our atom clouds, which feature a Mott insulator plateau surrounded by a dilute shell of individual atoms [32] which are pinned to their lattice sites by the gradient of the harmonic trapping potential [40]. Many of these individual atoms do not have neighbors for spin exchange and, therefore, do not feel an effective magnetic field, while those in the Mott insulator plateau do. The observed beat frequencies $\Omega = 0.90(1)J_{xy}/\hbar$ (Fig. 3) agree well with the predicted value of the superexchange-generated effective magnetic field $h_z = 0.89J_{xy}$. As expected, the beat note is more pronounced by spatially selecting the outer parts of the cloud [Fig. 3(a)] and disappears with a spin echo [Fig. 2(d)]. In Appendix B, we describe an alternate spectroscopic method to observe the effective magnetic field as a shift in the spin-flip frequency.

The presence of the effective magnetic field can also be directly imaged by introducing a sufficiently large gradient in the lattice depth between the chains. This can be achieved by vertically displacing the z lattice relative to the atom cloud (see Fig. 1), causing a gradient of the effective magnetic field. As this field sets the “spiraling” frequencies of the individual spin helices across the cloud (simply arising from the on-site precession of the spins

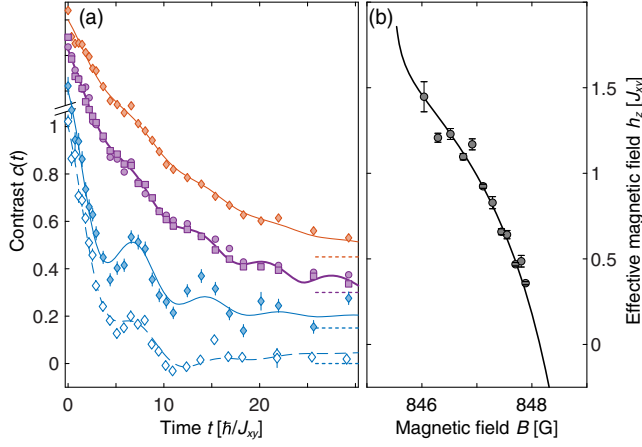


FIG. 3. Absolute measurement of the effective magnetic field value h_z as a beat note between the spin precession frequencies in the inner and outer parts of the cloud. (a) Transverse spin-helix contrast $c(t)$ for $\lambda = 23.5a$ (all filled symbols) and $\Delta \approx 1$. For measurements averaged over the whole atom cloud (purple), they are performed at $11E_R$ (\circ) and $13E_R$ (\square). The contrast at the center of the atom cloud for radii $r \leq 8.5a$ (orange filled symbols) decays slower with less pronounced oscillations, whereas the contrast in the spatial wings for radii $r \geq 20a$ (blue filled symbols, including approximately 7% of the atoms in the cloud) decays faster with more pronounced oscillations. Data points for diamonds are an average of measurements at $11E_R$ and $13E_R$. Open diamond symbols represent data for $\lambda = 10.4a$ and show the same oscillation frequency but decay faster due to spin transport. Lines are fits described in Appendix A. Curves are offset from each other for clarity. The dotted lines indicate their respective zeros. (b) The beat frequency Ω varies as a function of the externally applied magnetic field B . The measured values for $\hbar\Omega$ (points) follow the theoretical prediction (without any adjustable parameter) for the effective magnetic field h_z (solid line) which is tuned by varying the scattering lengths via Feshbach resonances.

about the S_z axis), this translates to an observable tilt of the whole stripe pattern [Fig. 4(a)].

The tilt angle grows linearly in time, with a rate proportional to the effective magnetic field and the gradient of the lattice depth (which we keep fixed). Externally applied magnetic fields change the scattering lengths via broad Feshbach resonances, and so we can tune the effective magnetic field. The observed rates for the tilt rotation versus applied magnetic field B are shown in Figs. 4(b) and 4(c) and agree well with our theoretical prediction. In particular, near $B = 848.1$ G, the spin $|\uparrow\rangle$ and $|\downarrow\rangle$ scattering lengths are identical $a_{\uparrow} = a_{\downarrow}$ and the effective magnetic field is zero, evinced by the absence of any tilt in time [Fig. 4(b); yellow data points].

We note that, in principle, such a rotation could also be caused by an external magnetic field gradient. However, the tilt angle would then not depend on the lattice depth V_z and

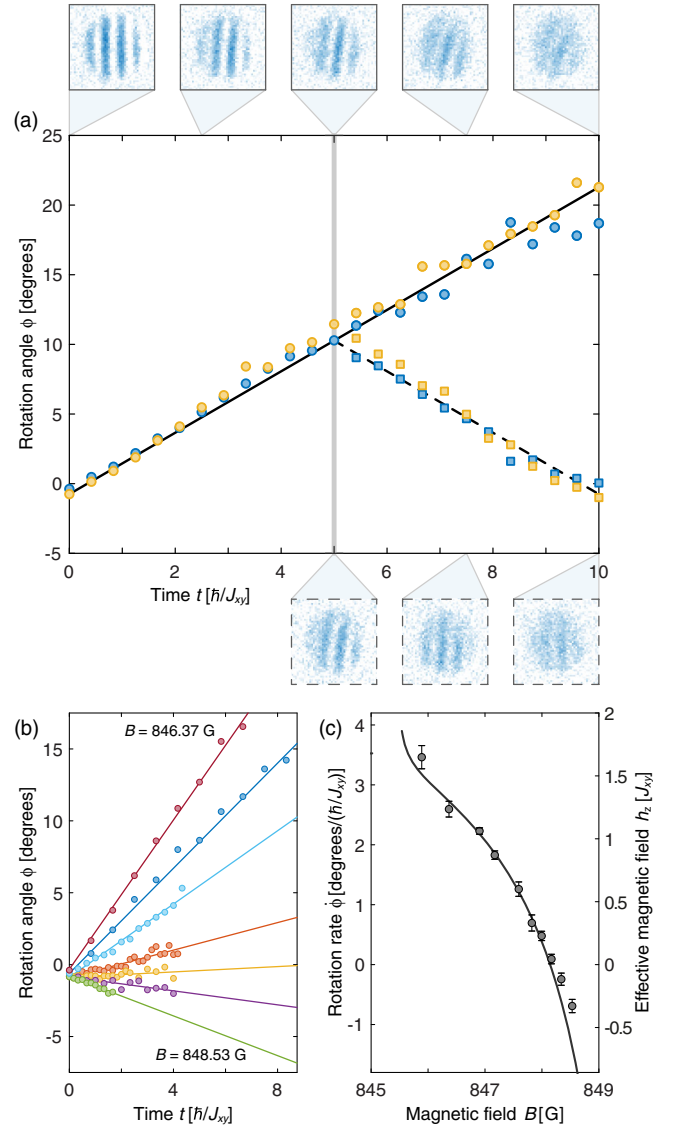


FIG. 4. Direct observation of the effective magnetic field through spin precession. (a) Rotation angle of the stripe pattern as a function of evolution time t (filled symbols) for two lattice depths $11E_R$ (blue) and $13E_R$ (yellow) without (solid line) and with (dashed line) spin-echo pulse at $t = 5\hbar/J_{xy}$. (b),(c) Tunability of the effective magnetic field h_z . (b) Rotation angle as a function of evolution time t for different magnetic fields $B = 846.37$ (red), 847.17 (blue), 847.59 (light blue), 848.00 (orange), 848.17 (yellow), 848.34 (purple), and 848.53 G (green). (c) Angular velocities obtained from linear fits in (b) compared to predicted effective magnetic fields h_z (solid line) with the scale factor between the two y axes as a fitting parameter yielding $\dot{\phi}\hbar/J_{xy} = 0.037h_z/J_{xy} = 2.1^\circ h_z/J_{xy}$, representing the (uncalibrated) gradient of the lattice depth. Times are normalized by the spin-exchange time \hbar/J_{xy} for the central part of the atom cloud. The scaling factor is consistent with a displacement of the z -lattice beam ($1/e^2$ radius of $125 \mu\text{m}$) by an amount of $29 \mu\text{m} = 55a$.

the external magnetic field B . In a sufficiently deep lattice ($V_z = 35E_R$), for up to at least 40 ms, we do not observe any discernible rotation, hence ruling out an external field gradient.

When an echo pulse is added, the direction of the stripe rotation is reversed, and, at twice the echo time, the stripe pattern is vertical again, resulting in high contrast for vertically integrated images [Fig. 4(a); bottom]. This shows how the spin echo eliminates the effect of inhomogeneous effective fields across the cloud, a technique we use below to quantify their contribution to the dephasing of transverse spin patterns.

D. Dephasing mechanisms for the transverse spin helix

We now elaborate on and quantify the effects of three possible dephasing mechanisms we identify, induced by the effective magnetic field.

1. Effect of inhomogeneity in the effective magnetic field between chains

The effect of inhomogeneity in the effective magnetic field strengths between chains in the ensemble, arising from slight variations in the lattice depth from the Gaussian nature of the laser beams, can be eliminated by applying a spin-echo pulse at half of the evolution time t .

Indeed, when adding spin-echo pulses to the experimental sequence, we find the Q -independent background decay rate γ_0 is reduced from $0.096(10)$ to $0.060(3)J_{xy}/\hbar$ [dashed lines in Fig. 2(e)]. This is compatible with an effective magnetic field distribution over different chains with a full width at half maximum (FWHM) of 8.2%, corresponding to variations in the lattice depth V_z of 1.6%, compatible with experimental parameters.

2. Effect of finite chain lengths

As noted before, the effective magnetic field of the ideal Heisenberg Hamiltonian Eq. (1) is necessarily nonuniform for systems of finite sizes. To elaborate, the effective magnetic field arises from superexchange involving nearest-neighbor pairs of atoms, indicated already in the Hamiltonian Eq. (1), where we deliberately write the magnetic field $\sum_{\langle ij \rangle} (S_i^z + S_j^z)$ as a sum over pairs $\langle ij \rangle$ of sites to emphasize this fact. This means, in particular, that, for a 1D chain, the effective magnetic field is reduced to $h_z/2$ at the ends, half the value in the bulk. For $h_z \neq 0$, this nonuniformity hence cannot simply be transformed away by going into an appropriate corotating frame. Although this reduced field is localized at the ends of the chain, it cannot be eliminated with an echo protocol, since its effect propagates along the chain via spin dynamics as illustrated in Fig. 10 (note the echo pulse removes inhomogeneous dephasing only for subsystems, which do not interact with each other, such as separate chains in the ensemble).

This edge effect results in differences in the relaxation between the transverse and the longitudinal spin helix: The spins at the edges dephase rapidly, and this perturbation

then propagates through the entire chain. We perform numerical simulations which show that, for chain lengths of 10–20 spins, the edge effect causes a dephasing rate of approximately $0.02J_{xy}/\hbar$ (Appendix E 4). Although the diameter of the Mott insulator plateau we experimentally realize is measured to be around 40 sites, we expect that holes (with an estimated concentration of 5%–10%) [27,32] in the outer region of the Mott plateau are localized by the gradient of the trapping potential and create effectively shorter chains in our sample. In contrast to that, in the central region of the Mott plateau, where the trapping potential is flat, holes are mobile, and their effect is discussed below.

The edge effect can be viewed as an inhomogeneity of the effective magnetic field realized within a single chain. In addition to this effect, we have a harmonic trapping potential in the experimental system, which along a given chain creates an additional inhomogeneity, since it creates an energy offset between neighboring sites and modifies the superexchange rate by up to approximately 10% (see the methods section in Ref. [32] for details). We estimate that this is somewhat less important than the effect of the 50% reduced effective field at the ends of the chain.

3. Effect of mobile holes

We now explore a dephasing mechanism beyond the pure spin model, namely, the presence of mobile holes in the system. For negligible interactions, the dynamics of holes can be described by a quantum random walk where the time-dependent wave function at site i for a hole initially localized at $i=0$ is the Bessel function $J_i(t/(\hbar/2\tilde{t}))$. The square of the Bessel function shows oscillations at frequencies $\omega = 4\tilde{t}/\hbar$ or periods of $T = (\pi/2)\hbar/\tilde{t}$. Now, for a hold time T and with an echo pulse at $T/2$ (described in the previous subsection), those fluctuations are “rectified” and lead to enhanced dephasing (note that the spin echo removes stationary inhomogeneous magnetic fields but can enhance the effect of time-dependent fluctuations [41]). This is evidence for hole-magnon coupling: Holes carry a localized magnetic field which couples to spin dynamics. Indeed, Fig. 5 shows a feature in the spin-echoed contrast at early times on the order of the tunneling time \hbar/\tilde{t} in accordance with these predictions, providing experimental evidence that mobile holes are possibly present. By using a series of echo pulses at frequency ω , one could map out the frequency spectrum of the effective magnetic field, using concepts from dynamic decoupling [41].

For times on the order of superexchange scales, the effect of the hole-induced fluctuating effective magnetic field can be captured by a simple model. From nuclear magnetic resonance, it is well known that the dephasing time T_2 of a localized spin at $z=0$ is related to the magnetic field fluctuations h_z (measured in units of energy) and their coherence time τ_c via $1/T_2 = \langle h_z^2 \rangle \tau_c / \hbar^2 = G(z=0, \omega=0) / \hbar^2$,

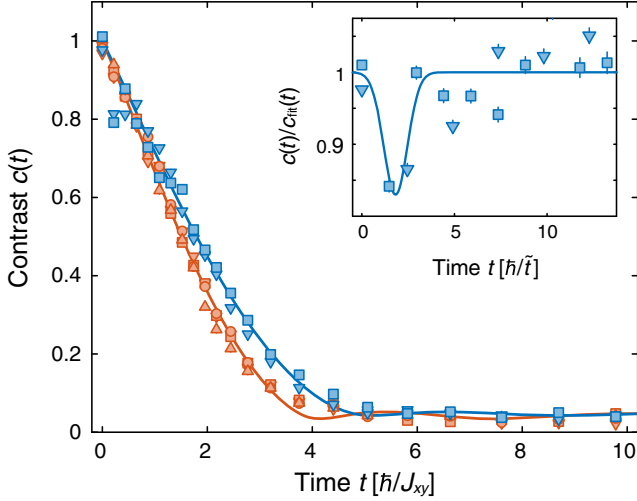


FIG. 5. Tunneling dynamics of mobile holes. Decay curves for the XX model ($\Delta \approx 0$) at $\lambda = 10.4a$ without a spin-echo pulse (orange) and with a spin-echo pulse (blue) after half the evolution time t , measured for different lattice depths $9E_R$ (Δ), $11E_R$ (\diamond), $13E_R$ (\square), and $15E_R$ (∇). The time axis has units of the corresponding spin-exchange times $\hbar/J_{xy} = 0.64$ (Δ), 1.71 (\diamond), 4.30 (\square), and 10.29 ms (∇). Solid lines are fits (see Appendix A). The spin echo generally slows down relaxation slightly by eliminating inhomogeneous dephasing, except at early times where relaxation is actually enhanced and the data points reproducibly deviate from the solid line (data points at $t = 0.22$ and $0.43\hbar/J_{xy}$ have to be excluded from fitting). The inset shows the data points divided by the fit function and plotted with time in units of the tunneling time \hbar/\tilde{t} , showing enhanced relaxation around 1–2 tunneling times (the solid line is a guide for the eye). More extensive studies with higher time resolution reproduce similar features at around the tunneling time, but their shape is sensitive to experimental conditions, including the atom number.

where $G(z, t) = \langle h_z(z, t)h_z(0, 0) \rangle$ is the autocorrelation of the fluctuating magnetic field along the chain [42]. The dephasing time T_2 is the same for spin patterns with arbitrary wave vector Q .

For a moving hole, the effective magnetic field has a correlation function $G(z, t)$ which is identical to the (normalized) density-density correlation function $J(z, t)$ of the hole, multiplied by h_z^2 [here, we neglect the fact that the effective magnetic field at a given site depends on the holes on the neighboring sites; see Eq. (1)]. For uncorrelated holes with hole probability p , the variance of the local occupation is p with a coherence time $\tau_c = 1.14(\hbar/2\tilde{t})$, where \tilde{t} is the tunneling matrix element [43]. The associated correlations of the fluctuating effective magnetic field determine the T_2 dephasing time for the spin helix $1/T_2 = 0.57h_z^2p/\tilde{t}\hbar$. Assuming $p = 0.1$ (10% hole fraction) and using $\tilde{t} = 6.15J_{xy}$ (at $V_z = 11E_R$) and $h_z/J_{xy} = 0.89$, this leads to an estimate of $1/T_2 \approx 0.007J_{xy}/\hbar$.

This simple model of magnon-hole dynamics indicates already the non-negligible effect of a small fraction of holes and strongly suggests that a more generalized model

beyond the pure spin Heisenberg model Eq. (1) should be considered. To this end and to substantiate the rough estimate of the dephasing rate from the simple model, we perform simulations of the bosonic \tilde{t} - J model which explicitly take into account the presence of holes in the Mott insulator near unity filling. This model allows holes to be present but does not include double occupancies of bosons, since they are suppressed by the large on-site repulsion U . See Appendix F for its explicit form and derivation beginning from the Bose-Hubbard model, as well as an interpretation of its constituent terms in terms of magnon-hole couplings. There, we also show that a non-zero field strength h_z is a *necessary* and *sufficient* condition for the \tilde{t} - J model to break spin rotational symmetry, justifying our identification of the effective magnetic field as the agent giving rise to differences in dynamics between the transverse and the longitudinal spin helix.

Numerical simulations using the bosonic \tilde{t} - J model for a mobile hole fraction of 10%, with experimentally realized parameters that would yield the XXX model ($\Delta = 1$) in the ideal spin limit, show a Q -independent dephasing at a rate around $0.026J_{xy}/\hbar$ for the experimental conditions in Fig. 2(e) (see Appendix E 2), supporting the simplified model of hole-induced dephasing presented above (but providing a rate 3 times higher). Note that we cannot experimentally measure the hole fraction and use here the typical range of values of 5%–10% observed or inferred in other experiments [27,32].

4. Summary of the dephasing mechanisms

At this stage, we account for the isotropy-breaking dephasing rate of 0.096 (in units of J_{xy}/\hbar) through more or less equal contributions from the edge effect (0.020), effective magnetic field inhomogeneity between chains which can be eliminated via spin echo (0.036), and mobile holes (0.013–0.026, assuming a hole fraction p between 5% and 10% and linear dependence on p), as well as a small deviation from isotropy (0.015). These numbers are summarized in Table I. We regard some of the numbers as only semiquantitative due to the nonexponential character of the measured and calculated decay curves, but they indicate which phenomena have to be accounted for in quantum simulations of spin dynamics using ultracold atoms in optical lattices.

5. Revisiting the XX model

Our considerations above illustrate the role of edge effects and a small number of holes in the dephasing of transverse spin. This should also contribute to the dephasing in the XX model. Hence, we revisit it via simulations of the bosonic \tilde{t} - J model with the appropriate experimental parameters (see Appendix E 1) and can now account for two experimental findings. For the Q -independent decay rate, we note that the $h_z = 1.43J_{xy}$ term is 1.6 times larger

TABLE I. Q -independent decay rates for different dephasing mechanisms at $\Delta \approx 1$, obtained through experimental studies (spin echo for field inhomogeneity) and extensive numerical simulations (edge effect, mobile holes, and experimental deviation from isotropy). Numbers should be regarded as semi-quantitative but, taken as a whole (second last row), strongly suggest that they account for the net decay rate experimentally observed (last row).

Dephasing mechanism	Decay rate (J_{xy}/\hbar)
Edge effect	0.020
Field inhomogeneity	0.036
Mobile holes	0.013–0.026
Experimental deviation from $\Delta = 1$	0.015
Total	0.084–0.097
Experimentally measured rate	0.096(10)

compared to our experimental realization of the XXX model, which explains the larger observed Q -independent dephasing rate $\gamma_0 = 0.20(2)J_{xy}/\hbar$ [Fig. 2(b)] semiquantitatively. Furthermore, the simulations show that the amplitude γ_1 of the $\cos(Qa)$ dependence is a function of the concentration of holes [see Figs. 2(b) and 8]. We find that the experimental data agree best with numerical simulations for 5% holes.

IV. CONCLUSIONS

We have used ultracold atoms to implement the Heisenberg model with tunable anisotropy. For the relaxation of transverse spin patterns, we have studied for the first time four decay mechanisms: intrinsic dephasing by anisotropic spin-exchange couplings, inhomogeneous dephasing through a static superexchange-induced effective magnetic field, dephasing through the ends of the chain, and dephasing by a fluctuating effective magnetic field due to the presence of mobile holes. One reason why several of these mechanisms have not been observed before is that most previous studies of spin dynamics in optical lattices have used either fermions [24], for which the \tilde{t} - J model is always explicitly spin rotationally symmetric and, therefore, $h_z = 0$, or bosons comprised of ^{87}Rb [25–28], for which the spin $|\uparrow\rangle$ and spin $|\downarrow\rangle$ scattering lengths are almost identical ($a_{\uparrow\uparrow} = 99.0a_0$, $a_{\uparrow\downarrow} = 99.0a_0$, and $a_{\downarrow\downarrow} = 100.4a_0$, with the Bohr radius a_0) [44], leading to a value of $h_z \approx 0.014J_{xy}$, approximately 100 times smaller than for ^7Li .

The experimental and theoretical results presented in this work go beyond pure spin physics. They illustrate effects caused by a small hole fraction that is generally present in cold atomic quantum simulators. A more complete description of spin dynamics in such systems, therefore, requires using the \tilde{t} - J model, which features magnon-hole couplings.

This coupling between density and spin is analogous to the interplay of spin and charge degrees of freedom in

strongly correlated electronic systems, which is important, for example, in understanding emergent many-body phenomena like high-temperature superconductivity in cuprates [33–35]. Therefore, our platform presents an elegant new setting where such physics can be emulated. More generally, we regard our work as a starting point for exploring spin dynamics in different dynamical regimes as well as in generalized Heisenberg models. Experimentally, the effect of mobile holes can be studied by varying the lattice depth over a large range, which affects hole dynamics (tunneling) differently than spin dynamics (superexchange). A quantum gas microscope will be able to select chains of a certain length and to measure spin and hole dynamics with single-site resolution. Exciting future directions include the study of spin polaron dynamics [45], realizing long-lived, metastable prethermal states in higher dimensions [14–16], and probing the onset of turbulent spin relaxation utilizing larger spin quantum numbers [17].

ACKNOWLEDGMENTS

We thank Y. K. Lee and H. Lin for experimental assistance, J. Rodriguez-Nieva for discussions, and J. de Hond for comments on the manuscript. We acknowledge support from the NSF through the Center for Ultracold Atoms and Grant No. 1506369, ARO-MURI Non-Equilibrium Many-Body Dynamics (Grant No. W911NF-14-1-0003), AFOSR-MURI Photonic Quantum Matter (Grant No. FA9550-16-1-0323), AFOSR-MURI Quantum Phases of Matter (Grant No. FA9550-14-1-0035), ONR (Grant No. N00014-17-1-2253), the Vannevar-Bush Faculty Fellowship, and the Gordon and Betty Moore Foundation EPiQS Initiative (Grant No. GBMF4306). W. W. H. is supported in part by the Stanford Institute of Theoretical Physics. Numerical simulations involving matrix product states were performed using the `TENPY` library [46].

APPENDIX A: DATA ANALYSIS

We determine the contrast \mathcal{C} by a fit $f(y, z) = g(y, z) \cdot [1 + \mathcal{C} \cos(Qz + \theta)]/2$ to the two-dimensional phase-contrast images (see Fig. 6). Here, $Q = 2\pi/\lambda$ is the wave vector, θ is a random phase which varies from shot to shot due to small magnetic bias field drifts, and $g(y, z)$ is a two-dimensional envelope function which accounts for the spatial distribution of all atoms $n = n_{\uparrow} + n_{\downarrow}$ inside a sphere of radius R such that $g(y, z) = A\sqrt{1 - y^2/R^2 - z^2/R^2} \cdot H(1 - y^2/R^2 - z^2/R^2)$ with the Heaviside function $H(r)$. During the evolution time t , the contrast $\mathcal{C}(t)$ decays, and we study the dependence of $c(t) = \mathcal{C}(t)/\mathcal{C}(0)$ on lattice depth V_z , wavelength λ , and anisotropy Δ .

For both longitudinal and transverse spin relaxation, we find the decay curves can be well described by the sum of a decaying part with decay rate γ and a (damped) oscillating part with frequency ω , resulting in a fitting function

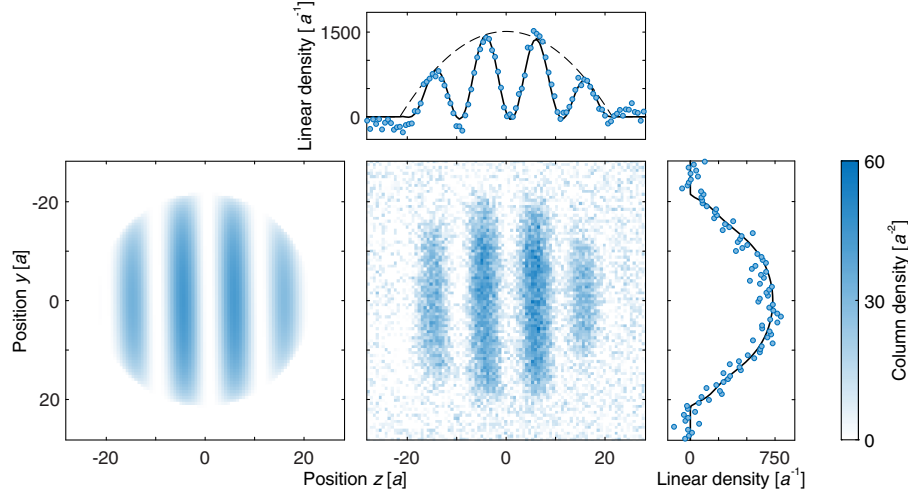


FIG. 6. Contrast measurement. The central image represents raw data and shows the distribution of atoms in the $|\uparrow\rangle$ state. The left image is the two-dimensional fit as described in Appendix A. Every pixel is a local measurement of the column density (number of $|\uparrow\rangle$ atoms per unit area). The image is projected (integrated) along both the horizontal z direction (right) and the vertical y direction (top) from $y, z = -42a$ to $+42a$ to obtain the linear densities (number of $|\uparrow\rangle$ atoms per unit length) for the measured data (points) and the fit (solid line). The dashed line in the y projection shows the (parabolic) envelope function for the spatial density distribution in the cloud. The y and z axes are displayed in units of the lattice spacing $a = 0.532 \mu\text{m}$.

$c(t) = (a_0 + b_0 \cos \omega t)e^{-\gamma t} + c_0$. Here, a_0 , b_0 , c_0 , ω , and γ are fitting parameters. These fits are used for Fig. 2(b) (purple), in Fig. 2(d) (blue), and for Fig. 2(e) (purple and blue). Special fitting procedures are used for the XX model and for the beat note due to the effective magnetic field.

1. XX model

The decay curves $c(t)$ for the transverse spin helix [Fig. 2(a)] clearly show a slower decay rate for larger values of Q . We can use the fitting function described above, with the only difference of adding the constant offset c_0 in quadrature $c(t) = \sqrt{[(a_0 + b_0 \cos \omega t)e^{-\gamma t}]^2 + c_0^2}$ [Fig. 2(a)] to reflect that the offset c_0 arises due to an experimental detection noise floor at the 10^{-2} level. The actual physical contrast does decay to zero $c(t) \rightarrow 0$. Remarkably, the fitted oscillation periods [e.g., $T = 11.6(4)\hbar/J_{xy}$ at $\lambda = 10.4a$] agree fairly well with the energy splitting $J_{xy}/2$ for the two-spin Heisenberg model [Fig. 2(c)], which implies an oscillation period of $T = 4\pi\hbar/J_{xy} \approx 12.57\hbar/J_{xy}$. With this fit function, the slower decay for large wave vectors Q shows up mainly in the oscillation frequency ω and not in the decay rate γ . For a simpler characterization of the decay, we obtain the initial decay rate by fitting a linear slope $c(t) = c_0(1 - \gamma t)$ to the initial decay in the range $c(t) \leq 0.4$. Results of such fits are shown in Fig. 2(b) (orange).

2. XXX model

a. Longitudinal spin relaxation [Fig. 2(e), purple]

As in our previous work [32] on spin transport, we use the fitting function $c(t) = (a_0 + b_0 \cos \omega t)e^{-\gamma t} + c_0$.

b. Transverse spin relaxation with spin echo [Figs. 2(d) and 2(e), blue]

The same fitting function yields oscillation frequencies ω and oscillating fractions $b_0/(a_0 + b_0)$ which agree fairly well with the longitudinal case, especially at large wave vectors Q , but with much larger error bars at small wave vectors Q , because the decay rate γ is much faster than the oscillations. For this reason, we constrain both parameters ω and $b_0/(a_0 + b_0)$ to the values obtained in the longitudinal case.

c. Transverse spin relaxation without spin echo [Figs. 2(d) and 2(e), orange; Fig. 3]

A beat note between the inner part and outer part of the cloud is visible (Fig. 3), due to the difference in effective magnetic fields. To determine the beat frequency Ω , we generalize the fitting function to the sum of two parts which interfere: $|c_1(t)e^{i\Omega t} + c_2(t)| = \sqrt{c_1(t)^2 + 2c_1(t)c_2(t)\cos(\Omega t) + c_2(t)^2}$. Here, $c_1(t) = (a_0 + b_0 \cos \omega t)e^{-\gamma t}$ is the contrast of the atoms in the inner part of the cloud, and $c_2(t) = c_2$ is the contrast of the isolated atoms in the outer part which preserve the contrast for a long time. We can neglect the background c_0 due to the detection noise. In $c_1(t)$, we again constrain the two parameters ω and $b_0/(a_0 + b_0)$ to the values obtained for longitudinal spin relaxation.

APPENDIX B: SPECTROSCOPIC OBSERVATION OF THE EFFECTIVE MAGNETIC FIELD

A spatially uniform effective magnetic field can always be transformed away in a suitable rotating frame. However, even then, it can still be observed as a shift of the spin-flip resonance. We rotate the spins via an adiabatic frequency

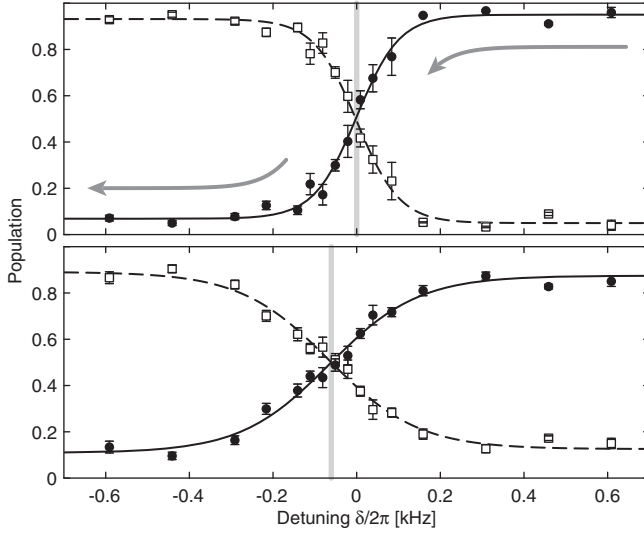


FIG. 7. Spectroscopic observation of the effective magnetic field h_z as a shift in the spin-flip frequency for $h_z < 0$ (bottom) compared to $h_z \approx 0$ (top). Shown is the fraction of atoms in each state as a function of the final detuning δ of a 22-ms sweep of the rf frequency, starting at $\delta = +30$ kHz with all atoms in the $|\uparrow\rangle$ state (closed circles) and no atoms in the $|\downarrow\rangle$ state (open squares). The detuning is relative to the single-particle transition frequency. The power of the rf drive is also ramped to zero after the frequency sweep to make the transition sharper. A nonzero detuning δ for equal spin populations compensates for the effective magnetic field h_z which shifts the curves for a lattice depth of $11E_R$ (bottom) compared to $35E_R$ (top) where $h_z \approx 0$. For the sweep experiment, we choose the second-lowest (closed circles) and third-lowest (open squares) hyperfine states of ${}^7\text{Li}$ due to the smaller sensitivity to external magnetic fields (originating from a smaller differential magnetic moment). At 1025 G, the scattering lengths are approximately $a_{\uparrow\uparrow} \approx a_{\downarrow\downarrow} \approx -50a_0$ and $a_{\uparrow\downarrow} \approx +350a_0$, leading to an estimate for an effective magnetic field of $h_z \approx -1.14J_{xy} \sim h \times (-100 \text{ Hz})$, which is consistent with our observation.

sweep, where the detuning corresponds to an external B_z field (in the rotating frame) and the Rabi frequency to a B_x field, realizing a Heisenberg model with magnetic fields. Starting from a fully polarized state with all atoms in the $|\downarrow\rangle$ state and large detuning of the rf, we reduce the B_z field adiabatically and observe the spin imbalance. The spins are balanced when the detuning compensates for the effective magnetic field created by superexchange. With this method, we can observe the effective field for different lattice depths (Fig. 7).

APPENDIX C: SEMICLASSICAL ANALYSIS AND SHORT-TIME EXPANSION OF SPIN DYNAMICS

1. The classical transverse spin helix with any wave vector Q does not evolve for any anisotropy Δ

We show here that, in the classical limit, the transverse spin helix with any wave vector Q does not evolve under

the XXZ Hamiltonian (assuming the effective magnetic field is uniform), for any isotropy Δ . The classical limit is reached by taking the spin-quantum number $S \rightarrow \infty$ or by treating the spins as classical vectors $\vec{S}_i = (S_i^x, S_i^y, S_i^z)$ of arbitrary length $S = |\vec{S}_i|$, which we set to $1/2$ for comparison to the quantum spin system.

We start with the system initialized at $t = 0$ in the helix state $S_i^\pm(0) = S e^{\pm i(Qz_i + \theta)}$, $S_i^z(0) = 0$, and we untwist the helix by using the rotation

$$\begin{pmatrix} S_i^x \\ S_i^y \\ S_i^z \end{pmatrix} = \begin{pmatrix} -\sin(Qz_i) & 0 & \cos(Qz_i) \\ \cos(Qz_i) & 0 & \sin(Qz_i) \\ 0 & 1 & 0 \end{pmatrix} \begin{pmatrix} T_i^x \\ T_i^y \\ T_i^z \end{pmatrix} \quad (\text{C1})$$

(we ignore the phase θ for simplicity), which gives $\vec{S}_i \mapsto \vec{T}_i$ with $T_i^\pm(0) = 0$, $T_i^z(0) = S$. The Hamiltonian Eq. (1) (with $h_z = 0$) then transforms as

$$\begin{aligned} H \mapsto H(Q) = & J_{xy} \sum_i [\cos(Qa)(T_i^x T_{i+1}^x + T_i^z T_{i+1}^z) \\ & + \sin(Qa)(T_i^z T_{i+1}^x - T_i^x T_{i+1}^z)] \\ & + J_z \sum_i T_i^y T_{i+1}^y. \end{aligned} \quad (\text{C2})$$

The Landau-Lifshitz (LL) equations of motion for classical spins read $\partial_t \vec{T}_i = \partial_{\vec{T}_i} H(Q) \times \vec{T}_i$. Upon changing variables to $T_i^\pm = T_i^x \pm iT_i^y$, we have

$$\begin{aligned} \dot{T}_i^+ = & \frac{1}{2} i \{ J_z (T_{i-1}^- + T_{i+1}^- - T_{i-1}^+ - T_{i+1}^+) T_i^z \\ & + J_{xy} [\sin(Qa) T_i^+ (T_{i-1}^- - T_{i+1}^- + T_{i-1}^+ - T_{i+1}^+) \\ & + 2T_i^z (T_{i-1}^z - T_{i+1}^z)] \\ & + \cos(Qa) [-(T_{i-1}^- + T_{i+1}^- + T_{i-1}^+ + T_{i+1}^+) T_i^z \\ & + 2T_i^+ (T_{i-1}^z + T_{i+1}^z)] \}, \end{aligned} \quad (\text{C3})$$

$$\dot{T}_i^- = \dot{T}_i^{+*}, \quad (\text{C4})$$

$$\begin{aligned} \dot{T}_i^z = & -\frac{1}{4} i \{ J_z (T_i^- + T_i^+) (T_{i-1}^- + T_{i+1}^- - T_{i-1}^+ - T_{i+1}^+) \\ & - J_{xy} (T_i^- - T_i^+) [\cos(Qa) (T_{i-1}^- + T_{i+1}^- + T_{i-1}^+ + T_{i+1}^+) \\ & + 2 \sin(Qa) (-T_{i-1}^z + T_{i+1}^z)] \}, \end{aligned} \quad (\text{C5})$$

and it is straightforward to verify that $T_i^\pm(t) = 0$, $T_i^z(t) = S$ is a solution to the LL equations, as claimed.

2. Stability of the classical spin-helix state: Dispersion relation of fluctuations

To understand the stability of the classical spin-helix states, we linearize the equations of motion about the classical solution and consider fluctuations. Now, T_i^z obeys

the constraint $T_i^z = \sqrt{S^2 - T_i^+ T_i^-}$, so fluctuations about the classical solution simply entail

$$T_i^\pm(t) = \bar{T}_i^\pm(t) + \delta T_i^\pm(t) + \mathcal{O}((\delta T)^2) = \delta T_i^\pm(t) + \mathcal{O}((\delta T)^2), \quad (\text{C6})$$

$$T_i^z(t) = S + \mathcal{O}((\delta T)^2). \quad (\text{C7})$$

Therefore, we get

$$\omega_k \begin{pmatrix} \delta T_k^+ \\ \delta T_k^- \end{pmatrix} = S J_{xy} \begin{pmatrix} -[-2 + \cos(ka)] \cos(Qa) - \Delta \cos(ka) & \cos(ka)[- \cos(Qa) + \Delta] \\ \cos(ka)[\cos(Qa) - \Delta] & [-2 + \cos(ka)] \cos(Qa) + \Delta \cos(ka) \end{pmatrix} \begin{pmatrix} \delta T_k^+ \\ \delta T_k^- \end{pmatrix} \quad (\text{C9})$$

with solution

$$\omega_k = \pm 2\sqrt{2} J_{xy} S \sqrt{\cos(Qa)[- \Delta \cos(ka) + \cos(Qa)] \sin^2(ka/2)}. \quad (\text{C10})$$

Reducing to $\Delta = 0$ reproduces the expression quoted in the main text for the XX model in Sec. III A. Note that we could have equivalently obtained the same dispersion relations by performing a spin-wave analysis, upon mapping the spins to Holstein-Primakoff bosons (in a large S expansion) and performing a Bogoliubov transformation to diagonalize the Hamiltonian in second order.

3. Short-time expansion of quantum dynamics

Owing to the factorizable nature of the initial spin-helix state, we can analytically derive the short-time quantum dynamics of the state without passing into a semiclassical limit as done before. The basic object is the Taylor expansion of a spin operator (in the transverse direction):

$$\langle S_i^+(t) \rangle = \langle S_i^+(0) \rangle + \langle \partial_t S_i^+(0) \rangle t + \frac{1}{2} \langle \partial_t^2 S_i^+(0) \rangle t^2 + \dots, \quad (\text{C11})$$

where $\langle \cdot \rangle$ is the expectation value in the spin state $|\psi(Q)\rangle = e^{-i \sum_i S_i^z Q z_i} |+\dots\rangle$, where $S_i^x |+\dots\rangle_i = S |+\dots\rangle_i$, and

$$\langle \partial_t S_i^+(0) \rangle = i \langle [H, S_i^+] \rangle, \quad (\text{C12})$$

$$\langle \partial_t^2 S_i^+(0) \rangle = - \langle [H, [H, S_i^+]] \rangle. \quad (\text{C13})$$

Since the Hamiltonian is a sum of strictly local terms and S_i^+ is an on-site term, the expressions in the commutators are comprised of only finite-range terms with support centered around site i . Using that the state factorizes into

$$\begin{aligned} \delta T_i^\pm &= \frac{iS}{2} [J_z (\delta T_{i-1}^- + \delta T_{i+1}^- - \delta T_{i-1}^+ - \delta T_{i+1}^+) \\ &\mp \cos(Qa) J_{xy} (\delta T_{i-1}^- + \delta T_{i+1}^- + \delta T_{i-1}^+ \\ &+ \delta T_{i+1}^+ - 4\delta T_i^\pm)]. \end{aligned} \quad (\text{C8})$$

We now expand in Fourier modes $\delta T_i^\pm = \sum_k \delta T_k^\pm e^{i(kz_i + \omega_k t)}$ with momentum k and dispersion ω_k . This reduces to an eigenvalue problem

a product state, we can easily evaluate the expression for these terms. We find for general spin S

$$i \langle [H, S_i^+] \rangle = 0, \quad (\text{C14})$$

$$- \langle [H, [H, S_i^+]] \rangle = -S^2 e^{iQz_i} [J_z - J_{xy} \cos(Qa)]^2. \quad (\text{C15})$$

(The vanishing of the term linear in t follows from time-reversal symmetry.) Therefore,

$$\langle S_i^+(t) \rangle = S e^{iQz_i} - \frac{1}{2} S^2 e^{iQz_i} [J_z - J_{xy} \cos(Qa)]^2 t^2 + \dots. \quad (\text{C16})$$

Extracting the Fourier component with wave vector Q gives the normalized contrast

$$c(t) = 1 - \frac{1}{2} S [J_z - J_{xy} \cos(Qa)]^2 t^2 + \dots. \quad (\text{C17})$$

A characteristic energy rate γ for the initial quadratic decay can, therefore, be defined as $c(t) = 1 - \gamma^2 t^2 + \dots$, yielding

$$\gamma := \sqrt{\frac{S}{2}} |J_{xy} [\Delta - \cos(Qa)]|. \quad (\text{C18})$$

Focusing now on $\Delta = 0$ and $S = 1/2$, this shows that a helix of wave vector Q decays with a rate going as $\gamma \propto |\cos(Qa)|$. For $\Delta = 1$, we recover that $\gamma \propto Q^2$ in the limit of $Q \ll 1/a$ (when the wavelength λ is large compared to the lattice spacing a). More generally, for arbitrary anisotropy Δ , there is a critical wave vector $(Q_c a) = \arccos(\Delta)$ where decay is expected to be very

slow; seeing such a dependence in experiments would be interesting. This prediction is actually in line with that the spin helix with wave vector $(Q_c a) = \arccos(\Delta)$ can be proven to be an *exact* eigenstate of the *XXZ* Hamiltonian with anisotropy Δ with appropriate boundary conditions, as shown in Refs. [38,39].

APPENDIX D: NUMERICAL SIMULATION DETAILS

Here, we present general details on the numerical simulations performed. Unless otherwise specified, we employ the time-evolving block decimation algorithm on matrix product states defined on 1D chains of length $L = 40a$, with large enough bond dimension to ensure convergence of local observables to a tolerance 10^{-4} , via the `TENPY` library [46].

In the absence of holes, we simulate the Heisenberg model (1), with the initial state the spin helix with wave vector Q , which reads locally $|\psi_i(Q)\rangle = e^{i(Qz_i + \theta)S_i^z}|+\rangle_i$, where $S_i^z|+\rangle_i = |+\rangle_i = (1/\sqrt{2})(|\uparrow\rangle_i + |\downarrow\rangle_i)$. Here, θ is the global initial phase of the spin helix, which varies from shot to shot in the experiment due to small magnetic field bias drifts (Appendix A). We measure $\langle S_i^x(t) \rangle$ and fit for each time slice a sine function in space with wave vector Q (allowing its phase to be an independent parameter); the amplitude of the sinusoidal modulation is the numerically determined contrast $c(t)$ normalized to unity at $t = 0$. We also average $c(t)$ over $\theta = 0, \pi/2$ to account for the fact that the global phase of the initial state in the experiments shifts from measurement to measurement (we find that averaging over these two values suffices to reproduce the full averaging over θ ; also see the methods section in Ref. [32]).

In the presence of holes, we simulate the bosonic \tilde{t} - J model [Eq. (F1)]. We assume holes occur independently on each site with probability p . In order to perform ensemble averaging over the different hole positions of the initial state, we employ the following computational trick. Let the on-site Hilbert space be spanned by the states $|0\rangle$, $|\uparrow\rangle_i := a_{i\uparrow}^\dagger|0\rangle$, and $|\downarrow\rangle_i := a_{i\downarrow}^\dagger|0\rangle$. We define a pure state on each site as

$$|\Psi_i(Q)\rangle = e^{i\varphi_i} \sqrt{1-p} |\psi_i(Q)\rangle + \sqrt{p} |0\rangle_i, \quad (\text{D1})$$

where φ_i is some phase with value in $[0, 2\pi)$. Clearly, in the limit $p \rightarrow 0$, the state $|\Psi(Q)\rangle := \prod_i |\Psi_i(Q)\rangle$ reduces to the pure-spin helix (i.e., without holes) with wave vector Q . Consider now the outer product of $|\Psi_i(Q)\rangle$ with itself when $p \neq 0$:

$$\begin{aligned} \rho_i &= (1-p) |\psi_i(Q)\rangle \langle \psi_i(Q)| \\ &+ e^{i\varphi_i} \sqrt{1-p} |\psi_i(Q)\rangle \langle 0|_i + \text{H.c.} + p |0\rangle_i \langle 0|_i. \end{aligned} \quad (\text{D2})$$

If we now average φ over the interval $[0, 2\pi)$ uniformly, the ensemble-averaged reduced density matrix is

$$\bar{\rho}_i = \frac{1}{2\pi} \int_0^{2\pi} d\varphi \rho_i = (1-p) |\psi_i(Q)\rangle \langle \psi_i(Q)| + p |0\rangle_i \langle 0|_i. \quad (\text{D3})$$

This reproduces the situation where holes occur locally and independently on each site i with probability p .

In our simulations, we choose a random set of phase angles $(\varphi_1, \dots, \varphi_N) \in [0, 2\pi)^N$ and time evolve the globally pure state $\prod_i |\Psi_i(Q)\rangle$ under the \tilde{t} - J Hamiltonian. We repeat the simulation with different sets of phase angles sampled randomly uniformly in $[0, 2\pi)^N$ and then average the extracted contrast.

We find that, in practice, there are remarkably only very small variations between different choices of phase angles [i.e., a given random choice of $\prod_i |\Psi_i(Q)\rangle$ is a typical configuration], allowing us to perform the ensemble average with relatively few repetitions (at most 50 runs for each Q and global phase θ).

APPENDIX E: NUMERICAL SIMULATION RESULTS

1. XX model

For the *XX* model, we utilize parameters $\Delta = 0$ and $h_z = 1.43J_{xy}$ (thus, simulating the experimental conditions at $V_z = 11E_R$), as well as $\tilde{t} = 4.11J_{xy}$, $J_{\uparrow\uparrow}/J_{\uparrow\downarrow} = -0.32$, and $J_{\downarrow\downarrow}/J_{\uparrow\downarrow} = 1.15$. Here, $J_{\sigma\sigma'} := -4\tilde{t}^2/U_{\sigma\sigma'}$.

Figure 8 shows decay curves for $p = 0, 0.05$, and 0.1 . The experimental decay rates $\gamma = 1/\tau$ [in Fig. 2(b)] are obtained from a linear fit $c(t) = c_0(1 - t/\tau)$ to the initial decay [$c(t) \leq 0.4$]. We use an equivalent procedure for the theoretical data and determine the time τ' where the numerical simulations show a contrast of $c(\tau') = 0.4$, which we then convert to the theoretical decay rate $\tau = (5/3)\tau'$. As shown in Fig. 2(b), the numerical data verifies the analytically predicted $\cos(Qa)$ dependence of the decay rate. This scaling starts to break down as $Q \rightarrow \pi/(2a)$, because higher-order terms in the expansion (either semiclassical or short-time) become important. Inclusion of holes washes out the $\cos(Qa)$ dependence.

2. XXX model

For the *XXX* model, we utilize parameters $\Delta = 1$ and $h_z = 0.80J_{xy}$ (thus, simulating the experimental conditions at $V_z = 11E_R$), as well as $\tilde{t} = 6.13J_{xy}$, $J_{\uparrow\uparrow}/J_{\uparrow\downarrow} = 0.61$, and $J_{\downarrow\downarrow}/J_{\uparrow\downarrow} = 1.40$.

Figures 9(a) and 9(b) show the results for a simulation involving 10% holes, i.e., $p = 0.1$. We fit the data between $c(t) = 0.9$ and 0.15 with a straight line (dashed) and obtain a decay rate defined as twice the slope of the fit (this factor is chosen because the slope of an exponential function at half decay is reduced by a factor of 2). Because of the nonexponential nature of the decay curves, for both

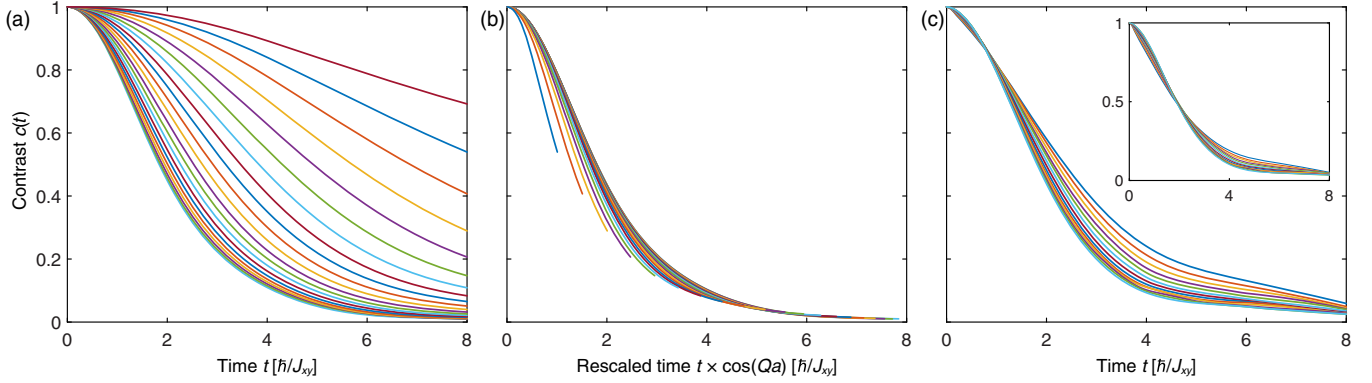


FIG. 8. Transverse spin-helix decay for the XX model obtained from numerical simulations, with hole probability $p = 0$ (a),(b), $p = 0.05$ (c), and $p = 0.1$ [(c), inset] with $h_z = 0$ (a),(b) and $h_z = 1.43J_{xy}$ (c) as in the experiment. The wavelengths in (a) are (from bottom to top) $\lambda = 31.3a, 23.5a, 18.8a, 15.7a, 13.4a, 11.7a, 10.4a, 9.4a, 8.5a, 7.8a, 7.2a, 6.7a, 6.3a, 5.9a, 5.6a, 5.3a, 5.0a, 4.8a, 4.6a, 4.4a$, and $4.0a$. The decay curves for pure spin dynamics (a) show a wave-vector dependence of decay rates of the form $\gamma \propto \cos(Qa)$. Using rescaled time $t \cos(Qa)$, all decay curves collapse almost perfectly for wavelengths $\lambda \geq 6.3a$, which covers the range studied in the experiment. The presence of holes washes out the $\cos(Qa)$ dependence (c), shown here for $\lambda \geq 6.3a$ and $p = 0.05$. At sufficiently high hole probability, e.g., $p = 0.1$ [(c), inset], the wave-vector dependence vanishes almost completely.

numerical simulations and experimental data, there is some arbitrariness in choosing “effective” decay rates which, depending on the parameterization, could differ by up to 50%. By further fitting the decay rates for the six smallest

values of Q values to the form $\gamma(Q) = DQ^2 + \gamma_0$ (in order to focus on the limiting $Q \rightarrow 0$ behavior), we obtain a Q -independent decay rate $\gamma_0 = 0.019J_{xy}/\hbar$ and a diffusion constant $D = 0.16a^2/(\hbar/J_{xy})$.

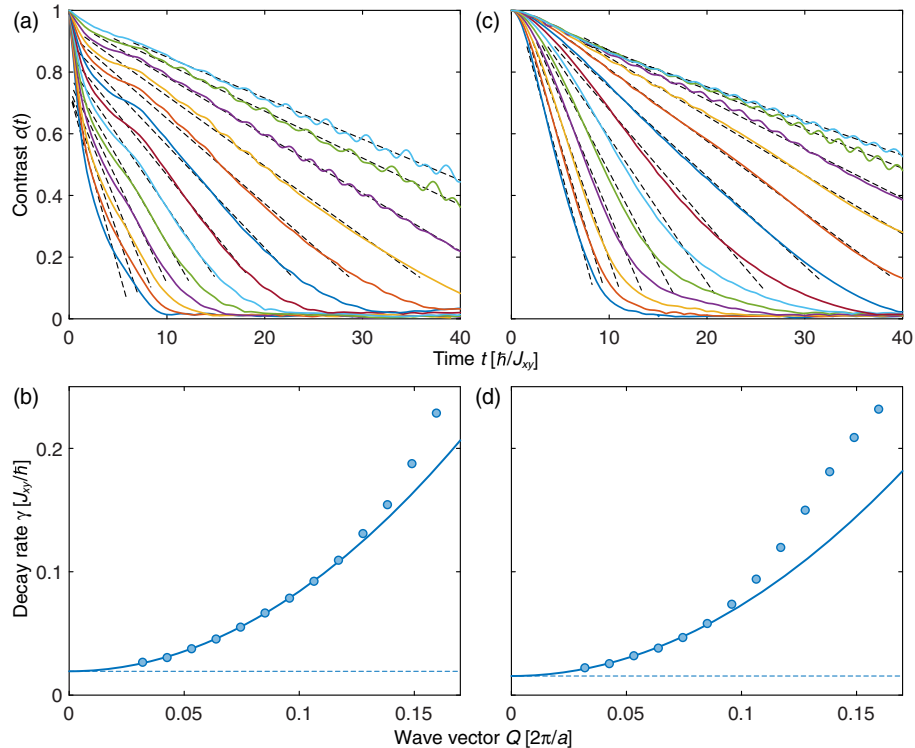


FIG. 9. Spin relaxation for the XXZ model. (a),(b) Isotropic model $\Delta = 1$ with finite hole concentration ($p = 0.1$). (c),(d) Slightly anisotropic $\Delta = 0.93$ with no holes ($p = 0$). The colored solid lines in (a) and (c) are decay curves $c(t)$ for different wavelengths $\lambda = 31.3a, 23.5a, 18.8a, 15.7a, 13.4a, 11.7a, 10.4a, 9.4a, 8.5a, 7.8a, 7.2a, 6.7a$, and $6.3a$ (from top to bottom). The dotted lines are linear fits to determine decay rates, which are shown in (b) and (d) with a fit $\gamma = DQ^2 + \gamma_0$ (solid line).

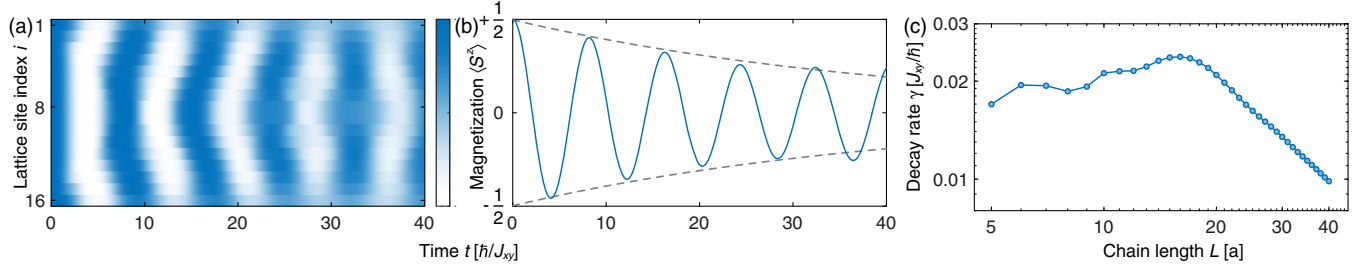


FIG. 10. Dephasing from the edges of the chains. (a),(b) Dynamics of an S_x -polarized ($Q = 0$) state for an $L = 16a$ finite chain, with anisotropy $\Delta = 1$ and $h_z = 0.8J_{xy}$ reflecting the parameters of the experiment. (a) shows how the initially homogeneous phase of the locally measured transverse spin $\langle S_i^x(t) \rangle$ gets distorted at the edges and how this perturbation propagates through the chain, leading to a loss of overall contrast of the total transverse magnetization $\sum_i \langle S_i^x(t) \rangle$ (b). A fit (dashed lines) to $\cos(\omega t + \phi)e^{-\gamma t}/2$ determines the decay rate γ , which is shown as a function of system size L in (c). A log-log plot shows the scaling $\gamma \propto L^{-1}$ for large L .

3. Near-isotropic XXZ model

We also investigate how a small deviation from the isotropic point affects dynamics. One reason is that our experimental data for the isotropic model is actually not taken exactly at the isotropic point but at $\Delta = 0.93 \pm 0.05$. In the two-site model, the triplet splitting of $J_{xy}(1 - \Delta)/2$ becomes $0.035J_{xy}/\hbar$, but the full simulation presented here shows that the effect is smaller.

We consider $\Delta = 0.93$ and $h_z = 0.89J_{xy}$ (thus, simulating the experimental conditions at $V_z = 11E_R$), as well as $\tilde{t} = 6.15J_{xy}$, $J_{\uparrow\uparrow}/J_{\uparrow\downarrow} = 0.53$, and $J_{\downarrow\downarrow}/J_{\uparrow\downarrow} = 1.41$. Figures 9(c) and 9(d) show the results for a simulation in the absence of holes. We use the same method as for the XXX model to determine decay rates from linear fits. We obtain a Q -independent decay rate $\gamma_0 = 0.015J_{xy}/\hbar$ and a diffusion constant $D = 0.15a^2/(\hbar/J_{xy})$.

4. Dephasing from edge effects

We also use numerical simulations to study how the inhomogeneity of the effective magnetic field at the ends of finite chains leads to dephasing for transverse spin components. We concentrate on the $Q \rightarrow 0$ limit, i.e., a state uniformly polarized in the S_x direction, with anisotropy $\Delta = 1$.

If the effective magnetic field is globally uniform, the transverse magnetization $\sum_i \langle S_i^x(t) \rangle$ just oscillates in time without decaying. However, the fact that the edges of the chain feel an effective magnetic field strength which is half that of the bulk causes dephasing of spins at the edges. This disturbance, in turn, propagates into the bulk [see Fig. 10(a)], so that the transverse magnetization decays in time [see Fig. 10(b)]. For long chains, the decay rate decreases as a function of length L , as the bulk dominates the edges. This trend starts only for chains with $L > 16a$. For smaller L , the trend is reversed due to few-body dynamics.

We also explore the effect of the effective magnetic field in the XX model. Comparison of simulations of the pure spin model with and without an effective magnetic field of $h_z = 1.43J_{xy}$ shows that the edge effect for chains of length $L = 40a$ give rise to a Q -independent decay rate of $0.04\hbar/J_{xy}$, which amounts to shifting the black curve in Fig. 2(b) (for $h_z = 0$) vertically.

APPENDIX F: DERIVATION OF THE BOSONIC \tilde{t} - J MODEL

We derive here the bosonic \tilde{t} - J model

$$\begin{aligned}
 H_{\tilde{t}-J} = & \sum_{\langle ij \rangle} \left[J_{xy} (S_i^x S_j^x + S_i^y S_j^y) + J_z S_i^z S_j^z - \frac{h_z}{2} [S_i^z (n_{j\uparrow} + n_{j\downarrow}) + (n_{i\uparrow} + n_{i\downarrow}) S_j^z] + c (n_{i\uparrow} + n_{i\downarrow}) (n_{j\uparrow} + n_{j\downarrow}) \right] \\
 & - \sum_{\langle ij \rangle, \sigma} \tilde{t} a_{i\sigma}^\dagger a_{j\sigma} + \text{H.c.} - \sum_{\langle ijk \rangle, \sigma} \left[\frac{\tilde{t}^2}{U_{\uparrow\downarrow}} a_{i\sigma}^\dagger n_{j\bar{\sigma}} a_{k\sigma} + \frac{\tilde{t}^2}{U_{\uparrow\downarrow}} a_{i\bar{\sigma}}^\dagger S_j^\sigma a_{k\sigma} + \frac{2\tilde{t}^2}{U_{\sigma\sigma}} a_{i\sigma}^\dagger n_{j\sigma} a_{k\sigma} \right] + \text{H.c.} \quad (\text{F1})
 \end{aligned}$$

quoted in the main text. Here, spin $\sigma = \uparrow, \downarrow$, and $a_{i\sigma}$ and $a_{i\sigma}^\dagger$ are bosonic lowering and raising operators, respectively, at site i , such that $S_i^\uparrow \equiv S_i^+ := a_{i\uparrow}^\dagger a_{i\downarrow}$, $S_i^\downarrow \equiv S_i^- = (S_i^+)^\dagger$, and $S_i^x = \frac{1}{2}(S_i^+ + S_i^-)$, $S_i^y = \frac{1}{2i}(S_i^+ - S_i^-)$, $S_i^z = \frac{1}{2}(n_{i\uparrow} - n_{i\downarrow})$ form a representation of the Pauli algebra, upon restricting

the on-site Hilbert space to be spanned by three states: an occupancy of a single boson (either spin $|\uparrow\rangle$ or $|\downarrow\rangle$) or no boson (hole). Also, $c = -(\tilde{t}^2/U_{\uparrow\uparrow} + \tilde{t}^2/U_{\downarrow\downarrow} + \tilde{t}^2/U_{\uparrow\downarrow})$.

The above Hamiltonian illustrates that the previously identified effective magnetic field term $\sum_{\langle ij \rangle} (h_z/2)(S_i^z + S_j^z)$ in fact stems from a direct *interaction* term describing

magnon-density coupling $S_i^z(n_{j\uparrow} + n_{j\downarrow}) + (i \leftrightarrow j)$, the latter of which reduces to the former upon taking the limit of no holes, i.e., $(n_{i\uparrow} + n_{i\downarrow}) = 1$ for every site i . The terms on the lower line represent dynamics of holes in different flavors: bare tunneling, density-assisted tunneling, and spin-flip-assisted tunneling, which are additional magnon-hole couplings. Note that they arise at the same order in perturbation theory (in $\tilde{t}/U_{\sigma\sigma'}$) as the pure spin couplings and, thus, in principle, cannot be neglected, although they *are* suppressed by the presence of a small hole probability p . By inspecting the expressions of J_z , h_z , and these extra terms as a function of $U_{\uparrow\uparrow}$, $U_{\uparrow\downarrow}$, and $U_{\downarrow\downarrow}$, we see that at $\Delta = 1$ (isotropic spin couplings) a nonzero h_z is a *necessary* and *sufficient* condition for the \tilde{t} - J model to break spin rotational symmetry. (Having spin rotational symmetry requires all on-site interaction energies to be equal $U_{\uparrow\uparrow} = U_{\uparrow\downarrow} = U_{\downarrow\downarrow}$.) This justifies our identification of the effective magnetic field as the agent giving rise to differences in dynamics between the transverse and the longitudinal spin helix.

To derive the bosonic \tilde{t} - J model, the starting point is the Bose-Hubbard Hamiltonian describing cold atoms moving in a deep optical lattice (so that they are confined to the lowest Bloch band):

$$H = - \sum_{\langle ij \rangle, \sigma} \tilde{t} (a_{i\sigma}^\dagger a_{j\sigma} + \text{H.c.}) + \frac{1}{2} \sum_{i, \sigma} U_{\sigma\sigma} n_{i\sigma} (n_{i\sigma} - 1) + U_{\uparrow\downarrow} \sum_i n_{i\uparrow} n_{i\downarrow}. \quad (\text{F2})$$

We assume two components $\sigma = \uparrow, \downarrow$ and $U_{\sigma\sigma'} \gg \tilde{t}$, such that there are at most singly occupied sites. We derive the effective model in this limit. We do not assume $U_{\uparrow\uparrow}$, $U_{\uparrow\downarrow}$, and $U_{\downarrow\downarrow}$ are necessarily equal between themselves.

We employ the expansion detailed in Ref. [47], where it is shown how having multiple emergent $U(1)$ charges emerge in an effective Hamiltonian. The general setup is as such: Let $\Gamma_1, \dots, \Gamma_m$ be m mutually commuting operators with integer eigenvalue spacings, and consider the Hamiltonian

$$H = \vec{\omega} \cdot \vec{\Gamma} + V, \quad (\text{F3})$$

where V need not commute with Γ_i . In the limit of large $|\vec{\omega}|$, we can derive an effective Hamiltonian

$$H_{\text{eff}} = \vec{\omega} \cdot \vec{\Gamma} + H'_0 + \frac{1}{2} \sum_{\vec{n} \neq 0} \frac{[H'_0, H'_{-\vec{n}}]}{\vec{n} \cdot \vec{\omega}} + \dots \quad (\text{F4})$$

(this turns out to be the so-called van Vleck expansion). The effective Hamiltonian has emergent symmetries $[H_{\text{eff}}, \Gamma_i] = 0$; i.e., the Hamiltonian is symmetric with respect to the m $U(1)$ charges Γ_i . Here, H'_n is the \vec{n} th Fourier mode of the “interaction” Hamiltonian defined on the m -torus \mathbb{T}^m :

$$H'(\vec{\theta}) = U_0^\dagger(\vec{\theta}) V U_0(\vec{\theta}), \quad (\text{F5})$$

$$U_0(\vec{\theta}) = e^{-i\vec{\theta} \cdot \vec{\Gamma}}, \quad (\text{F6})$$

$$H'_n = \frac{1}{(2\pi)^m} \int_{\mathbb{T}^m} d^m \theta e^{-i\vec{n} \cdot \vec{\theta}} H'(\vec{\theta}). \quad (\text{F7})$$

Applying this formalism to the Bose-Hubbard model, we note that interactions there consist of three kinds:

$$U_{\downarrow\downarrow} \Gamma_1; \quad \Gamma_1 = \sum_i \frac{1}{2} n_{i\downarrow} (n_{i\downarrow} - 1), \quad (\text{F8})$$

$$U_{\uparrow\uparrow} \Gamma_2; \quad \Gamma_2 = \sum_i \frac{1}{2} n_{i\uparrow} (n_{i\uparrow} - 1), \quad (\text{F9})$$

$$U_{\uparrow\downarrow} \Gamma_3; \quad \Gamma_3 = \sum_i n_{i\uparrow} n_{i\downarrow} \quad (\text{F10})$$

and that Γ_i have integer eigenvalues and mutually commute. We, therefore, identify $\omega_1 = U_{\downarrow\downarrow}$, $\omega_2 = U_{\uparrow\uparrow}$, and $\omega_3 = U_{\uparrow\downarrow}$. We define

$$U_0(\vec{\theta}) := \exp(-i\vec{\theta} \cdot \vec{\Gamma}), \quad (\text{F11})$$

which gives us

$$H'(\vec{\theta}) := U_0(\vec{\theta})^\dagger \sum_{\langle ij \rangle, \sigma} \tilde{t} (a_{i\sigma}^\dagger a_{j\sigma} + \text{H.c.}) U_0(\vec{\theta}). \quad (\text{F12})$$

We have

$$\begin{aligned} e^{i\theta_3 \Gamma_3} a_{i\uparrow}^\dagger e^{-i\theta_3 \Gamma_3} &= a_{i\uparrow}^\dagger + (i\theta_3) [n_{i\uparrow} n_{i\downarrow}, a_{i\uparrow}^\dagger] + \frac{(i\theta_3)^2}{2!} \\ &\times [n_{i\uparrow} n_{i\downarrow}, [n_{i\uparrow} n_{i\downarrow}, a_{i\uparrow}^\dagger]] + \dots \\ &= a_{i\uparrow}^\dagger + (i\theta_3) a_{i\uparrow}^\dagger n_{i\downarrow} + \frac{(i\theta_3)^2}{2!} a_{i\uparrow}^\dagger (n_{i\downarrow}^\dagger)^2 + \dots \\ &= a_{i\uparrow}^\dagger e^{i\theta_3 n_{i\downarrow}}. \end{aligned} \quad (\text{F13})$$

Therefore,

$$e^{i\theta_3 \Gamma_3} a_{i\uparrow}^\dagger e^{-i\theta_3 \Gamma_3} = a_{i\uparrow}^\dagger e^{i\theta_3 n_{i\downarrow}}, \quad (\text{F14})$$

$$e^{i\theta_3 \Gamma_3} a_{i\uparrow} e^{-i\theta_3 \Gamma_3} = a_{i\uparrow} e^{-i\theta_3 n_{i\downarrow}}, \quad (\text{F15})$$

$$e^{i\theta_3 \Gamma_3} a_{i\downarrow}^\dagger e^{-i\theta_3 \Gamma_3} = a_{i\downarrow}^\dagger e^{i\theta_3 n_{i\uparrow}}, \quad (\text{F16})$$

$$e^{i\theta_3 \Gamma_3} a_{i\downarrow} e^{-i\theta_3 \Gamma_3} = a_{i\downarrow} e^{-i\theta_3 n_{i\uparrow}}. \quad (\text{F17})$$

Next,

$$e^{i\theta_2\Gamma_2} a_{i\uparrow}^\dagger e^{-i\theta_2\Gamma_2} = a_{i\uparrow}^\dagger + (i\theta_2) \left[\frac{1}{2} n_{i\uparrow} (n_{i\uparrow} - 1), a_{i\uparrow}^\dagger \right] + \frac{(i\theta_2)^2}{2!} \left[\frac{1}{2} n_{i\uparrow} (n_{i\uparrow} - 1), \left[\frac{1}{2} n_{i\uparrow} (n_{i\uparrow} - 1), a_{i\uparrow}^\dagger \right] \right] + \dots \quad (\text{F18})$$

A single commutator yields

$$\begin{aligned} \left[\frac{1}{2} n_{i\uparrow} (n_{i\uparrow} - 1), a_{i\uparrow}^\dagger \right] &= \frac{1}{2} [n_{i\uparrow}, a_{i\uparrow}^\dagger] (n_{i\uparrow} - 1) + \frac{1}{2} n_{i\uparrow} [(n_{i\uparrow} - 1), a_{i\uparrow}^\dagger] \\ &= \frac{1}{2} a_{i\uparrow}^\dagger (n_{i\uparrow} - 1) + \frac{1}{2} n_{i\uparrow} a_{i\uparrow}^\dagger \\ &= a_{i\uparrow}^\dagger n_{i\uparrow} \end{aligned} \quad (\text{F19})$$

so the full expression becomes

$$\begin{aligned} e^{i\theta_2\Gamma_2} a_{i\uparrow}^\dagger e^{-i\theta_2\Gamma_2} &= a_{i\uparrow}^\dagger + (i\theta_2) a_{i\uparrow}^\dagger n_{i\uparrow} + \frac{(i\theta_2)^2}{2!} a_{i\uparrow}^\dagger (n_{i\uparrow})^2 + \dots \\ &= a_{i\uparrow}^\dagger e^{i\theta_2 n_{i\uparrow}}. \end{aligned} \quad (\text{F20})$$

Similarly, we have

$$e^{i\theta_2\Gamma_2} a_{i\uparrow} e^{-i\theta_2\Gamma_2} = e^{-i\theta_2 n_{i\uparrow}} a_{i\uparrow}. \quad (\text{F21})$$

Therefore, there are four terms in $H'(\vec{\theta})$:

$$U_0(\vec{\theta})^\dagger a_{i\uparrow}^\dagger a_{j\uparrow} U_0(\vec{\theta}) = a_{i\uparrow}^\dagger e^{i(\theta_3 n_{i\downarrow} + \theta_2 n_{i\uparrow})} e^{-i(\theta_3 n_{j\downarrow} + \theta_2 n_{j\uparrow})} a_{j\uparrow}, \quad (\text{F22})$$

$$U_0(\vec{\theta})^\dagger a_{j\uparrow}^\dagger a_{i\uparrow} U_0(\vec{\theta}) = a_{j\uparrow}^\dagger e^{i(\theta_3 n_{j\downarrow} + \theta_2 n_{j\uparrow})} e^{-i(\theta_3 n_{i\downarrow} + \theta_2 n_{i\uparrow})} a_{i\uparrow}, \quad (\text{F23})$$

$$U_0(\vec{\theta})^\dagger a_{i\downarrow}^\dagger a_{j\downarrow} U_0(\vec{\theta}) = a_{i\downarrow}^\dagger e^{i(\theta_3 n_{i\uparrow} + \theta_1 n_{i\downarrow})} e^{-i(\theta_3 n_{j\uparrow} + \theta_1 n_{j\downarrow})} a_{j\downarrow}, \quad (\text{F24})$$

$$U_0(\vec{\theta})^\dagger a_{j\downarrow}^\dagger a_{i\downarrow} U_0(\vec{\theta}) = a_{j\downarrow}^\dagger e^{i(\theta_3 n_{j\uparrow} + \theta_1 n_{j\downarrow})} e^{-i(\theta_3 n_{i\uparrow} + \theta_1 n_{i\downarrow})} a_{i\downarrow}. \quad (\text{F25})$$

Now, the \vec{n} th Fourier mode of $H'(\vec{\theta})$ enforces projectors of certain occupation numbers between sites. For example, for the first term and $n_1 = 0$, $n_2 = 0$, $n_3 = 1$, this is

$$a_{i\uparrow}^\dagger \mathbb{P}_{n_{i\downarrow} - n_{j\downarrow} = 1} \mathbb{P}_{n_{i\uparrow} - n_{j\uparrow} = 0} a_{j\uparrow}. \quad (\text{F26})$$

We evaluate Eq. (F4), and the result is Eq. (F1) (ignoring the constant term $\vec{\omega} \cdot \vec{\Gamma}$).

-
- [1] W. Heisenberg, *Mehrkörperproblem und Resonanz in der Quantenmechanik*, *Z. Phys.* **38**, 411 (1926).
[2] P. A. M. Dirac, *On the Theory of Quantum Mechanics*, *Proc. R. Soc. A* **112**, 661 (1926).
[3] J. H. V. Vleck, *The Theory of Electric and Magnetic Susceptibilities*, International Series of Monographs on Physics (Oxford University, New York, 1932).
[4] A. Auerbach, *Interacting Electrons and Quantum Magnetism* (Springer-Verlag, Berlin, 1994).

- [5] K. Binder and A. P. Young, *Spin Glasses: Experimental Facts, Theoretical Concepts, and Open Questions*, *Rev. Mod. Phys.* **58**, 801 (1986).
[6] L. Savary and L. Balents, *Quantum Spin Liquids: A Review*, *Rep. Prog. Phys.* **80**, 016502 (2017).
[7] R. Vasseur and J. E. Moore, *Nonequilibrium Quantum Dynamics and Transport: From Integrability to Many-Body Localization*, *J. Stat. Mech.* (2016) 064010.
[8] B. Bertini, F. Heidrich-Meisner, C. Karrasch, T. Prosen, R. Steinigeweg, and M. Žnidarič, *Finite-Temperature Transport in One-Dimensional Quantum Lattice Models*, *Rev. Mod. Phys.* **93**, 025003 (2021).
[9] M. Ljubotina, M. Žnidarič, and T. Prosen, *Spin Diffusion from an Inhomogeneous Quench in an Integrable System*, *Nat. Commun.* **8**, 16117 (2017).
[10] S. Gopalakrishnan and R. Vasseur, *Kinetic Theory of Spin Diffusion and Superdiffusion in XXZ Spin Chains*, *Phys. Rev. Lett.* **122**, 127202 (2019).
[11] E. Ilievski, J. De Nardis, M. Medenjak, and T. Prosen, *Superdiffusion in One-Dimensional Quantum Lattice Models*, *Phys. Rev. Lett.* **121**, 230602 (2018).

- [12] B. Bertini, M. Collura, J. De Nardis, and M. Fagotti, *Transport in Out-of-Equilibrium XXZ Chains: Exact Profiles of Charges and Currents*, *Phys. Rev. Lett.* **117**, 207201 (2016).
- [13] O. A. Castro-Alvaredo, B. Doyon, and T. Yoshimura, *Emergent Hydrodynamics in Integrable Quantum Systems out of Equilibrium*, *Phys. Rev. X* **6**, 041065 (2016).
- [14] M. Babadi, E. Demler, and M. Knap, *Far-from-Equilibrium Field Theory of Many-Body Quantum Spin Systems: Prethermalization and Relaxation of Spin Spiral States in Three Dimensions*, *Phys. Rev. X* **5**, 041005 (2015).
- [15] S. Bhattacharyya, J. F. Rodriguez-Nieva, and E. Demler, *Universal Prethermal Dynamics in Heisenberg Ferromagnets*, *Phys. Rev. Lett.* **125**, 230601 (2020).
- [16] J. F. Rodriguez-Nieva, A. Schuckert, D. Sels, M. Knap, and E. Demler, *Transverse Instability and Universal Decay of Spin Spiral Order in the Heisenberg Model*, arXiv:2011.07058.
- [17] J. F. Rodriguez-Nieva, *Turbulent Relaxation after a Quench in the Heisenberg Model*, *Phys. Rev. B* **104**, L060302 (2021).
- [18] C. Gross and I. Bloch, *Quantum Simulations with Ultracold Atoms in Optical Lattices*, *Science* **357**, 995 (2017).
- [19] D. Jaksch, C. Bruder, J. I. Cirac, C. W. Gardiner, and P. Zoller, *Cold Bosonic Atoms in Optical Lattices*, *Phys. Rev. Lett.* **81**, 3108 (1998).
- [20] A. B. Kuklov and B. V. Svistunov, *Counterflow Superfluidity of Two-Species Ultracold Atoms in a Commensurate Optical Lattice*, *Phys. Rev. Lett.* **90**, 100401 (2003).
- [21] L.-M. Duan, E. Demler, and M. D. Lukin, *Controlling Spin Exchange Interactions of Ultracold Atoms in Optical Lattices*, *Phys. Rev. Lett.* **91**, 090402 (2003).
- [22] J. J. García-Ripoll and J. I. Cirac, *Spin Dynamics for Bosons in an Optical Lattice*, *New J. Phys.* **5**, 76 (2003).
- [23] E. Altman, W. Hofstetter, E. Demler, and M. D. Lukin, *Phase Diagram of Two-Component Bosons on an Optical Lattice*, *New J. Phys.* **5**, 113 (2003).
- [24] M. A. Nichols, L. W. Cheuk, M. Okan, T. R. Hartke, E. Mendez, T. Senthil, E. Khatami, H. Zhang, and M. W. Zwierlein, *Spin Transport in a Mott Insulator of Ultracold Fermions*, *Science* **363**, 383 (2019).
- [25] T. Fukuhara *et al.*, *Quantum Dynamics of a Mobile Spin Impurity*, *Nat. Phys.* **9**, 235 (2013).
- [26] T. Fukuhara, P. Schauß, M. Endres, S. Hild, M. Cheneau, I. Bloch, and C. Gross, *Microscopic Observation of Magnon Bound States and Their Dynamics*, *Nature (London)* **502**, 76 (2013).
- [27] S. Hild, T. Fukuhara, P. Schauss, J. Zeiher, M. Knap, E. Demler, I. Bloch, and C. Gross, *Far-from-Equilibrium Spin Transport in Heisenberg Quantum Magnets*, *Phys. Rev. Lett.* **113**, 147205 (2014).
- [28] R. C. Brown, R. Wyllie, S. B. Koller, E. A. Goldschmidt, M. Foss-Feig, and J. V. Porto, *Two-Dimensional Superexchange-Mediated Magnetization Dynamics in an Optical Lattice*, *Science* **348**, 540 (2015).
- [29] L. W. Cheuk, M. A. Nichols, K. R. Lawrence, M. Okan, H. Zhang, and M. W. Zwierlein, *Observation of 2D Fermionic Mott Insulators of ^{40}K with Single-Site Resolution*, *Phys. Rev. Lett.* **116**, 235301 (2016).
- [30] M. F. Parsons, A. Mazurenko, C. S. Chiu, G. Ji, D. Greif, and M. Greiner, *Site-Resolved Measurement of the Spin-Correlation Function in the Fermi-Hubbard Model*, *Science* **353**, 1253 (2016).
- [31] A. Mazurenko, C. S. Chiu, G. Ji, M. F. Parsons, M. Kanász-Nagy, R. Schmidt, F. Grusdt, E. Demler, D. Greif, and M. Greiner, *A Cold-Atom Fermi-Hubbard Antiferromagnet*, *Nature (London)* **545**, 462 (2017).
- [32] P. N. Jepsen, J. Amato-Grill, I. Dimitrova, W. W. Ho, E. Demler, and W. Ketterle, *Spin Transport in a Tunable Heisenberg Model Realized with Ultracold Atoms*, *Nature (London)* **588**, 403 (2020).
- [33] J. Spalek, *t-J Model Then and Now: A Personal Perspective from the Pioneering Times*, *Acta Phys. Pol. A* **111**, 409 (2007).
- [34] F. C. Zhang and T. M. Rice, *Effective Hamiltonian for the Superconducting Cu Oxides*, *Phys. Rev. B* **37**, 3759 (1988).
- [35] P. W. Anderson, P. A. Lee, M. Randeria, T. M. Rice, N. Trivedi, and F. C. Zhang, *The Physics behind High-Temperature Superconducting Cuprates: The Plain Vanilla Version of RVB*, *J. Phys. Condens. Matter* **16**, R755 (2004).
- [36] M. Koschorreck, D. Pertot, E. Vogt, and M. Köhl, *Universal Spin Dynamics in Two-Dimensional Fermi Gases*, *Nat. Phys.* **9**, 405 (2013).
- [37] S. Trotzky, S. Beattie, C. Luciuk, S. Smale, A. B. Bardou, T. Enss, E. Taylor, S. Zhang, and J. H. Thywissen, *Observation of the Leggett-Rice Effect in a Unitary Fermi Gas*, *Phys. Rev. Lett.* **114**, 015301 (2015).
- [38] V. Popkov, X. Zhang, and A. Klümper, *Phantom Bethe Excitations and Spin Helix Eigenstates in Integrable Periodic and Open Spin Chains*, *Phys. Rev. B* **104**, L081410 (2021).
- [39] X. Zhang, A. Klümper, and V. Popkov, *Phantom Bethe Roots in the Integrable Open Spin- $\frac{1}{2}$ XXZ Chain*, *Phys. Rev. B* **103**, 115435 (2021).
- [40] I. Dimitrova, N. Jepsen, A. Buyskikh, A. Venegas-Gomez, J. Amato-Grill, A. Daley, and W. Ketterle, *Enhanced Superexchange in a Tilted Mott Insulator*, *Phys. Rev. Lett.* **124**, 043204 (2020).
- [41] C. L. Degen, F. Reinhard, and P. Cappellaro, *Quantum Sensing*, *Rev. Mod. Phys.* **89**, 035002 (2017).
- [42] C. P. Slichter, *Principles of Magnetic Resonance*, Springer Series in Solid-State Sciences (Springer, Berlin, 1990).
- [43] The prefactor 1.14 is somewhat arbitrarily obtained by integrating the probability for a localized particle to be on the original site, $J_0[t/(\hbar/2\tau)]^2$ to the first zero of the Bessel function J_0 .
- [44] B. J. Verhaar, E. G. M. van Kempen, and S. J. J. M. F. Kokkelmans, *Predicting Scattering Properties of Ultracold Atoms: Adiabatic Accumulated Phase Method and Mass Scaling*, *Phys. Rev. A* **79**, 032711 (2009).
- [45] G. Martinez and P. Horsch, *Spin Polarons in the t-J Model*, *Phys. Rev. B* **44**, 317 (1991).
- [46] J. Hauschild and F. Pollmann, *Efficient Numerical Simulations with Tensor Networks: Tensor Network Python (TENPY)*, *SciPost Phys. Lect. Notes* **5** (2018). Code available from <https://github.com/tenpy/tenpy>.
- [47] D. V. Else, W. W. Ho, and P. T. Dumitrescu, *Long-Lived Interacting Phases of Matter Protected by Multiple Time-Translation Symmetries in Quasiperiodically Driven Systems*, *Phys. Rev. X* **10**, 021032 (2020).

Appendix C

Catching Bethe phantoms and quantum many-body scars: Long-lived spin-helix states in Heisenberg magnets

P. N. Jepsen, Y. K. Lee, H. Lin, I. Dimitrova, Y. Margalit, W. W. Ho, W. Ketterle
Catching Bethe phantoms and quantum many-body scars: Long-lived spin-helix
states in Heisenberg magnets
arXiv:2110.12043 (2021)

Catching Bethe phantoms and quantum many-body scars: Long-lived spin-helix states in Heisenberg magnets

Paul Niklas Jepsen,^{1,2,3} Yoo Kyung Lee,^{1,2,3} Hanzhen Lin,^{1,2,3} Ivana
Dimitrova,^{3,4} Yair Margalit,^{1,2,3} Wen Wei Ho,^{4,5} and Wolfgang Ketterle^{1,2,3}

¹*Department of Physics, Massachusetts Institute of Technology, Cambridge, MA 02139, USA*

²*Research Laboratory of Electronics, Massachusetts Institute of Technology, Cambridge, MA 02139, USA*

³*MIT-Harvard Center for Ultracold Atoms, Cambridge, MA, USA*

⁴*Department of Physics, Harvard University, Cambridge, MA 02138, USA*

⁵*Department of Physics, Stanford University, Stanford, CA 94305, USA*

Exact solutions for quantum many-body systems are rare and provide valuable insight to universal phenomena. Here we show experimentally in anisotropic Heisenberg chains that special helical spin patterns can have very long lifetimes. This finding confirms the recent prediction of phantom Bethe states, exact many-body eigenstates carrying finite momenta yet no energy. We theoretically find analogous stable spin helices in higher dimensions and in other non-integrable systems, where they imply non-thermalizing dynamics associated with quantum many-body scars. We use phantom spin helices to directly measure the interaction anisotropy which has a major contribution from short-range off-site interactions that have not been observed before. Phantom helix states open new opportunities for quantum simulations of spin physics and studies of many-body dynamics.

The dynamics of strongly-interacting, quantum many-body systems is an active frontier of research. It has broad implications ranging from understanding fundamental phenomena like quantum thermalization or the lack thereof [1–5], to realizing new forms of matter (e.g. time crystals [6, 7]) and to controlling entanglement for quantum information processing [8, 9].

However, analyzing in full such systems is difficult due to their complexity. Exactly-solvable models are therefore especially important and desirable since they can directly reveal the physical mechanisms behind universal phenomena. For example, the transverse field Ising model in one spatial dimension can be solved in terms of free fermions and serves as a paradigmatic model for quantum criticality [10, 11].

The spin-1/2 anisotropic Heisenberg model in one dimension, which is given by

$$H = J_{xy} \sum_{\langle ij \rangle} [S_i^x S_j^x + S_i^y S_j^y + \Delta S_i^z S_j^z], \quad (1)$$

is another such example. Here, the transverse and longitudinal spin couplings (between neighboring sites i, j) are J_{xy} and $J_z := \Delta J_{xy}$, where Δ is the spin-exchange anisotropy. While the model seems simple and has been known to be solvable by the Bethe ansatz for almost a century [12, 13], it gives rise to rich dynamics which are still not completely understood. Indeed, only recently was it predicted that the isotropic system ($\Delta = 1$) yields an exotic Kardar-Parisi-Zhang superdiffusive regime of transport [14–16] which has been subsequently experimentally confirmed by [17]. Yet another surprise has come from the recent theoretical discovery of a special set of degenerate many-body eigenstates in the model for any anisotropy — so-called phantom Bethe states [18]. These are states composed of quasiparticles which carry momentum but contribute zero energy (relative to the ferromagnetic “vacuum” state), akin to ghost parti-

cles, hence the name phantom. Simple patterns of spins winding in the transverse plane — i.e. spin-helix states — also share these phantom properties if their pitch λ or wavevector $Q := 2\pi/\lambda = Q_p$, where Q_p satisfies the phantom condition

$$\Delta = \cos(Q_p a), \quad (2)$$

with a being the lattice spacing. These states, which we call phantom helix states, are exact many-body eigenstates and do not decay. Since interactions, even in an integrable model, are expected to cause a system to locally relax to a (generalized) Gibbs ensemble [13, 19], such a long-lived and far-from-equilibrium state represents a surprising exception to (generalized) quantum thermalization.

In this work, we systematically explore the dynamics of spin-helix states using our versatile ultracold atom quantum simulator platform with tunable anisotropy [20, 21]. Specifically, we study their decay as a function of wavevector Q for different fixed anisotropies Δ , and find a non-monotonic decay rate with a pronounced minimum near the expected special value Q_p . This is the signature of the phantom spin-helix state, confirming the predictions of [18]. We further theoretically establish generalizations of the phantom spin-helix states to Heisenberg systems of higher dimensions, with higher spin quantum numbers, and for non-cubic lattice geometries. While 1D spin-1/2 models are integrable, these generalizations are not; therefore, the existence of stable far-from-equilibrium helices in such systems leads to genuinely non-thermalizing dynamics associated with quantum many-body scars [22]. We propose an experimental protocol to realize them with ultracold atoms. Lastly, we demonstrate how dynamics of phantom helices can be used as an important tool for quantum simulations of spin physics. Using the phantom condition (Eq. 2) it is now possible to experimentally determine the anisotropy

Δ . We find that the anisotropy is strongly affected by nearest-neighbor (i.e. off-site) interactions of the underlying Hubbard model, which have not been observed before for contact interactions.

Spin-helix states & the phantom condition. In this work, we study transverse spin-helix states

$$|\psi(Q)\rangle = \prod_n [\cos(\theta/2) |\uparrow\rangle_n + \sin(\theta/2) e^{-iQz_n} |\downarrow\rangle_n]. \quad (3)$$

The polar angle θ determines the local longitudinal spin component $\langle S_n^z \rangle$ which is constant along the chain, and z_n is the position of the n -th spin (see Fig. 1a,b). In the classical limit, *any* transverse spin helix is stable for *any* anisotropy since the torques exerted on a given spin by its neighbors cancel exactly [21]. Therefore, the decay of a spin helix is due to quantum fluctuations. However, for wavevectors Q_p fulfilling the phantom condition for $|\Delta| \leq 1$ (Eq. 2), the fluctuations from the two nearest neighbors *also* cancel exactly, making these special helices particularly long-lived. Intriguingly, one can show that they are in fact many-body eigenstates of the Heisenberg model (Eq. 1) for infinite systems, or for finite systems with appropriate boundary conditions [18]. For the finite chains with open boundaries that we prepared in our experiments, the phantom spin helix is only metastable — defects will propagate from the ends of the chain into the bulk, resulting in a nonzero but small decay rate [21].

For the isotropic system ($\Delta=1$), the phantom spin helix has wavevector $Q_p=0$ and thus reduces to a spin-polarized product state, which is a trivial eigenstate of this model. For $\Delta=0$ the phantom condition gives $Q_p a = \pi/2$, so that angles between neighboring spins are 90° (assuming all spins lie in the S^x - S^y plane, i.e. $\theta = \pi/2$). To explain intuitively how this state is metastable, consider a spin which points e.g. in the S^x direction, with quantum fluctuations in the S^y - S^z plane. For $J_z=0$, there is no interaction from the S^z component, while the S^y component causes no precession on the neighboring spins, which also point along the $\pm S^y$ -direction. In the following, we will demonstrate the existence of these long-lived phantom helices for general Δ , and confirm the predictions of the phantom condition Eq. 2.

Experimental methods. As in our previous work [20, 21], the spin model is implemented by loading ultracold lithium-7 atoms in the two lowest hyperfine states into a three-dimensional optical lattice. This system is well-described by a two-component Bose-Hubbard model. Two of the three lattice potentials are kept high at $35 E_R$ creating a bundle of isolated 1D-chains. The lattice depth of the third axis V_0 is set to a value between $9 E_R$ and $11 E_R$, which is deep enough such that the system remains in the Mott insulating regime while still allowing for spin dynamics. Here $E_R = \hbar^2/(8ma^2)$ is the recoil energy, m the atomic mass, and \hbar the Planck constant.

Because particle motion is suppressed in the Mott insu-

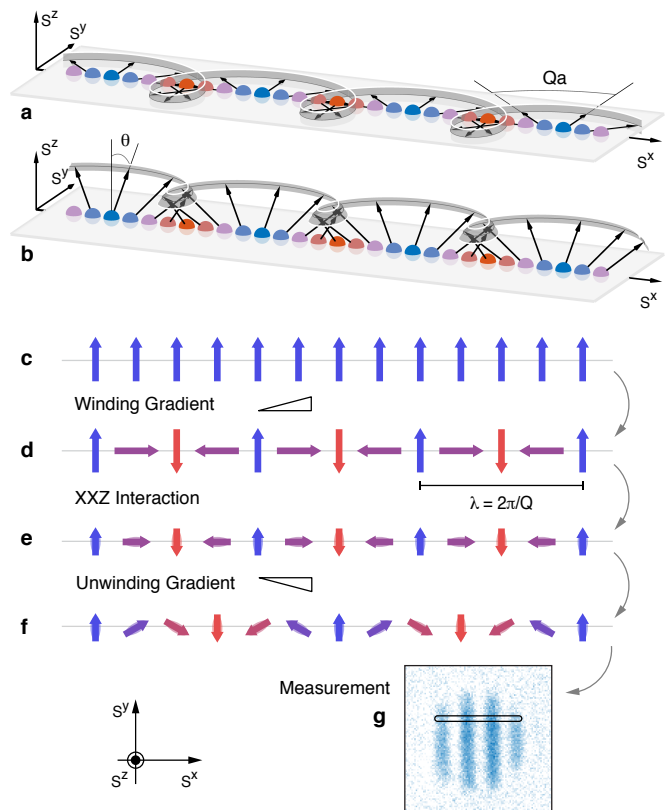


FIG. 1. Preparation and observation of spin-helix states. We prepare a transverse spin helix in the S^x - S^y plane, i.e. $\theta = \pi/2$ (a), or with arbitrary polar angle θ (b). An initially spin-polarized state in the S^y direction (c) is wound into a spin helix with variable wavevector Q using a magnetic field gradient, here illustrated for $Qa = \pi/2$ (d). This state evolves under the XXZ Heisenberg Hamiltonian (e). After unwinding the remaining spin modulation to a resolvable wavevector (f), the local S^y -magnetization is imaged in-situ (g). Only the S^x and S^y components of the spin are shown for c-f.

lator, the dynamics of the remaining degrees of freedom can be described using a pure spin model. By mapping the two hyperfine states onto spins $|\uparrow\rangle$ and $|\downarrow\rangle$, we can realize the spin-1/2 Heisenberg XXZ model (Eq. 1) in which the interactions are mediated by superexchange [23–26]. The transverse and longitudinal spin couplings are given by

$$\begin{aligned} J_z &= 4\tilde{t}^2/U_{\uparrow\downarrow} - (4\tilde{t}^2/U_{\uparrow\uparrow} + 4\tilde{t}^2/U_{\downarrow\downarrow}) \\ J_{xy} &= -4\tilde{t}^2/U_{\uparrow\downarrow}, \end{aligned} \quad (4)$$

where \tilde{t} is the tunneling matrix element between neighboring sites and $U_{\uparrow\uparrow}$, $U_{\uparrow\downarrow}$, $U_{\downarrow\downarrow}$ are the on-site interaction energies. The spin couplings (Eq. 4) can be varied over two orders of magnitude by changing the lattice depth V_0 , which scales the entire Hamiltonian. We control the anisotropy $\Delta := J_z/J_{xy}$ via an applied magnetic field B , which tunes the interactions through Feshbach resonances [20, 21, 27]. In our realization, the transverse coupling is antiferromagnetic ($J_{xy} > 0$).

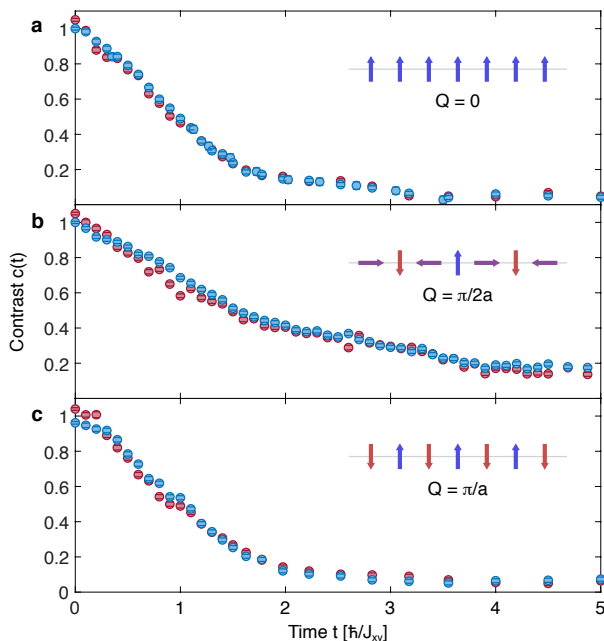


FIG. 2. **Decay of spin-helix states.** Spin-helix contrast $c(t)$ measured for $\Delta \approx 0$ at two different lattice depths $9 E_R$ (red) and $11 E_R$ (blue), for three wavevectors. **a**, $Qa = 0$, all spins aligned. **b**, $Qa = \pi/2$, neighboring spins perpendicular, and an eigenstate for $\Delta = 0$. **c**, $Qa = \pi$, all spins anti-aligned. Decay curves collapse for each wavevector when times are normalized in units of \hbar/J_{xy} . The contrast lifetime is significantly larger for $Qa = \pi/2$ compared to $Qa = 0$ and $Qa = \pi$.

The transverse spin helix is created by RF pulses to tilt the spins to a finite polar angle θ , followed by magnetic field gradients to wind a helix [21, 28, 29]. Time evolution is initiated by rapidly lowering V_0 . The dynamics following this quench are governed by the 1D XXZ model (Eq. 1, Fig. 1e) with a selected anisotropy Δ . After a variable evolution time t , the dynamics are frozen by rapidly increasing V_0 ; the sample is then imaged.

Our imaging system limits the direct observation of spin modulations to a wavelength of $\lambda > 6a$. In order to image spin helices at any value of Q , we first unwind the remaining spin modulation to a wavelength of $\lambda \approx 10a$ by applying a π -pulse followed by a magnetic field gradient as in Fig. 1f. After unwinding, we turn the transverse helix into a population modulation by applying a $\pi/2$ -pulse. In the end, we detect the spatial distribution of spin $|\uparrow\rangle$ atoms in-situ with state-selective polarization-rotation imaging (Fig. 1g). Compared to our previous work [20, 21], this novel unwinding step extends our observable range of wavevectors Q all the way to $Qa = \pi$, where neighboring spins are anti-aligned. Integrating the images along a direction perpendicular to the chains yields a 1D spatial profile of sinusoidal population modulation over all spin chains (Fig. 1g). As described in Refs. [20, 21], we determine the normalized contrast $c(t)$ which decays during the evolution time t and obtain a decay rate γ by using a linear fit at early times.

Experimental observations of phantom helices.

Fig. 2 illustrates the contrast decay $c(t)$ for spin helices with different wavevectors Q at $\Delta \approx 0$. We see that the decay for $Qa = \pi/2$ is noticeably slower than that of $Qa = 0$ or π . This non-monotonic behavior is the signature of phantom spin helices. This feature is emphasized in Fig. 3 by comparing the contrast decay rates γ at various values of Q . According to the phantom condition Eq. 2, the wavevector Q_p with the smallest decay rate changes as a function of Δ . Since the superexchange interactions in Eq. 4 depend on the scattering lengths, we can tune Δ smoothly by varying the magnetic field. Indeed, in Fig. 3 we see Q_p varies accordingly as predicted.

The fit function $\gamma(Q) = \gamma_1 |\Delta - \cos(Qa)| + \gamma_0$ was derived from a short-time expansion of the spin-helix contrast $c(t)$ [21]. Here Δ , γ_1 and γ_0 are treated as free fit parameters, where γ_0 represents a background decay rate accounting for effects such as finite chain length, holes in the spin chains, and inhomogeneous dephasing [21]. The predicted Δ based on Eq. 4 and previously determined scattering lengths [30] agrees qualitatively with the Δ we fit (see Fig. 4). We also observe phantom helix states for various polar angles in Fig. 3b-d. This confirms the prediction [18] that there is a whole family of phantom helix states for a given value of Δ . We find that a larger absolute value of the total S^z magnetization (i.e. θ close to 0 or π) leads to an overall slower decay.

For anisotropies $|\Delta| > 1$ (Fig. 3a,e; open symbols) there is no longer a stable spin-helix eigenstate [18]. We see instead that the minimum decay rate is always at $Q = 0$ for $\Delta \geq 1$ and $Qa = \pi$ for $\Delta \leq -1$. Comparing decay rates across Δ in this range, we find a Q -independent increase relative to the $|\Delta| = 1$ case which is monotonous in $|\Delta| - 1$.

Our improved imaging protocol allows us to access new parameter regimes beyond previous work. For the isotropic system ($\Delta = 1$) we had observed diffusive spin transport, characterized by $\gamma(Q) \approx \gamma_1 Q^2 a^2 / 2 + \gamma_0$ [20, 21, 28]. However, we now see this quadratic behavior break down for large Q when the wavelength λ becomes comparable to the lattice spacing a . The fastest decay occurs for the Néel state ($Qa = \pi$), where neighbouring spins are anti-aligned. This directly demonstrates that this *classical* antiferromagnetic state is *not* the ground state of the *quantum* antiferromagnetic Heisenberg Hamiltonian. Nevertheless, the Néel state is an exact highly-excited eigenstate for $\Delta = -1$ (Fig. 3e).

Extension to higher dimensions. The phantom spin-helix states were originally discovered in 1D as a coherent superposition of phantom Bethe states, special degenerate solutions to the Bethe ansatz equations [18]. This raises the question if they are a phenomenon tied exclusively to integrability. We find that they are not: we can show that stationary phantom helix states exist for any anisotropy, for the anisotropic Heisenberg model defined on hypercubic lattices in *arbitrary* spatial dimensions and *arbitrary* spin quantum numbers. Specifically, we consider the gener-

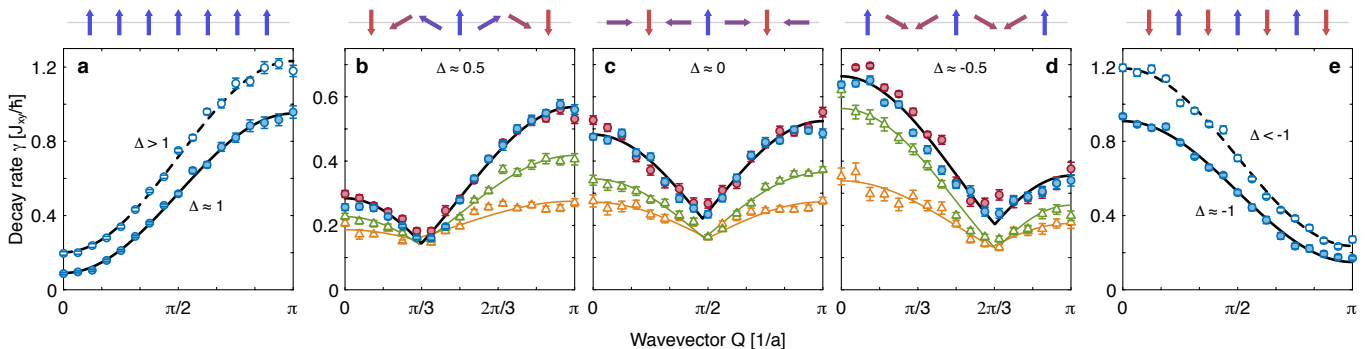


FIG. 3. **Observation of phantom helix states.** Decay rate γ as a function of wavevector Q , shown for fitted anisotropies Δ ranging from positive (a-b) through zero (c) to negative values (d-e) measured at lattice depths of $9 E_R$ (red) and $11 E_R$ (blue). The decay rate minimum occurs at a wavevector Q_p which increases smoothly from $Q_p a = 0$ for $\Delta \approx 1$ (a) to $Q_p a = \pi$ for $\Delta \approx -1$ (e). The long-lived spin pattern in the S^x - S^y plane is illustrated on top of each panel. Fits $\gamma(Q) = \gamma_1 |\Delta - \cos(Qa)| + \gamma_0$ (lines) are used to find Q_p and the anisotropies Δ shown in Fig. 4. In addition to the purely transverse helices (polar angle $\theta = \pi/2$, circles), panels (b-d) also show the decay of spin helices with polar angles $\theta = 5\pi/12$ (green triangles) and $\theta = 2\pi/3$ (orange triangles). The curves above were measured at applied magnetic fields of $B = 847.887$ G ($\Delta > 1$) and 847.286 G ($\Delta \approx 1$) (a), 845.760 G (b), 842.905 G (c), 839.376 G (d), 833.004 G ($\Delta \approx -1$) and 827.287 G ($\Delta < -1$) (e).

alization of the spin-helix states (see Supplementary Materials) in d dimensions specified by a wavevector $\mathbf{Q} = (Q_1, \dots, Q_d)$, and only require that $\mathbf{Q} = \mathbf{Q}_p := Q_p \mathbf{x}$, where $\mathbf{x} \in \{-1, 1\}^d$ is a binary vector of -1 s and 1 s, and Q_p ($0 \leq Q_p a \leq \pi$) satisfies the phantom condition (Eq. 2). For example, for the Heisenberg model with $\Delta = 1/2$ on a 2D square lattice so that $Q_p a = \pi/3$, there are four such wavevectors: $\mathbf{Q}_p a = (\pi/3, \pi/3)$, $(\pi/3, -\pi/3)$, $(-\pi/3, \pi/3)$, $(-\pi/3, -\pi/3)$; all such states are phantom helices (see Fig. S1). In fact, non-trivial phantom helix states also exist for non-hypercubic lattices, e.g. triangular and kagome lattices (see Fig. S2), but only for the special value of the anisotropy $\Delta = -1/2$. We prove these statements in the Supplementary Material.

Our experimental protocol can be extended to two or three dimensions to directly observe quantum scarred dynamics associated with these special helices. An experimental complication is that near Feshbach resonances, any magnetic field gradient is projected along the direction of the strong bias field. Therefore, to wind a helix with arbitrary $\mathbf{Q} = (Q_x, Q_y, Q_z)$ vectors, one must load atoms into a deep 3D lattice, ramp to low fields B where appropriate gradients in any direction can be created easily, wind the transverse spin helix with arbitrary \mathbf{Q} , and then return to the high fields near Feshbach resonances. Because of the small scattering lengths of lithium-7 at low field, a very deep optical lattice is required to stay in the Mott insulator regime.

Measurement of Anisotropy. Besides being of fundamental interest, the phantom helix states also have practical applications. We can use the sensitivity of the phantom helix states to measure the spin-exchange anisotropy $\Delta := J_z/J_{xy}$ precisely as a function of applied magnetic field B (shown in Fig. 4). Until now, there has been no protocol to directly measure Δ ; it could only be derived [20, 21] from measured scattering lengths $a_{\uparrow\uparrow}$, $a_{\uparrow\downarrow}$, $a_{\downarrow\downarrow}$ [27, 30] using Eq. 4. Fig. 4 compares our mea-

sured Δ to the predictions based on scattering lengths. They agree quite well far from the Feshbach resonances. We will first discuss the accuracy of our determination of Δ and possible systematic errors, then comment on the new physics near Feshbach resonances.

Repeated measurements of Δ have a reproducibility of better than 0.1, clearly visible by the small random scatter of the data points in Fig. 4. In addition, there are several possible systematic effects. (1) The lineshapes of contrast decay are non-exponential and differ between short and long decay times (visible in Fig. 2), partly due to a beat note between the precession of atoms in the spin chains and isolated atoms in the outer part of the cloud [21]. The resulting oscillations average out for long decay times, but not for shorter decay times. By using different fit functions, we estimate that $|\Delta|$ in Fig. 4 could be overestimated by at most ~ 0.1 .

(2) Our fit function $\gamma(Q) = \gamma_1 |\Delta - \cos(Qa)| + \gamma_0$ was derived from a short-time quadratic expansion of the decay of contrast [21]. However, experimentally, we can only observe the contrast at intermediate times where the decay is more linear (as already discussed in previous work [20, 21, 28]). Numerical simulations reveal that different methods of extracting γ can lead to a systematic overestimation of $|\Delta|$ by up to ~ 0.15 . The effect is maximum around $|\Delta| \approx 0.5$, and falls off for $|\Delta|$ closer to 0 or 1.

(3) A systematic shift of $|\Delta|$ would also occur if there were another Q -dependent decay mechanism due to background decay (e.g. holes) or decay propagating from the ends of the chain. Several of these issues can be addressed experimentally in the future by using a quantum gas microscope and observing dynamics in single isolated spin chains.

Some of the discrepancies in Fig. 4 can be explained by corrections to the underlying standard Hubbard model [20, 31, 32] which include density-dependent tunneling

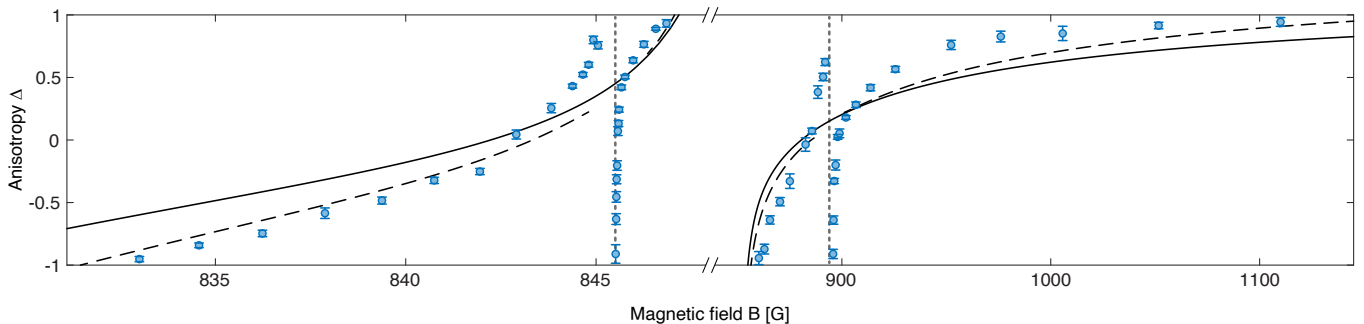


FIG. 4. **Tuning the anisotropy with magnetic fields.** Measured anisotropies Δ are compared to the standard model for superexchange given by Eq. 4 (solid line) using previously measured scattering lengths [30]. The black dashed line includes the bond-charge correction to tunneling [31] and a small adjustment of the background scattering length of $a_{\uparrow\downarrow}$, which was not tightly constrained by previous measurements. Major deviations near the two Feshbach resonances at 845.506 and 893.984 G (vertical dotted lines) are evidence for off-site interactions.

[33], higher-band corrections to U [34, 35], and off-site contact interactions [20]. However, only contributions from off-site interactions get large near a Feshbach resonance. Therefore, the phantom helix states reveal that spin-spin interactions near a Feshbach resonance are dominated by off-site interactions which have never been observed for contact interactions¹. Off-site interactions originate from the small overlap of a Wannier function on one site with those of its neighbours [37] and add a correction term to J_z in Eq. 4 of $2(V_{\uparrow\uparrow} + V_{\downarrow\downarrow} - 2V_{\uparrow\downarrow})$ [20] where $V_{\uparrow\uparrow}$, $V_{\uparrow\downarrow}$, $V_{\downarrow\downarrow}$ are the off-site interaction energies. In a forthcoming publication, we will show that the current model for off-site interactions [31, 32, 37] is insufficient near a Feshbach resonance.

Discussion and outlook. Previous studies of the Heisenberg Hamiltonian have focused on the ground state [38–40], low-lying elementary excitations including magnons [41, 42] and Bethe strings [43, 44], or on *unstable* dynamics far away from equilibrium [17, 20, 21, 28, 45]. This work captures a new class of excitations for the Heisenberg model: the phantom spin helices. These are highly-excited yet long-lived *metastable* states. Their stability is not a result of symmetry, but rather due to a delicate cancellation of interactions.

We have theoretically explored spin-helix states in systems in higher dimensions, for different spin quantum numbers, and in various lattice geometries, which are not integrable. We find that for the special initial condition of a phantom helix state, the system does not relax to thermal equilibrium as one would naïvely expect, despite the presence of strong interactions. Such dynamics in non-integrable, many-body systems constitute examples of “weak ergodicity-breaking”, or what are now known as “quantum many-body scars” [22]. We note that while various toy models hosting exact quantum many-body scars have already been discussed in the literature, such

models are primarily theoretical constructs which are difficult to realize experimentally [46–49]. In contrast, we demonstrate that one of the simplest examples of a many-body system (the XXZ Heisenberg model) can support quantum many-body scars, a fact which has been overlooked thus far. The simplicity implies that probing such scarred dynamics experimentally is relatively straightforward, and we propose a way to observe them with an extension of our current experimental setup to higher dimensions.

We expect phantom helix states to have applications for quantum simulations of spin physics. We have demonstrated the potential of the phantom helix states as a sensitive tool to directly measure the anisotropy Δ . They have revealed that even short-range interactions can lead to strong off-site interactions in spin models. This can now be used to realize extended Hubbard models [32, 37] including the quantum lattice gas (or t - V) model [50] which supports a supersolid phase [51]. In the future, these long-lived helix states could be an intermediate step in preparing other many-body quantum states or be used for robust quantum sensing [52]. An intriguing question is what will ultimately limit the stability of these states if periodic boundary conditions are realized with ring-shaped atom arrays [53]. Such studies are likely to provide new insight into the rich dynamics of Heisenberg spin models.

Acknowledgements. We thank J. Rodriguez-Nieva for helpful discussions, and J. Amato-Grill for important advice. We thank Jinggang Xiang for experimental assistance, Julius de Hond for comments on the manuscript, and M. Zwierlein for sharing equipment. **Funding:** We acknowledge support from the NSF through the Center for Ultracold Atoms and Grant No. 1506369, the Vannevar-Bush Faculty Fellowship, and DARPA (grant number W911NF2010090). W.W.H. is supported in part by the Stanford Institute of Theoretical Physics. **Author contributions:** P. N. J., Y. K. L., H. L., W. W. H. and W. K. conceived the experiment. P. N. J., Y. K. L., H. L., I. D., and Y. M. performed the experiment.

¹Off-site interactions were observed for long-range dipolar interactions [36].

P. N. J., Y. K. L., and H. L. analyzed the data. W. W. H. generalized the findings to higher dimensions. All authors discussed the results and contributed to the writing of the manuscript. **Competing interests:** The authors

declare no competing financial interests. **Data and materials availability:** The data that support the findings of this study are available from the corresponding author upon reasonable request.

-
- [1] J. Berges, S. Borsányi, C. Wetterich, *Phys. Rev. Lett.* **93**, 142002 (2004).
- [2] M. Rigol, V. Dunjko, V. Yurovsky, M. Olshanii, *Phys. Rev. Lett.* **98**, 050405 (2007).
- [3] M. Gring, *et al.*, *Science* **337**, 1318 (2012).
- [4] C. Eigen, *et al.*, *Nature* **563**, 221 (2018).
- [5] D. A. Abanin, E. Altman, I. Bloch, M. Serbyn, *Rev. Mod. Phys.* **91**, 021001 (2019).
- [6] S. Choi, *et al.*, *Nature* **543**, 221 (2017).
- [7] J. Zhang, *et al.*, *Nature* **543**, 217 (2017).
- [8] F. Arute, *et al.*, *Nature* **574**, 505 (2019).
- [9] F. Flamini, N. Spagnolo, F. Sciarrino, *Rep. Prog. Phys.* **82**, 016001 (2018).
- [10] P. Jordan, E. Wigner, *Zeitschrift für Physik* **47**, 631 (1928).
- [11] S. Sachdev, *Quantum Phase Transitions* (Cambridge University Press, 2011), second edn.
- [12] H. Bethe, *Zeitschrift für Physik* **71**, 205 (1931).
- [13] F. Franchini, *An Introduction to Integrable Techniques for One-Dimensional Quantum Systems* (Springer International Publishing, 2017).
- [14] M. Žnidarič, *Phys. Rev. Lett.* **106** (2011).
- [15] M. Ljubotina, M. Žnidarič, T. Prosen, *Nature Communications* **8**, 16117 (2017).
- [16] M. Ljubotina, M. Žnidarič, T. Prosen, *Phys. Rev. Lett.* **122**, 210602 (2019).
- [17] D. Wei, *et al.*, arXiv:2107.00038 [cond-mat.quant-gas] 30 June 2021).
- [18] V. Popkov, X. Zhang, A. Klümper, *Phys. Rev. B* **104**, L081410 (2021).
- [19] A. C. Cassidy, C. W. Clark, M. Rigol, *Phys. Rev. Lett.* **106**, 140405 (2011).
- [20] P. N. Jepsen, *et al.*, *Nature* **588**, 403–407 (2020).
- [21] P. N. Jepsen, *et al.*, arXiv:2103.07866 [cond-mat.quant-gas] (14 March 2021)
- [22] M. Serbyn, D. A. Abanin, Z. Papić, *Nature Physics* **17**, 675 (2021).
- [23] A. B. Kuklov, B. V. Svistunov, *Phys. Rev. Lett.* **90**, 100401 (2003).
- [24] L.-M. Duan, E. Demler, M. D. Lukin, *Phys. Rev. Lett.* **91**, 090402 (2003).
- [25] J. J. García-Ripoll, J. I. Cirac, *New Journal of Physics* **5**, 76 (2003).
- [26] E. Altman, W. Hofstetter, E. Demler, M. D. Lukin, *New Journal of Physics* **5**, 113 (2003).
- [27] J. Amato-Grill, N. Jepsen, I. Dimitrova, W. Lunden, W. Ketterle, *Phys. Rev. A* **99**, 033612 (2019).
- [28] S. Hild, *et al.*, *Phys. Rev. Lett.* **113**, 147205 (2014).
- [29] S. Trotzky, *et al.*, *Phys. Rev. Lett.* **114**, 015301 (2015).
- [30] T. Secker, J. Amato-Grill, W. Ketterle, S. Kokkelmans, *Phys. Rev. A* **101**, 042703 (2020).
- [31] D.-S. Lühmann, O. Jürgensen, K. Sengstock, *New Journal of Physics* **14**, 033021 (2012).
- [32] O. Dutta, *et al.*, *Reports on Progress in Physics* **78**, 066001 (2015).
- [33] O. Jürgensen, F. Meinert, M. J. Mark, H.-C. Nägerl, D.-S. Lühmann, *Phys. Rev. Lett.* **113**, 193003 (2014).
- [34] G. K. Campbell, *et al.*, *Science* **313**, 649 (2006).
- [35] S. Will, *et al.*, *Nature* **465**, 197 (2010).
- [36] S. Baier, *et al.*, *Science* **352**, 201 (2016).
- [37] J. C. Amadon, J. E. Hirsch, *Phys. Rev. B* **54**, 6364 (1996).
- [38] M. F. Parsons, *et al.*, *Science* **353**, 1253 (2016).
- [39] L. W. Cheuk, *et al.*, *Science* **353**, 1260 (2016).
- [40] A. Mazurenko, *et al.*, *Nature* **545**, 462 (2017).
- [41] T. Fukuhara, *et al.*, *Nature Physics* **9**, 235 (2013).
- [42] T. Fukuhara, *et al.*, *Nature* **502**, 76 (2013).
- [43] Z. Wang, *et al.*, *Nature* **554**, 219 (2018).
- [44] A. K. Bera, *et al.*, *Nature Physics* **16**, 625 (2020).
- [45] M. A. Nichols, *et al.*, *Science* **363**, 383 (2019).
- [46] N. Shiraishi, *et al.*, *Phys. Rev. Lett.* **119**, 030601 (2017).
- [47] D. K. Mark, *et al.*, *Phys. Rev. B* **101**, 195131 (2020).
- [48] S. Chattopadhyay, *et al.*, *Phys. Rev. B* **101**, 174308 (2020).
- [49] S. Moudgalya, *et al.*, *Phys. Rev. B* **102**, 085140 (2020).
- [50] M. A. Cazalilla, R. Citro, T. Giamarchi, E. Orignac, M. Rigol, *Rev. Mod. Phys.* **83**, 1405 (2011).
- [51] H. Matsuda, T. Tsuneto, *Progress of Theoretical Physics Supplement* **46**, 411 (1970).
- [52] S. Dooley, *PRX Quantum* **2**, 020330 (2021).
- [53] P. Scholl, *et al.*, arXiv:2107.14459 [quant-ph] (30 July 2021).

SUPPLEMENTARY MATERIAL

I. PHANTOM SPIN HELICES IN HIGHER-DIMENSIONS, ARBITRARY SPIN QUANTUM NUMBERS, AND NON-HYPERCUBIC GEOMETRIES

In this section we extend the phenomenology of stable phantom helices to Heisenberg models in higher dimensions, arbitrary spin quantum numbers, and non-hypercubic geometries. Specifically, we prove that for any given anisotropy in the easy-plane $|\Delta| \leq 1$, there exist phantom helices which are *exact* many-body eigenstates of the model, provided (i) the phantom condition (Eq. 2 of the main text) holds; and (ii) appropriate boundary conditions are taken.

A. Model and spin-helix states

We consider the quantum Heisenberg XXZ model for any spatial dimensionality d , spin- S , and lattice geometry. The Hamiltonian is given by a sum over pairwise nearest-neighbor interactions (we set $J_{xy} = 1$ for simplicity):

$$H(\Delta) := \sum_{\langle ij \rangle} (S_i^x S_j^x + S_i^y S_j^y) + \Delta S_i^z S_j^z, \quad (5)$$

where S_i^α ($\alpha = x, y, z$) are spin- S operators.

The generalization of a spin-helix state from the spin-1/2 case (Eq. 3 of the main text) is given by

$$|\psi(\mathbf{Q})\rangle = \prod_i \left[e^{-i\mathbf{Q} \cdot \mathbf{r}_i S_i^z} e^{-i\theta S_i^y} |S\rangle_i \right]. \quad (6)$$

Here $|S\rangle_i$ is the local maximal spin state satisfying $(\mathbf{S}_i \cdot \mathbf{S}_i)|S\rangle_i = S(S+1)|S\rangle_i$ and $S_i^z|S\rangle_i = S|S\rangle_i$. $\mathbf{Q} = (Q_1, \dots, Q_d)$ is a d -dimensional wavevector parameterizing the winding rate and direction of the spiral, and \mathbf{r}_i is the coordinate of the spin at site i . Therefore, Eq. (6) locally describes a state created by rotation by angle θ from the z -polarized state around the S^y -axis, before a winding in the S^x - S^y by a site-dependent angle $\mathbf{Q} \cdot \mathbf{r}_i$.

B. Statement of results

For the model and state above, we have the following statements (we set the lattice spacing to $a = 1$ for brevity):

Theorem 1 (phantom spin helices for the hypercubic lattice). *Consider a d -dimensional hypercubic lattice of volume $L_1 \times L_2 \times \dots \times L_d$ and the anisotropic spin- S Heisenberg model with anisotropy Δ defined on it. Let $|\Delta| \leq 1$, which we parameterize as $\Delta = \cos(Q_p)$ (the “phantom condition”) for $Q_p \in [0, \pi)$. Define the wavevector $\mathbf{Q}_p := Q_p \mathbf{x}$ where \mathbf{x} is a binary vector $\mathbf{x} = (x_1, \dots, x_d) \in \{-1, 1\}^d$, and suppose that the linear dimensions L_i are such that $L_i = 2\pi m_i / Q_p$ for some $m_i \in \mathbb{N}$. Then, the spin helix with wavevector \mathbf{Q}_p and any polar angle θ is an exact eigenstate of the model with energy $E = S^2 \cos(Q_p) \times \# \text{Links}$.*

Theorem 2 (phantom spin helices for the 2D triangular and kagome lattices). *Consider a 2-dimensional regular triangular or kagome lattice, and the anisotropic spin- S Heisenberg model with anisotropy $\Delta = -1/2$ defined on it. Define $Q_p = 2\pi/3$ so that $\cos(2\pi/3) = -1/2 = \Delta$. Then the spin helix with wavevector $\mathbf{Q}_p = (2Q_p, 0)$ or $(4Q_p, 0)$ and any polar angle θ , is an exact eigenstate of the model with energy $E = S^2 \cos(Q_p) \times \# \text{Links}$, provided the lattice dimensions are such that it is commensurate with the spiral pattern.*

Remarks. Figure S1 shows an illustration of the phantom helix for a 2D square lattice, while figure S2 shows the phantom helix for the 2D triangular and kagome lattices. Note the phantom helix state for the triangular lattice is known as the 120° Néel ordered state in condensed matter physics, which is the ground state of the classical antiferromagnetic Heisenberg model. We show here that it is an exact eigenstate for the quantum Heisenberg model for $\Delta = -1/2$. For the kagome lattice, the phantom helix state it is also known as the $\sqrt{3} \times \sqrt{3}$ state.

Proof. Define the local term of the Hamiltonian

$$h_{ij} = (S_i^x S_j^x + S_i^y S_j^y) + \cos(Q_p) S_i^z S_j^z \quad (7)$$

so that $H(\cos(Q_p)) = \sum_{\langle ij \rangle} h_{ij}$. Consider a local part of the spin-helix state with wavevector \mathbf{Q}_p , specifically on a pair of neighboring spins i, j :

$$|\psi\rangle_{ij} = e^{-i\Phi_i S_i^z} e^{-i\theta S_i^y} |S\rangle_i \otimes e^{-i\Phi_j S_j^z} e^{-i\theta S_j^y} |S\rangle_j \quad (8)$$

$$= e^{-i\Phi_i (S_i^z + S_j^z)} \left(e^{-i\theta S_i^y} |S\rangle_i \otimes e^{-i\theta \Phi_j S_j^z} e^{-i\theta S_j^y} |S\rangle_j \right) \quad (9)$$

where $\Phi_i = \mathbf{Q} \cdot \mathbf{r}_i$ and $\delta\Phi_{ji} = (\Phi_j - \Phi_i)$. A simple but key property is that for the set-ups described in either Theorem, $e^{-i\delta\Phi_{ji}} = e^{-iQ_p}$ or e^{iQ_p} for *any* nearest-neighbor pair of sites. (Clearly this is true for any hypercubic lattice. For the triangle lattice with primitive vectors $\mathbf{b}_1 = (1, 0)$, $\mathbf{b}_2 = (1/2, \sqrt{3}/2)$ we have $e^{\pm i\frac{2\pi}{3}} = e^{\mp iQ_p}$. For the kagome lattice the primitive vectors are $\mathbf{b}_1 = (2, 0)$ and $\mathbf{b}_2 = (1, \sqrt{3})$ while the lattice vectors within each unit cell are $\mathbf{a}_1 = \frac{1}{2}\mathbf{b}_1$, $\mathbf{a}_2 = \frac{1}{2}\mathbf{b}_2$ and so the result is the same as the triangular lattice).

With this in mind, we evaluate the action of h_{ij} on the state (dropping indices i, j for brevity)

$$\begin{aligned} & e^{-i\Phi_i (S^z \otimes \mathbb{I} + \mathbb{I} \otimes S^z)} (S^x \otimes S^x + S^y \otimes S^y + \cos(Q_p) S^z \otimes S^z) \left[e^{-i\theta S^y} |S\rangle \otimes e^{\mp iQ_p S^z} e^{-i\theta S^y} |S\rangle \right] \\ &= e^{-i\Phi_i (S^z \otimes \mathbb{I} + \mathbb{I} \otimes S^z)} (\mathbb{I} \otimes e^{\mp iQ_p S^z}) (S^x \otimes (S^x \cos(Q_p) \mp S^y \sin(Q_p)) + S^y \otimes (S^y \cos(Q_p) \pm S^x \sin(Q_p)) + \cos(Q_p) S^z \otimes S^z) \\ & \quad \times \left[e^{-i\theta S^y} |S\rangle \otimes e^{-i\theta S^y} |S\rangle \right] \\ &= e^{-i\Phi_i (S^z \otimes \mathbb{I} + \mathbb{I} \otimes S^z)} (\mathbb{I} \otimes e^{\mp iQ_p S^z}) (\cos(Q_p) (S^x \otimes S^x + S^y \otimes S^y + S^z \otimes S^z) \mp \sin(Q_p) (S^x \otimes S^y - S^y \otimes S^x)) \\ & \quad \times \left[e^{-i\theta S^y} |S\rangle \otimes e^{-i\theta S^y} |S\rangle \right]. \end{aligned} \quad (10)$$

The term proportional to $\cos(Q_p)$ is $\mathbf{S}_i \cdot \mathbf{S}_j$, and the state on the RHS of the last line of the above equation is a uniformly polarized state, so it evaluates to the original state up to a multiplicative factor

$$S^2 \cos(Q_p) |\psi\rangle_{ij}. \quad (11)$$

Now we just have to evaluate the term proportional to $\sin(Q_p)$. Ignoring the factor $e^{-i\Phi_i (S^z \otimes \mathbb{I} + \mathbb{I} \otimes S^z)} (\mathbb{I} \otimes e^{\mp iQ_p S^z})$ we have

$$\begin{aligned} & \mp \sin(Q_p) (S^x \otimes S^y - S^y \otimes S^x) \left[e^{-i\theta S^y} |S\rangle \otimes e^{-i\theta S^y} |S\rangle \right] \\ &= \mp \sin(Q_p) (e^{-i\theta S^y} \otimes e^{-i\theta S^y}) ((S^x \cos(\theta) + S^z \sin(\theta)) \otimes S^y - S^y \otimes (S^x \cos(\theta) + S^z \sin(\theta))) |S\rangle \otimes |S\rangle \\ &= \mp \sin(Q_p) (e^{-i\theta S^y} \otimes e^{-i\theta S^y}) (\cos(\theta) (S^x \otimes S^y - S^y \otimes S^x) + \sin(\theta) S (\mathbb{I} \otimes S^y - S^y \otimes \mathbb{I})) |S\rangle \otimes |S\rangle. \end{aligned} \quad (12)$$

Now we make use of the fact that

$$S^y |S\rangle = i S^x |S\rangle \quad (13)$$

(this follows from the definition of $|S\rangle$ as the highest-weight state, $S^x = \frac{1}{2}(S^+ + S^-)$, and $S^y = \frac{1}{2i}(S^+ - S^-)$).

Therefore

$$(S^x \otimes S^y - S^y \otimes S^x) |S\rangle \otimes |S\rangle = 0 \quad (14)$$

and Eq. (12) becomes

$$\mp \sin(Q_p) (e^{-i\theta S^y} \otimes e^{-i\theta S^y}) i \sin(\theta) S (\mathbb{I} \otimes S^x - S^x \otimes \mathbb{I}) |S\rangle \otimes |S\rangle. \quad (15)$$

We add a trivial term

$$\mp \sin(Q_p) (e^{-i\theta S^y} \otimes e^{-i\theta S^y}) i \cos(\theta) S (\mathbb{I} \otimes S^z - S^z \otimes \mathbb{I}) |S\rangle \otimes |S\rangle \quad (16)$$

to it, so that Eq. (12) is equal to

$$\pm i S \sin(Q_p) (\mathbb{I} \otimes S^z - S^z \otimes \mathbb{I}) (e^{-i\theta S^y} \otimes e^{-i\theta S^y}) |S\rangle \otimes |S\rangle. \quad (17)$$

Reinstating the factor $e^{-i\Phi_i (S^z \otimes \mathbb{I} + \mathbb{I} \otimes S^z)} (\mathbb{I} \otimes e^{\mp iQ_p S^z})$ which commutes with $(\mathbb{I} \otimes S^z - S^z \otimes \mathbb{I})$, we hence have

$$h_{ij} |\psi\rangle_{ij} = S^2 \cos(Q_p) |\psi\rangle_{ij} \pm i S \sin(Q_p) (S_j^z - S_i^z) |\psi\rangle_{ij}. \quad (18)$$

This is our final result. The $(S_i^z - S_j^z)$ term cancels out in the bulk when summed over all sites (it telescopes), so

$$H(\cos(Q_p)) |\psi(\mathbf{Q}_p)\rangle = (S^2 \cos(Q_p) \times \#Links) |\psi(\mathbf{Q}_p)\rangle \quad (19)$$

as claimed. ■

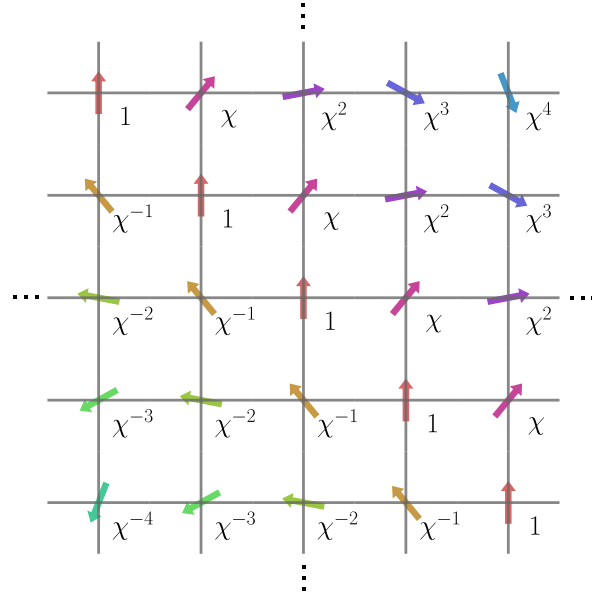


FIG. S1. **Phantom spin helix for the square lattice.** Each vertex carries a phase, which denotes the state's local expectation value $\langle S_i^+ \rangle = \langle S_i^x \rangle + i\langle S_i^y \rangle$. Here, $\chi := e^{-iQ_p}$. We have assumed the spiral lies fully in the transverse plane (polar angle $\theta = \pi/2$), but the latter condition can be straightforwardly lifted to allow for arbitrary polar angles. Thus, the depicted helix has the particular wavevector $\mathbf{Q} = (Q_p, Q_p)$, where $\Delta = \cos(Q_p)$ ($0 \leq Q_p \leq \pi$). Other valid phantom spin-spirals for this geometry are those with wavevectors satisfying $\mathbf{Q}_p = Q_p \mathbf{x}$, where $\mathbf{x} \in \{-1, 1\}^2$.

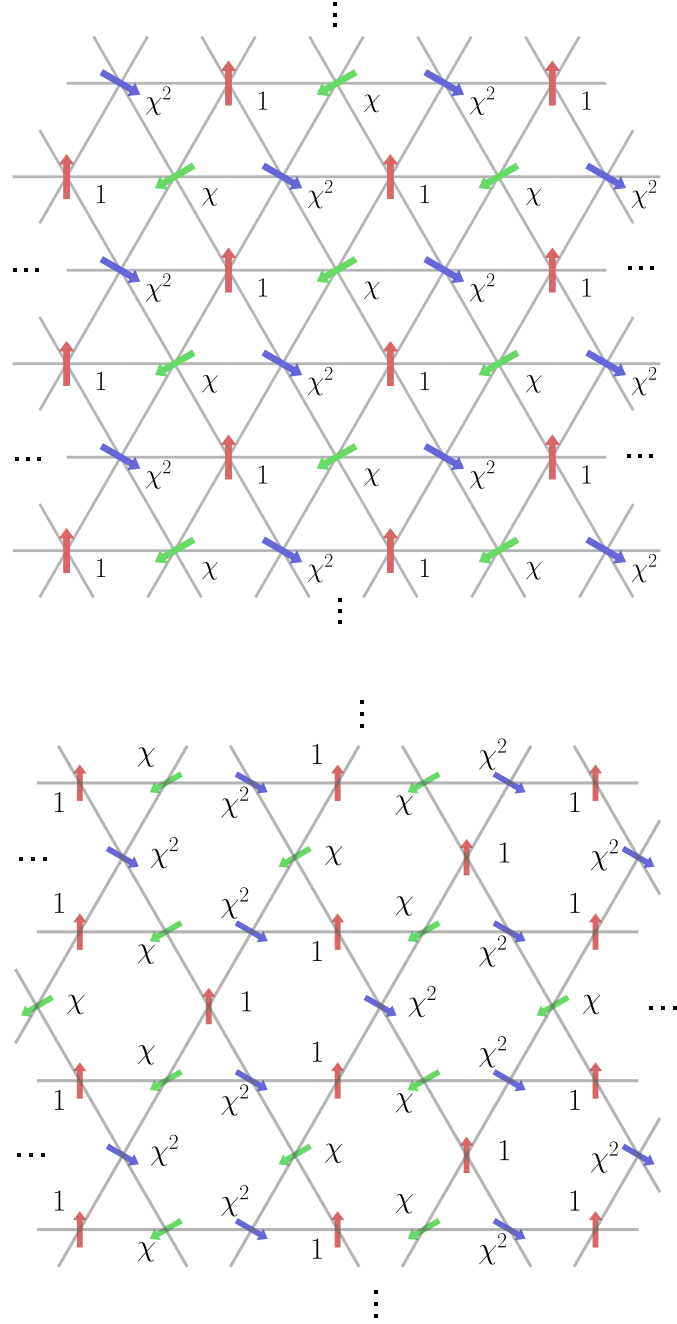


FIG. S2. **Phantom spin helices for triangular and kagome lattices.** As in the case for the square lattice, we label each vertex with a phase denoting the local expectation value $\langle S_i^+ \rangle$, defining $\chi := e^{-iQ_p}$. However, in this case, only $Q_p = 2\pi/3$ and $\Delta = -1/2$ defines a valid phantom spin helix. Thus, the spin can only point in one of three directions in the S^x - S^y plane (denoted by three different colors), with relative angle $2\pi/3$ between them. Note that the collinear neighbors of each red spin are blue and green spins, and the interactions of the blue and green spins with the red spin cancel for each line. In this way, one can understand the 2D phantom helix states as arising from simple “stacking” together of phantom helices of 1D chains.

Bibliography

- [1] Auerbach, A. *Interacting Electrons and Quantum Magnetism* (Springer-Verlag, 1994).
- [2] Zhang, J., Pagano, G., Hess, P. W., Kyprianidis, A., Becker, P., Kaplan, H., Gorshkov, A. V., Gong, Z.-X. & Monroe, C. Observation of a many-body dynamical phase transition with a 53-qubit quantum simulator. *Nature* **551**, 601–604 (2017).
- [3] Bernien, H., Schwartz, S., Keesling, A., Levine, H., Omran, A., Pichler, H., Choi, S., Zibrov, A. S., Endres, M., Greiner, M., Vuletić, V. & Lukin, M. D. Probing many-body dynamics on a 51-atom quantum simulator. *Nature* **551**, 579–584 (2017).
- [4] Barends, R. *et al.* Digital quantum simulation of fermionic models with a superconducting circuit. *Nature Communications* **6**, 7654 (2015).
- [5] Davis, E. J., Periwal, A., Cooper, E. S., Bentsen, G., Evered, S. J., Van Kirk, K. & Schleier-Smith, M. H. Protecting spin coherence in a tunable Heisenberg model. *Phys. Rev. Lett.* **125**, 060402 (2020).
- [6] Signoles, A., Franz, T., Ferracini Alves, R., Gärttner, M., Whitlock, S., Zürn, G. & Weidemüller, M. Glassy dynamics in a disordered heisenberg quantum spin system. *Phys. Rev. X* **11**, 011011 (2021).
- [7] Trotzky, S., Cheinet, P., Fölling, S., Feld, M., Schnorrberger, U., Rey, A. M., Polkovnikov, A., Demler, E. A., Lukin, M. D. & Bloch, I. Time-resolved observation and control of superexchange interactions with ultracold atoms in optical lattices. *Science* **319**, 295–299 (2008).
- [8] Gross, C. & Bloch, I. Quantum simulations with ultracold atoms in optical lattices. *Science* **357**, 995–1001 (2017).
- [9] Vasseur, R. & Moore, J. E. Nonequilibrium quantum dynamics and transport: from integrability to many-body localization. *Journal of Statistical Mechanics: Theory and Experiment* **2016**, 064010 (2016).
- [10] Bertini, B., Heidrich-Meisner, F., Karrasch, C., Prosen, T., Steinigeweg, R. & Žnidarič, M. Finite-temperature transport in one-dimensional quantum lattice models. *Rev. Mod. Phys.* **93**, 025003 (2021).

- [11] Ljubotina, M., Žnidarič, M. & Prosen, T. Spin diffusion from an inhomogeneous quench in an integrable system. *Nature Communications* **8**, 16117 (2017).
- [12] Gopalakrishnan, S. & Vasseur, R. Kinetic theory of spin diffusion and superdiffusion in XXZ spin chains. *Phys. Rev. Lett.* **122**, 127202 (2019).
- [13] Ilievski, E., De Nardis, J., Medenjak, M. & Prosen, T. Superdiffusion in one-dimensional quantum lattice models. *Phys. Rev. Lett.* **121**, 230602 (2018).
- [14] Bethe, H. Zur theorie der metalle. *Zeitschrift für Physik* **71**, 205–226 (1931).
- [15] Nichols, M. A., Cheuk, L. W., Okan, M., Hartke, T. R., Mendez, E., Senthil, T., Khatami, E., Zhang, H. & Zwierlein, M. W. Spin transport in a Mott insulator of ultracold fermions. *Science* **363**, 383–387 (2019).
- [16] Brown, R. C., Wyllie, R., Koller, S. B., Goldschmidt, E. A., Foss-Feig, M. & Porto, J. V. Two-dimensional superexchange-mediated magnetization dynamics in an optical lattice. *Science* **348**, 540–544 (2015).
- [17] Fukuhara, T., Kantian, A., Endres, M., Cheneau, M., Schauß, P., Hild, S., Bellem, D., Schollwöck, U., Giamarchi, T., Gross, C., Bloch, I. & Kuhr, S. Quantum dynamics of a mobile spin impurity. *Nature Physics* **9**, 235–241 (2013).
- [18] Fukuhara, T., Schauß, P., Endres, M., Hild, S., Cheneau, M., Bloch, I. & Gross, C. Microscopic observation of magnon bound states and their dynamics. *Nature* **502**, 76–79 (2013).
- [19] Hild, S., Fukuhara, T., Schauß, P., Zeiher, J., Knap, M., Demler, E., Bloch, I. & Gross, C. Far-from-equilibrium spin transport in Heisenberg quantum magnets. *Phys. Rev. Lett.* **113**, 147205 (2014).
- [20] Koschorreck, M., Pertot, D., Vogt, E. & Köhl, M. Universal spin dynamics in two-dimensional Fermi gases. *Nature Physics* **9**, 405–409 (2013).
- [21] Trotzky, S., Beattie, S., Luciuk, C., Smale, S., Bardon, A. B., Enss, T., Taylor, E., Zhang, S. & Thywissen, J. H. Observation of the Leggett-Rice effect in a unitary fermi gas. *Phys. Rev. Lett.* **114**, 015301 (2015).
- [22] Palzer, S., Zipkes, C., Sias, C. & Köhl, M. Quantum transport through a Tonks-Girardeau gas. *Phys. Rev. Lett.* **103**, 150601 (2009).
- [23] Sommer, A., Ku, M., Roati, G. & Zwierlein, M. W. Universal spin transport in a strongly interacting Fermi gas. *Nature* **472**, 201–204 (2011).
- [24] Krinner, S., Lebrat, M., Husmann, D., Grenier, C., Brantut, J.-P. & Esslinger, T. Mapping out spin and particle conductances in a quantum point contact. *Proceedings of the National Academy of Sciences* **113**, 8144–8149 (2016).

- [25] Cheuk, L. W., Nichols, M. A., Lawrence, K. R., Okan, M., Zhang, H. & Zwierlein, M. W. Observation of 2D fermionic Mott insulators of ^{40}K with single-site resolution. *Phys. Rev. Lett.* **116**, 235301 (2016).
- [26] Parsons, M. F., Mazurenko, A., Chiu, C. S., Ji, G., Greif, D. & Greiner, M. Site-resolved measurement of the spin-correlation function in the Fermi-Hubbard model. *Science* **353**, 1253–1256 (2016).
- [27] Mazurenko, A., Chiu, C. S., Ji, G., Parsons, M. F., Kanász-Nagy, M., Schmidt, R., Grusdt, F., Demler, E., Greif, D. & Greiner, M. A cold-atom Fermi–Hubbard antiferromagnet. *Nature* **545**, 462–466 (2017).
- [28] Jepsen, P. N., Amato-Grill, J., Dimitrova, I., Ho, W. W., Demler, E. & Ketterle, W. Spin transport in a tunable Heisenberg model realized with ultracold atoms. *Nature* **588**, 403–407 (2020).
- [29] Jepsen, P. N., Ho, W. W., Amato-Grill, J., Dimitrova, I., Demler, E. & Ketterle, W. Transverse spin dynamics in the anisotropic heisenberg model realized with ultracold atoms. *Phys. Rev. X* **11**, 041054 (2021).
- [30] Jepsen, P. N., Lee, Y. K., Lin, H., Dimitrova, I., Margalit, Y., Ho, W. W. & Ketterle, W. Catching Bethe phantoms and quantum many-body scars: Long-lived spin-helix states in Heisenberg magnets. *arXiv e-prints* arXiv:2110.12043 (2021).
- [31] Jordan, P. & Wigner, E. Über das Paulische Äquivalenzverbot. *Zeitschrift für Physik* **47**, 631–651 (1928).
- [32] Ganahl, M., Rabel, E., Essler, F. H. L. & Evertz, H. G. Observation of complex bound states in the spin-1/2 Heisenberg XXZ chain using local quantum quenches. *Phys. Rev. Lett.* **108**, 077206 (2012).
- [33] Wei, D., Rubio-Abadal, A., Ye, B., Machado, F., Kemp, J., Srakaew, K., Hollerith, S., Rui, J., Gopalakrishnan, S., Yao, N. Y., Bloch, I. & Zeiher, J. Quantum gas microscopy of Kardar-Parisi-Zhang superdiffusion. *arXiv e-prints* arXiv:2107.00038 (2021).
- [34] Jaksch, D., Bruder, C., Cirac, J. I., Gardiner, C. W. & Zoller, P. Cold bosonic atoms in optical lattices. *Phys. Rev. Lett.* **81**, 3108–3111 (1998).
- [35] Kuklov, A. B. & Svistunov, B. V. Counterflow superfluidity of two-species ultracold atoms in a commensurate optical lattice. *Phys. Rev. Lett.* **90**, 100401 (2003).
- [36] Duan, L.-M., Demler, E. & Lukin, M. D. Controlling spin exchange interactions of ultracold atoms in optical lattices. *Phys. Rev. Lett.* **91**, 090402 (2003).
- [37] García-Ripoll, J. J. & Cirac, J. I. Spin dynamics for bosons in an optical lattice. *New Journal of Physics* **5**, 76–76 (2003).

- [38] Altman, E., Hofstetter, W., Demler, E. & Lukin, M. D. Phase diagram of two-component bosons on an optical lattice. *New Journal of Physics* **5**, 113–113 (2003).
- [39] Schrieffer, J. R. & Wolff, P. A. Relation between the Anderson and Kondo Hamiltonians. *Phys. Rev.* **149**, 491–492 (1966).
- [40] Luttinger, J. M. & Kohn, W. Motion of electrons and holes in perturbed periodic fields. *Phys. Rev.* **97**, 869–883 (1955).
- [41] Amato-Grill, J., Jepsen, N., Dimitrova, I., Lunden, W. & Ketterle, W. Interaction spectroscopy of a two-component Mott insulator. *Phys. Rev. A* **99**, 033612 (2019).
- [42] Amadon, J. C. & Hirsch, J. E. Metallic ferromagnetism in a single-band model: Effect of band filling and coulomb interactions. *Phys. Rev. B* **54**, 6364–6375 (1996).
- [43] Secker, T., Amato-Grill, J., Ketterle, W. & Kokkelmans, S. High-precision analysis of Feshbach resonances in a Mott insulator. *Phys. Rev. A* **101**, 042703 (2020).
- [44] Dimitrova, I., Jepsen, N., Buyskikh, A., Venegas-Gomez, A., Amato-Grill, J., Daley, A. & Ketterle, W. Enhanced superexchange in a tilted Mott insulator. *Phys. Rev. Lett.* **124**, 043204 (2020).
- [45] Bradley, C. C., Sackett, C. A. & Hulet, R. G. Bose-Einstein condensation of lithium: Observation of limited condensate number. *Phys. Rev. Lett.* **78**, 985–989 (1997).
- [46] Ketterle, W., Durfee, D. S. & Stamper-Kurn, D. M. Making, probing and understanding Bose-Einstein condensates. In Inguscio, M., Stringari, S. & Wieman, C. E. (eds.) *Bose-Einstein Condensation in Atomic Gases*, 67–176 (IOS Press, Amsterdam, 1999).
- [47] Popkov, V., Zhang, X. & Klümper, A. Phantom Bethe excitations and spin helix eigenstates in integrable periodic and open spin chains. *Phys. Rev. B* **104**, L081410 (2021).
- [48] Zhang, X., Klümper, A. & Popkov, V. Phantom Bethe roots in the integrable open spin- $\frac{1}{2}$ XXZ chain. *Phys. Rev. B* **103**, 115435 (2021).
- [49] Busch, T., Englert, B.-G., Rzazewski, K. & Wilkens, M. Two cold atoms in a harmonic trap. *Foundations of Physics* **28**, 549–559 (1998).
- [50] Lühmann, D.-S., Jürgensen, O. & Sengstock, K. Multi-orbital and density-induced tunneling of bosons in optical lattices. *New Journal of Physics* **14**, 033021 (2012).

- [51] Ljubotina, M., Žnidarič, M. & Prosen, T. A class of states supporting diffusive spin dynamics in the isotropic Heisenberg model. *Journal of Physics A: Mathematical and Theoretical* **50**, 475002 (2017).
- [52] Antal, T., Rácz, Z., Rákos, A. & Schütz, G. M. Transport in the XX chain at zero temperature: Emergence of flat magnetization profiles. *Phys. Rev. E* **59**, 4912–4918 (1999).
- [53] Gobert, D., Kollath, C., Schollwöck, U. & Schütz, G. Real-time dynamics in spin- $\frac{1}{2}$ chains with adaptive time-dependent density matrix renormalization group. *Phys. Rev. E* **71**, 036102 (2005).
- [54] Misguich, G., Pavloff, N. & Pasquier, V. Domain wall problem in the quantum XXZ chain and semiclassical behavior close to the isotropic point. *SciPost Phys.* **7**, 25 (2019).
- [55] Castro-Alvaredo, O. A., Doyon, B. & Yoshimura, T. Emergent hydrodynamics in integrable quantum systems out of equilibrium. *Phys. Rev. X* **6**, 041065 (2016).
- [56] Bertini, B., Collura, M., De Nardis, J. & Fagotti, M. Transport in out-of-equilibrium XXZ chains: Exact profiles of charges and currents. *Phys. Rev. Lett.* **117**, 207201 (2016).
- [57] Spalek, J. t-J Model Then and Now: a Personal Perspective from the Pioneering Times. *Acta Physica Polonica A* **111**, 409 (2007).
- [58] Zhang, F. C. & Rice, T. M. Effective Hamiltonian for the superconducting Cu oxides. *Phys. Rev. B* **37**, 3759–3761 (1988).
- [59] Anderson, P. W., Lee, P. A., Randeria, M., Rice, T. M., Trivedi, N. & Zhang, F. C. The physics behind high-temperature superconducting cuprates: the plain vanilla version of RVB. *Journal of Physics: Condensed Matter* **16**, R755–R769 (2004).
- [60] Degen, C. L., Reinhard, F. & Cappellaro, P. Quantum sensing. *Rev. Mod. Phys.* **89**, 035002 (2017).